SUPERVISORY WIDE-AREA CONTROL FOR MULTI-MACHINE POWER SYSTEM

A THESIS SUBMITTED TO THE UNIVERSITY OF MANCHESTER

FOR THE DEGREE OF DOCTOR OF PHILOSOPHY

IN THE FACULTY OF ENGNIEERING AND PHYSICAL SCIENCES

2011

By

Xuejiao Yang

School of Electrical and Electronic Engineering

Contents

List of Tables

List of Figures

List of Abbreviation

A/D	Analog-to-Digital
ARE	Algebraic Riccati Equation
AVR	Automatic Voltage Regulator
D/A	Digital-to-Analog
EKF	Extended Kalman Filter
FACTS	Flexible AC Transmission System
LHP	Left-Half Plane
LMI	Linear Matrix Inequality
LQR	Linear Quadratic Regulator
LQG	Linear Quadratic Gaussian
LQG/LTR	Linear Quadratic Gaussian/Loop Trasfer Recovery
LTR	Loop Transfer Recovery
MDLQG	Modified Discrete LQG
MIMO	Multi-Input Multi-Output
MPC	Model Predictive Control
PMU	Phasor Measurment Unit
PSS	Power System Stabilizer
SISO	Single-Input Single-Output
SVC	Static VAr Compensator
TCSC	Thyristor Controlled Series Compensation
WAMS	Wide Area Measurement System
ZOH	Zero-Order Hold

Abstract

With the increasing demand for electrical power and the growing need for the restructuring of the power industry, electric power systems have become highly complex with inherent complicated dynamics. Therefore, the study of power system stability has continued to receive significant attention from both academic researchers and industrial practitioners. This thesis focuses on supervisory wide-area control for rotor angle stability of multi-machine power systems using Linear Quadratic Gaussian/Loop Transfer Recovery (LQG/LTR) control theory with guaranteed robustness. The supervisory controllers are developed in both continuous-time and discrete-time framework and their performances and robustness are assessed using both frequency-domain tools, and time-domain simulation results.

The impact of the communication time-delays that commonly exist in wide-area power system control on the performance and robustness of the closed-loop system is investigated. In particular, different methods of incorporating such time-delays into the design of the supervisory LQG controller are considered. This thesis proposes a modified supervisory LQG controller that utilizes the Extended Kalman Filter to estimate the unknown/varying time-delays. Simulation results obtained using numerical examples involving non-linear power system models demonstrate the benefits of the proposed scheme for both time-invariant and time-varying delays. The resulting supervisory control scheme is well suited for maintaining power system stability in the presence of communication time-delays.

Declaration

No portion of the work referred to in the thesis has been submitted in support of an application for another degree or qualification of this or any other university, or other institution of learning.

Copyright Statement

Acknowledgement

The work and research presented in this thesis are funded by the UK Universities group Overseas Research Scholarship (ORS) as well as the Department of Electrical and Electronic Engineering at The University of Manchester.

First and foremost, I would like to express my deepest thanks and sincere gratitude to my supervisor, Dr. Ognjen Marjanovic. I am greatly grateful to him, not only for his enthusiasm, all along support, excellent supervision, and valuable consultation, but also for the constant inspiration and encouragement that he generously provided. His thoughtful guidance, unlimited assistant, and critical remarks made this thesis possible. I really feel lucky to have him as my supervisor. I would like to express my deep gratitude to my advisor Prof. Jovica Milanonic for his valuable advice and support on my research. I am also very grateful to Prof. Hong Wang who introduced me and offered me the opportunity to study PhD in Control System Centre.

I would also like to thank academic staff from Control System Centres, The University of Manchester, particularly Dr. Williams Heath and Dr. Zhengtao Ding, for their encouragement, valuable suggestions and useful discussion on my research work.

Further sincere thanks to all my colleagues in Control System Centre, as well as in Power System Group, for the enjoyable time I work with them and their constant help on my research. They are Dr. Soon Kiat Yee, Dr. Ambrose Adegbege, Mobolaji Osinuga, Sonke Engelken, Olufemi Osunnuyi, Dr. Joaquin Carrasco, Dr. Yiqun Zou, Dr. Zhueyue Song, Qian Lu, Xiafei Tang, and Lipeng Yan. Also many thanks go to my friends in UK and China for their encouragement and support.

Last but not least, I would like to express my special thanks to my dear parents, for their great love, persistent supports and endless encouragement.

To my beloved parents

Chapter 1

Introduction

1.1 Background

Power system stability has been recognized as an important issue for secure system operation since the 1920s. It is defined by Kundur [1] as “the property of a power system that enables it to remain in a state of operating equilibrium under normal operating conditions and to regain an acceptable state of equilibrium after being subjected to a disturbance”. With the increasing demand for power supply and the growing need for the restructuring of the power industry, electric power systems have become highly complex dynamic systems. Therefore, the study of power system stability has continued to receive significant attention from both academic researchers and industrial practitioners.

Stability problems are broadly characterized in two categories: rotor angle stability and voltage stability. Rotor angle stability refers to the ability of a power system to maintain all the synchronous machines in synchronism. Instability is then usually caused by the loss of synchronism, which may exist between one machine and the rest of the system or between different parts of the system. Voltage stability involves the ability of the power system to maintain voltages at all buses under normal operating conditions, even after experiencing a disturbance. The instability is mainly

caused by the failure of the power system to meet the demand for reactive power. This thesis focuses on the rotor angle stability of a multi-machine power system.

As stated in [1], the issue of rotor angle stability involves the study of the electromechanical oscillations inherent in power systems. There are two main types of electromechanical oscillations: local mode oscillations in the frequency range of 0.7 *Hz* and 2 *Hz*; and inter-area oscillations in the frequency range of 0.1 *Hz* and 0.7 *Hz*. Local mode oscillations involve one or more synchronous machines at a power station swinging against the rest of the power system. Inter-area oscillations refer to the swinging of many machines in one part of the power system against machines in another part of the system. This type of oscillations is a system-wide phenomenon and the corresponding inter-area modes are usually poorly-damped in large interconnected power systems. This damping of inter-area mode becomes even worse due to the increasing long distance power transfers in today's interconnected grid. As a result, poorly-damped inter-area oscillations may lead to the instability of the power system and may result in blackouts. Some notable incidents in the history of power system failures are listed as examples [2-5]:

- Detroit Edison (DE)-Ontario Hydro (OH)-Hydro Quebec (HQ) systems experienced several power failures in both early 1960's and 1985.
- Over 70 incidents of unstable inter-area oscillations were observed in the Mid-Continent Area Power Pool (MAPP) system in North America in 1971 and 1972.
- In 1982 and 1983, the State Energy Commission of Western Australia (SECWA) experienced poorly damped system oscillations.
- On August 10, 1996, a major outage occurred in the Western Electric Coordinating Council (WECC) system due to lightly damped low frequency inter-area oscillations.
- In August 2003, oscillations were observed as the cause for the largest blackouts in the north-eastern US/Canada interconnection system.
- On November 4, 2006, severe power oscillations were observed in the European interconnected power system.

The traditional approach for the damping of inter-area oscillations, as well as local-mode oscillations, is to install power system stabilizers (PSSs). A PSS uses local signals, such as rotor speed, power or frequency in order to compute adequate supplementary input signals to the generation excitation system. PSSs have been shown to be effective in improving the damping of both local mode oscillations and certain inter-area oscillations when appropriately tuned [6, 7]. Since PSSs operations are based on local measurements, their effectiveness in damping inter-area modes is limited. The damping may be insufficient for severe disturbances or the increasing inter-area oscillations caused by the heavy power transfer in today's interconnected power systems. Several researchers have proposed modifications to the design of PSSs in order to improve their performance [8-11]. In [8, 9], the design of a PSS was mainly modified by proposing an improved tuning method. On the other hand, PSS was retuned by selecting different input signals in [10], while work in reference [11] considered the coordination of PSSs in multi-machine power system. However, electromechanical oscillations in wide-area power system may be insufficiently damped with these modified local PSSs, particularly when subjected to large disturbance.

Since the late 1990s, Flexible AC Transmission System (FACTS) devices have been proposed for the enhancement of power system stability. These include Static VAr Compensator (SVC) and Thyristor Controlled Series Compensation (TCSC) [12]. FACTS devices were initially designed for two main objectives: (1) to improve the power transfer capability of transmission systems and (2) to maintain the power flow over designated routes [13]. Many researchers also explored the potential of FACTS devices for damping of electromechanical oscillations [14]. These results led to increased interest in designing controllers for FACTS devices in order to improve damping of electromechanical oscillations [15-20]. However, the feasibility of FACTS devices for improving the damping of electromechanical oscillations has been questioned due to the high cost of their implementation [21, 22]. It is also important to note that both conventional PSS and FACTS devices are local controllers, and are only effective in damping local modes. Their effectiveness in damping inter-area modes is limited because inter-area modes are usually not controllable and observable in the generator's local signals as compared to local modes [23].

There has recently been an increased interest in applying Wide Area Measurement System (WAMS) and control devices to improve damping of inter-area oscillations, hence improving the overall power system stability. These wide-area damping control schemes rely on the Phasor Measurement Unit (PMU) technology and have been shown to significantly improve the damping of inter-area oscillatory modes. For example, Kamwa and co-workers [23] illustrate that wide-area stabilizing controllers have significant potential for improving the dynamic performance of power system when implemented on few sites only. New PSSs were designed by using the supplementary input from remote PMUs which geographically spread over nine electrically coherent areas in this reference. Using Hydro-Quebec examples, Kamwa *etal* also shows that wide-area measurements result in both clean and robust observability of inter-area oscillations and the load voltage collapse phenomenon. It was also shown that the transient stability margin can only be extended with wide-area control, and the impact on the inter-area mode damping with wide-area control is 1.5 to 2 times stronger than that of local PSSs. A more comprenhencive overview about Wide Area Monitoring, Protection and Control Systems can be found in [24], in which Terzija *etal* discuss a number of challenging pointes relevant for current and future development of Smart Grid solutions, also those relevant for control applications based on wide area measurements.

1.2 Literature Review

Among the wide-area control schemes, the wide-area damping controller has been shown to have significant advantages in terms of reliability and operational flexibility [23]. Each generator may be equipped with a local controller, called Power System Stabilizer (PSS), whose role is to improve damping of the power system and therefore to deal with the oscillatory electromechanical modes. A supervisory controller is placed at a control centre receiving remote signals from PMUs, as well as providing supplementary control signals back to each machine together with the local control signals from the local PSS. The supervisory controller provides sufficient damping on the electromechanical modes if the local PSSs are not effective or if there is severe disturbance acting on a power system. In addition, from an economic viewpoint, it may be more cost effective to implement centralized

controllers that utilise existing control devices rather than to install new control devices [22].

1.2.1 Controller Design

Several design methods based on WAMS technology have been proposed to address the supervisory damping control problem. The simplest of these uses a lead-lag block compensator, which is similar to the conventional Power System Stabiliser (PSS) [10, 23]. This controller is usually designed in a similar way to the conventional PSS, which is based on a fixed operating condition of the linearised power system model. H_∞ control is a well-known advanced control technique for its robustness to the uncertainties and has been used in wide-area damping control by a number of researchers [18, 25-28]. However, it was found to be prone to pole-zero cancellation between the system plant and the controller when based on the solution of the Algebraic Riccati Equation (ARE) method, as shown in [29]. Also, since the H_∞ control method considers the worst-case scenario, the resulting controller is likely to be overly conservative when dealing with less severe disturbances. Furthermore, the feasibility of the whole design procedure may be questioned due to the difficulty in selecting the weighting functions [30, 31].

Linear Quadratic Gaussian (LQG) control is considered to be a cornerstone of modern optimal control theory and has been widely applied in the control of multi-variable systems [32, 33]. This approach involves deigning an optimal full state-variable feedback (linear quadratic regulator (LQR)) and the observer (Kalman filter) to provide the state estimates for the feedback function. The control method benefits from the separation principle, which allows the controller to be designed in a straightforward manner for multivariable systems even by solving two separate matrix equations [34]. The important feature of LQG control theory is that it enables controller designers to trade off regulation performance and control effort. In terms of control design, due to reference input changes, the LQG type of cost function is often a more practical criterion when minimizing tracking errors or control signal variations compared to the H_∞ control method [35]. In addition, the process

disturbance and measurement noise can be taken into account during the LQG design procedure. This additional step can easily be accommodated in the standard LQG design. It is also straightforward to increase the roll-off of the LQG controller by adjusting the open-loop transfer function [36]. The resulting closed-loop system (under certain conditions) is guaranteed to be asymptotically stable.

It has been pointed out that there are no guaranteed performance and robustness properties for the LQG-controlled system [29]. Kwakernaak [37] and Doyle and Stein [38, 39] proposed the Loop Transfer Recovery (LTR) procedure to recover the performance and robustness properties at either the plant input or the plant output. With the combination of the recovery procedure, a robust controller design technique (LQG/LTR) with guaranteed robustness is proposed in [39] and further discussed by Stein and Athans [40]. This control method has also been adopted in control of power system stability problems. In [41], the design of PSS based on the LQG/LTR technique is proposed to formulate more robust stabilizers. Later on, Dalela and Radman [42] proposed LQR and LQG control procedures as a supplementary controller to PSSs in order to increase stability and reliability of the system. However, they only considered simple power systems. LQG or LQG/LTR control methods have also been applied to the damping of inter-area oscillation modes by some researchers. Shaalan [43] implements an LQG controller for load frequency control problem. The LQG controller provides better robustness as well as tracking performance compared to the PI (Proportional and Integral) controller. LQG/LTR control based on closed-loop iterative identification method is proposed in [44] and applied to a SVC to increase the damping of low-frequency oscillations in multi-machine power systems. Son [20] introduces the LQG/LTR technique into the design of TCSC devices for the damping controller design. More recently, Zolotas *etal* [31] presents LQG/LTR damping control scheme for a proposed minimum-phase square system augmentation to improve the inter-area mode oscillations of power systems.

1.2.2 Discrete-Time Control

The controllers reviewed in Section 1.2.1 are all designed under the assumption that the control algorithm executes instantaneously, i.e. assuming that the sampling period is infinitely small. In other words, all of these controllers are assumed to be

represented as continuous-time systems. In practice, however, this assumption may be highly unrealistic, especially when considering large-scale systems described by high-order dynamic models possessing potentially large numbers of input and output variables. This is particularly true when considering the problem of rotor angle stability for which the dominant dynamics are in the frequency range of 0.1 to 2.0 *Hz*. In such applications the issue of sampling may prove to be a critical performance-limiting parameter. Therefore, it would be advantageous to investigate and understand this impact by addressing the problem of multi-area supervisory control using discrete-time framework. Several publications have focused on the design of discrete-time controllers for power systems. In particular, PSS was implemented using sampled values of voltage and current on a microprocessor in [45]. Digital control was adopted to generating units by updating the control parameters and set-points at regular intervals in [46] and where each generating unit is configured with its own mini-computer for local digital control. Digital AVR and PSS were designed to enhance the stability of power systems in [47, 48]. In [49], the analysis of asymptotical stability of digital control in power systems with a special emphasis on digital PSS was considered. Power systems with digital controllers are treated as nonlinear hybrid dynamical systems, and analyzed in a more exact way compared to the conventional linear analysis for digital controls.

Sampling of the continuous-time signal from the plant and its conversion to a sequence of numbers is the fundamental property of the design of the discrete-time controllers. These digital numbers are processed by a discrete-time controller. Then the digital signals from the discrete-time controller are reconstructed and applied to the plant. Various reconstructions are typically used: Shannon Reconstruction, Zero-Order Hold (ZOH), and Higher-Order Holds [50]. For the design procedure of discrete-time controllers, it is quite common to carry out a continuous design first, followed by the discretisation of the continuous-time controller. Thus, it is important to perform discretisation in a proper manner to maintain the desired performance.

In order to minimise the amount of degradation that occurs during discretisation it is desirable to maximise the sampling rate of the controller. However, the sampling rate is limited by several factors, such as PMU data reporting rates, bandwidth of communication links, the cost of hardware and capability of available instruments,

etc. Therefore, the selection of an appropriate sampling rate is a critical issue that has a direct impact on the design of discrete-time controllers and, subsequently, the performance and robustness of the resulting closed-loop system.

1.2.3 Consideration of Communication Time-Delay

As stated in Section 1.1, WAMS and wide-area damping control rely on the availability of PMU and communication equipment. The PMU devices are used to sample voltage and current waveforms of a bus at a sampling rate as high as 30 *Hz* [51]. Transmission of the measurement acquired might be between different generating units or substations over large distances. As a result, it is widely accepted that communication time-delays will inevitably be present [52]. These time-delays are typically in the range of 0.3-1.0 second [51], and may be caused by measurement processing, transmission, synchronization and control signal calculation or transmission. Since these time-delays are comparable to the time periods of some of the critical inter-area modes, their presence directly impacts the performance of the installed wide-area controllers that utilise this delayed information [52-54]. Therefore, time-delays should be accounted for in the design of the wide-area damping control. Classical control design procedures explicitly account for the presence of communication time-delays by utilising the concept of a phase margin, as explained in [29]. However, phase information is not readily available when considering multivariable control problems, such as the one addressed in this thesis.

Several researchers have proposed power system damping controller design with the consideration of time-delays. In [55], time-delay was represented by the first-order Pade approximation in order to design a wide-area power system controller using TCSC. The designed controller was applied to a 24-generator system and the results showed the use of multiple input signals for the design of TCSC allows the controller be more effective in providing additional damping to the inter-area modes. Dotta *etal* [56] proposed a centralized optimal power system controller-based Linear Quadratic Regulation methodology (LQR) for the enhancement of power system small-signal stability by using the second-order Pade approximation of the transmission time-delays. The Smith prediction approach was utilized to compensate time-delays associated with communication and measurements in [57]. When the open-loop of

the power system has lightly damped poles, however, the Smith predictor approach does not ensure a minimum damping ratio of the closed-loop poles [58]. In [51] and [58], a H_∞ control strategy based on the unified Smith predictor (USP) was proposed to design a centralized power system damping controller which was a 2-input 1-output controller. This design may be inappropriate for multi-input multi-output (MIMO) controller design. Wu *etal* [59] proposed the design of a supervisory power system stabilizer (SPSS) accounting for time-delays based on the H_∞ gain scheduling theory. However, the designed SPSS can only tolerate time-delays on the order of 100 *ms*, which may be insufficient in wide-area damping control with some types of communication link, such as power line or satellite link [60]. The LMI approach was used by [61] to design an adaptive supervisory controller for the stabilization of a multi-machine power system considering signal transmission delays. The time-delay was considered as a structured uncertainty in the controller design. Since the supervisory adaptive controller was designed based on the H_∞ methodology and can tolerate 0.7 seconds time-delay, the designed controller may be overly conservative when dealing with less severe disturbances or longer time-delays.

1.3 Aims of the Research

In order to successfully introduce new technology to real-world problems it is critical to fully understand the impact of its practical implementation on the performance and the robustness of the resulting closed-loop system. Therefore, the main focus of this thesis is to investigate the impact of two critical factors on the performance of the designed wide-area supervisory controllers. These two critical factors are discrete-time implementation and the presence of communication time-delays.

Firstly, the design of the supervisory controller is to be conducted in the continuous-time framework using optimal control theory and utilising the frequency-domain analysis tools in order to properly tune the resulting controller so that the closed-loop system possesses adequate robustness and performance qualities. In particular, Linear quadratic Gaussian/Loop Transfer Recovery (LQG/LTR) methodology is to be used, which, compared to some other more advanced techniques such as H_∞,

addresses the ‘average’ rather than ‘worst case’ scenarios, resulting in less conservative controller. Furthermore, the tuning of LQG/LTR controller is typically performed using a small number of user-specified parameters, which significantly simplifies the design procedure when considering high-order multivariable systems such as the one used in this thesis.

There has been a number of publications [99, 100] that discuss the danger of relying on the mathematical conveniences of the optimal control theory and ignoring the intuitive tools utilised by the classical control methodologies, which are mostly employing frequency-domain analysis methods. Therefore, these frequency-domain analysis tools and concepts will be employed throughout this thesis in order to assess the performance and the robustness of the closed-loop system.

Once the continuous-time controller is successfully designed, then the next step will be to re-design supervisory wide-area controller but using discrete-time framework. Discrete-time controller will also be designed using LQG/LTR methodology and using frequency domain analysis tools. Additionally, dependence of the resulting closed-loop system performance on the critical factor of sampling period will be investigated in detail. Sampling period is particularly important in the applications that involve large-scale systems with relatively fast dynamics, such as the one employed in this thesis.

The important additional implication of using discrete-time controller is that the impact of computational delays is automatically accounted for and assumed to be equal to the sampling period. Hence, this thesis aims to investigate the impact of computation time, required for the execution of a control algorithm, on the performance of the closed-loop system. It should be noted that the computation time may be an important factor when dealing with high-order large-scale systems that have relatively high open-loop bandwidth, such as the one considered in this thesis. In these cases the assumption of continuous-time implementation maybe highly inappropriate since it assumes unrealistic computational power.

Due to the fact that the modern power systems are operated over large geographical areas and the fact that the final control element, e.g. generator, may be several hundred miles away from the supervisory controller, it is inevitable that some

communication time-delay will occur. Therefore, this thesis will investigate the impact that such communication time-delays have on the performance and robustness of the closed-loop system. Also, different methods of integrating the time-delays into the design of the supervisory LQG/LTR controller will be investigated. These will include rational approximations of the time-delays in continuous-time framework and exact representation of time-delays when designing discrete-time supervisory controller.

Finally, this thesis aims to propose a novel approach of estimating communication time-delays by using Extended Kalman Filter technique and combining it with the discrete-time LQG/LTR controller. Extended Kalman Filter will be employed to estimate the actual time-delays present in the communication channel, which are likely to be unknown and time-varying. Estimated time-delays will then be used to update the prediction model, which is utilised by the supervisory wide-area controller. As a result, the controller is expected to be capable of maintaining power system stability in the presence of communication time-delays.

1.4 Main Contributions of the Thesis

The main contributions of the thesis are summarized as follows:

- Design of the supervisory continuous-time LQG/LTR-based wide-area controller that incorporates integral action and is based on loop shaping methodology. The desired power system specifications, such as system bandwidth, are met by using frequency-domain analysis tools.
- Design of the supervisory discrete-time LQG/LTR controller used for the damping of inter-area oscillations that incorporates integral action and is tuned using frequency-domain analysis tools. Particular focus is placed on the impact that the sampling period has on the performance and robustness of the resulting closed-loop system. Finally, it is shown how to re-design discrete-time controller, by reducing the bandwidth, in order to recover some of the performance sacrificed when increasing the sampling period.

- Detailed analysis of the impact that the communication time-delays have on the performance of the continuous-time and discrete-time LQG/LTR controller designed to improve damping of the inter-area electromechanical mode. Different rational approximations used to represent the time delay in a transfer function form are utilized for continuous-time controller design. These different approximations are compared and the results confirm that the Pade Approximation is the most appropriate method used when designing continuous-time controllers that are intended to be robust to communication time-delays. In the case of discrete-time controller design, time-delay is represented exactly without resorting to rational approximation. Nevertheless, the delay margin is found to be similar for both continuous-time and discrete-time controllers.
- Proposal of a modified supervisory LQG controller (MDLQG) for the system with unknown time delays that incorporates Extended Kalman Filter (EKF). Both constant and varying unknown time-delays are considered in the design. Methodology is demonstrated using both numerical examples and the test power system simulation. It is very important to point out, however, that the methodology of employing EKF has been proposed independently by [101] who applied the method to a far simpler single-input, two-output system. However, the author of this thesis was completely unaware of that research work, which was published at the same time as the submission of the conference paper detailing results from this thesis regarding employment of EKF. It is clear from the proximity of the publication dates of [101] and the conference paper written by the author of the thesis that the respective research projects were conducted independently of each other without any mutual awareness of each other's work.

1.5 Outline of the Thesis

Chapter 1: Introduction describes the basic concepts related to the issue of the power system stability and rotor angle stability in particular. Review of WAMS based wide-area damping control methods is also provided. Particular focus in the review is placed on the control methods, discrete-time implementation and the

considerations of communication time-delays. Aim of the PhD project is then presented along with the main contributions of the thesis. Finally, the outline of the thesis is provided.

Chapter 2: Power Systems: Stability, Modelling and Tools for Analysis introduces the basic concepts necessary to understand the issues surrounding power system stability and electromechanical oscillations. A detailed description of the modelling for each of the main power system components is presented. These components include synchronous generator, excitation system, power system stabilizers (PSS), transmission lines, transformer, FACTS devices, typical electrical loads and the electrical network. Modal analysis method is then introduced followed by the modelling and analysis of a test multi-machine power system.

Chapter 3: Continuous-Time LQG/LTR for Multi-Machine Power System considers the design of a supervisory continuous-time LQG/LTR controller for wide-area damping control of power systems, using the loop shaping methodology. The controller is tuned such that certain frequency domain characteristics are satisfied, such as the bandwidth and peak values of the closed-loop transfer functions. The proposed LQG/LTR controller is compared with the conventional local PSS regulators in order to demonstrate its effectiveness for the damping control of a multi-machine power system. Also, the controller is assessed in terms of its robustness to the changes in the operating conditions.

Chapter 4: Discrete-Time LQG/LTR for Multi-Machine Power System focuses on the design of the supervisory LQG/LTR controller using discrete-time framework to represent open-loop dynamics of the studied power system. Also, this chapter focuses on the impact that the sampling period has on the performance of the closed-loop control system. The effectiveness and robustness of the designed supervisory discrete-time LQG/LTR controller is then verified using the non-linear power system simulation with and without auxiliary Power System Stabilizers. Also, the robustness of the supervisory controller with respect to changing operating conditions is assessed by changing the power transfer between the two areas in the studied power system.

Chapter 5: LQG/LTR for Multi-Machine Power System with Time-Delay considers the design of both continuous-time and discrete-time LQG/LTR controller for multi-machine power system in the presence of communication time-delays. In the case of continuous-time LQG/LTR control, two main rational approximations are used to the model the time-delays. These two approximations are also extensively compared. Discrete-time LQG/LTR control of a power system is considered using exact expressions for the time-delays rather than resorting to rational approximations. Different time delays are used to examine the effectiveness of the proposed controllers in terms of the achieved delay margins and their influence on the damping of the critical inter-area mode. Performance and robustness of the designed controllers are assessed using both frequency-domain analysis, which relies on the linear description of the system dynamics, and time-domain analysis, which utilises high-fidelity non-linear simulation model of a power system.

Chapter 6: Supervisory Controller Development using Extended Kalman Filter for System with Unknown Time-Delay proposes a modified discrete-time LQG/LTR controller that utilises Extended Kalman Filter technique in order to estimate unknown and varying communication time-delays. Effectiveness of the proposed approach is verified using numerical example followed by the evaluation on multi-machine power system for both small signal and large signal disturbances.

Chapter 7: Conclusions and Future Work presents the main conclusions of the research presented in this thesis and suggests topics that should be considered in the future work.

Chapter 2

Power System: Stability, Modelling and Tools for Analysis

2.1 Introduction

This chapter firstly introduces some basic concepts necessary to understand the issue of power system stability. The modelling of the main components of the power system is then described. These components include transmission lines, transformer, synchronous generator, excitation system, PSS regulators, FACTS devices, typical electrical loads and the electrical network. The effective power system analysis method, namely modal analysis, is then introduced together with the concepts of eigenvalues and eigenvectors, mode shapes as well as the participation and damping factors.

Based on these fundamental concepts, the linearised state-space representation of the test power system, which is a 2-area 4-machine 8-bus power system, is presented and analysed using frequency-domain tools. This test power system and its linearised state-space model will be used throughout the thesis.

As stated in the previous chapter, the focus of this thesis is on the issue of the rotor angle stability, especially on the damping of inter-area electromechanical oscillatory modes. The other issues regarding the stability of voltage and frequency will not be considered in this thesis due to the time constraints.

2.2 Power System Stability

Rotor angle stability is defined as the ability of interconnected synchronous machines of a power system to remain in synchronous [1]. When a synchronous machine loses synchronism with the rest of the system, the speed of its rotor is different from that required to generate voltages at system frequency. DeMello and Concordia [62] developed insights into the inner workings of the synchronous machine, and established the concept of damping and synchronizing torque in the system. in particular, it can be shown that system stability depends on the changes of the following two components for each of the synchronous machines:

$$\Delta T_e = T_s \Delta\delta + T_D \Delta\omega \tag{2.1}$$

where

$T_s \Delta\delta$ is the *synchronizing torque* component which is in the phase with the rotor angle perturbation $\Delta\delta$

$T_D \Delta\omega$ is the *damping torque* component which is in the phase with the speed deviation $\Delta\omega$

In the case of insufficient synchronising torque, the instability of the power system will occur through an aperiodic drift in rotor angle. On the other hand, insufficient damping torque may result in oscillatory instability.

Rotor angle stability is usually characterized as either small-signal or transient stability, according to [1], both of which will be briefly introduced in the remainder of this thesis.

2.2.1 Small Signal Stability

Clearly as the name suggests, small signal stability is the ability of power system to maintain synchronism under small disturbances. Theses disturbances could be small variations in loads and generation. The disturbances are considered to be small if the resulting dynamic behaviour can be adequately represented using linear model description.

Due to the fact that the system dynamics can be represented using linear model, modal analysis can be readily applied for the determination of small signal stability. Instability arising from small-signal disturbances manifests itself in one of the following two forms:

i. Steady increase in generator rotor angle due to lack of synchronizing torque.
ii. Rotor oscillations of increasing amplitude due to lack of sufficient damping torque.

2.2.2 Transient Stability

Transient stability is the ability of the power system to maintain synchronism when subjected to a severe transient disturbance [1]. Severe transient disturbances may be resulted from a loss of generation or a large load, faults on the transmission network, etc. System response subjected to such large disturbances involves large changes of generator rotor angles, power flows, bus voltages among other system variables and is influenced by the non-linear power-angle relationship. In large power system, transient stability may not always occur as first swing instability; it could be the result of the superposition of several modes of oscillation causing large excursions of rotor angle beyond the first swing [1].

2.3 Electromechanical Oscillations

As mentioned in the previous section, small signal stability problem is usually one of insufficient damping of system oscillations. It is caused by the interaction between the electrical and mechanical processes in the power system, also named as electromechanical oscillation. Theses oscillations are inherent in the power system. Electromechanical oscillations can be caused by small disturbances such as changes in generation or load. They may also be initiated by large disturbances such as faults in the system or heavy loading. The stability of the whole power system is largely depended on the stability of such electromechanical modes. If the electromechanical modes are unstable or poorly damped, the overall system response will be diverging or sustained oscillatory.

These electromechanical oscillations can be mainly divided into local mode oscillations and inter-area oscillations. They will be further discussed in the following.

Local Mode Oscillations

This type of oscillation generally involves one or more synchronous machines at a power station swing together against a comparatively large power system or load centre. The frequency of this oscillation is in the range of 0.7 to 2 Hz. The corresponding local modes are usually dealt with the more conventional methods of tuning as discussed in [63, 64].

Inter-Area Oscillations

Inter-area oscillations usually involve combinations of many machines in one part of a power system swing against machines in another part of the power system. They are normally in the frequency range of 0.1 to 0.7 Hz [65]. Inter-area oscillation is a system wide phenomenon and the corresponding inter-area modes are usually poorly damped. The damping characteristic of the inter-area mode is dictated by the tie-line strength, the nature of the loads and the power flow through the interconnection and the interaction of loads with the dynamics of generators and their associated controls. Many researches have been made on the study of this oscillation, such as the dynamic properties of these oscillations [66], the review of the instances of such occurrences of poorly damped or unstable inter-area modes [65].

As stated above, electromechanical oscillations have serious impacts on the operation of the system. Inter-area oscillations in the interconnected large power system clearly identify inadequate damping as the primary factor leading to system separation. The amount of damping and the frequency of oscillation varies with system operating conditions [67]. Over the years, many incidents of system outage resulting from the inter-area oscillations have been reported: inter-connected Detroit Edison (DE)-Ontario Hydro (OH)-Hydro Quebec (HQ) systems in early 1960's [68]; the power blackout of August 10, 1996 in the Western Electricity Co-ordination Council (WECC) experienced unstable low frequency inter-area oscillations following the outage of four 400 kV lines [69]; and recent 2003 blackout in eastern Canada and US

[70]. Therefore, stability of the overall system is heavily influenced by the electromechanical oscillations. The damping of the inter-area oscillations will be mostly concerned in this thesis.

2.4 Power System Modelling

The modelling of different components of the power system is introduced. Due to this research is focused on the short-term stability, governor action and prime movers are not reviewed and modelled.

2.4.1 Transmission Lines

The most important roll to transmit and distribute power from power station to individual consumers within transmission and distribution networks or connect a power station to a substation is transmission lines. It can be either overhead lines or underground cables. Overhead lines are mostly used to transmit long-distance high-voltage electric power in transmission system. On the other hand, underground cables are responsible for the transmission of low- and medium-voltage among urban distribution system. A transmission line is characterized by four parameters: series resistance *R*, series inductance *L*, shunt conductance *G* and shunt capacitance *C* with the following description.

Series Resistance, R. Resistance of the lines, which are determined from manufacturers' database.

Series Inductance, L. The line inductance depends on the flux linkages within the conductor across section and external flux linkages. The value of inductance per phase depends on the self geometric mean distance, denoted as D_s , and the geometric mean of the distances between the conductors of the three phase, denoted as D_{eq}.

Shunt Conductance, G. It indicates the losses raised by leakage currents along insulator strings and corona, which is usually ignored due to the small effect on the power lines.

Shunt Capacitance, C. The capacitance between conductors is the charge per unit of potential difference, which is the charge between the conductors of a transmission line. Its value mostly depends on the conductor radius *r*, the permittivity of the dielectric medium *k*, and D_{eq}.

The four parameters are distributed throughout the length of the line. The line performance can be represented by the following equations on a per-phase basis.

$$z = R + j\omega L \tag{2.2}$$

$$y = G + j\omega C \tag{2.3}$$

Equation (2.2) represents the series impedance per unit length per phase, and equation (2.3) shows the shunt admittance per unit length per phase.

2.4.2 Transformers

The transformer is a well-known device that links the parts of the power system with different voltage levels. In addition to changing the voltage levels, transformers are also used to control the voltage and reactive power flow. Due to their functions, power system transformers can be classified into three categories [71]:

Generator step-up transformers. They connect the generator to the transmission system.

Transmission transformers. They connect different parts of the transmission systems that operate at different voltage levels; or connect the transmission and distribution systems.

Distribution transformers. They transform the voltage from a high level to a low voltage level required by the individual consumer.

Due to the large number of voltage levels involved in a power system, as well as system variables, the per unit values and equations are used for simpler computation and solutions [71]. Figure 2.1 shows the per unit equivalent circuit of a two-winding transformer. The resulting equivalent circuit equations are expressed in (2.4) and (2.5) as follows [1].

$$\overline{v}_p = \overline{n}_p{}^2 \overline{Z}_{p0} \overline{i}_p + \frac{\overline{n}_p}{\overline{n}_s} \overline{v}_s - \overline{n}_s{}^2 \frac{\overline{n}_p}{\overline{n}_s} \overline{Z}_{s0} \overline{i}_s \tag{2.4}$$

$$\overline{v}_s = \frac{\overline{n}_s}{\overline{n}_p} \overline{v}_p - \overline{n}_p{}^2 \frac{\overline{n}_s}{\overline{n}_p} \overline{Z}_{p0} \overline{i}_p + \overline{n}_s{}^2 \overline{Z}_{s0} \overline{i}_s \tag{2.5}$$

where the superbars denote per unit values, $\overline{v}_p$, $\overline{v}_s$, $\overline{i}_p$, $\overline{i}_s$ are the per unit phase voltages and currents, and

$Z_{p0} = Z_p$ at nominal primary side tap position

$Z_{s0} = Z_s$ at nominal secondary side tap position

$n_{p0} =$ primary side nominal number of turns

$n_{s0} =$ secondary side nominal number of turns

The standard equivalent circuit of Figure 2.1 is shown in Figure 2.2 with:

$$\overline{n} = \frac{\overline{n}_p}{\overline{n}_s} = \frac{n_p n_{s0}}{n_{p0} n_s} \tag{2.6}$$

$$\overline{Z}_e = \overline{n}_s^2 \left(\overline{Z}_{p0} + \overline{Z}_{s0} \right) = \left(\frac{n_s}{n_{s0}} \right)^2 \left(\overline{Z}_{p0} + \overline{Z}_{s0} \right) \tag{2.7}$$

This standard representation form of equivalent circuit equations is widely used of two-winding transformer in power systems [1].

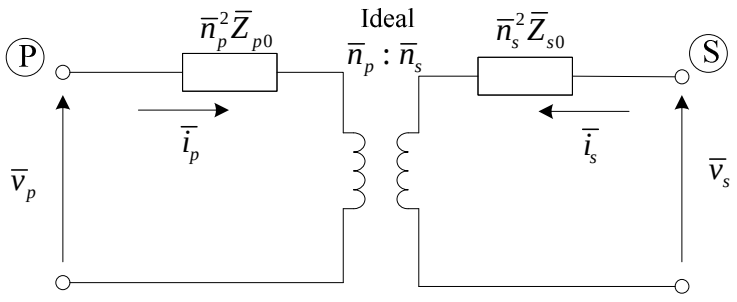

Figure 2.1 Per unit equivalent circuit of a two-winding transformer [1]

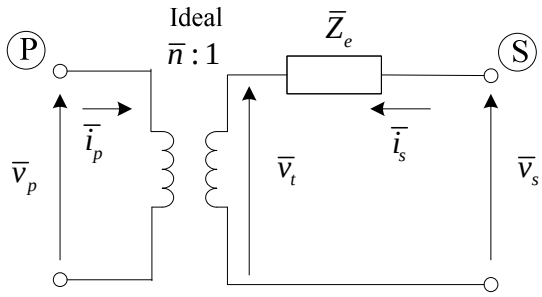

Figure 2.2 Standard equivalent circuit of Figure 2.1 [1]

2.4.3 Synchronous Generator

As previously mentioned, the power system stability problem is largely one of keeping interconnected synchronous machines in synchronism. Therefore, an understanding of their characteristics and accurate modelling of their dynamic properties are of fundamental importance to the study of the power system stability. There are two basic types of synchronous machines, round rotor machine and salient pole machine. Figure 2.3 shows the block diagram of the generator with the associated excitation control. More details on the structure and introduction of synchronous machine can be found in [1, 71, 72].

A practical model derived by Saidy and Hughes [73] is used in this thesis, it is also named model 2*d*2*q*. This model is considered appropriate for representation of round rotor machines, as well as salient pole machines. The set of different equations that describes the dynamics of this model are given below [73].

$$\dot{E}_q^{''} = \frac{1}{T_{d0}^{''}}\left[E_q^{'} - \left(X_d^{'} - X_d^{''}\right) I_d - E_q^{''}\right] + \dot{E}_q^{'} \tag{2.8}$$

$$\dot{E}_q^{'} = \frac{1}{T_{d0}^{'}}\left[E_{fd} - \left(X_d - X_d^{'}\right) I_d - E_q^{'}\right] \tag{2.9}$$

$$\dot{E}_d^{''} = \frac{1}{T_{q0}^{''}}\left[E_d^{'} - \left(X_q^{'} - X_q^{''}\right) I_q - E_d^{''}\right] \tag{2.10}$$

$$\dot{E}_d^{'} = \frac{1}{T_{q0}^{'}}\left[\left(X_q - X_q^{'}\right) I_q - E_d^{'}\right] \tag{2.11}$$

$$\dot{\omega} = \frac{2\pi f_0}{2H}\left[P_m - P_e\right] \tag{2.12}$$

$$\dot{\delta} = \omega - 2\pi f_0 \tag{2.13}$$

$$V_d = E_d^{''} + X_q^{''} I_q \tag{2.14}$$

$$V_q = E_q^{''} - X_d^{''} I_d \tag{2.15}$$

$$V_t = \sqrt{V_d^2 + V_q^2} \tag{2.16}$$

$$P_e = V_d I_d + V_q I_q \tag{2.17}$$

where

ω	rotor speed;
δ	rotor angle;
$X_d, X_d^{'}, X_d^{''}$	*d*-axis synchronous, transient, sub-transient reactance;
$X_q, X_q^{'}, X_q^{''}$	*q*-axis synchronous, transient, sub-transient reactance;
$T_{d0}^{'}, T_{d0}^{''}$	*d*-axis open-circuit transient, sub-transient time constant;
$T_{q0}^{'}, T_{q0}^{''}$	*q*-axis open-circuit transient, sub-transient time constant;
H	inertia constant;
I_d, I_q	generator *d*-axis, *q*-axis current;
V_d, V_q, V_t	generator *d*-axis, *q*-axis, terminal voltage;
P_e	electrical power.

For salient pole machines, there is $X_q^{'} = X_q$, the *d*-axis transient voltage component, $E_d^{'}$, is equal to zero. Consequently, equation (2.11) is eliminated.

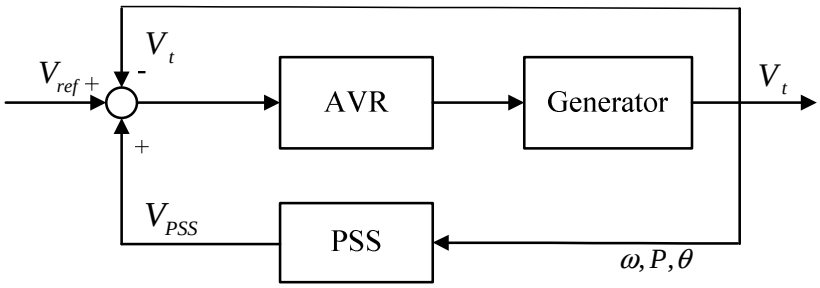

Figure 2.3 Block diagram of the generator with excitation control

2.4.4 Generator Excitation System

The generator excitation system consists of an exciter and an Automatic Voltage Regulator (AVR). An exciter can be either rotating or static. The AVR regulates the generator terminal voltage by controlling the amount of current supplied to the generator filed winding by the exciter [71]. The standard IEEE type DC1A exciter block diagram is shown in Figure 2.4. K_E is the ratio of the resistance of the exciter field circuit and the slope of the air-gap line or the line tangent to the linear portion of the open circuit saturation curve. T_E refers to the integration of the forward loop. $S_E(E_{fd})$ represents the saturation function. The voltage regulator is represented by a gain K_A with time constant T_A. The outputs of these regulators are usually limited by either by the effects of saturation or the power supply limitation [1]. The measured generator terminal voltage V_t is compared with the reference voltage V_{ref} to produce the voltage error ΔV. The final inputs of the generator excitation system, V_i, is the error voltage compensated with the voltage from Power System Stabilizer (PSS) V_{PSS}. The output of AVR is the field voltage which is usually limited by either the effects of saturation or the power supply and can be easily represented as limits on the output values of the regulator.

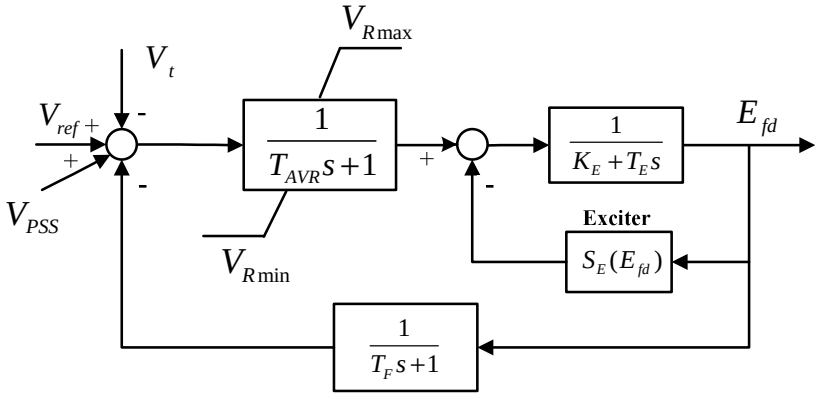

Figure 2.4 Block diagram of IEEE type DC1A exciter

2.4.5 Power System Stabilizer

Power system stabilizers (PSS) are used to provide damping torque for the synchronous machines by generating supplementary control signals for the excitation system in order to suppress oscillations. Electromechanical oscillations of small magnitude and low frequency exist in the interconnected power system and often persist for long periods of time, and in some cases even impose limitations on the power transfer capability. In addition, the generator voltage regulator action will pose a detrimental impact upon the dynamic stability of the power system when the synchronizing torque of synchronous machines is increased in order to improve the transient stability of the power system. Figure 2.5 shows the general structure of a PSS. Equation (2.18) represents the transfer function of the general structure of PSS.

$$\begin{aligned} H(s) &= K_{PSS}\left(\frac{1+T_1 s}{1+\alpha T_1 s}\right)^N W(s)F(s) \\ &= K_{PSS}\left(\frac{1+T_1 s}{1+\alpha T_1 s}\right)^N \left(\frac{T_W s}{1+T_W s}\right)\left(\frac{1+T_A s}{1+T_B s}\right) \end{aligned} \tag{2.18}$$

N is the number of lead-lag blocks, *W(s)*, *F(s)* is washout and low pass filter respectively. K_{PSS} is the gain of the transfer function, α and T_1 refers to the lead-lag constant and time constant respectively. T_W, T_A, and T_B ($T_W = 1s \sim 20s$, typically $3s \sim 10s$; $T_B/T_A < 10$) are time constants of *W(s)* and *F(s)*.

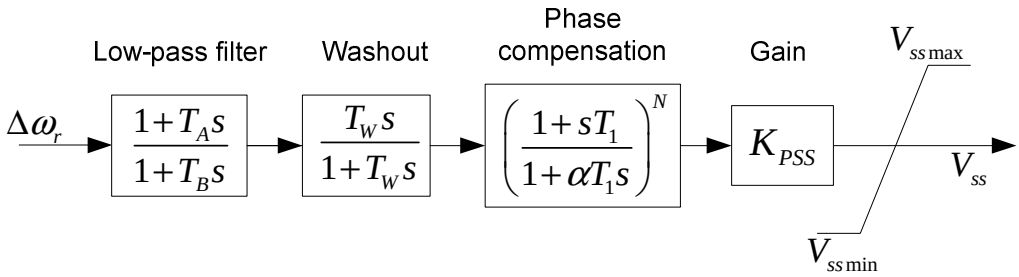

Figure 2.5 Major elements of a PSS [1]

2.4.6 FACTS Devices

Flexible AC Transmission Systems, named FACTS, was first issued in the United States to improve the control of the transmission systems in the late 1980s [13]. The FACTS devices have been widely introduced for various applications with two original main objectives [13]:

1) To increase the power transfer capability of transmission systems;
2) To keep power flow over designated routs.

The FACTS devices are typically categorised into two types. The first type utilizes reactive impedances or a tap-changing transformer with thyristor switching to provide the control; the second type uses static converters as voltage sources [13].

The devices, the Static Var Compensator (SVC), thyristor-controlled series capacitor (TCSC) and phase-shifter all belong to the first group. Each device acts on one of the three parameters determining power transmission. SVC acts on voltage, TCSC acts on transmission impedance and phase-shifter acts on transmission angle. The second type of FACTS devices employs converter-based synchronous voltage source. Devices such as Static Synchronous Compensator (STATCOM), Static Synchronous Series Compensator (SSSC), Unified Power Flow Controller (UPFC) and the Interline Power Flow Controller (IPFC) all belong to the second type of FACTS devices. The STATCOM controls the voltage by reactive shunt compensation. The SSSC controls the effective transmission impedance through series compensation. The UPFC can control all three transmission parameters (voltage, impedance, voltage angle), as well as the real and reactive power flow in the line [13].

SVC was firstly used in mid-1970s. It has been known that SVC has significant benefits on voltage regulation, as well as the improvement of transient stability and dynamic stability [1]. In addition, SVC can mitigate the power oscillations and has been utilized to damp the inter-area modes and to maintain system stability. The structure and modelling of SVC is described in the following mainly from reference [74]. The model of SVC is represented by the per unit equations (2.19). Figure 2.6 depicts the block diagram of the transient model of the SVC [74].

$$\begin{bmatrix} \dot{x}_c \\ \dot{\alpha} \end{bmatrix} = f\left(x_c, \alpha, V, V_{ref}\right) \tag{2.19a}$$

$$0 = \begin{bmatrix} B_e - \left[2a - \sin 2\alpha - \pi\left(2 - X_L / X_C\right)\right] / \pi X_L \\ I - V_i B_e \\ Q - V_i^2 B_e \end{bmatrix} \tag{2.19b}$$

where most variables are defined in Figure 2.6, x_c and $f(\cdot)$ denote the control system state variables and the control system function respectively. The control function $f(\cdot)$ depends on the type of control system used.

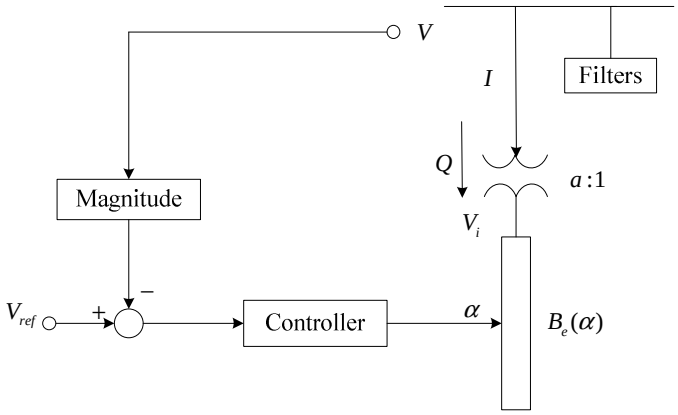

Figure 2.6 Block diagram of the transient stability model of SVC [74]

2.4.7 Loads

It is known that load characteristics have a significant impact on system stability [1, 75]. Load models are typically classified into two types: static loads and dynamic loads. Static load models express as algebraic functions of the bus voltage magnitude and frequency. Dynamic loads need to be modelled with dynamic equations or differential equations. For static load models, the voltage dependency of load characteristics has been expressed by the following exponential model:

$$\begin{aligned} P &= P_0 \left(\frac{V}{V_0}\right)^a \\ Q &= Q_0 \left(\frac{V}{V_0}\right)^b \end{aligned} \tag{2.20}$$

where P and Q are active and reactive components of the load when the bus voltage is V. The subscript 0 identifies the values of the respective variables of the initial operating condition. With the exponents a and b equal to 0, 1, 2, the model represents constant power, constant current, and constant impedance characteristics respectively.

2.5 Multi-Machine Network Power Flow Analysis

Previous sections of this chapter introduce and discuss different power system components. Next, the analytical techniques for detailed analysis of power system as a network are described in this section.

2.5.1 Bus Classification

There are four quantities are associated with each bus: active power P, reactive power Q, voltage magnitude V, and voltage angle θ. Depending on which of these variables are specified, buses are classified as follows:

- *PV* bus: named voltage-controlled bus. Active power and voltage magnitude are specified. Depending on the characteristics of the individual devices, limits to the reactive power are specified.
- *PQ* bus: named load bus. Active and reactive power are specified.
- Slack bus: voltage magnitude and phase angle are specified. The slack bus is the only bus with known voltage.

2.5.2 Network Equations

The electrical network consists of inter-linked transmission lines and transformers, each of which can be modelled by the π-equivalent circuits described in Section 2.4.1 and 2.4.2. The nodal network equations in terms of the node admittance matrix are formed by the combined individual models as follows [1]:

$$\begin{bmatrix} \vec{I}_1 \\ \vec{I}_2 \\ \cdots \\ \vec{I}_N \end{bmatrix} = \begin{bmatrix} \vec{Y}_{11} & \vec{Y}_{12} & \cdots & \vec{Y}_{1N} \\ \vec{Y}_{21} & \vec{Y}_{22} & \cdots & \vec{Y}_{2N} \\ \cdots & \cdots & \cdots & \cdots \\ \vec{Y}_{N1} & \vec{Y}_{N2} & \cdots & \vec{Y}_{NN} \end{bmatrix} \begin{bmatrix} \vec{V}_1 \\ \vec{V}_1 \\ \cdots \\ \vec{V}_1 \end{bmatrix} \tag{2.21}$$

where

N total number of nodes;

$\vec{Y}_{ii}$ self-admittance of node i, and is equal to the sum of all the admittances terminating at node i;

$\vec{Y}_{ij}$ mutual admittance between nodes i and j, and is equal to the negative of the sum of all admittances nodes i and j;

$\vec{I}_i$ current injection at node i, and is equal to the algebraic sum of the currents in all the branches terminating at node i;

$\vec{V}_i$ voltage at node i.

The complex admittance and voltage can be written as $\vec{Y}_{ij} = Y_{ij}\angle\theta_{ij}$, and $\vec{V}_i = V_i\angle\delta_i$. The active power and reactive power then can be derived from equation (2.21) as follows:

$$\begin{aligned} P_i &= V_i^2 Y_{ii}\cos\theta_{ii} + \sum_{j=1, j\neq i}^{N} V_i V_j Y_{ij}\cos(\delta_i - \delta_j - \theta_{ij}) \\ Q_i &= -V_i^2 Y_{ii}\sin\theta_{ii} + \sum_{j=1, j\neq i}^{N} V_i V_j Y_{ij}\sin(\delta_i - \delta_j - \theta_{ij}) \end{aligned} \tag{2.22}$$

When the rectangular co-ordinate system (a, b) is used, the voltage and current is represented as follows, shown in Figure 2.7.

$$\vec{V} = Ve^{j\delta} = V_a + jV_b, \qquad \vec{I} = Ie^{j\beta} = I_a + jI_b$$

and the real and reactive power now is represented as:

$$P_i = V_{ai}I_{ai} + V_{bi}I_{bi}, \qquad Q_i = V_{bi}I_{bi} - V_{ai}I_{ai}$$

Expressing the complex admittance in rectangular co-ordinates in terms of conductance G and susceptance B, as $\vec{Y}_{ij} = G_{ij} + jB_{ij}$, and substituting it to equation (2.21), the current injection at each node i is obtained as:

$$\vec{I}_i = I_{ai} + jI_{bi} = \sum_{j=1}^{N} \vec{Y}_{ij}\vec{V}_j = \sum_{j=1}^{N} (G_{ij} + jB_{ij})(V_{aj} + jV_{bj})$$

thus the real and imaginary parts of currents are represented as:

$$I_{ai} = \sum_{j=1}^{N} \left(G_{ij} V_{aj} - B_{ij} V_{bj} \right), \qquad I_{bi} = \sum_{j=1}^{N} \left(B_{ij} V_{aj} + G_{ij} V_{bj} \right)$$

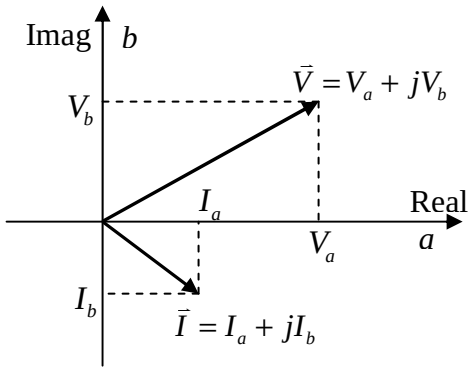

Figure 2.7 Voltage and current on the complex plane

2.5.3 Linearisation of Power Network Equations

The real and reactive power injection at each node is a non-linear function of the system voltages, i.e. $P = P(V, \delta)$ and $Q = Q(V, \delta)$. In order to linearise these expressions, Newton-Raphson method is used predominantly [1]. This linearisation method utilizes the first order Taylor expansion and neglects the higher-order terms. The resulting linear relationship between power flows and voltage magnitudes and angles can then be written as:

$$\begin{bmatrix} \Delta P \\ \Delta Q \end{bmatrix} = \begin{bmatrix} J_{11} & J_{12} \\ J_{21} & J_{22} \end{bmatrix} \begin{bmatrix} \Delta \delta \\ \Delta V \end{bmatrix} \tag{2.23}$$

where ΔP and ΔQ denote the deviations of the real and reactive power at all the system nodes from their nominal values, respectively, $\Delta \delta$ is the vector of voltage angle deviations from their nominal values, and ΔV is the vector of voltage magnitude deviations from their nominal values. The elements of Jacobian submatrices, J_{11}, J_{12}, J_{21}, J_{22}, are the partial derivatives of the functions shown in equation (2.24).

$$J_{11} = \frac{\partial P}{\partial \delta}, \; J_{12} = \frac{\partial P}{\partial V}, \; J_{21} = \frac{\partial Q}{\partial \delta}, \; J_{22} = \frac{\partial Q}{\partial V} \tag{2.24}$$

Substituting (2.24) into (2.23) produces the following linearised relationship:

$$\begin{bmatrix} \Delta P \\ \Delta Q \end{bmatrix} = \begin{bmatrix} \dfrac{\partial P}{\partial \delta} & \dfrac{\partial P}{\partial V} \\ \dfrac{\partial Q}{\partial \delta} & \dfrac{\partial Q}{\partial V} \end{bmatrix} \begin{bmatrix} \Delta \delta \\ \Delta V \end{bmatrix} \tag{2.25}$$

2.5.4 Network Reduction

The size of the network can be reduced by eliminating some of the nodes. These nodes must be removed in such a way that the currents and nodal voltages at the retained nodes are unchanged [71]. Kron's method is utilized in reduction of the network. Equation (2.26) performs Kron's reduction formula.

$$\tilde{y}_{ij} = y_{ij} - \frac{y_{ik} y_{kj}}{y_{kk}} \tag{2.26}$$

for $i = 1, 2, ..., k, ..., N$, and $j = 1, 2, ..., k, ..., N$. $\tilde{y}_{ij}$ is the new admittance between node *i* and *j* after the elimination of node *k*.

2.6 Modal Analysis

2.6.1 Eigenvalues and Eigenvectors

The eigenvalues of a matrix, *A*, are given by the values of the scalar parameter λ for which there exist non-trivial solutions to the equation

$$A\Phi = \lambda\Phi \tag{2.27}$$

where *A* is an $n \times n$ matrix, Φ is an $n \times 1$ vector. The *n* solutions of (2.27) are the eigenvalues of *A*, which are $\lambda = \lambda_1, \lambda_2, ..., \lambda_n$. These eigenvalues may be real or complex. For any eigenvalue λ_i, the *n*-column vector Φ_i which satisfies (2.27) is called the right eigenvector of *A* associated with the eigenvalue λ_i. It is showed as

$$A\Phi_i = \lambda_i \Phi_i, \qquad i = 1, 2, ..., n \tag{2.28}$$

$$\Phi_i = \begin{bmatrix} \Phi_{1i} & \Phi_{2i} & \cdots & \Phi_{ni} \end{bmatrix}^T$$

Similarly, the *n*-row vector Ψ_i which satisfies $\Psi_i A = \Psi_i \lambda_i$, $i = 1, 2, ..., n$ is called the left eigenvector associated with the eigenvalue λ_i.

Eigenvalues of a system physically refer to the modes of oscillations. They could be real or complex conjugate pairs. A real eigenvalue corresponds to a non-oscillatory mode, and each pair of complex eigenvalue corresponds to an oscillatory mode. The stability of a power system can be determined by the eigenvalues, that is, small signal stability would be maintained if all the eigenvalues in the system have negative real parts [1, 76]. Degree of stability is decided by how far the eigenvalues located away from the imaginary axis in the left half plane (LHP). The further away from the imaginary axis, the more stable the system will be. Right eigenvector associated with the mode accounts for the mode shape. It defines the relative distribution of the mode through the system dynamic states. The information of the observability of an oscillation mode can be reflected by the corresponding component of the right eigenvector. Left eigenvector associated with the mode gives the distribution of the states. It has a direct effect on the amplitude of a mode excited by a specific input. The information of the controllability of a mode can be reflected by the corresponding component of the left eigenvector [30].

2.6.2 Damping Factors

As stated above, each pair of the complex conjugate eigenvalue corresponds to an oscillatory mode. They are in the form of $\lambda = \sigma \pm j\omega$. The real component of the eigenvalue gives the damping, and the imaginary component gives the frequency of oscillation. A positive real part represents oscillation of increasing amplitude whereas negative real part represents a damped oscillation [1]. To determine the rate of decay of the amplitude of the oscillation, the damping ratio ζ is used and defined as

$$\zeta = \frac{-\sigma}{\sqrt{\sigma^2 + \omega^2}} \tag{2.29}$$

2.6.3 Mode Shapes

As stated in the previous sections, electromechanical modes can be classified into local and inter-area model. Mode shape analysis could achieve the classification of the type of a mode simply based on its frequency. The mode shape could be specified

by the right eigenvector. In local oscillations, only a small percentage of the generators have significant involvement in the oscillation illustrated in Figure 2.8(a). Inter-area modes involve all or a large number of generators and can represent the case where the generators split into two or more sub-groups and oscillate against each other as shown in Figure 2.8(b).

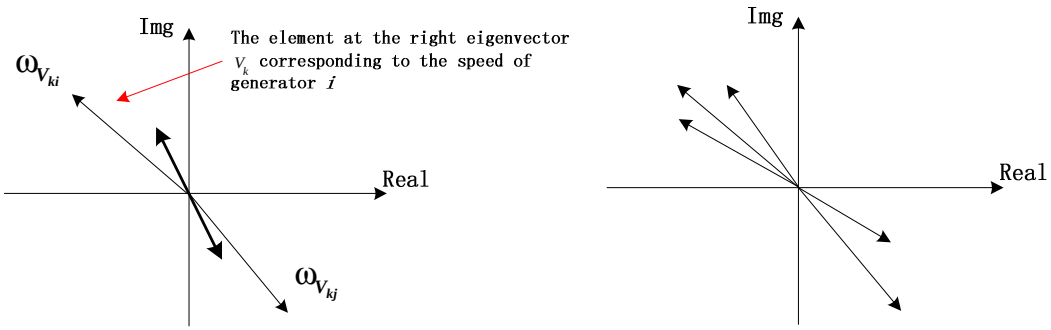

Figure 2.8 Mode shape of local and inter-area mode

2.6.4 Participation Factors

Participation factor [77] is a measure of the relative participation of the *k*-th state variable in the *i*-th mode, and vice versa. It is calculated as follows

$$p_{ki} = \phi_{ki}\varphi_{ik} \tag{2.30}$$

where ϕ_{ki} is the *k*-th entry of the right eigenvector Φ_i and φ_{ik} is the *k*-th entry of the left eigenvector Ψ_i. ϕ_{ki} measures the activity of *k*-th state in the *i*-th mode; φ_{ik} weighs the contribution of this activity to the mode; p_{ki} measures the net participation of the *k*-th state in the *i*-th mode. By using the eigenvector normalization, the sum of the participation factors associated with any mode $(\sum_{i=1}^{n} p_{ki})$ or with any state variable $(\sum_{k=1}^{n} p_{ki})$ is equal to 1.

Participation factors play an important role to identify the electromechanical modes. For electromechanical modes, the corresponding participation factors for generator state variable, such as angular speed, angular deviation, electrical power etc, will be

among of the highest compared with other states. Participation factors are also applied in model reduction, which is useful in large power systems [29].

2.7 Test Power System

2.7.1 System Modelling

A single line diagram of the test system is shown in Figure 2.9. This two-area system was created by Ontario Hydro for a research report commissioned by the Canadian Electrical Association. This system was designed to exhibit the different types of oscillations that occur in an interconnected system [78, 79]. The two-area system consists of two active networks in which each one has two generators. The two active areas are connected via one AC transmission line. A Static Var Compensator (SVC) connects to bus 7 for providing reactive power support. The full set of the system parameters i.e., the generator, transformer and transmission line parameters, as well as the controller settings of the AVR and Governor are given in Appendix A.1.

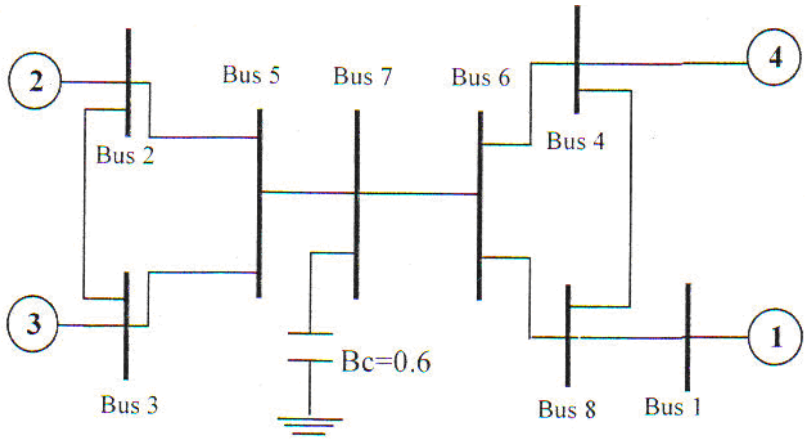

Figure 2.9 Single Line Diagram of Test System

The system base set for p.u. system is 100MVA. At a steady sate, Generator 2, 3, 4 supply 90 MW active power to the system respectively *i.e.* 0.9 p.u., whereas Generator 1 produces 193 MW active power. The loads modelled in system are all consumed to be of constant impedance type for all operation conditions. The load in Area 1 consumes 253 MW active power, and the load in Area 2 consumes 210 MW active power. As a consequence, the there is an active power flow of 30 MW over

the AC tie line from Area 1 (generation area) to Area 2 (demand area). Modelling of each components of this power system is given in the following.

Generators

The block diagram of the generator with the associated excitation control implemented in this test power system has been shown in Figure 2.3. Generator 1, 3 and 4 are round rotor machines, Generator 2 is a salient pole machine, and Generator 1 is the reference generator. Each generator is controlled by the AVR. In the modelling of this study, speed deviation $\Delta\omega$ and angle deviation $\Delta\delta$ will be utilized instead of speed ω and angle δ stated in equations (2.11) and (2.12). The speed deviation of Generator 1, $\Delta\omega$, is set to be the reference speed, namely $\Delta\omega_{ref}$. Hence, the 1st order derivative of angle speed of Generator 2, 3 and 4 will be equal to the speed deviation minus the reference speed $\Delta\omega_{ref}$. The state-space model representation of each generator can be referred to Appendix A.2.

Generator Excitation System

The standard IEEE type DC1A exciter in the 2nd order and AVR are implemented for this test power system, which has been shown in Figure 2.4. The parameter values of AVR are given in Appendix A.1. The voltage limits shown in Figure 2.4 are given as follows.

$$V_{R\max} = 5.5\,,\; V_{R\min} = -5.5$$

Power System Stabilizer (*PSS*)

In the application of the 4-machine, 8-bus test power system, the transfer function of the structure of PSS is the same as shown in (2.18). Two lead-lag blocks are used, that is *N* is equal to 2. For each PSS, the input signal is the speed deviation from the corresponding generator, and the output signal of the PSS is the complementary

voltage which will be fed into the AVR. The parameter values of PSS are given in Appendix A.1.

Load

As the modelling of loads has been stated in Section 2.4.7, the load model used in this study is the constant impedance model and represented by a constant shunt admittance connected to the bus. The resulting model is expressed as follows

$$Y_{load} = \frac{P_0 - jQ_0}{|V_0|^2} \tag{2.31}$$

where P_0, Q_0 and V_0 are given in (2.20).

Bus Classification

There are 8 buses in this 2-area 4-machine power system. Bus 1 is the slack bus, Bus 2 ~ 4 are *PV* buses, and Bus 5 ~ 8 are *PQ* buses. Table 2.1 shows the reactive power limits of slack bus and *PV* buses applied in this test power system.

Table 2.1 Reactive power limits

Bus No.	Bus Type	$Q_{\min}$	$Q_{\max}$
1	Slack	$-\infty$	$+\infty$
2	*PV*	-0.6	4
3	*PV*	-0.6	4
4	*PV*	-0.6	4

2.7.2 Modal Analysis

The linearized state-space model of the test power system contains 35 states, 4 inputs, and 12 outputs. All the eigenvalues corresponding to the states are listed in Appendix A. As stated in the previous sections, each pair of complex conjugate eigenvalues corresponds to an oscillatory mode. Figure 2.10 shows the location of the dominant

eigenvalues with positive imaginary parts. The dashed line in Figure 2.10 shows the location of all the eigenvalues with damping ratio of 5%, which is utilised as a margin used to classify modes as either poorly-damped or well-damped. The eigenvalues located above the margin correspond to the poorly-damped modes, and the eigenvalues located bellow the margin refer to the well-damped modes. It can be seen in Figure 2.10 that there is one eigenvalue with the damping ratio smaller than 5%, which is related to inter-area mode.

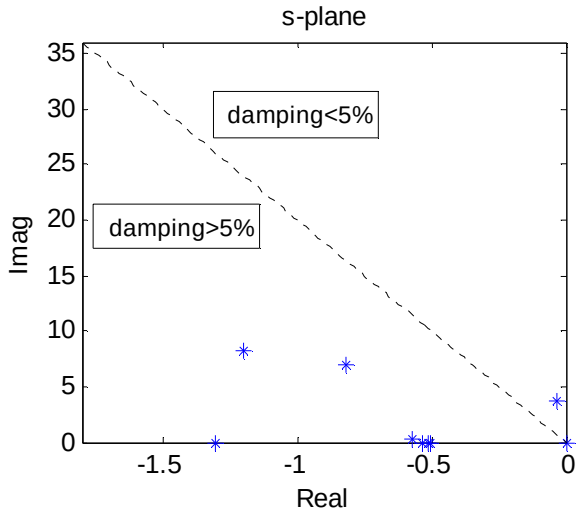

Figure 2.10 Dominant eigenvalues of the test power system without PSS

Table 2.2 Electromechanical modes between 0.1*Hz* and 2.5*Hz*

Modes	Eigenvalues	Modes	Eigenvalues
19, 20	$-7.6715 \pm 7.2435i$	21, 22	$-8.5474 \pm 4.4955i$
23, 24	$-1.1962 \pm 8.2158i$	25, 26	$-0.8186 \pm 6.9826i$
27, 28	$-0.0353 \pm 3.6734i$		

As only the electromechanical modes are concerned, all the electromechanical modes with the frequencies in the range of 0.1 *Hz* and 2.5 *Hz* and corresponding eigenvalues are calculated listed in Table 2.2. Figure 2.11 is the stem plot of the location of the states with the largest and second largest Participation Factors values for each of the modes located in the frequency range between 0.1 *Hz* and 2.5 *Hz*.

The eletromechanical modes are then identified based on participation factors in Figure 2.11 and the corresponding speed state or angle state of the four generators. This test power system model has three primary oscillatory modes of interaction. These modes and the corresponding damping factors are shown in Table 2.3. Mode 1, $-1.1962 \pm 8.2158i$, is dominated by Generators 2 and 3. The second mode, $-0.8186 \pm 6.9826i$, is dominated by Generators 1 and 4. Mode 1 and mode 2 are local modes in frequency 1.31 *Hz* and 1.11 *Hz* respectively. Mode 3 is an inter-area mode in frequency 0.58 *Hz* which is of particular interested. This mode represents the interactions of Generators 1 and 4 against Generators 2 and 3 through the tie line between bus 5 and bus 7. The damping ratio of the three modes is 14.4%, 11.6%, and 0.96% respectively. It is clear that the damping ratio of the 3rd mode is quite small, that means the inter-area mode is poorly damped.

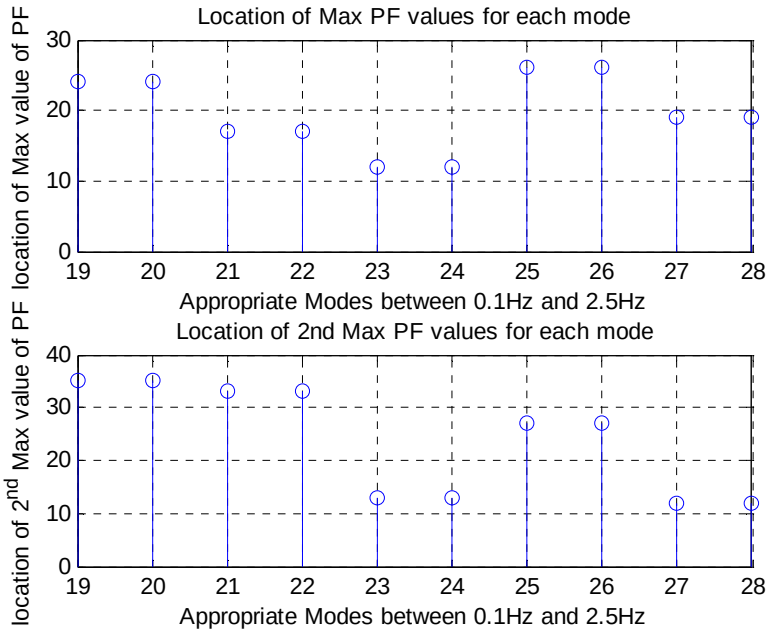

Figure 2.11 Location of maximum and 2nd maximum PF values

Table 2.3 Electromechanical modes of the test power system

Modes	Eigenvalues	Frequency (Hz)	Damping Ratio %
1	$-1.1962 \pm 8.2158i$	1.31	14.4
2	$-0.8186 \pm 6.9826i$	1.11	11.6
3	$-0.0353 \pm 3.6734i$	0.58	0.96

Figure 2.12 shows the mode shapes of the three modes with positive frequencies. Figure 2.12(a) shows the first local mode dominated by Generators 2 and 3. Figure 2.12(b) shows the second local mode dominated by Generators 1 and 4. The mode shape of the inter-area mode is shown in Figure 2.12(c). It is obvious the inter-area mode that Generators 1 and 4 (Area 1) oscillate in phase against of Generators 2 and 3 (Area 2).

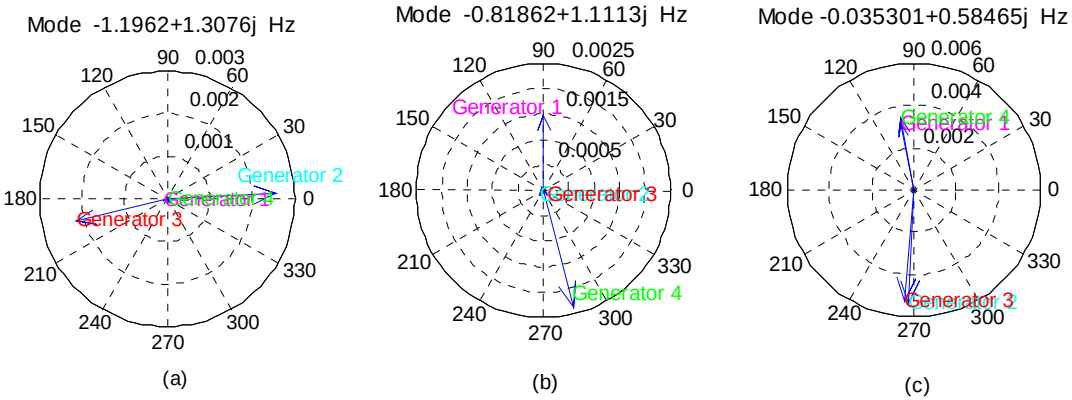

Figure 2.12 Mode shapes of the three modes

2.8 Summary

The basic concepts regarding power system stability, modelling and modal analysis method have been briefly introduced in this chapter. It has been shown that the power system stability can be analysed using system eigenvalues, eigenvectors and damping ratios. Thus, it is highly recommended to apply modal analysis in order to study stability issues considered in this thesis. The test power system, which is a 2-area 4-machine 8-bus power system simulation, has also been described. Due to the flexibility of the available tools, all the work involving the power system and associated controller design, including the closed-loop system implementation, will be performed using Matlab and Simulink throughout the thesis.

Chapter 3

Continuous-Time LQG/LTR for Multi-Machine Power System

3.1 Introduction

Classical control methodologies focus on the regulation problem in which a single resource, which is considered as the system input, is manipulated in order to control a single variable-of-interest, considered to be controlled variable. This normally leads to satisfaction of some local objective but it rarely leads to the satisfactory control of the system as a whole. Also, the problem of non-effective or even destabilising interaction amongst local controllers is often cited as a typical problem when employing this type of control structure. On the other hand, implementation of the multivariable control scheme allows for the coordinated manipulation of several different resources in order to simultaneously control multitude of variables-of-interest that may be dispersed across the large-scale system, such as the one studied in this thesis.

The Linear Quadratic Gaussian control design methodology that employs the Loop Transfer Recovery (LQG/LTR) is a well-known advanced multivariable control technique. The continuous-time LQG/LTR design for multivariable systems was initially proposed by Doyle and Stein [39] and later expanded by Stein and Athans [40]. This approach consists of designing both the optimal full state- feedback controller (Linear Quadratic Regulator abbreviated as LQR) [37, 85] and the

associated observer, termed Kalman Filter, that provides the optimal state estimate to the full state-feedback controller. Using the method of Loop Transfer Recovery (LTR), the well-documented robustness and performance qualities obtained when utilising LQR controller are then partially recovered by the LQG controller.

The continuous-time LQG/LTR approach has been extensively used for the control of multivariable systems [32, 33]. It also has been applied specifically to power systems [20, 31, 41, 80, 81]. In particular, the Power System Stabiliser (PSS) was designed by utilizing LQG/LTR method in [41] but only for the case of single-input single-output (SISO) one-machine infinite-bus power system. LQG controller was also used in [80] to regulate the local electromechanical modes using excitation control but also restricted to SISO single machine infinite-bus power system. In [20], LQG/LTR technique was introduced into the design of TCSC devices for damping electromechanical oscillations. Only local signals were considered as the input signal in this damping controller design. Zolotas *etal* [31] also presented LQG/LTR damping control scheme in order to improve the inter-area mode oscillations via a proposed minimum-phase square system augmentation.

This chapter details the design of the continuous-time supervisory LQG/LTR controller applied to the 2-area, 4-machine power system simulation. Control design is based on the LQG methodology, which includes the procedure of recovering the robustness and performance properties of the classical optimal control regulator using the technique known as Loop Transfer Recovery (LTR). Designed controller is firstly assessed using linearised small-signal model of the power system and then it is applied to the non-linear simulation. In both of these case studies, it is assumed that the power system is not equipped with the local acting PSSs. In the final case study reported in this chapter, supervisory LQG/LTR controller is implemented on the power system simulation in which each of the generators is equipped with its own local PSS regulator.

3.2 Multivariable Frequency-Domain Design

The methodology of loop shaping represents a pillar stone of the modern MIMO control system design. The use of singular values to analyse and design multivariable

feedback control systems in the frequency domain was initially introduced by Doyle and Stein in 1981 [39]. In their pioneering paper they showed how the classical loop shaping ideas of feedback design could be generalized to multivariable systems through the use of singular values, and also how to deal with the unstructured uncertainty when designing the feedback controllers. To describe this methodology, the standard feedback configuration is considered and illustrated in Figure 3.1. The plant *G* is shown to be interconnected with controller *K* in the classical feedback configuration. Closed-loop system shown in Figure 3.1 has three types of exogenous inputs, which are reference commands *r*, disturbances *d*, and measurement noise *n*. Controller outputs are designated by *u* and the measured outputs utilised by the controller are denoted by *y*. Some fundamental definitions are given in the remainder of this section. More details can be found in [29, 39].

Loop Transfer Function is formally given as a product of the controller transfer function and the open-loop system transfer function:

$$L = GK \tag{3.1}$$

Sensitivity Transfer Function describes the relationship between the output disturbances and the controlled outputs:

$$S = \left(I + L\right)^{-1} \tag{3.2}$$

Complementary Sensitivity Transfer Function describes the relationship between the set-points and the controlled outputs:

$$T = L\left(I + L\right)^{-1} = I - S \tag{3.3}$$

For a constant $m \cdot n$ complex matrix *A*, the *i*-th singular value σ_i is the square root of the *i*-th eigenvalue of $A^H A$, where A^H is the complex conjugate transpose of *A*:

$$\sigma_i(A) = \sqrt{\lambda_i\left(A^H A\right)} \tag{3.4}$$

where $\lambda(\cdot)$ denotes eigenvalues and the maximum and minimum singular values are defined respectively as:

$$\bar{\sigma}\left(A\right) = \sqrt{\lambda_{\max}\left(A^H A\right)}, \quad \underline{\sigma}\left(A\right) = \sqrt{\lambda_{\min}\left(A^H A\right)} \tag{3.5}$$

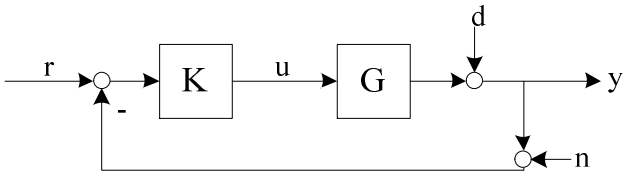

Figure 3.1 Standard Feedback Configuration

3.2.1 Frequency-Domain Performance Specification

It could be reasonably argued that it is impossible for any system to be fully characterised by a given man-made dynamic model. In other words, the model uncertainty is inevitable. This uncertainty may be caused by parameter changes, or by neglected dynamics, or by a host of other unspecified effects [39]. Then the actual plant *G*' can be expressed by the nominal plant *G* with the model uncertainties of two types.

For additive uncertainties:

$$G'(j\omega) = G(j\omega) + \Delta G(j\omega) \tag{3.6a}$$

with

$$\bar{\sigma}\left[\Delta G(j\omega)\right] < l_a(\omega) \qquad \forall \omega \geq 0 \tag{3.6b}$$

For multiplicative uncertainties:

$$G'(j\omega) = \left[I + M(j\omega)\right] G(j\omega) \tag{3.7a}$$

with

$$\bar{\sigma}\left[M(j\omega)\right] < l_m(\omega) \qquad \forall \omega \geq 0 \tag{3.7b}$$

where $l_a(\cdot)$ and $l_m(\cdot)$ are known positive scalar functions of frequency ω. The uncertainty descriptions above belong to the class of unstructured uncertainties [29]. In this thesis, discussion will be restricted to the multiplicative uncertainties of (3.7a). The bounding functions $l_m(\omega)$ in (3.7) commonly have the properties that they are small at low frequencies and increase to unity and above at higher frequencies [39]. This reflects the fact that the model adequately represents system dynamics in the low-frequency region while the discrepancy between the model and the system is much more pronounced in the high-frequency region. Once a design model, $G(s)$, is

specified along with the unstructured uncertainty description in the form of (3.7), the feedback control design should satisfy the Performance Condition and the Stability Condition through the use of frequency shaping method [39]. These two conditions are described in more detail in the following.

Performance Conditions – Low-Frequency Specifications

For MIMO systems, frequency domain conditions for performance objectives should satisfy the following inequality:

$$\underline{\sigma}[GK(j\omega)] \gg 1, \quad \text{for } \omega < \omega_d \tag{3.8}$$

Where ω_d denotes the range of frequencies that are present in the spectral density function of the disturbance, $GK(j\omega)$ is the frequency response of the loop gain *GK*. In words, this condition requires high feedback in the low-frequency region in order to adequately reject the disturbances. By ensuring that *GK* is very large, the sensitivity transfer function relating disturbance to the controlled variable is made to be very small.

Another low-frequency performance bound may be derived from the steady-state error considerations. In order to make the steady-state error in response to a unit step at *r* equal to zero, the integral action may be included for the controller design. A final consideration in terms of the low-frequency behaviour of *GK* refers to the issue of balancing the singular values at low frequencies. In other words, it is highly desirable to have maximum and minimum singular values, namely $\bar{\sigma}(GK)$ and $\underline{\sigma}(GK)$, close to each other, i.e. minimising the condition number of the loop transfer function matrix *GK*. This would ensure that the system responds to set-point changes and persistent disturbances in a similar manner in all 'input channels'.

Stability Conditions – High-Frequency Specifications

The control design needs to satisfy not only the stability of the nominal feedback system, $GK[I+GK]^{-1}$, but also the robustness stability of the nominal system *G* with uncertainties, $G'K[I+G'K]^{-1}$. The following constraint is derived:

$$\underline{\sigma}[GK(j\omega)] < 1/l_m(\omega), \quad \text{for all } 0 \le \omega < \infty \tag{3.9}$$

3.3 Continuous-Time LQG/LTR Control

A linear multivariable plant described by a transfer function $G(s)$ can be represented by the following linear time-invariant state-space model:

$$\begin{aligned} \dot{x} &= Ax + Bu + w \\ y &= Cx + Du + v \end{aligned} \tag{3.10}$$

Where $x(t) \in \mathbb{R}^n$, $u(t) \in \mathbb{R}^m$, and $y(t) \in \mathbb{R}^r$ are system state, input and output vectors respectively, w and v are the process noise and measurement noise respectively, which are assumed to be uncorrelated zero-mean Gaussian white noise processes with the following covariances:

$$\begin{aligned} E\{ww^T\} &= W, \quad & E\{vv^T\} &= V, \\ E\{wv^T\} &= 0, \quad & E\{vw^T\} &= 0. \end{aligned} \tag{3.11}$$

where E is the expectation operator.

3.3.1 LQG Control

The LQG control problem is to find the optimal control $u(t)$ which minimizes

$$J^* = E\left\{ \lim_{T\to\infty} \frac{1}{T} \int_0^T \left[x^T Q x + u^T R u \right] dt \right\} \tag{3.12}$$

where Q and R are constant weighting matrices such that $Q = Q^T \geq 0$ and $R = R^T > 0$. The solution to the LQG problem is achieved by solving the two related problems described below. First problem is concerned with the design of the optimal state-feedback controller which is normally referred to as Linear Quadratic Regulator (LQR). Second problem is concerned with the design of the optimal state estimator, which takes form of a state observer.

Optimal State-Feedback. For the following system state-space model:

$$\begin{aligned} \dot{x} &= Ax + Bu \\ y &= Cx \end{aligned} \tag{3.13}$$

with non-zero initial state $x(0)$, find the optimal control $u(t)$ which minimizes the cost function

$$J = \int_0^\infty \left[x(t)^T Q x(t) + u(t)^T R u(t) \right] dt \tag{3.14}$$

The optimal state-feedback control law is given in the state-feedback form:

$$u(t) = -K_r x(t) \tag{3.15}$$

where

$$K_r = R^{-1} B^T P_r \tag{3.16}$$

And P_r is the unique symmetric nonnegative definite solution of the algebraic Riccati equation (ARE):

$$A^T P_r + P_r A - P_r B R^{-1} B^T P_r + Q = 0 \tag{3.17}$$

Kalman Filter. Provide the optimal estimate $\hat{x}$ of the state x, so that $E\left\{ \left[x - \hat{x} \right]^T \left[x - \hat{x} \right] \right\}$ is minimized. The Kalman filter has the structure of

$$\dot{\hat{x}} = A\hat{x} + Bu + K_f (y - C\hat{x}) \tag{3.18}$$

The optimal Kalman filter gain K_f is given by

$$K_f = P_f C^T V^{-1} \tag{3.19}$$

where P_f is the unique symmetric nonnegative definite solution of ARE

$$P_f A^T + A P_f - P_f C^T V^{-1} C P_f + W = 0 \tag{3.20}$$

LQG controller. The LQG controller consists of both LQR regulator and Kalman Filter, as shown in Figure 3.2. Optimal regulator is applied not to the measured state variables but their estimates provided by the Kalman Filter-based observer. The state-space realisation of the resulting LQG controller is given in the following form:

$$K_{LQG}(s) = \left[\begin{array}{c|c} A - BK_r - K_f C & K_f \\ \hline -K_r & 0 \end{array} \right] \tag{3.21}$$

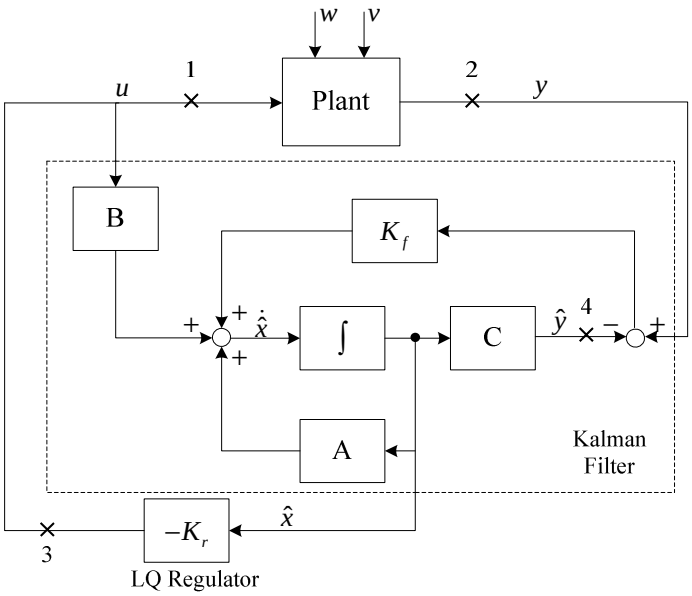

Figure 3.2 LQG control closed-loop

One of the main theoretical results concerning LQR regulator and Kalman Filter is the fact that the optimal gain matrices K_r and K_f exist, and the closed-loop system is internally stable, provided the systems with state-space realizations $\left(A, B, \sqrt{Q}\right)$ and $\left(A, \sqrt{W}, C\right)$ are stabilizable and detectable. This result revolutionised the manner in which the controller design was viewed. While previously the control engineer would explicitly choose the values of the controller gains and then check to see if the nominal stability is ensured, now the control engineer simply picked the cost function weights and the controller gains were synthesised automatically by a computer, which solved the Algebraic Riccati Equations given in (3.17) and (3.20).

3.3.2 Performance and Robustness Properties of LQR

Assuming the system is deterministic and all the states are directly measured, LQR controller is well known for the possession of sound performance and robustness properties [82, 83]. One of these properties, which is termed the optimal return difference relation, will be discussed and utilized in this thesis. This relation is concerned with the following LQR loop transfer matrix:

$$L_r(s) = K_r \left(sI - A\right)^{-1} B \tag{3.22}$$

In particular, the optimal return difference relation shows that the following return difference identity holds true [85]:

$$\left[I + L_r(j\omega)\right]^H R\left[I + L_r(j\omega)\right] = R + G_r^H \bar{Q} G_r, \quad \forall\, 0 \le \omega \le \infty \tag{3.23}$$

where

$$G_r = M\left(sI - A\right)^{-1} B \tag{3.24}$$

$R = R^T$, $\bar{Q} = \bar{Q}^T \ge 0$ and $Q = M^T \bar{Q} M$. Using the definition of singular values with $R = \eta I$ implies that

$$\begin{aligned} \sigma_i[I + L_r(j\omega)] &= \sqrt{\lambda_i\left[I + \frac{1}{\eta}\left(G_r \bar{Q}^{1/2}\right)^H \left(G_r \bar{Q}^{1/2}\right)\right]} \\ &= \sqrt{I + \frac{1}{\eta}\lambda_i\left[\left(G_r \bar{Q}^{1/2}\right)^H \left(G_r \bar{Q}^{1/2}\right)\right]} \\ &= \sqrt{I + \frac{1}{\eta}\sigma_i^2\left(G_r \bar{Q}^{1/2}\right)} \end{aligned} \tag{3.25}$$

This result governs the following performance and stability robustness properties of LQG loop at the plant inputs.

Performance Properties

For all frequencies where $\sigma_i\left[L_r\right] \gg 1$, the following approximation of (3.25) is established for the LQR loop:

$$\sigma_i\left[L_r(j\omega)\right] \approx \sigma_i\left[\sqrt{\bar{Q}} M\left(sI - A\right)^{-1} B\right] \Big/ \sqrt{\eta} \tag{3.26}$$

for each singular value σ_i, thus we can choose M and η to tune the multivariable loop such that $\underline{\sigma}\left(L_r\right)$ and $\bar{\sigma}\left(L_r\right)$ are reasonably close together [39].

Robustness Properties

According to (3.24), for all ω the minimum singular value satisfies

$$\underline{\sigma}\left[I + L_r(j\omega)\right] \ge 1, \quad \forall\, 0 \le \omega \le \infty \tag{3.27}$$

This implies that [39]

$$\underline{\sigma}\left[I + L_r^{-1}(j\omega) \right] \geq 1/2 \quad , \quad \forall\ 0 \leq \omega \leq \infty \tag{3.28}$$

In [39], it is shown that the LQR loop is guaranteed to remain stable for all unstructured uncertainties at plant input which satisfies $\Delta(\omega) < 0.5$.

3.3.3 Loop Transfer Recovery (LTR)

Both the optimal state-feedback regulator LQR and the Kalman filter possess some robustness and performance qualities [29]. However, when combined together to form the resulting LQG controller, these properties are lost [29]. Both Kwakernaak [37] and Doyle and Stein [38, 39] proposed a method of either designing the Kalman filter such that the LQR robustness properties are recovered at the plant input, or designing the LQR such that Kalman filter robustness properties are recovered at the plant output. Both of these variants are collectively known as Loop Transfer Recovery (LTR) procedure because they attempt to recover sound properties attained using either LQR or the Kalman Filter. Note that the structure of the resulting LQG/LTR controller remains the same as the one shown in Figure 3.2. However, the approach of tuning either LQR or Kalman Filter is modified in order to partially recover optimal loop transfer function.

Recovery at the Plant Input: Kalman Filter gain K_f is calculated such that the loop transfer function $K_{LQG}(s)G(s)$ approaches $K_r(sI - A)^{-1}B$, which is the loop transfer function obtained using optimal full-state feedback LQR regulator. The system must be minimum phase and must have at least as many outputs as inputs i.e. $r \geq m$. The resulting procedure consists of the following two steps [39]:

Step 1 Additional columns of zeros are appended to B and the additional rows of zeros are appended to K_r so that $C\left(sI - A\right)^{-1}B$ and $K_r\left(sI - A\right)^{-1}B$ are both square.

Step 2 Kalman Filter gain K_f is synthesised by solving (3.20) with modified noise intensity matrices given as $W = W_0 + BB^T$ and $V = q_v I$. Parameter q_v is then

reduced until the LQG loop gain at the plant input has converged sufficiently closely to the optimal regulator loop gain. Note that typically W_0 can be chosen as a zero matrix.

Recovery at the Plant Output: LQR controller gain K_r is chosen such that the loop transfer function $G(s)K_{LQG}(s)$ approaches $C(sI-A)^{-1}K_f$, which is the loop transfer function obtained using optimal state observer. Once again, it is required that the open-loop system is minimum phase. In addition, it is necessary for the open-loop system to have at least as many inputs as outputs in order to recover loop transfer The recovery at plant input can be considered as a dual to the recovery at plant output with the details regarding the procedure found in [29, 32].

Due to the fact that the power system considered in this thesis has more outputs than inputs the recovery of the loop transfer function at the plant input is performed and the detailed design is presented in Section 3.5.2.

3.4 Selection of Cost Function Weights

Finding the appropriate values for the cost function weights specified in (3.14) is not a trivial task. Conceptually, the control designer selects the weights in order to appropriately reflect the inevitable compromise between the requirement to regulate system outputs and the requirement of physically realisable controller action. Typically, values used in the cost function weights are chosen by trial and error with the evaluation done predominantly in the time-domain. The control performance specifications are often given in terms of the maximum allowed deviations of the states and the control signals for a given disturbance. In particular, Bryson and Ho [84] suggest structuring the weight matrix $Q = M^T \bar{Q} M$ so that the cost function specified in (3.14) can be reformulated in terms of the controlled outputs rather than state variables:

$$J = \int_0^\infty \left[y(t)^T \bar{Q} y(t) + u(t)^T R u(t) \right] dt \quad \text{for } M = C$$

Then $\bar{Q}$ and R can be selected to be diagonal matrices with their entries equal to the inverse values of the squares of the allowed deviations for each of the outputs.

Denote the maximum deviations of the *r* outputs as Δy_1, …, Δy_r, and the maximum deviations of the *m* inputs as Δu_1, …, Δu_m. Then the resulting weight matrices *Q* and *R* are constructed as follows:

$$\bar{Q} = \begin{bmatrix} 1/\Delta y_1^2 & \cdots & 0 \\ \vdots & \ddots & \vdots \\ 0 & \cdots & 1/\Delta y_r^2 \end{bmatrix} \tag{3.29}$$

and

$$R = \begin{bmatrix} 1/\Delta u_1^2 & \cdots & 0 \\ \vdots & \ddots & \vdots \\ 0 & \cdots & 1/\Delta u_m^2 \end{bmatrix} \tag{3.30}$$

Note that there is a scalar ratio between the state and the control terms, denoted as ρ, which can be explicitly included in the parameterisation of the weighting matrices, i.e. we have $Q = \rho M^T \bar{Q} M$. Thus (3.25) can be rewritten as

$$\sigma_i \left[I + L_r(j\omega) \right] = \sqrt{I + \rho \sigma_i^2 \left[G_r \bar{Q}^{1/2} \right]} \tag{3.31}$$

From (3.31) it can be observed that an increase in ρ by a factor of α leads to an increase in regulator gain K_r and loop gain L_r by a factor of $\sqrt{\alpha}$. The implication of this is that the closed-loop system's bandwidth and the peak values of the sensitivity and the complementary sensitivity transfer function are directly related to the changes in ρ. More specifically, increase in the value of ρ is likely to cause closed-loop system bandwidth to increase, which results in faster response to set-point changes and disturbances. However, as a result of increasing ρ, the peak values of the sensitivity and complementary sensitivity transfer function are highly likely to rise too, resulting in the deterioration of robustness.

3.5 Continuous-Time LQG/LTR for Power System

The schematic block diagram of the closed-loop system, including 2-area 4-machine power system simulation and the supervisory controller, is shown in Figure 3.3. The modelling of the power system is detailed in Chapter 2. Output (measured) signals

are chosen to be electrical power, terminal voltage and speed deviation of each of the four generators. These 12 measurements are then continuously fed back to the supervisory controller, which computes the appropriate control signal for each of the four generators. The control signals from the supervisory controller are then injected into the power system by being added to the set-points of the local AVR for each of the generators. It is important to note that the work reported in this chapter mainly focuses on the power system that does not include Power System Stabilizers (PSSs), as shown in Figure 3.3. However, in Section 3.7, the PSSs are assumed to be implemented for each of the four generators in order to investigate the impact that their presence has on the overall closed-loop system when controlled using LQG/LTR.

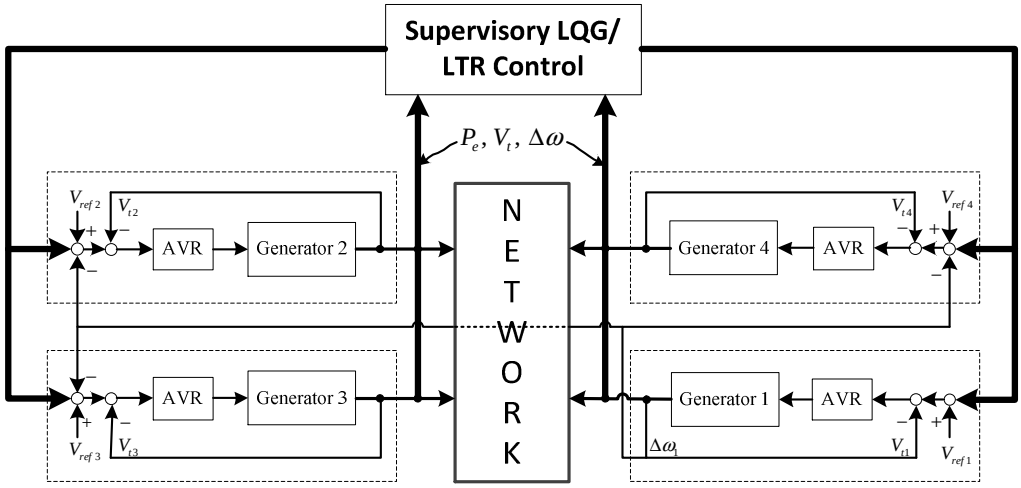

Figure 3.3 Schematic Block Diagram of the Supervisory Controlled Power System

3.5.1 Optimal Regulator Design

In order to increase the loop gain at low frequencies and, therefore, reduce the sensitivity transfer function at low frequencies, the integral action should be incorporated into the supervisory optimal controller. By incorporating the integral action, it is ensured that the $\underline{\sigma}\big(L(0)\big)=\infty$ and therefore $\bar{\sigma}\big(S(0)\big)=0$, which ensures complete rejection of the persistent disturbances and satisfactory tracking of piecewise-constant set-points [32]. Placing poles of the augmented model at the origin, however, violates the assumption of asymptotic stabilizability, which is

required during the loop transfer recovery step in the controller design. Therefore, the poles are placed in the vicinity of the origin. In this particular application the poles are placed at -0.001, which is virtually at the origin when compared to the closed-loop system's bandwidth [32]. The state-space representation of the integrator sub-system is given as:

$$\dot{x}_i = A_i x_i + y \tag{3.32}$$

Where $A_i = -0.001 I_{12}$. By augmenting the original state-space model given in (3.13) with this additional sub-system, the overall model of the power system is represented as follows:

$$\begin{aligned} \begin{bmatrix} \dot{x} \\ \dot{x}_i \end{bmatrix} &= \begin{bmatrix} A & 0 \\ C & A_i \end{bmatrix} \begin{bmatrix} x \\ x_i \end{bmatrix} + \begin{bmatrix} B \\ 0 \end{bmatrix} u \\ y &= \begin{bmatrix} C & 0 \end{bmatrix} \begin{bmatrix} x \\ x_i \end{bmatrix} + Du \end{aligned} \tag{3.33}$$

where $A_a = \begin{bmatrix} A & 0 \\ C & A_i \end{bmatrix}$, $B_a = \begin{bmatrix} B \\ 0 \end{bmatrix}$, $C_a = \begin{bmatrix} C & 0 \end{bmatrix}$, and $D_a = D$ are the augmented model state-space matrices. The dimensionality of the weighting matrices Q and R needs also to be modified in order to accommodate for the presence of the additional integrator states. The optimal regulator gain is then obtained by solving the ARE (3.17) and applying (3.16) using the augmented state-space model given in (3.33).

Two controllers are designed using different values of the cost function weights. These controllers are designated as K_r^0 and K_r^*, respectively. In both cases the parameter ρ, discussed in Section 3.4, is set equal to 100 in order to ensure satisfactory bandwidth and robustness properties, quantified by the peak value of the complementary sensitivity transfer function.

In the case of K_r^0 the cost function weights are selected pragmatically:

$$Q_{P_{ei}} = Q_{V_{ti}} = Q_{\Delta\omega_i} = 10 \text{ for } \quad i = 1, \ldots, 4 . \tag{3.34}$$

On the other hand, the cost function weights used to design K_r^* were obtained initially according to (3.32) and (3.33). Then, the further refinement of their values was performed by ensuring that the performance measures, such as the bandwidth

and the peak of the complementary sensitivity transfer function, are satisfied. Their final values were given as follows:

$$\begin{aligned} &Q_{P_{e1}} = 4\cdot10^{-2},\ Q_{P_{e2}} = 4\cdot10^{-1},\ Q_{P_{e3}} = 4\cdot10^{-1},\ Q_{P_{e4}} = 4\cdot10^{-2}, \\ &Q_{V_{t1}} = 5\cdot10^{-1},\ Q_{V_{t2}} = 5\cdot10^{-1},\ Q_{V_{t3}} = 5\cdot10^{-1},\ Q_{V_{t4}} = 5\cdot10^{-1}, \\ &Q_{\Delta\omega_1} = 1\cdot10^{3},\ Q_{\Delta\omega_2} = 1\cdot10^{3},\ Q_{\Delta\omega_3} = 1\cdot10^{3},\ Q_{\Delta\omega_4} = 1\cdot10^{3}. \end{aligned} \tag{3.35}$$

The maximum and minimum singular value plots of $L(j\omega)$, $\bar{\sigma}(L)$ and $\underline{\sigma}(L)$, obtained using K_r^0 and K_r^*, denoted as $L_r^0(s) = K_r^0(sI - A_a)^{-1}B_a$ and $L_r^*(s) = K_r^*(sI - A_a)^{-1}B_a$, respectively, are shown in Figure 3.4. Figure 3.5 shows the corresponding singular value plots of $S(j\omega)$ and $T(j\omega)$. Also, Table 3.1 summarises the important performance measures obtained for the power system when controlled using K_r^0 and K_r^*. In the case of K_r^*, it is observed that the cross-over frequencies for $\bar{\sigma}(L)$ and $\underline{\sigma}(L)$ as well as the bandwidth ω_B are reduced when compared to K_r^0. The consequence of such reduction in the closed-loop system's bandwidth is improved robustness to the uncertainties present in the high frequency region at the expense of a more sluggish response to disturbances or set-point changes. Such reduction in the bandwidth is a direct consequence of the reduction in the cost function weightings Q_{P_e} and Q_{V_t}, which play the dominant role in influencing system performance. Also, as shown in Figure 3.5 as well as in Table 3.1, maximum peak of $T(j\omega)$, $\|T(j\omega)\|_\infty$ denoted as M_T, is reduced from 1.65 *dB* using K_r^0 down to 1.1*dB* for K_r^*, indicating the improvement in the performance and robustness. Finally, damping of the inter-area electromechanical mode is increased from 52.66% to 67.1% when using optimal regulator K_r^*. This further demonstrates the benefits of implementing K_r^* as opposed to K_r^0 in terms of the improved damping of the inter-area mode as well as the robustness of the closed-loop system.

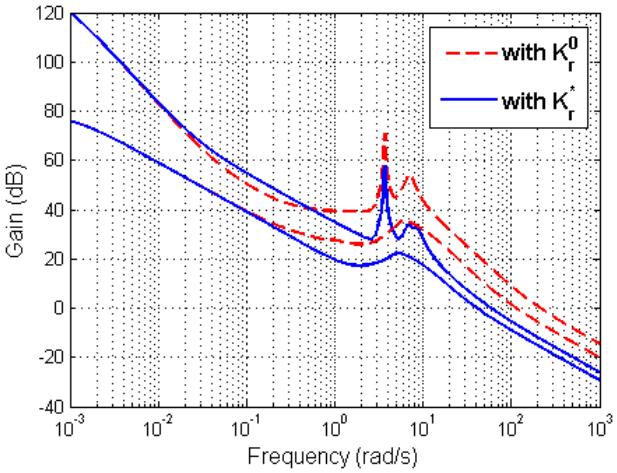

Figure 3.4 Singular value plots of loop transfer function L_r^0 vs. L_r^*

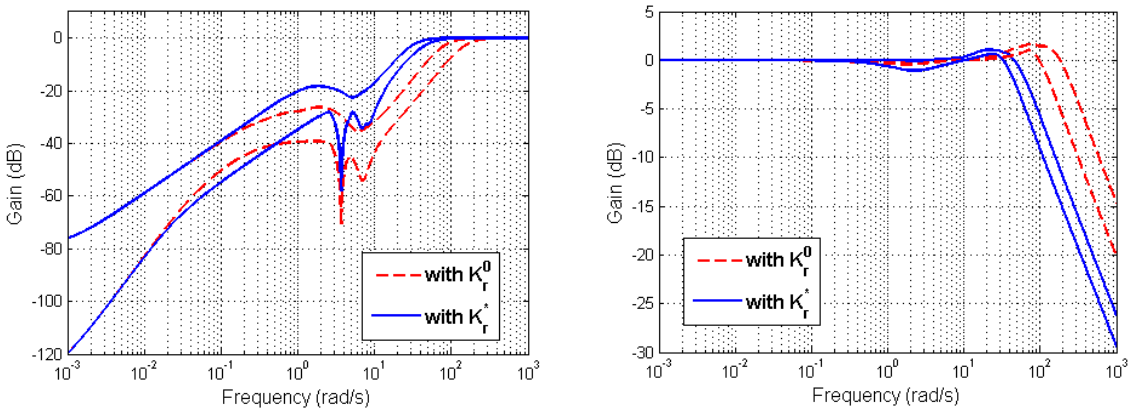

Figure 3.5 $\sigma(S)$ and $\sigma(T)$ of the optimal regulator loop using K_r^0 and K_r^*

Table 3.1 System performance properties

Controller	Inter-area mode		M_S (*dB*)	M_T (*dB*)	ω_B (*rad/s*)	$\omega_{\underline{\sigma}(L)}$ (*rad/s*)	$\omega_{\bar{\sigma}(L)}$ (*rad/s*)	Roll-off Rate *dB/decade*
	ζ (%)	f (*Hz*)						
K_r^0	52.66	0.44	0	1.65	80	113	211	20
K_r^*	67.10	0.60	0	1.10	30.2	40.4	58.5	20

3.5.2 Recovery at Plant Input

Since the 4-machine, 8-bus power system contains more outputs than inputs, Kalman Filter is designed so that the optimal regulator loop gain is recovered at the plant input, as discussed in Section 3.3.3. Recovery is achieved by setting $W = E\left(ww^T\right) = \Gamma\bar{W}\Gamma^T$ and $V = E\left(vv^T\right) = qI$ where W and V are the noise intensity matrices discussed in Section 3.3.3. By setting $\Gamma = B_a$, $\bar{W} = I$, the recovery is achieved as q tends to zero. The Kalman filter gain K_f is then obtained by solving the ARE (3.20) and applying (3.19).

Once K_f has been designed, the state-space realization of the LQG controller is given as:

$$K_{LQG}^*(s) = \left[\begin{array}{c|c} A_a - B_a K_r^* - K_f C_a & K_f \\ \hline -K_r^* & 0 \end{array}\right]$$

Figure 3.6 shows the singular values of the LQG loop transfer function $-K_{LQG}^* G_a$ (the solid lines), compared with the singular values of the LQR regulator loop transfer function $K_r^*\left(sI - A_a\right)^{-1} B_a$ (the dashed lines), for $q = 1$, 10^{-2}, 10^{-4} and 10^{-6}. It can be observed that for $q = 10^{-6}$ virtually the full recovery is achieved. Figure 3.7 shows the Bode plot of $S(j\omega)$ and $T(j\omega)$ with loop transfer recovery achieved using $q = 10^{-6}$. The closed-loop bandwidth is then equal to 29.5 *rad/s*, and the maximum peaks of $S(j\omega)$ and $T(j\omega)$, $\left\|S(j\omega)\right\|_\infty$ and $\left\|T(j\omega)\right\|_\infty$ denoted as M_S and M_T, respectively, are smaller than 2 *dB*, indicating satisfactory robustness and performance. Table 3.2 compares the system performance measures obtained for the closed-loop system when controlled by using K_{LQG}^* and K_r^*. It is clearly shown in this table that the two closed-loop control systems achieve very similar performance, thereby demonstrating successful recovery of the loop transfer function at the plant input. Furthermore, the damping ratio of the electromechanical mode is reduced insignificantly from 67.1% to 67.05% when using LQG/LTR as opposed to LQR controller. This further demonstrates the fact that the performance deterioration when

using LQG/LTR is minimal and that almost complete loop transfer recovery is achieved in this particular case study.

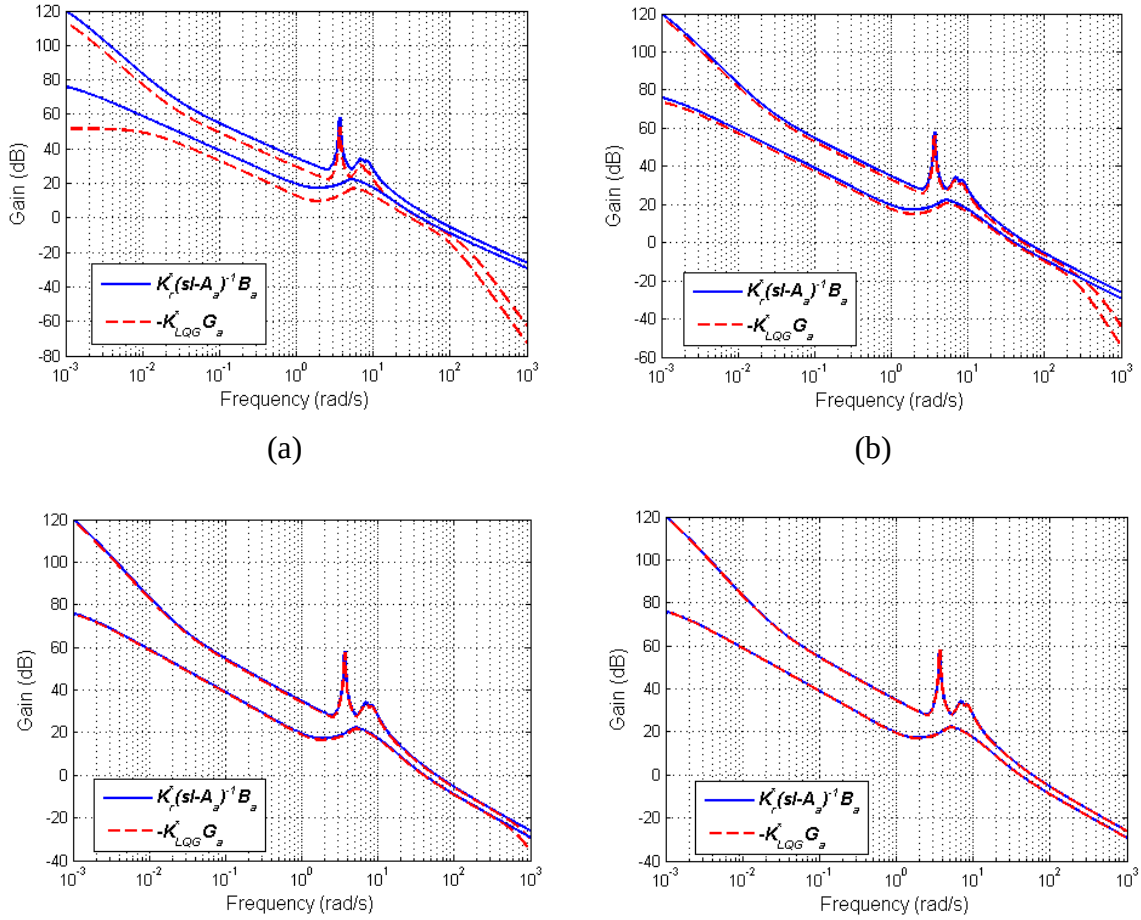

(a) (b)

(c) (d)

Figure 3.6 LTR for (a) $q=1$, (b) $q=10^{-2}$, (c) $q=10^{-4}$, (d) $q=10^{-6}$

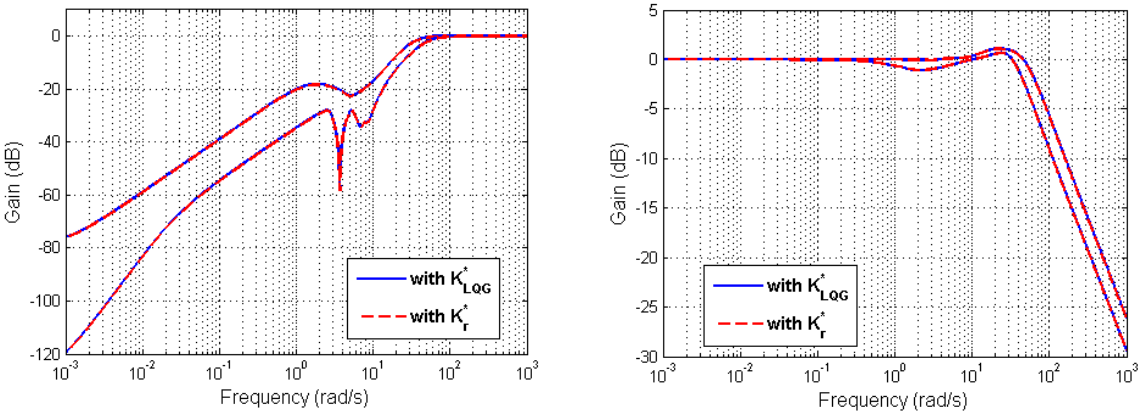

(a) S(s) (b) T(s)

Figure 3.7 $\sigma(S)$ and $\sigma(T)$ of the closed-loop using K_{LQG}^* and K_r^*

Table 3.2 System performance properties using K_{LQG}^{*} and K_{r}^{*}

Controller	Inter-area mode		M_S (*dB*)	M_T (*dB*)	ω_B (*rad/s*)	$\omega_{\underline{\sigma}(L)}$ (*rad/s*)	$\omega_{\bar{\sigma}(L)}$ (*rad/s*)	Roll-off Rate *dB/decade*
	$\zeta(\%)$	$f(Hz)$						
K_{r}^{*}	67.10	0.60	0	1.10	30.2	40.4	58.5	20
K_{LQG}^{*}	67.05	0.60	0	1.11	29.5	39.9	57.6	20

3.5.3 Robustness to Various Operating Conditions

The robustness of the designed supervisory continuous-time LQG/LTR controller K_{LQG}^{*} is assessed by changing the operating conditions under which the power system operates. Due to the nonlinearity of the power system model, it is expected that the linear realisation will differ for different operating conditions. However, the supervisory controller is expected to be sufficiently robust to maintain stability and satisfactory performance of the closed-loop system for all these different operating conditions.

Changes in operating conditions are realized by decreasing and increasing the power output of Generators 2, 3 and 4 by 10%. Figure 3.8 shows the singular value plots of $L(j\omega)$, $S(j\omega)$ and $T(j\omega)$ for different operating conditions: (a) generation of Generator 2 is decreased by 10%; (b) generation of Generator 2 is increased by 10%; (c) generation of Generator 3 is decreased by 10%; (d) generation of Generator 3 is increased by 10%; (e) generation of Generator 4 is decreased by 10%; (f) generation of Generator 4 is increased by 10%. It can be observed that there is insignificant change in the performance of the LQG/LTR controlled system for various operating conditions compared to that at the nominal operating condition. This indicates that the optimally-tuned supervisory continuous-time LQG/LTR controller designed for nominal operating condition is sufficiently robust to maintain the satisfactory performance for various operating conditions.

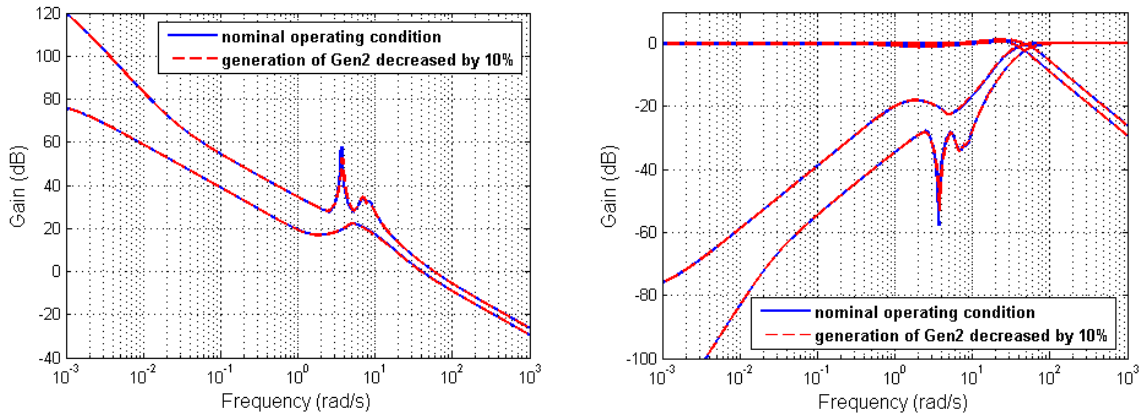

(a) Generation of Generator 2 decreased by 10%

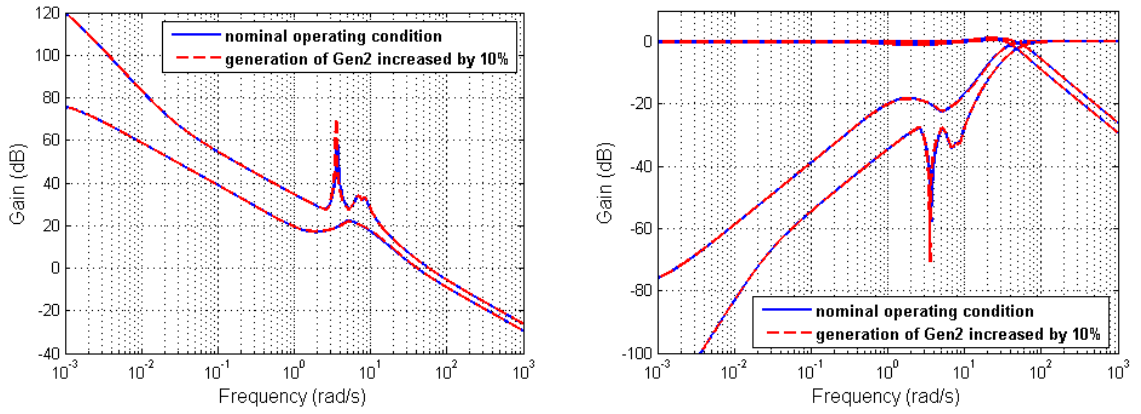

(b) Generation of Generator 2 increased by 10%

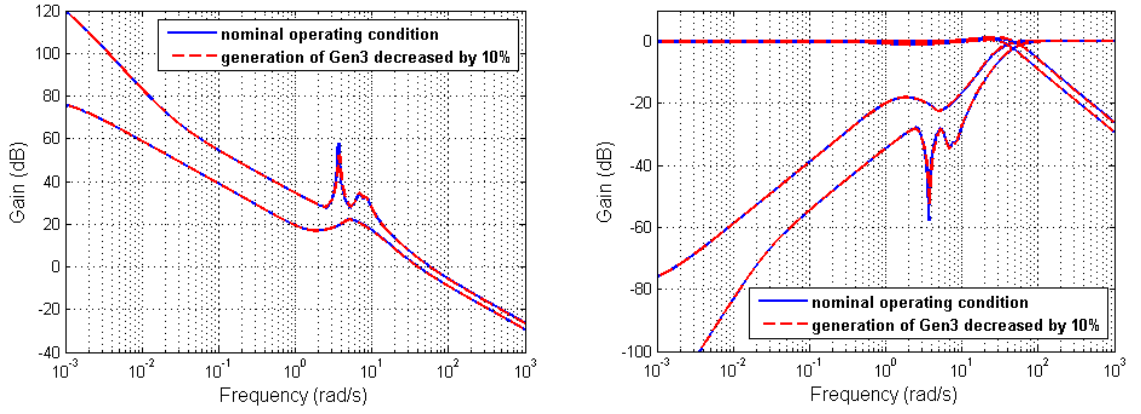

(c) Generation of Generator 3 decreased by 10%

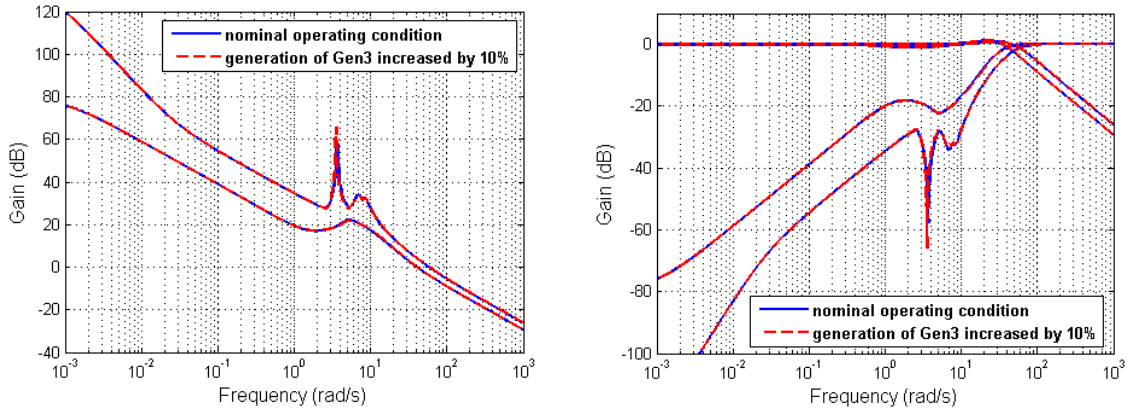

(d) Generation of Generator 3 increased by 10%

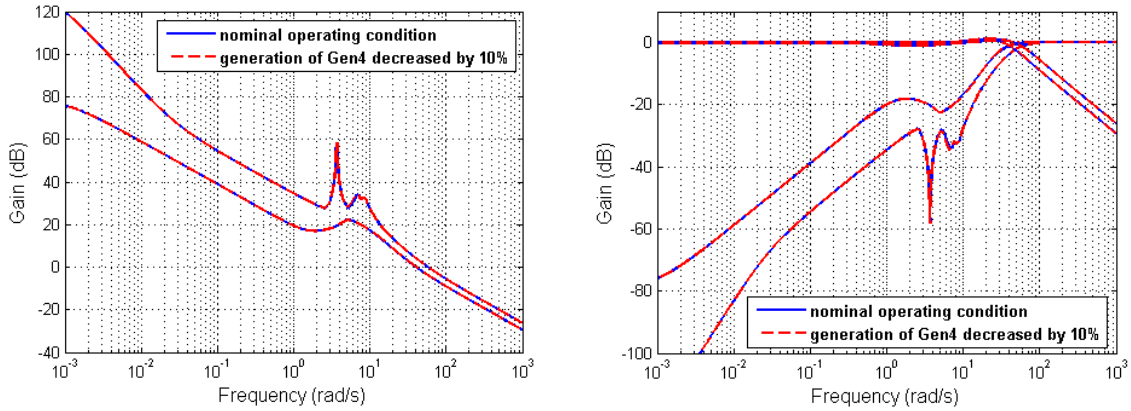

(e) Generation of Generator 4 decreased by 10%

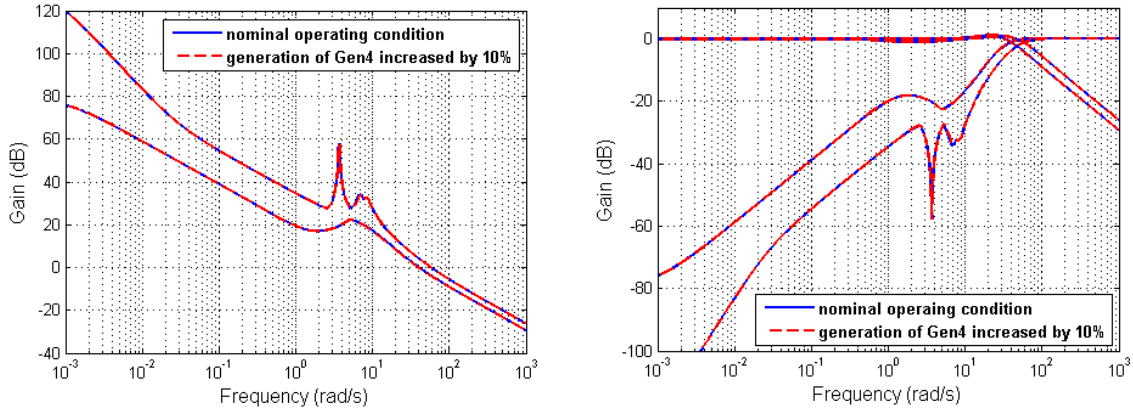

(f) Generation of Generator 4 increased by 10%

Figure 3.8 $\sigma(L)$, $\sigma(S)$ and $\sigma(T)$ for various operating conditions

Table 3.3 lists closed-loop system's performance measures for different operating conditions. Of particular interest is degradation of the inter-area mode's damping when the operating conditions change. This is particularly evident in the cases where the power output of generators 2 and 3 is increased. In those cases the damping ratio reduces to less than 34%. It can also be observed that the maximum peak of $T(j\omega)$, M_T, is increased, indicating degradation of the performance and robustness. However, these changes in the performance measures are not significant. Also, the bandwidth is arguably unaffected and remains between 28 *rad/s* and 30 *rad/s*. Therefore, it can be concluded that for small-signal disturbances the designed controller is sufficiently robust when controlling the power system under different operating conditions. However, it is important to note that the robustness analysis reported in this section was performed using linear realisation of the power-system, which facilitates the usage of frequency response tools. In order to properly assess robustness of the designed LQG/LTR controller to large-signal disturbances, nonlinear model of the power system is used and the results are reported in Section 3.6.

Table 3.3 System performance properties for various operating conditions

Loop TF	Inter-area mode		M_S (*dB*)	M_T (*dB*)	ω_B (*rad/s*)	$\omega_{\underline{\sigma}(L)}$ (*rad/s*)	$\omega_{\bar{\sigma}(L)}$ (*rad/s*)	Roll-off Rate *dB/decade*
	ζ (%)	f (*Hz*)						
Nominal Case	67.1	0.60	0	1.11	29.5	39.9	57.6	20
G2 decreased by 10%	60.1	0.59	0	1.29	28.5	39.0	57.5	20
G2 increased by 10%	32.4	0.51	0	1.16	29.7	40.4	57.4	20
G3 decreased by 10%	59.8	0.56	0	1.30	28.7	39.2	56.5	20
G3 increased by 10%	33.1	0.45	0	1.13	29.7	40.3	58.4	20
G4 decreased by 10%	56.1	0.42	0	1.36	28.7	40.3	57.6	20
G4 increased by 10%	50.8	0.41	0	1.18	29.0	39.2	57.6	20

3.6 Non-linear Power System Simulation

In order to properly assess the suitability of the designed LQG/LTR controller for the control of the considered power system, it is necessary to implement it on the non-linear simulation of the power system. Once implemented, the controller is assessed in terms of its ability to reject small-signal disturbances, which is discussed in Section 3.6.1, as well as the large-signal disturbances, discussed in Section 3.6.2 and 3.6.3. Finally, the robustness of the designed controller with respect to the changing operating conditions is assessed in Section 3.6.4.

3.6.1 *Case 1*: Small Disturbance

The small-signal disturbance is implemented by increasing the set-point for the terminal voltage of Generator 2 by 2.5% at time 0.2 seconds. The nominal steady-state value of the terminal voltages of each generator is 1 p.u.. Thus the new steady-state value of the terminal voltage of Generator 2 is 1.025 p.u., and the rest of the generators' terminal voltages are kept at 1 p.u. Steady-state values of the generators' speed deviations and electric powers are assumed to remain unchanged. Dotted lines in Figure 3.9 represent the response of the original system to the small disturbance, while the solid lines refer to the system response with the supervisory continuous-time LQG/LTR controller. Figure 3.9 clearly shows that the speed deviation of each generator of the open-loop system is under-dapmed, thus the open-loop power system is unstable when subjected to a small disturbance. On the other hand, LQG/LTR maintains the stability with satisfactory response to the applied disturbance.

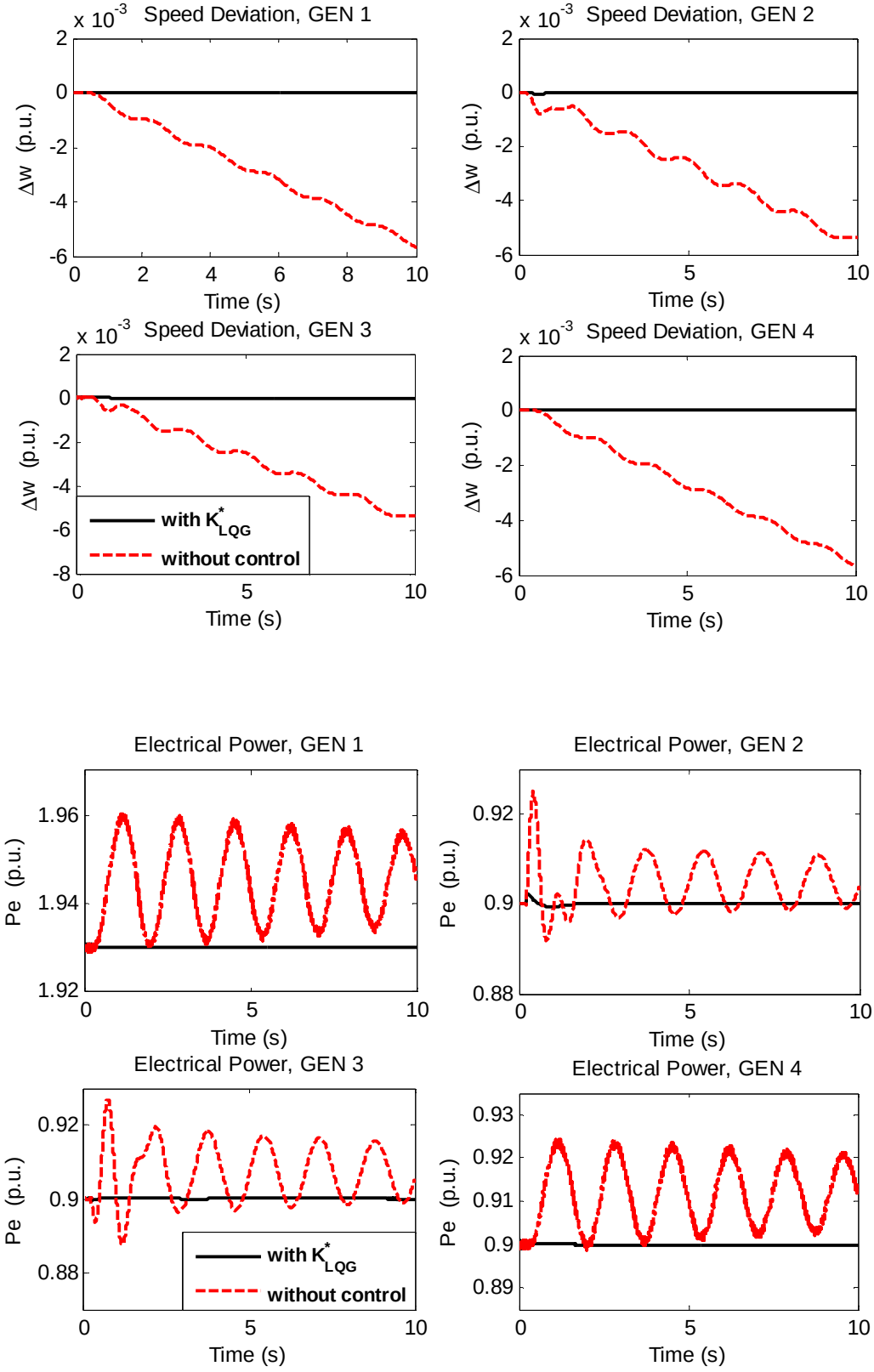
x 10^-3 Speed Deviation, GEN 1
Δw (p.u.)
Time (s)
x 10^-3 Speed Deviation, GEN 2
Δw (p.u.)
Time (s)
x 10^-3 Speed Deviation, GEN 3
Δw (p.u.)
with K*LQG
without control
Time (s)
x 10^-3 Speed Deviation, GEN 4
Δw (p.u.)
Time (s)
Electrical Power, GEN 1
Pe (p.u.)
Time (s)
Electrical Power, GEN 2
Pe (p.u.)
Time (s)
Electrical Power, GEN 3
Pe (p.u.)
with K*LQG
without control
Time (s)
Electrical Power, GEN 4
Pe (p.u.)
Time (s)

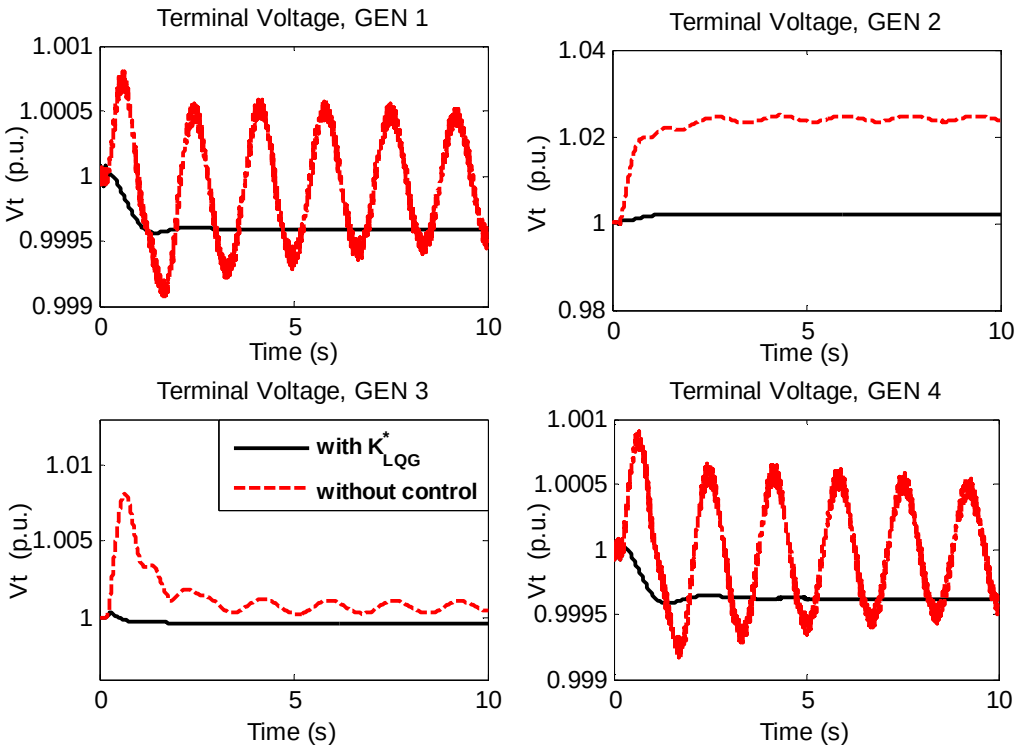

Figure 3.9 System response to small disturbance

3.6.2 *Case 2*: Self-cleared Three-phase Fault

A three-phase fault is applied at bus 5 at time 1 second. The fault is then cleared with auto-reclosing of the circuit breaker after 4 cycles (80 *ms*). The time response of speed deviation, electrical power and terminal voltage of generators are shown in Figure 3.10 for both the open-loop and the closed-loop system configuration. The open-loop system is shown to be unstable when subjected to a large disturbance. On the other hand, the supervisory continuous-time LQG/LTR is effective in stabilising the power system after the fault has been cleared.

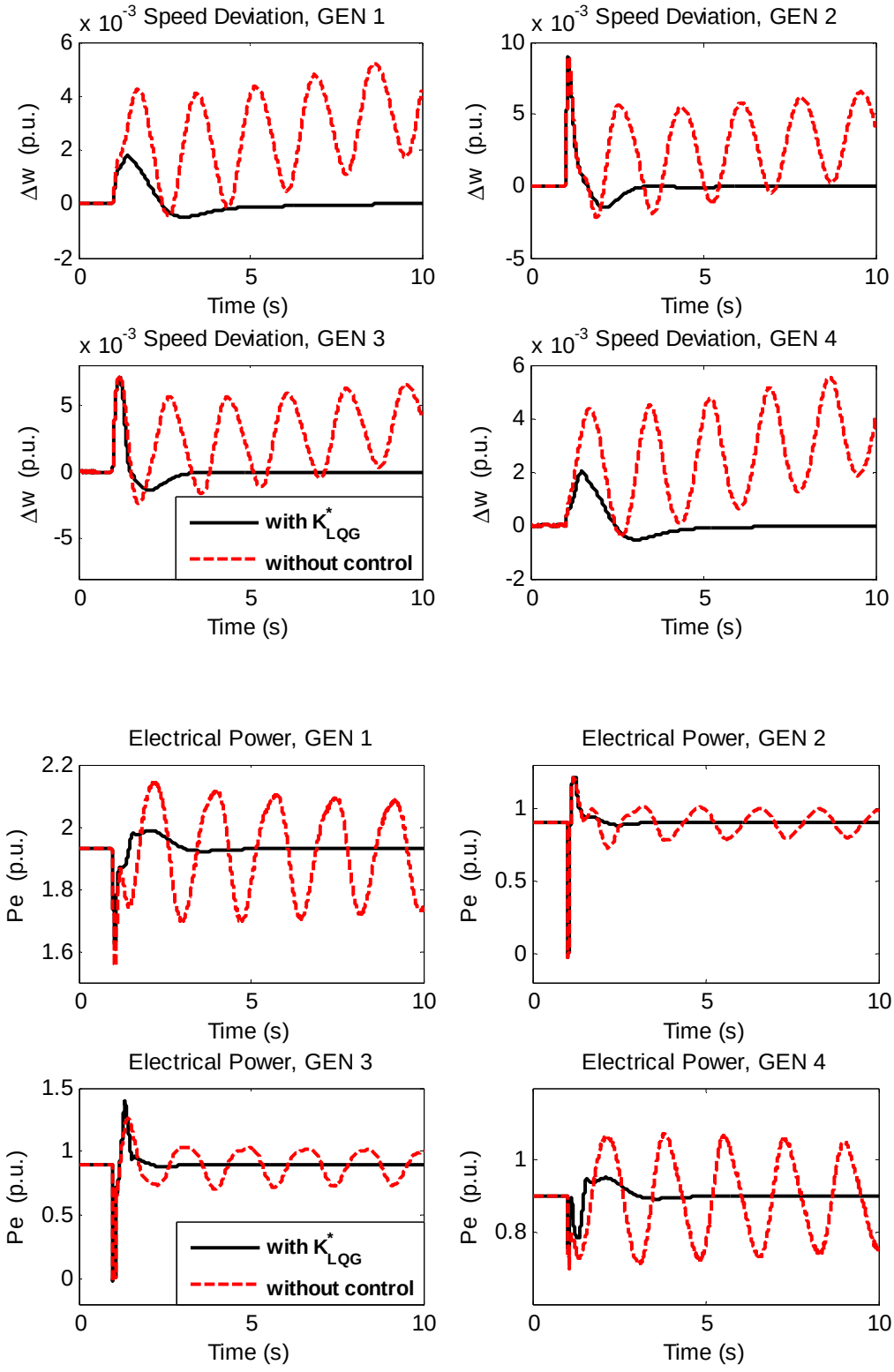
x 10-3 Speed Deviation, GEN 1
Δw (p.u.)
Time (s)
x 10-3 Speed Deviation, GEN 2
Δw (p.u.)
Time (s)
x 10-3 Speed Deviation, GEN 3
Δw (p.u.)
with K*LQG
without control
Time (s)
x 10-3 Speed Deviation, GEN 4
Δw (p.u.)
Time (s)
Electrical Power, GEN 1
Pe (p.u.)
Time (s)
Electrical Power, GEN 2
Pe (p.u.)
Time (s)
Electrical Power, GEN 3
Pe (p.u.)
with K*LQG
without control
Time (s)
Electrical Power, GEN 4
Pe (p.u.)
Time (s)

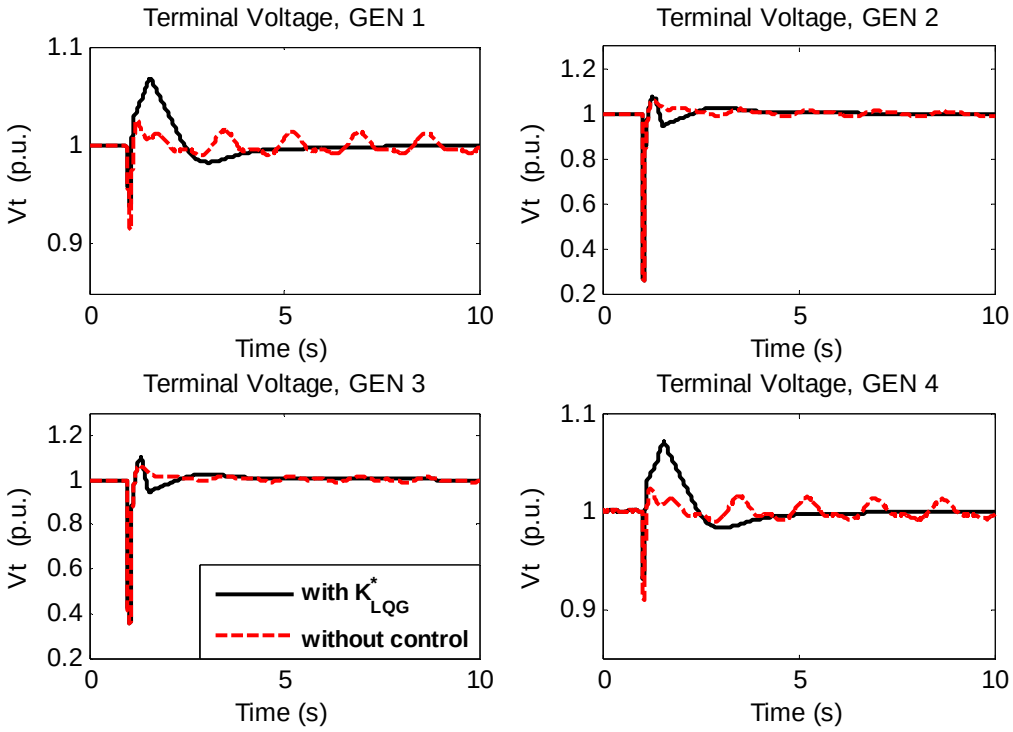

Figure 3.10 System response to a self-cleared three-phase fault

3.6.3 *Case 3*: Three-Phase Fault by Disconnecting Line 4

Figure 3.11 shows the open-loop and the closed-loop time responses of the power system following a three-phase short-circuit fault applied on the transmission line between buses 5 and 7, followed by the action of disconnecting the faulty transmission line after 4 cycles (80 *ms*). This case is modelled by doubling the reactance of the transmission line, which represents the scenario in which one of the two lines between buses 5 and 7 is permanently disconnected. The time responses of the open-loop system are found to be unstable for this particular disturbance, as shown in Figure 3.11. Once again, the supervisory LQG/LTR controlled system satisfactorily damps electromechanical oscillations and maintains the stability of the closed-loop system.

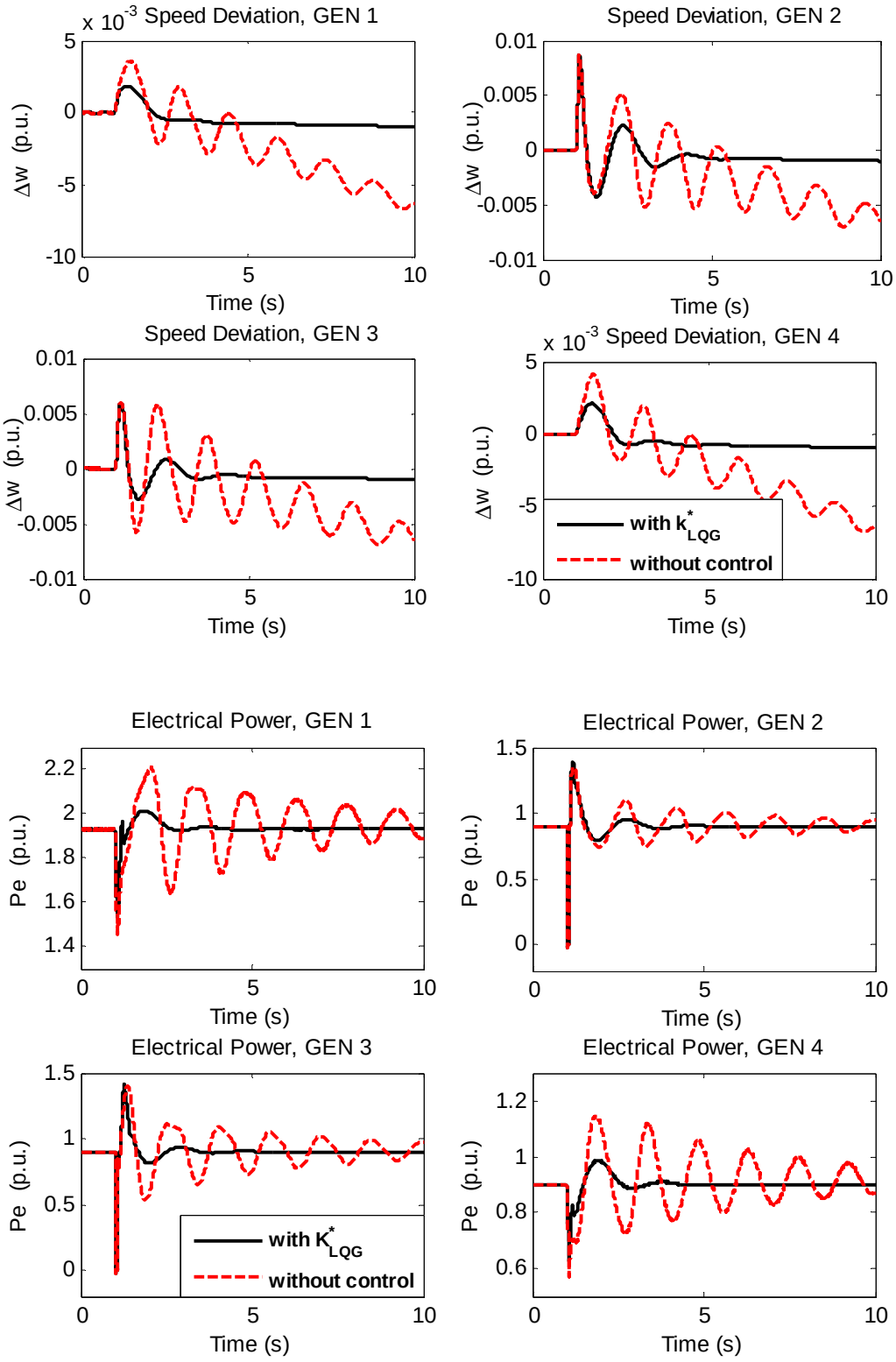
x 10^-3 Speed Deviation, GEN 1
Δw (p.u.)
Time (s)
Speed Deviation, GEN 2
Δw (p.u.)
Time (s)
Speed Deviation, GEN 3
Δw (p.u.)
Time (s)
x 10^-3 Speed Deviation, GEN 4
Δw (p.u.)
with k*LQG
without control
Time (s)
Electrical Power, GEN 1
Pe (p.u.)
Time (s)
Electrical Power, GEN 2
Pe (p.u.)
Time (s)
Electrical Power, GEN 3
Pe (p.u.)
with K*LQG
without control
Time (s)
Electrical Power, GEN 4
Pe (p.u.)
Time (s)

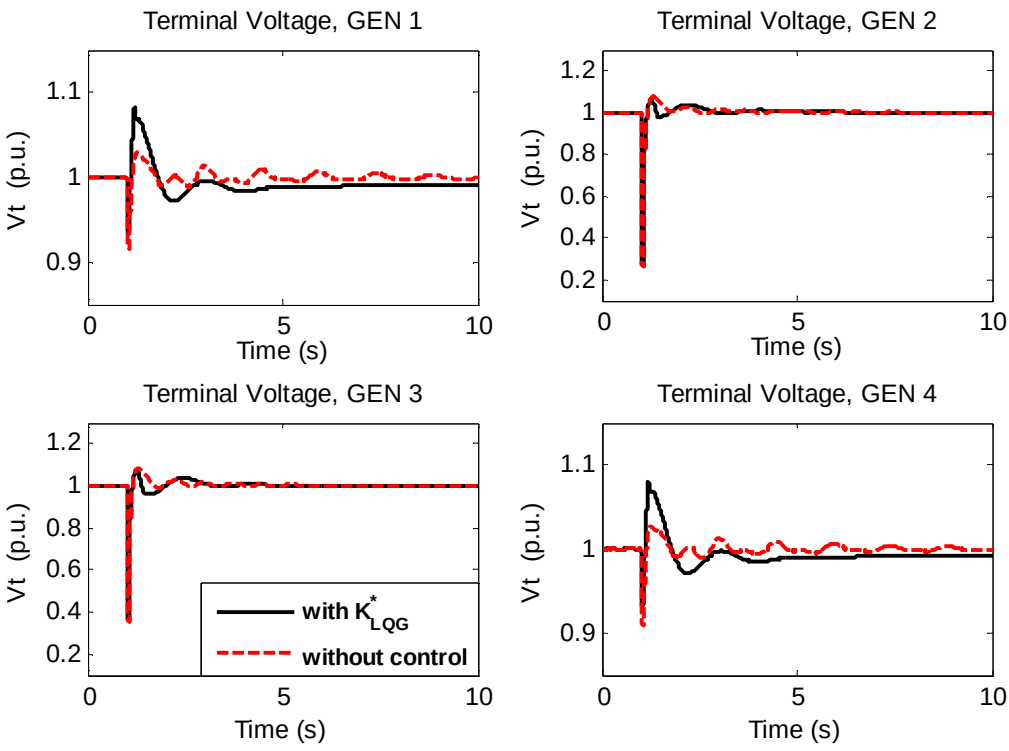

Figure 3.11 System response to a three-phase fault by disconnecting line

3.6.4 *Case 4*: Varying Operating Conditions

Robustness of the supervisory LQG/LTR controller to the changes in the operating conditions was assessed for small-signal disturbances in Section 3.5.3. However, in order to properly assess the robustness for large-signal disturbances it is necessary to implement the supervisory controller on the nonlinear model of the power system.

Therefore, the supervisory controller K_{LQG}^{*} is applied on the non-linear model of the power system under different operating conditions. Large-signal disturbance is a self-cleared three-phase fault applied at bus 5 at time 1 second with the self-clearing time of 80 *ms*. Different operating conditions are realized by decreasing and increasing the power output of Generators 2, 3 and 4 by 10% at each time. Figure 3.12 shows the electrical power output of the four generators for different operating conditions, when controlled by K_{LQG}^{*}. It is clearly observed that the open-loop power system is unstable for all the considered operating conditions when subjected to a large-signal disturbance. On the other hand, the stability is preserved by the supervisory controller in the presence of a self-cleared three-phase fault and under different

operating conditions. However, the settling time of the response is longer than that observed in Section 3.6.2. In particular, the settling time observed in Section 3.6.2 was found to be 3.5 seconds while the settling time of the response considered in this section is equal to 5.5 seconds. Such degradation in performance is somewhat expected due to the fact that the controller was tuned for nominal operating condition. Nevertheless, it is clearly shown that the designed supervisory controller is sufficiently robust when controlling power system under different operating conditions.

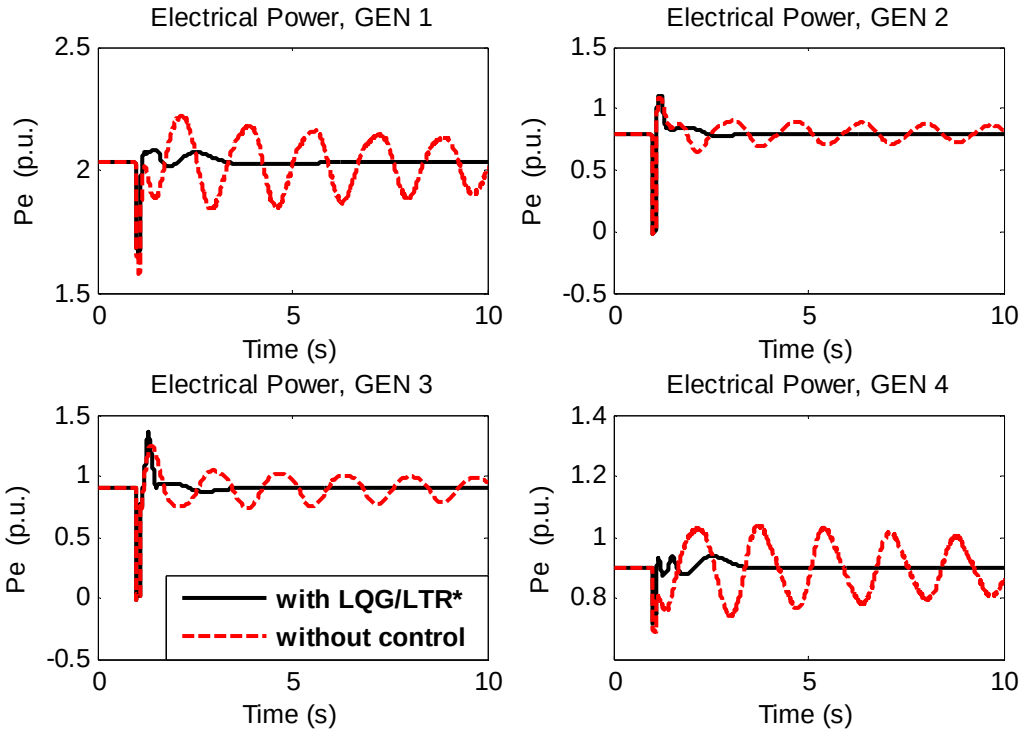

(a) Generation of Generator 2 decreased by 10%

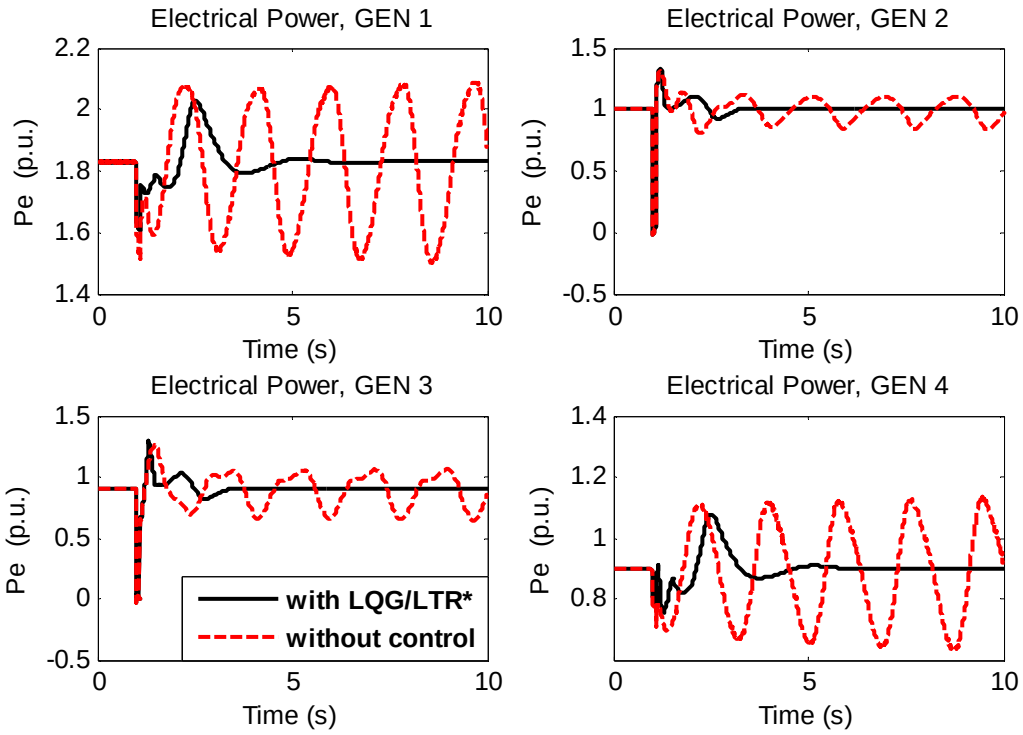

(b) Generation of Generator 2 increased by 10%

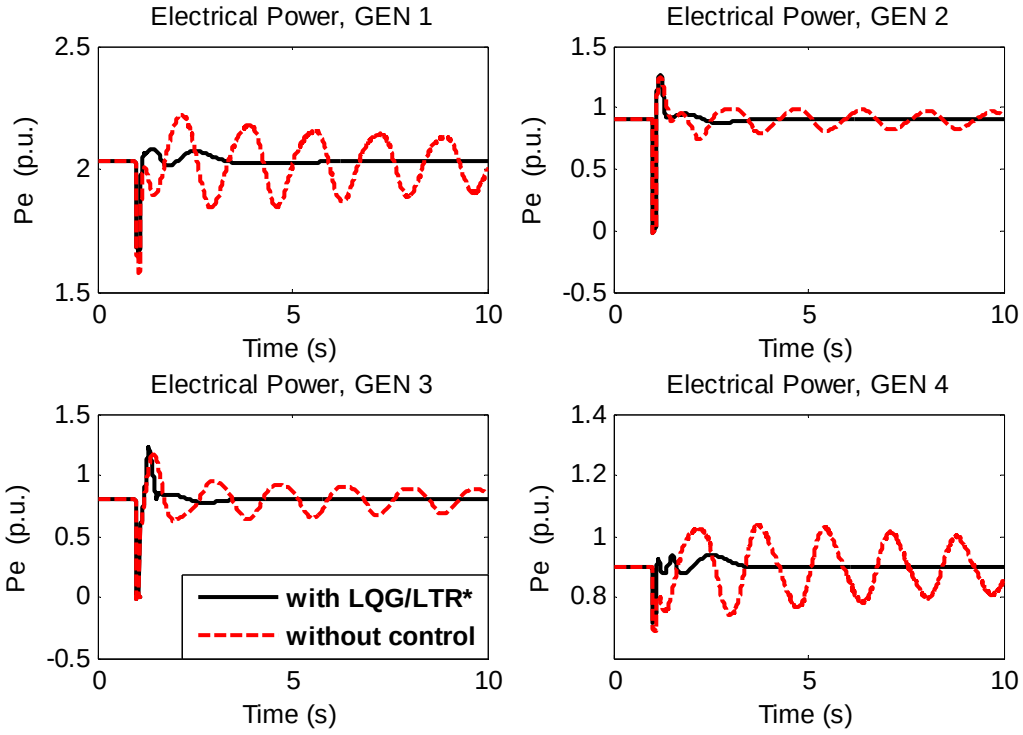

(c) Generation of Generator 3 decreased by 10%

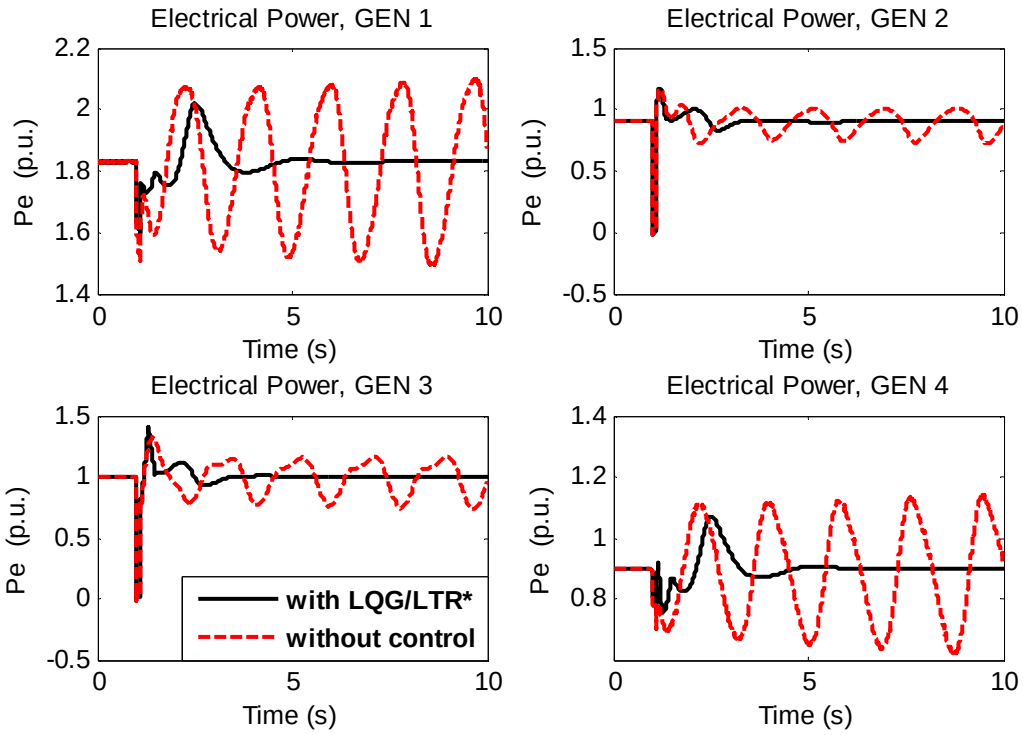

(d) Generation of Generator 3 increased by 10%

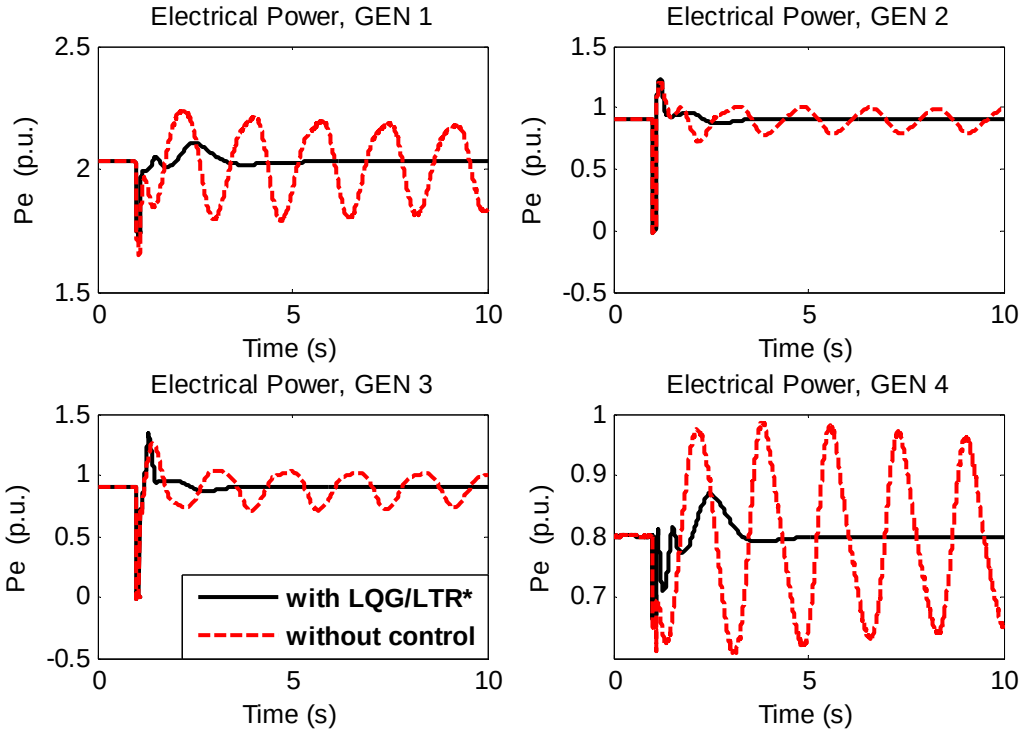

(e) Generation of Generator 4 decreased by 10%

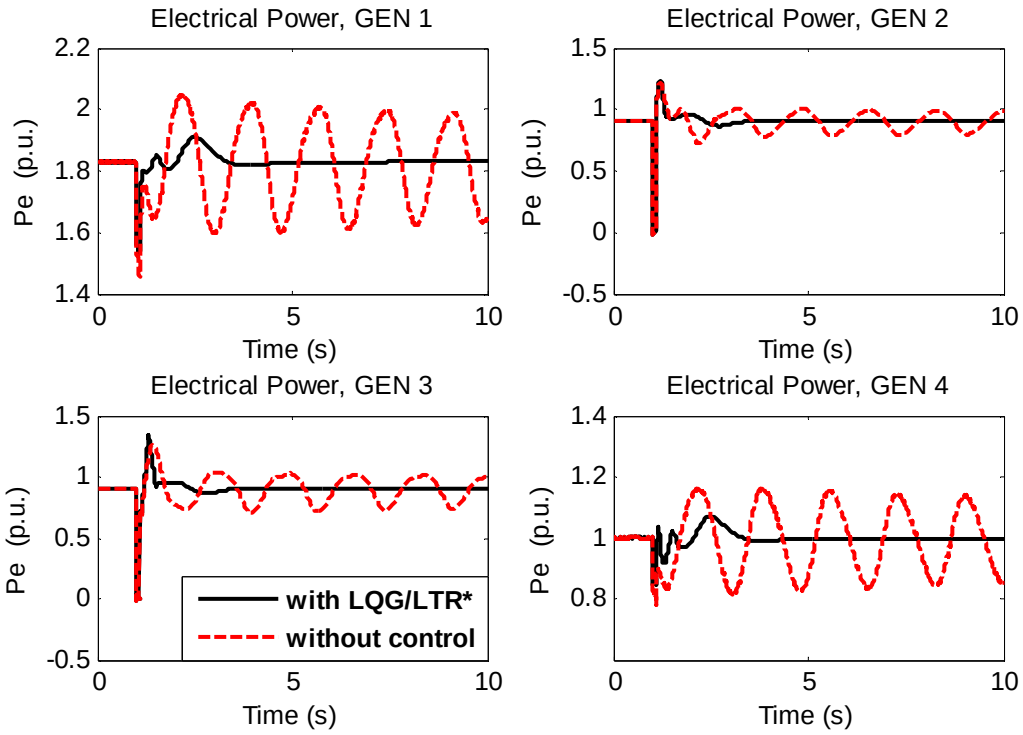

(f) Generation of Generator 4 increased by 10%

Figure 3.12 Electrical power output for various operating conditions

3.7 LQG/LTR for Power System Installed with PSS

3.7.1 Power System Installed with PSS

In this section, PSS is applied onto each generator of the considered power system in order to improve damping of the electromechanical oscillations by using the supplementary input signals to the generation excitation system. Figure 3.13 shows the block diagram that represents the structure of the power system with the supervisory controller implemented in addition to AVR and PSS regulators.

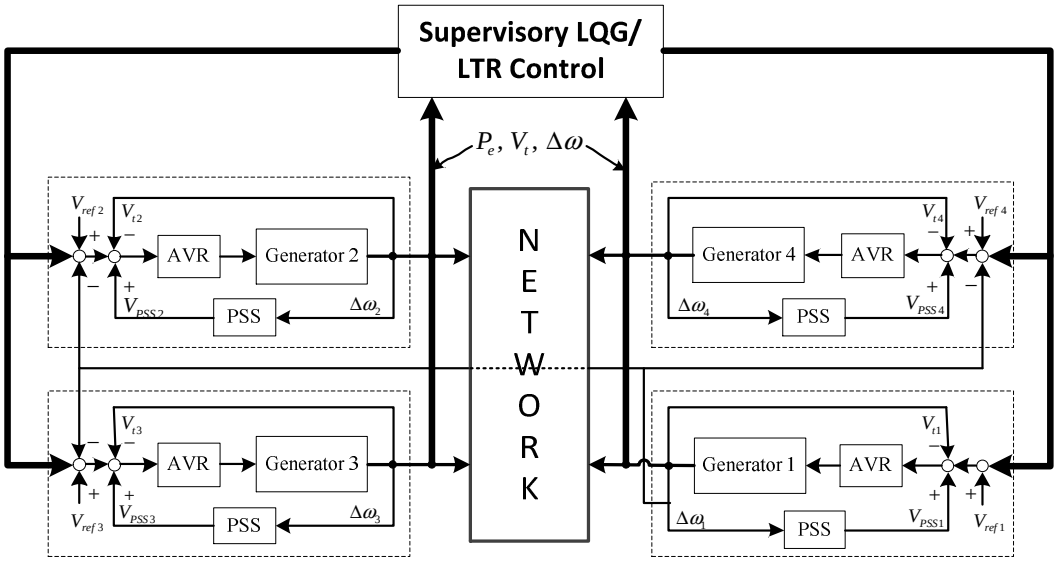

Figure 3.13 Schematic Block Diagram of the Supervisory Controlled Power System

Modelling and tuning of PSS is discussed in Chapter 2, Section 2.4.5 where the controller order N is chosen to be 2 (two lead-lag blocks) in the application. The resulting linearised state-space model of the power system, including PSS regulators as its integral part, has 51 states, 4 inputs, and 12 outputs. Figure 3.14 shows the locations of the dominant open-loop poles with positive imaginary part for the system with and without PSS, respectively. It is observed that the damping of the electromechanical modes is improved by the application of PSS, which is unsurprising. Table 3.4 lists the frequencies and the damping ratios of the electromechanical modes. Both Figure 3.22 and Table 3.4 show that the damping of the three electromechanical modes has been improved by adding local PSS controllers. Also, it is observed that the two local modes are well-damped, while the damping to inter-area mode is still insufficient and, as a result, the supervisory controller may be required.

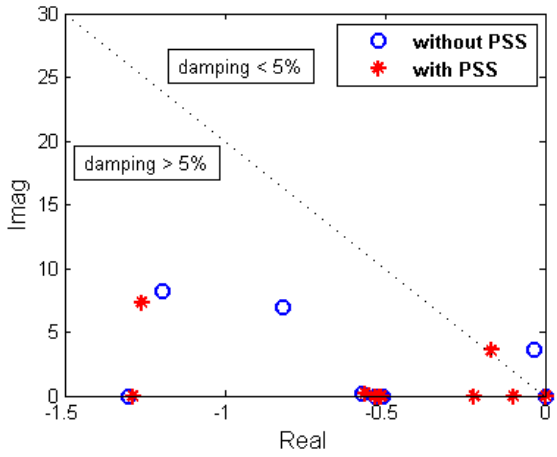

Figure 3.14 Dominant poles of the system without PSS & with PSS

Table 3.4 Electromechanical modes of the 4-machine, 8-bus power system

	Without PSS			With PSS		
Modes	Pole Locations	f (*Hz*)	ζ (%)	Pole Locations	f (*Hz*)	ζ (%)
Local 1	$-1.1962 \pm 8.2158i$	1.32	14.4	$-1.6176 \pm 8.5822i$	1.39	18.5
Local 2	$-0.8186 \pm 6.9826i$	1.12	11.6	$-1.2607 \pm 7.3485i$	1.19	16.9
Inter-area	$-0.0353 \pm 3.6734i$	0.58	0.96	$-0.1693 \pm 3.5833i$	0.57	4.7

Figure 3.15 shows the maximum and minimum singular value plots of the open-loop power system transfer function with and without PSS. It can be seen that the behaviour of the two systems is almost identical for the frequencies above 1 *rad/s*. At low frequencies, however, the gain of the system installed with PSS is smaller than that of without PSS. In particular, for frequencies up to 0.1 *rad/s*, $\bar{\sigma}(G)$ for the system without PSS is greater by approximately 7 *dB*. Also, the resonant peaks, occurring at frequencies 3.7 *rad/s* and 7.2 *rad/s*, are observed to be reduced by 14 *dB* and 3 *dB*, respectively, for the system that has PSS controllers installed. This indicates that the damping of electromechanical modes is improved by applying local PSS controllers.

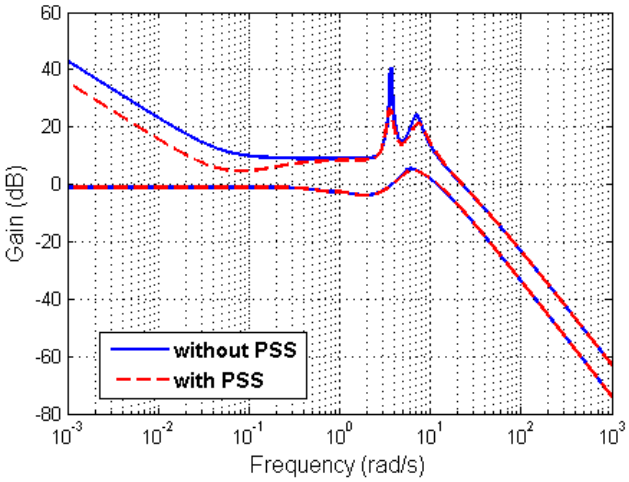

Figure 3.15 Singular value plots of open-loop power system

3.7.2 Continuous-time LQG/LTR

The state-space model of the power system installed with PSS is expressed in (3.36):

$$\begin{aligned} \dot{x} &= A_{PSS}x + B_{PSS}u + w \\ y &= C_{PSS}x + v \end{aligned} \tag{3.36}$$

where $x(t)$, $u(t)$, and $y(t)$ are system state, input and output vectors respectively. A_{PSS}, B_{PSS}, C_{PSS} are the matrices of the state-space model depicting 4-machine power system with local PSS installed for each of the generators. The same synthesis procedure as discussed in Section 3.5 is followed in this section to design the supervisory continuous-time LQG/LTR controller. The integral action is also introduced by applying model (3.33) in order to form an augmented state-space model. The augmented model is denoted as G_{PSS_a}, which is expressed by the following state-space model.

$$\begin{aligned} \dot{x}_a &= A_{PSS\_a}x_a + B_{PSS\_a}u + w \\ y &= C_{PSS\_a}x_a + D_{PSS\_a}u + v \end{aligned} \tag{3.37}$$

where A_{PSS_a}, B_{PSS_a}, C_{PSS_a} and D_{PSS_a} are the augmented state-space model matrices, and x_a is the augmented state vector. The cost function weightings used for the controller design are denoted as Q', R', W' and V', respectively, and are expressed as follows:

$$Q' = \rho M'^{T} \bar{Q} M', \quad R' = I, \; W' = \Gamma' \bar{W} \Gamma'^{T}, \; V' = qI. \tag{3.38}$$

where

$$M' = C_{PSS\_a}, \; \bar{Q} = diag\left\{Q_{P_e}, Q_{V_t}, Q_{\Delta\omega}\right\}, \; \Gamma' = B_{PSS\_a}. \tag{3.39}$$

with

$$\begin{aligned} &Q_{P_{e1}} = 4 \cdot 10^{-2}, \; Q_{P_{e2}} = 4 \cdot 10^{-1}, \; Q_{P_{e3}} = 4 \cdot 10^{-1}, \; Q_{P_{e4}} = 4 \cdot 10^{-2}, \\ &Q_{V_{t1}} = 5 \cdot 10^{-1}, \; Q_{V_{t2}} = 8 \cdot 10^{-2}, \; Q_{V_{t3}} = 8 \cdot 10^{-2}, \; Q_{V_{t4}} = 5 \cdot 10^{-1}, \\ &Q_{\Delta\omega_1} = 1 \cdot 10^{3}, \quad Q_{\Delta\omega_2} = 2 \cdot 10^{2}, \; Q_{\Delta\omega_3} = 2 \cdot 10^{2}, \; Q_{\Delta\omega_4} = 1 \cdot 10^{3}. \end{aligned} \tag{3.40}$$

This particular choice of the cost function weighting matrices was made to ensure that the closed-loop system performance and robustness measures, discussed in Section 3.3, are satisfied.

The resulting supervisory continuous-time LQG/LTR controller is denoted as K_{LQG}^{P}. The supervisory controller K_{LQG}^{*} designed for the system without PSS in Section 3.5 is also applied onto the system with PSSs. This represents the scenario in which the controller is initially designed for the power system that has no PSS regulators implemented and then it is deployed in the situations in which PSS regulators are present. Figures 3.16 and 3.17 show the maximum and the minimum singular value plots of closed-loop transfer function $L(s)$, sensitivity transfer function $S(s)$ and the complementary sensitivity transfer function $T(s)$ of the system with K_{LQG}^{P} and K_{LQG}^{*}, respectively. Table 3.5 lists the corresponding performance measures obtained for the power system when controlled by K_{LQG}^{P} and K_{LQG}^{*}. In the case of K_{LQG}^{P} the cross-over frequencies for $\bar{\sigma}(L)$ and $\underline{\sigma}(L)$ are reduced by 1.6 *rad/s* when compared to K_{LQG}^{*}. Maximum peak of the complementary sensitivity transfer function is smaller indicating the improvement in terms of the performance and robustness, when compared to K_{LQG}^{*}. Applying controller K_{LQG}^{P} improves the damping of the inter-area electromechanical mode when compared to K_{LQG}^{*}, improvement of 64.44% compared 56.08% respectively. However, it is also very reassuring to observe that the supervisory controller designed assuming absence of PSS regulators, i.e. K_{LQG}^{*}, behaves satisfactorily even if they are present.

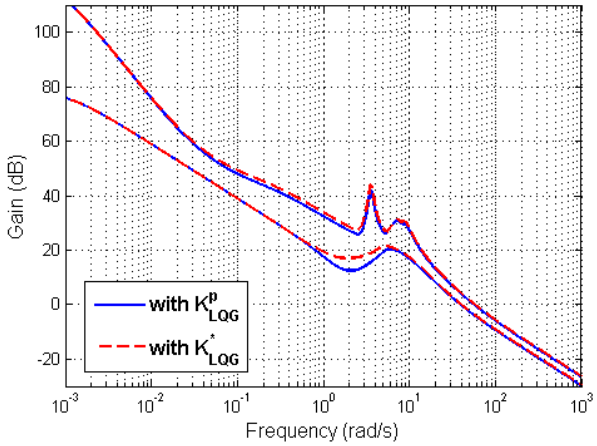

Figure 3.16 $\sigma(L)$ of the system with PSS applying K_{LQG}^{P} and K_{LQG}^{*}

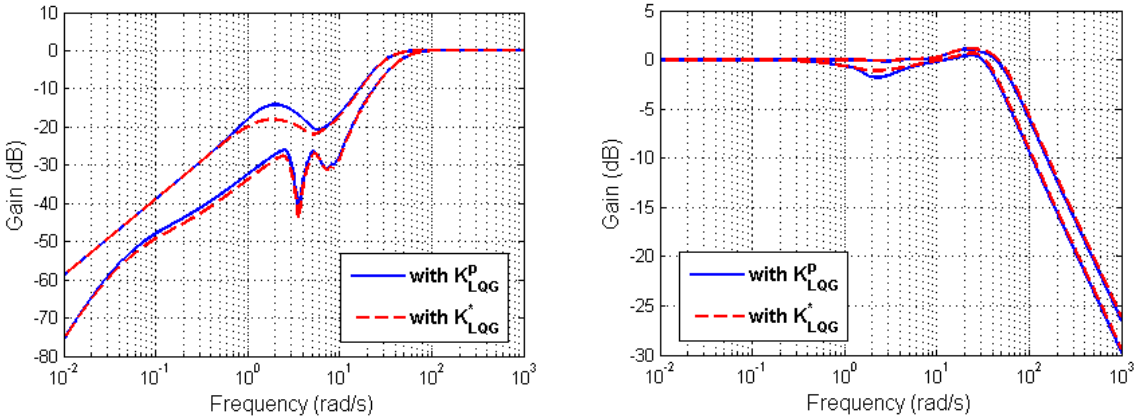

Figure 3.17 $\sigma(S)$ and $\sigma(T)$ of the system with PSS applying K_{LQG}^{P} and K_{LQG}^{*}

Table 3.5 System performance properties

Controller	Inter-area mode		M_S (*dB*)	M_T (*dB*)	ω_B (*rad/s*)	$\omega_{\underline{\sigma}(L)}$ (*rad/s*)	$\omega_{\bar{\sigma}(L)}$ (*rad/s*)	Roll-off Rate *dB/decade*
	$\zeta(\%)$	$f(Hz)$						
K_{LQG}^{P}	64.44	0.57	0	1.2	29.2	38.4	56.0	20
K_{LQG}^{*}	56.08	0.43	0	1.0	29.6	40.0	57.6	20

3.7.3 Non-linear Simulation

In order to fully assess the effectiveness and the robustness of the designed continuous-time LQG/LTR controller, non-linear simulation of the power system,

including PSS regulators is utilised. A three-phase fault is applied at bus 5 at time 1 second. The fault is cleared with auto-reclosing the circuit breaker after 4 cycles (80 *ms*).

The unstable time response of the open-loop system without PSS or supervisory controller implemented is shown in Figure 3.18 with a dotted line. The inclusion of PSS resulted in an increase of the damping of the inter-are oscillation mode. As a result, the responses are stable as shown in Figure 3.18 (blue dashed line). However, the inter-area mode is still lightly-damped and as a result the system's response is still rather oscillatory with the settling time greater than 10 seconds when subject to a severe disturbance. The solid lines in Figure 3.18 represent the time response of the power system equipped with both PSS and the supervisory LQG/LTR controller K_{LQG}^{p}. The resultant response of the closed-loop system is clearly shown to achieve satisfactory level of damping with the minimal settling time.

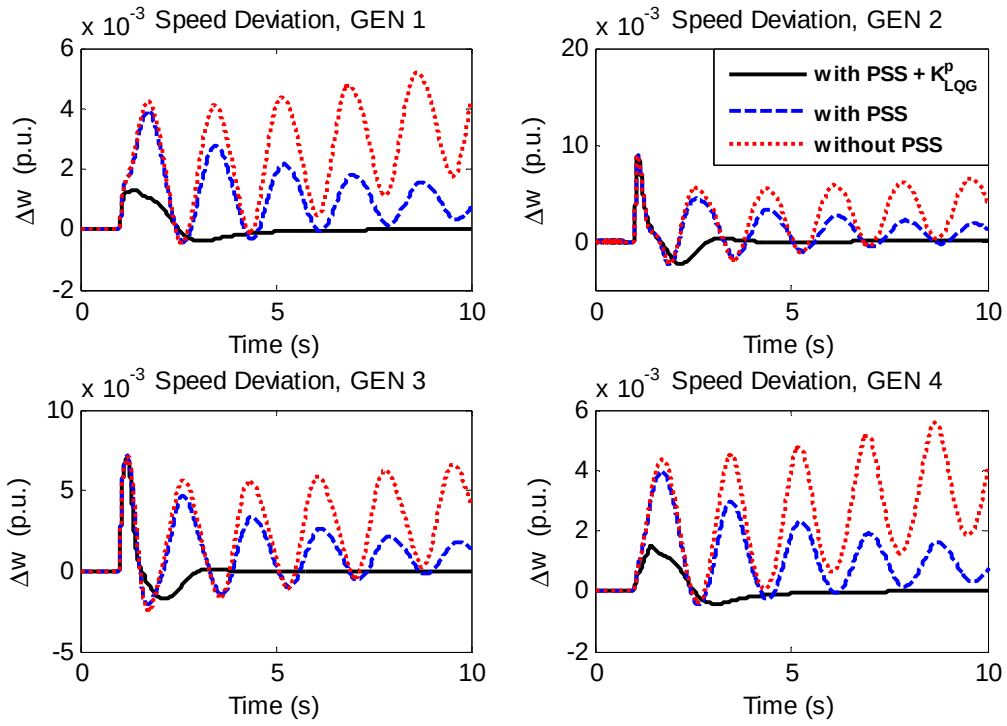

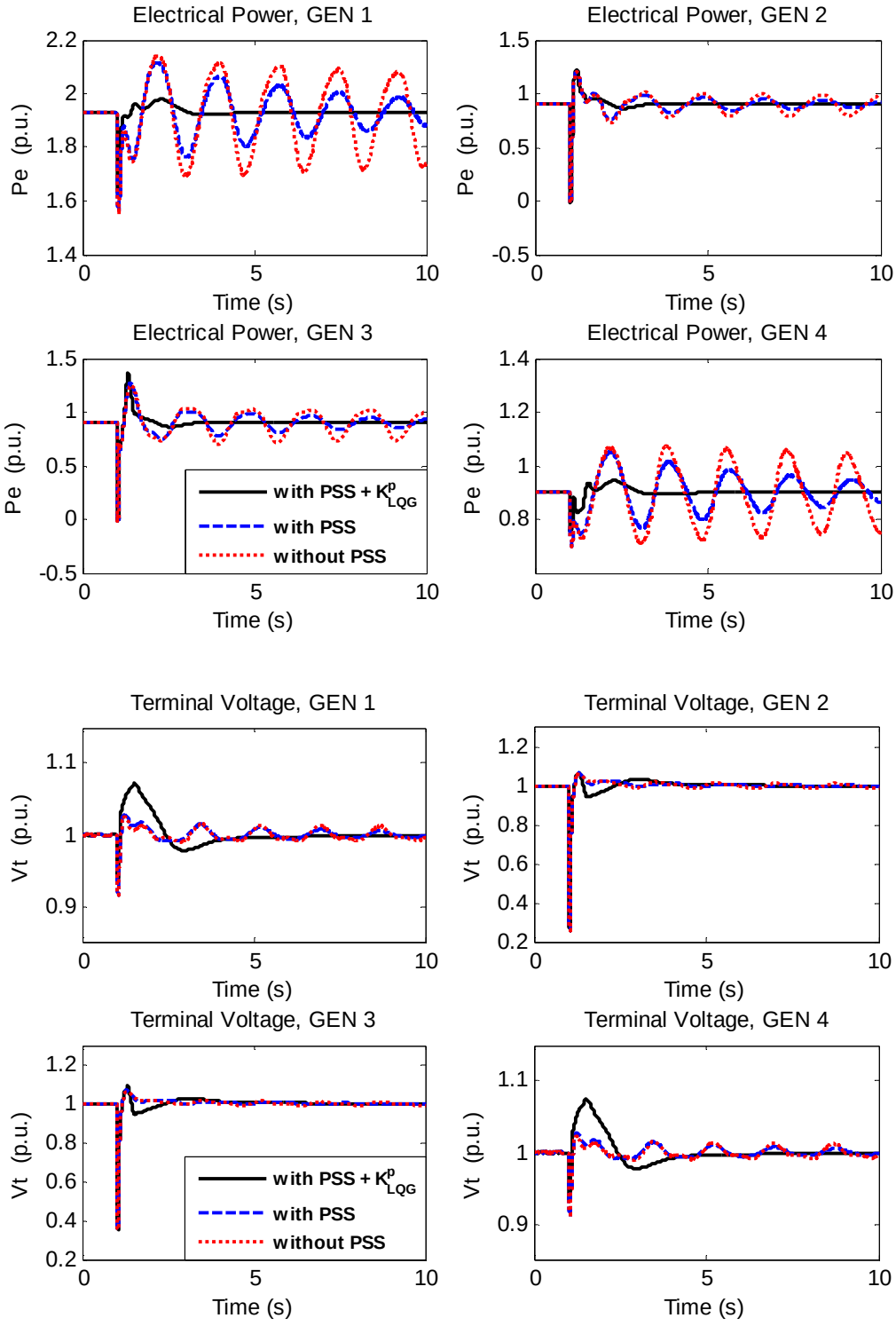

Figure 3.18 System responses to a self-cleared three-phase fault

Next, controllers K_{LQG}^{P} and K_{LQG}^{*} are compared in the presence of the three-phase fault and the results are shown in Figure 3.19. It can be observed that the speed deviation and the magnitude of the electrical power output are smaller when the

power system is controlled by the supervisory controller K_{LQG}^{P} when compared to K_{LQG}^{*} during transient period, which illustrates the superiority of K_{LQG}^{P} and K_{LQG}^{*} in terms of the improved damping of the inter-area mode as well as the effectiveness in stabilising the power system and rejecting large disturbances. Nevertheless, the fact that K_{LQG}^{*} managed to achieve satisfactory response is a positive result indicating satisfactory robustness of the controller that was designed for the power system without any PSS regulators implemented.

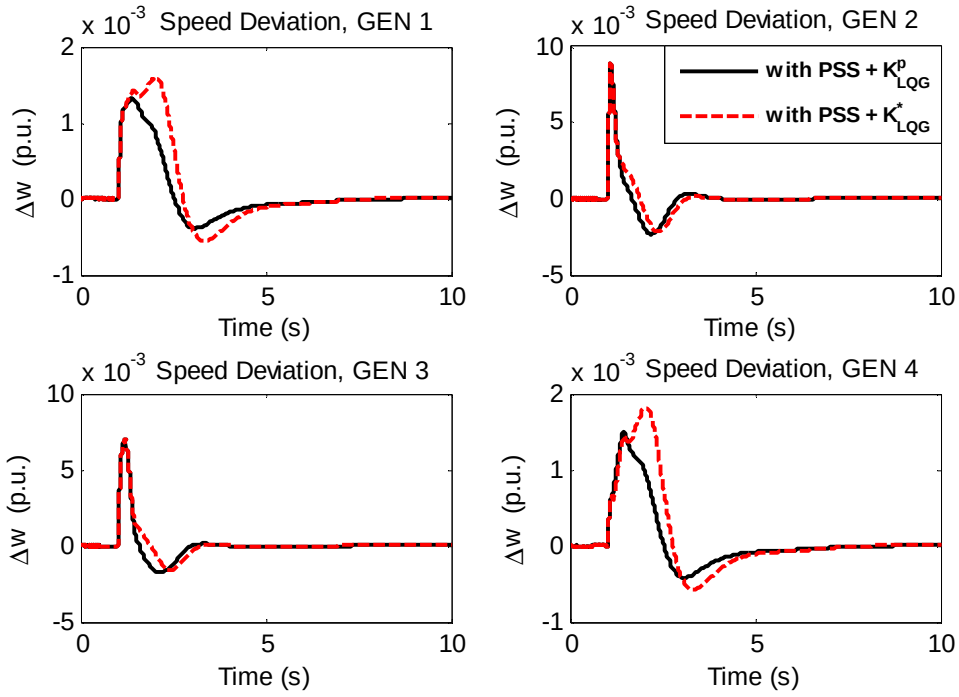

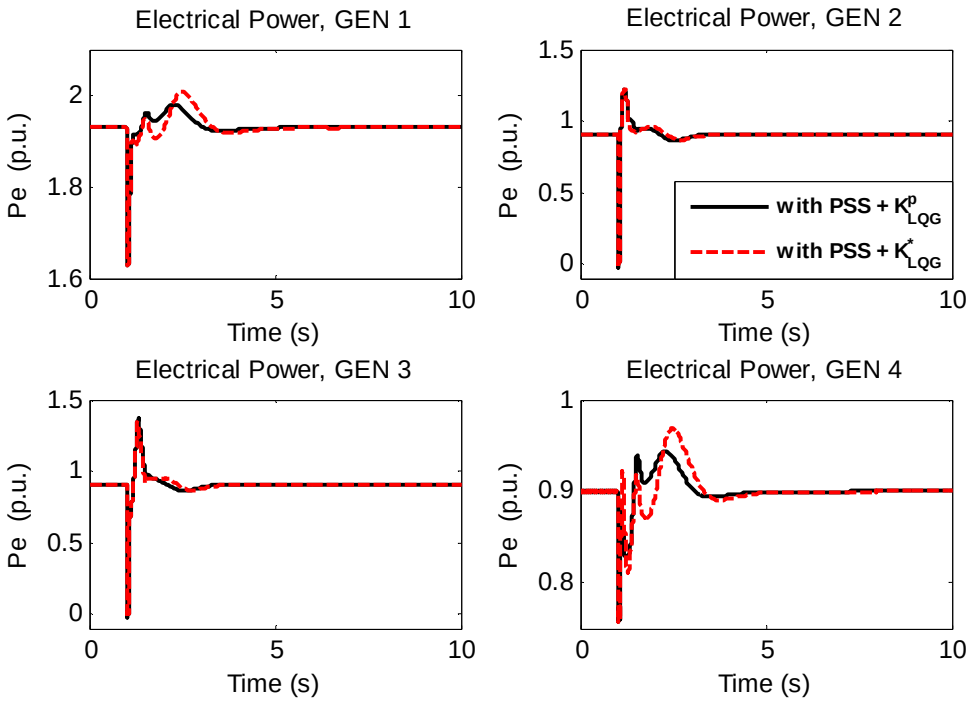

Figure 3.19 System responses for K_{LQG}^{P} and K_{LQG}^{*}

3.8 Summary

This chapter was concerned with the design of the supervisory optimal controller using LQG/LTR design procedure in order to improve the damping of the electromechanical oscillations of the multi-machine power system. This supervisory controller used the local information (rotor angle, voltage and electrical power output) from each generator in order to improve the rotor-angle stability in the presence of both small-signal and large-signal disturbances. Loop transfer recovery procedure at the plant input was used to recover the robustness and performance properties of the classical optimal control regulator.

The performance and the robustness of the resulting closed-loop system were analysed using frequency domain tools and assuming linear system model. Also, the small-signal and large-signal disturbances were applied to assess the stability of the non-linear power system regulated by the designed supervisory controller. In addition, the robustness of the designed controller was assessed by considering power system operation under different operating conditions. All the results demonstrated the ability of the designed supervisory controller to improve rotor angle stability of the multi-machine power system.

Additionally, the supervisory continuous-time LQG/LTR controller was designed for the multi-machine power system equipped with the local PSS regulators. Corresponding results clearly showed that the designed controller was sufficiently effective and robust in enhancing the wide-area power system stability in the presence of PSS regulators and regardless of whether or not PSS regulators were assumed to be installed during the supervisory controller's design.

Chapter 4

Discrete-Time LQG/LTR for Multi-Machine Power System

4.1 Introduction

In Chapter 3, a continuous-time supervisory LQG/LTR controller was designed to improve the closed-loop system response by increasing the damping of the oscillatory electromechanical modes. This controller is assumed to execute continuously in time, i.e. with the sampling frequency tending to infinity. Such assumption is not unusual in the field of power system control. In fact, majority of the researchers assume continuous-time implementation when designing wide-area controllers [20, 31, 41-44]. However, the resulting control systems' capabilities are heavily reliant on a critical assumption that the sampling rates of the practical computers used to implement designed controllers are sufficiently high to ensure that the performance is not compromised. Such assumption may become inadequate when considering control of large-scale power systems, containing many areas and generating units, for which computation time may not be sufficiently small to warrant the controller design in continuous-time. This is particularly true when considering the problem of rotor angle stability for which the dominant dynamics are found in the frequency range of 0.1 to 2.0 *Hz*. In such control applications the sampling and computation time may prove to be critical performance-limiting parameters. Therefore, it would be advantageous to investigate and understand this

impact by addressing the problem of multi-area supervisory control using discrete-time framework. Then, the performance of the resulting discrete-time controller can be assessed for different values of the sampling period.

When developing discrete-time controllers, it is quite common to carry out continuous-time design first, followed by the discretisation of the resulting continuous-time controller. Such practice is often followed despite the availability of the design methods in discrete-time framework [86]. However, it is argued in this thesis that it would be advantageous to consider controller design in the discrete-time framework by firstly discretising the open-loop system dynamics. As a result, the early design decisions regarding sampling period, and possible sampling skew or computational delay can be incorporated into the actual controller design through their integration into the discrete-time model of an open-loop system [86].

Therefore, this chapter focuses on the design of the supervisory LQG/LTR controller using discrete-time framework to represent open-loop dynamics of the studied power system. Also, this chapter focuses on the analysis of the impact that the sampling period has on the performance of the closed-loop control system. The effectiveness and robustness of the designed supervisory discrete-time LQG/LTR controller is then verified on the non-linear power system simulation with and without Power System Stabilizers. Both small-signal and large-signal disturbances are applied to the power system simulation in order to evaluate the designed controller. Also, the robustness of the supervisory controller with respect to changing operating conditions is assessed by changing the power transfer between the two areas in the studied power system.

4.2 *z*-Plane Specifications

In order to use the design methods discussed in Chapter 3 for the synthesis of the discrete-time controllers it is necessary for the system model as well as the performance specifications to be translated into the *z*-plane. Poles in the *s*-plane $s = \sigma + j\omega_n$ are mapped to $z = e^{sT_s}$ in the *z*-plane. Note that the real part of the pole in the *s*-plane (σ) is mapped to the radius of the pole in the *z*-plane as $r = e^{\sigma T_s}$,

while the natural frequency in *s*-plane (ω_n) is mapped to the angle of the pole in polar coordinates in the *z*-plane as $\theta = \omega_d T_s$ where $\omega_d = \sqrt{1-\zeta^2}\,\omega_n$ [87]. The left half of the *s*-plane is mapped into the interior of unit circle centred at the origin in the *z*-plane. The mapping of the margin to distinguish the poorly-damped and the well-damped oscillation modes in the *s*-plane to the *z*-plane is shown in Figure 4.1. The eigenvalue located inside the dashed curve is well-damped, and between the dashed curve and the unit circle is poorly-damped.

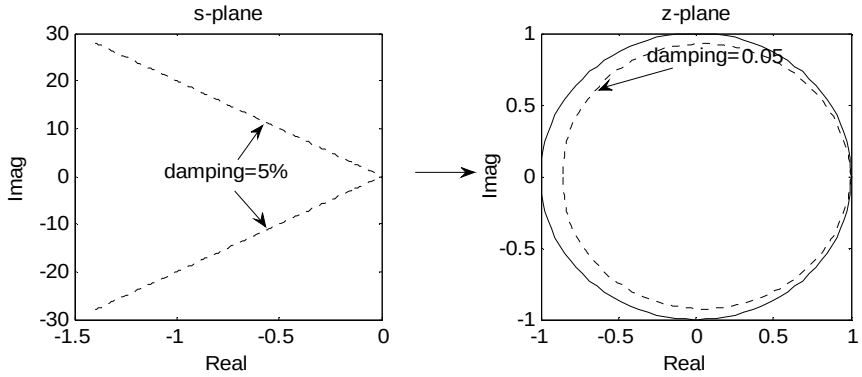

Figure 4.1 Mapping of the damping margin

Figure 4.2 shows the mapping between the location of the pole in *s*-plane to the the location of that same pole in the *z*-plane for sampling period $T_s = 0.01$. It can be seen that the dominant poles located near the imaginary axis in the *s*-plane are mapped to be located near the unit circle in the *z*-plane. Therefore, the pole located on the unit circle in the z-plane indicates that the open-loop power system is not stable.

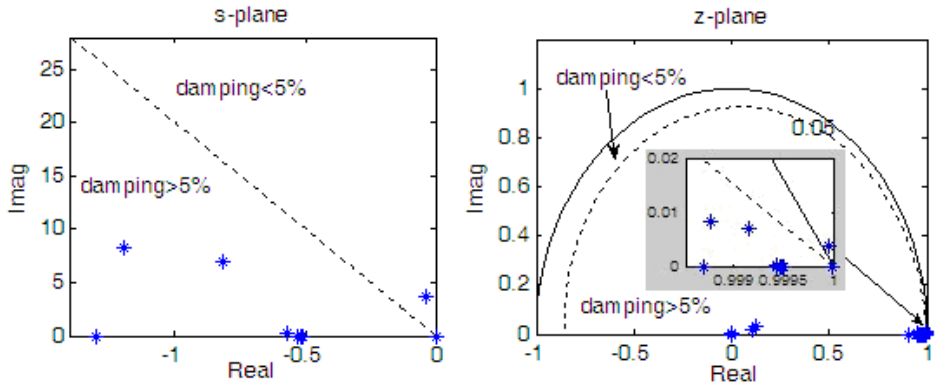

Figure 4.2 Eigenvalues of 4-Generator system without PSS

The left part of Figure 4.3 displays the three electromechanical oscillation modes in the *s*-plane, the right part of Figure 4.3 shows the corresponding discrete-time electromechanical oscillation modes for different sampling periods $T_s = 0.001$, 0.01, 0.05 and 0.1 seconds, respectively, in the *z*-plane. The pole located above the dashed line in *s*-plane indicates that the inter-area oscillation mode is poorly-damped. The discrete-time eigenvalues corresponding to the inter-area oscillation mode for different sampling periods are all located between the margin curve and the unit circle in *z*-plane, i.e. they also appear to be poorly-damped. Thus, the properties of the oscillatory modes observed using discrete-time framework coincide with those observed using continuous-time framework.

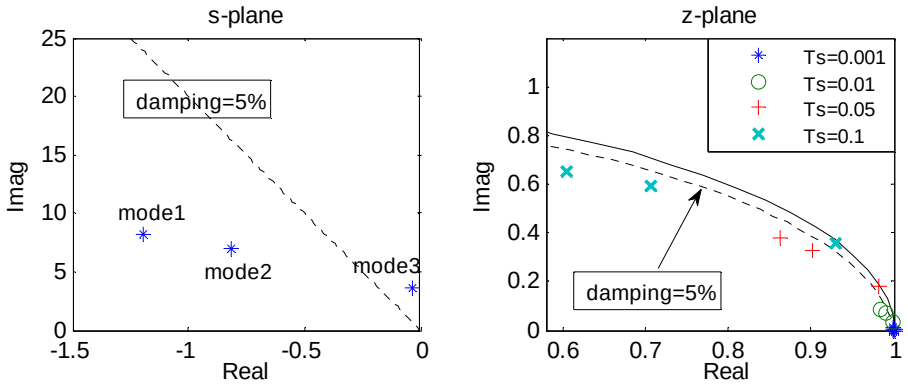

Figure 4.3 Electromechanical oscillation modes

It is important to note that the frequency domain plot of $G(e^{j\omega T_s})$ repeats for $\omega = n\omega_s$ to $(n+1)\omega_s$, $n = 0, 1, 2, \ldots$. ($\omega_s = 2\pi / T_s$). Thus it is necessary to plot $G(e^{j\omega T_s})$ only for the range of $\omega = 0$ to $\omega_N = \omega_s / 2$, where $\omega_N = \omega_s / 2$ is known as Nyquist frequency [50]. Once *z* is replaced by $e^{j\omega T_s}$ in the *z*-domain transfer function, all the frequency-domain analysis techniques available for continuous-data systems can be applied to discrete-data systems [87].

4.3 Discrete-Time LQG/LTR

In order to design supervisory discrete-time LQG controller it is necessary to translate the corresponding control problem from the continuous-time into the discrete-time framework. This procedure comprises of converting continuous-time

system model, given in (3.10), and the controller's cost function, given in (3.12), into their discrete-time equivalents, under the assumption that the zero-order-hold (ZOH) devices are used for the signal reconstruction.

4.3.1 Discretisation of the Plant

Assuming periodic sampling with period T_s:

$$t = kT_s, \quad k = 0, 1, ...$$

The resulting input signal $u(t)$, reconstructed using Zero-Order-Hold (ZOH) device, is constant over the sampling period, and the equivalent discrete-time system corresponding to (3.10) is given by [50]:

$$\begin{aligned} x(k+1) &= \Phi x(k) + \Gamma u(k) + w_k \\ y(k) &= Cx(k) + v_k \end{aligned} \tag{4.1}$$

with

$$\Phi = e^{AT_s}, \ \Gamma = \int_0^{T_s} e^{As} ds B. \tag{4.2}$$

Where w_k and v_k are discrete-time Gaussian white noise processes with zero mean and covariance given as [88]:

$$\begin{aligned} W_k &= E\left\{w_k w_k^T\right\} = \int_0^{T_s} e^{As} W (e^{As})^T ds, \\ V_k &= E\left\{v_k v_k^T\right\} = V(k), \\ E\left\{w_k v_k^T\right\} &= 0, \ E\left\{v_k w_k^T\right\} = 0. \end{aligned} \tag{4.3}$$

The calculation of Φ and Γ is usually done by using the following series expansion:

$$\Psi = \int_0^{T_s} e^{As} ds = IT_s + \frac{AT_s^2}{2!} + \frac{A^2 T_s^3}{3!} + \cdots + \frac{A^i T_s^{i+1}}{(i+1)!} + \cdots \tag{4.4}$$

Where Φ and Γ are calculated by:

$$\Phi = I + A\Psi, \ \Gamma = \Psi B. \tag{4.5}$$

4.3.2 Discretisation of the cost function

The continuous-time cost function (3.14) is transformed into its discrete-time equivalent by integrating (3.14) over a time interval of length T_s , which denotes the sampling period [50]:

$$J_k^* = E\left\{\sum_{k=0}^{\infty} x(k)^T Q_k x(k) + u(k)^T R_k u(k)\right\} \tag{4.6}$$

where

$$\begin{aligned} Q_k &= \int_0^{T_s} \Phi(s)^T Q \Phi(s) ds, \\ R_k &= \int_0^{T_s} \left[\Gamma(s)^T Q \Gamma(s) + R\right] ds. \end{aligned} \tag{4.7}$$

and $\Phi(s)$ and $\Gamma(s)$ are defined as

$$\Phi(s) = e^{As},\ \Gamma(s) = \int_0^s e^{At} dt B\,. \tag{4.8}$$

It is assumed that Q_k is positive semidifinite and that R_k is positive definite.

Note that the discrete-time cost function weighting matrices Q_k and R_k given in (4.6) and (4.7) are affected by the sampling period T_s. Numerical calculations involved in computing Φ and Γ can be referred to reference [87].

4.3.3 Discrete-Time LQG

The discrete-time LQG control problem is to find the optimal control sequence $u(k)$ which minimizes the cost function (4.6) when the process is described by (4.1). Note that the control sequence as well as the cost function in (4.6) and the system dynamics in (4.1) are defined in discrete-time assuming the presence of ZOH reconstruction devices. Analogous to continuous-time, discrete-time separation theorem is used to allow the synthesis of discrete-time LQG controller to be split into two sub-problems, which can be solved separately. One of these is the discrete-time optimal regulator control problem, solution of which is full state feedback control

law gain K_{r_k}. The other problem is concerned with optimal state estimation and its solution is the discrete-time Kalman Filter gain K_{f_k}.

Given the deterministic model of the plant (4.1) (without process and measurement noises), the discrete-time optimal control law that minimizes the cost function

$$J_k = \sum_{k=0}^{\infty} x(k)^T Q_k x(k) + u(k)^T R_k u(k) \tag{4.9}$$

is given by

$$u(k) = -K_{r\_k} \hat{x}(k \mid k) \tag{4.10}$$

where K_{r_k} is the optimal regulator gain

$$K_{r\_k} = \left(R_k + \Gamma^T P_{r\_k}(k) \Gamma \right)^{-1} \Gamma^T P_{r\_k}(k) \Phi \tag{4.11}$$

and P_{r_k} is the positive semidefinite solution of the discrete algebraic Riccati equation (DARE)

$$P_{r\_k}(k) = \Phi^T P_{r\_k}(k+1) \Phi - K_{r\_k}{}^T \left(R_k + \Gamma^T P_{r\_k}(k+1) \Gamma \right) K_{r\_k} + Q_k \tag{4.12}$$

where Q_k and R_k are the discrete-time weighting matrices which are defined as in (4.7).

The discrete-time Kalman filter provides the optimal estimate $\hat{x}(k \mid k)$ of the state $x(k)$, so that $E\left\{ \left[x(k) - \hat{x}(k \mid k) \right]^T \left[x(k) - \hat{x}(k \mid k) \right] \right\}$ is minimized. The discrete-time Kalman filter implementation consists of two steps at each time *k*, described below. One of these is time update, by which $\hat{x}(k-1 \mid k-1)$ is updated to $\hat{x}(k \mid k-1)$, and the other is measurement update, in which the measurement of $y(k)$ at time *k* is incorporated to provide the updated estimate $\hat{x}(k \mid k)$.

Time update:

$$\hat{x}(k \mid k-1) = \Phi \hat{x}(k-1 \mid k-1) + \Gamma u(k-1) \tag{4.13}$$

$$P_{f\_k}(k \mid k-1) = \Phi P_{f\_k}(k-1 \mid k-1) \Phi^T + W_k \tag{4.14}$$

Measurement update:

$$K_{f\_k} = P_{f\_k}(k \mid k-1) C^T \left[C P_{f\_k}(k \mid k-1) C^T + V_k \right]^{-1} \tag{4.15}$$

$$P_{f\_k}(k \mid k) = \left[I - K_{f\_k} C \right] P_{f\_k}(k \mid k-1) \tag{4.16}$$

$$\hat{x}(k \mid k) = \hat{x}(k \mid k-1) + K_{f\_k} \left[y(k) - C\hat{x}(k \mid k-1) \right] \tag{4.17}$$

where P_{f_k} is positive definite, and $K_{f\_k}(k)$ is the discrete-time Kalman filter gain.

The discrete-time LQG controller can then be described by the following:

$$K_{dLQG}(z) = \left[\begin{array}{c|c} \Phi - \Gamma K_{r\_k} - K_{f\_k} C & K_{f\_k} \\ \hline -K_{r\_k} & 0 \end{array} \right] \tag{4.18}$$

4.3.4 Loop Transfer Recovery

Loop Transfer Recovery (LTR) is applied to the discrete-time LQG controller following the similar procedure to that presented in Section 3.3.3. First of all, note that $G_d(z)$ is denoted as the transfer function of the discrete-time model. Two cases are considered as follows.

Recovery at plant input: Discrete-time Kalman filter gain $K_{f\_k}(k)$ is obtained such that the loop transfer function $K_{dLQG}(z)G_d(z)$ approaches the optimal regulator loop gain $K_{r\_k}(k)(zI - A)^{-1}B$. The open-loop system must be minimum phase and must have at least as many outputs as inputs i.e. $r \geq m$.

Recovery at plant output: Discrete-time LQR regulator gain $K_{r\_k}(k)$ is obtained such that the loop transfer function $G_d(z)K_{dLQG}(z)$ approaches the Kalman Filter loop gain $C(zI - A)^{-1}K_{f\_k}(k)$. The open-loop system must be minimum phase and must have at least as many inputs as outputs i.e. $r \leq m$.

4.3.5 Discrete-Time Cost Function Weighting Selection

For discrete-time LQG, the cost function weights Q_k and R_k are calculated by applying transformation described in (4.7) and (4.8) to their continuous-time variants.

By doing this, the cost function used to synthesise the optimal controller is transformed from the continuous-time to the discrete-time framework. It can be shown that the value of ratio of Q_k/R_k is equal to the value of ratio of Q/R, which is designated as ρ. The discrete-time LQR loop transfer matrices is derived as

$$L_{r\_d}(e^{j\omega}) = K_{r\_k}(zI - \Phi)^{-1}\Gamma \tag{4.19}$$

which satisfies the following return difference identity:

$$\left[I + L_{r\_d}(e^{j\omega})\right]^H R_k \left[I + L_{r\_d}(e^{j\omega})\right] = R_k + G_{r\_d}^H Q_k G_{r\_d}, \quad \forall 0 \le \omega < \infty \tag{4.20}$$

where

$$G_{r\_d} = M(zI - \Phi)^{-1}\Gamma \tag{4.21}$$

Therefore:

$$\begin{aligned}\sigma_{i\_d}[I + L_{r\_d}(e^{j\omega})] &= \sqrt{\lambda_i\left[I + \rho\left(G_{r\_d}Q_k^{1/2}\right)^H\left(G_{r\_d}Q_k^{1/2}\right)\right]} \\ &= \sqrt{I + \rho\lambda_i\left[\left(G_{r\_d}Q_k^{1/2}\right)^H\left(G_{r\_d}Q_k^{1/2}\right)\right]} \\ &= \sqrt{I + \rho\sigma_{i\_d}^2\left[G_{r\_d}Q_k^{1/2}\right]}\end{aligned} \tag{4.22}$$

From (4.22) we can see that an increase in ρ by a factor α leads to an increase in regulator gain K_{r_k} and loop gain L_{r_d} by a factor $\sqrt{\alpha}$.

4.4 Discrete-Time LQG/LTR for Power System

The block diagram of the closed-loop system, including 2-area 4-machine power system simulation, supervisory discrete-time controller, the analog-to-digital (A/D) converter, the digital-to-analog (D/A) converter and a zero-order hold (ZOH), is shown in Figure 4.4. The modelling of the power system is discussed in Chapter 2. It is assumed that the analogue measurements are sampled by A/D converter with the sampling period T_s. Once the discrete-time supervisory controller computes the required digital control signals, D/A converts them to analogue signals which are fed to the power system. ZOH device is then used to complete the reconstruction of the

analogue signal by holding each sample value constant for a duration of one sample interval.

The performance of the discrete-time control system is critically influenced by the choice of the sampling period T_s [50]. From the viewpoint of the controller design, it is desirable to select the sampling period to be as small as possible in order to recover the performance achieved by the equivalent continuous-time controller [87]. However, from the implementation perspective, if the sampling period is chosen to be too small then the computational requirement exerted on the control system may be prohibitively high. In the case of wide-area control design, this also leads to the problem of selecting suitable Phase Measurement Units (PMU) data reporting rates [89]. Therefore, there is an inevitable compromise between the cost and the performance when selecting an appropriate sampling period.

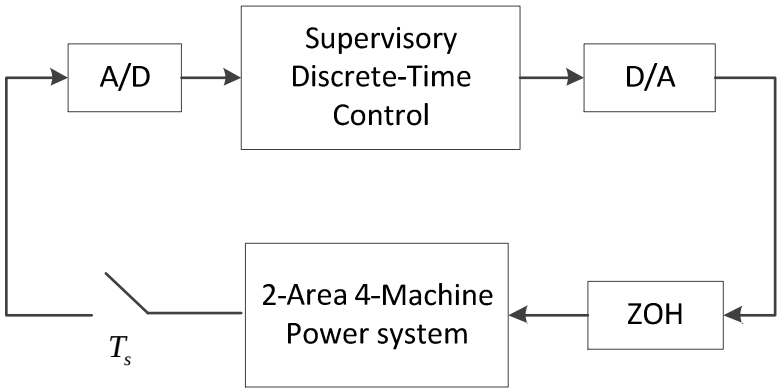

Figure 4.4 Block diagram of the supervisory discrete-time controlled power system

The first step when designing discrete-time LQG/LTR controller is to discretise the open-loop power system model using the procedure outlined in Section 4.3.1. Once the model is transformed into the discrete-time framework then the standard discrete-time LQG/LTR design procedure can be applied. Note, however, that the selection of sampling period directly influences realisation of the discrete-time model and, therefore, has far-reaching consequences on the performance and robustness of the resulting closed-loop control system. In this chapter it is initially assumed that the sampling period is equal to $T_s = 0.01$ seconds. Decision to start with such small sampling period was made in order to allow the design of a benchmark discrete-time

controller. Subsequently, LQG/LTR controllers with larger sampling periods can then be compared against this benchmark.

Once the open-loop system is discretised it is important to assess its fidelity with respect to the corresponding continuous-time model. Since both of these models are of linear time-invariant type, it is appropriate to compare them in frequency domain. Figure 4.5 shows the singular value plots of the open-loop frequency responses for the power system model given in discrete-time and the continuous-time power system model. It is clearly observed that the system performance of the discrete-time model is very similar to the performance of the continuous-time model within the range of frequencies from 0 Hz to 50 Hz. This indicates that the sampling period of $T_s = 0.01$ seconds is sufficiently small to allow discrete-time model to replicate the great majority of the continuous-time system behaviour.

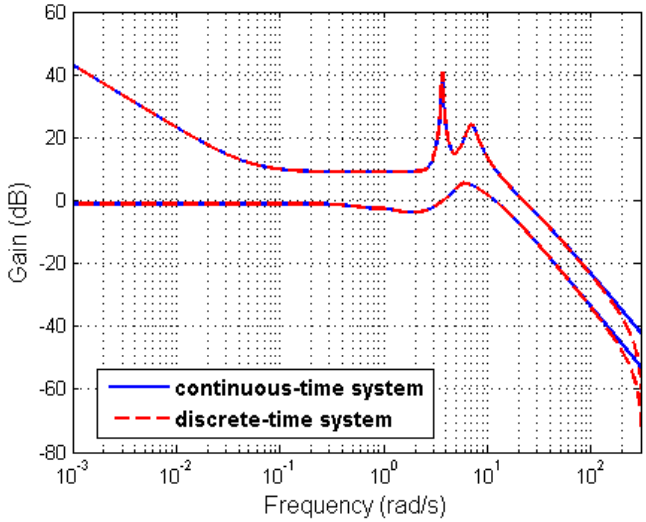

Figure 4.5 Singular value plot of open-loop transfer function

4.4.1 Discrete-Time Optimal Regulator Design

Similarly to its continuous-time counterpart, discrete-time LQG/LTR controller incorporates integral action in order to track persistent disturbances and ensure accurate set-point tracking. This is achieved by augmenting the state-space model with the integrator sub-system whose poles are placed on the unit circle, which is in

accordance with the mapping of poles from *s*-plane to *z*-plane as stated in Section 4.2. The nominal system model (4.1) is augmented as follows:

$$\begin{bmatrix} x(k+1) \\ x_i(k+1) \end{bmatrix} = \begin{bmatrix} \Phi & 0 \\ C & I \end{bmatrix} \begin{bmatrix} x(k) \\ x_i(k) \end{bmatrix} + \begin{bmatrix} \Gamma \\ 0 \end{bmatrix} u(k) \tag{4.23}$$

where $\Phi_a = \begin{bmatrix} \Phi & 0 \\ \Gamma & I \end{bmatrix}$, $\Gamma_a = \begin{bmatrix} \Gamma \\ 0 \end{bmatrix}$, $C_a = \begin{bmatrix} C & 0 \end{bmatrix}$, and $D_a = D$ are denoted as the state-space matrices related to the discrete-time model.

In order to translate continuous-time LQG cost function into its discrete-time equivalent, the weighting matrices Q_k and R_k are derived by using the discretisation procedure given in equation (4.7) on the matrices *Q* and *R*, stated in Section 3.7 and related to continuous-time LQG cost function. The discrete-time optimal regulator gain, denoted as K_{r_d}, is then obtained by solving the discrete-time Riccatti equation:

$$P_{r\_k}(k) = \Phi_a^T P_{r\_k}(k+1)\Phi_a - K_{r\_k}{}^T \left(R_k + \Gamma_a^T P_{r\_k}(k+1)\Gamma_a \right) K_{r\_k} + Q_k$$

where P_{r_k} is positive semidefinite.

Figure 4.6 shows the maximum and minimum singular value plots of the resulting discrete-time optimal regulator loop transfer function $L_{r\_d} = K_{r\_d}(zI - \Phi_a)^{-1}\Gamma_a$ (red dash line) compared with the continuous-time optimal regulator loop transfer function $L_r^*(s) = K_r^*(sI - A_a)^{-1}B_a$ (blue solid line), which was designed in Section 3.5. Figure 4.7 shows the corresponding singular value plots of the sensitivity transfer function *S* and complementary sensitivity transfer function *T*. Also, Table 4.1 summarises the important performance measures obtained for the power system when controlled using K_r^* and K_{r_d}, respectively. In the case of discrete-time optimal regulator K_{r_d}, the cross-over frequencies for $\bar{\sigma}(L)$ and $\underline{\sigma}(L)$ as well as the bandwidth ω_B are somewhat reduced when compared to K_r^*. Also, maximum peak of *T*, M_T, is increased from 1.1 *dB* to 1.41 *dB*, thereby indicating the degradation in the performance and robustness when compared to K_r^*. Finally, damping of the inter-area electromechanical mode is reduced from 67.1% to 66.9% when using optimal regulator K_{r_d}. These changes in values indicate degradation of

discrete-time controller's performance and robustness. However, the observed differences are deemed to be insignificant and it is expected that the discrete-time controller will deliver performance that is almost identical to that obtained using its continuous-time equivalent.

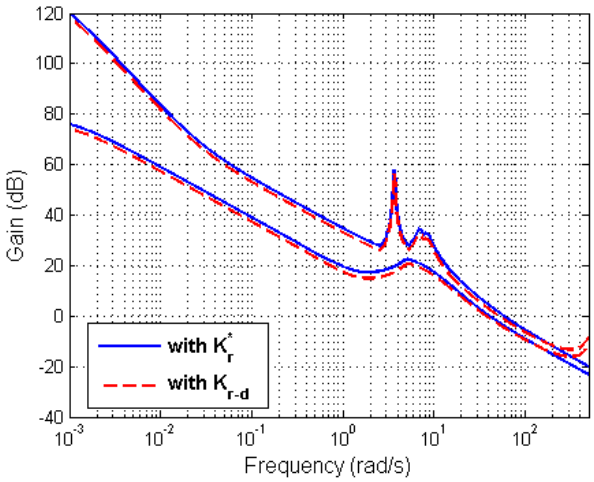

Figure 4.6 $\sigma(L)$ for K_r^* and K_{r_d}

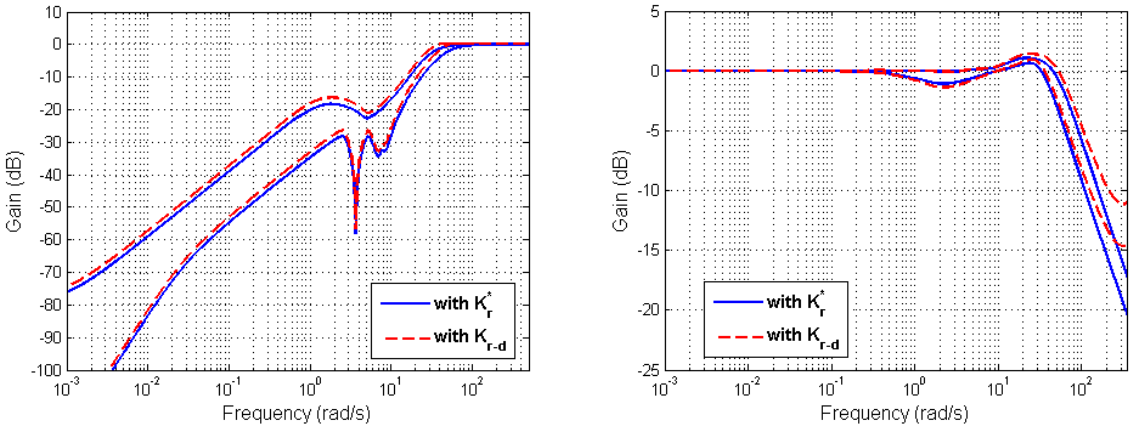

Figure 4.7 $\sigma(S)$ and $\sigma(T)$ for K_r^* and K_{r_d}

Table 4.1 System performance properties

Controller	Inter-area mode		M_S (*dB*)	M_T (*dB*)	ω_B (*rad/s*)	$\omega_{\underline{\sigma}(L)}$ (*rad/s*)	$\omega_{\bar{\sigma}(L)}$ (*rad/s*)	Roll-off Rate *dB/decade*
	$\zeta(\%)$	$f(Hz)$						
K_r^*	67.10	0.60	0	1.10	30.2	40.4	58.5	20
K_{r_d}	66.9	0.60	0	1.41	26.0	37.0	51.2	20

4.4.2 Loop Transfer Recovery at the Plant Input

The discrete-time Kalman Filter is designed in order to recover the optimal discrete-time regulator (discrete-time LQR) loop gain at the plant input. The covariance of the discrete-time Gaussian white noises W_k and V_k is given by (4.3), assuming ZOH type of analogue signal reconstruction. Similarly to continuous-time LQG/LTR procedure, it can be shown that as q tends to zeros, the recovery of the optimal regulator loop gain at the plant input is achieved [29]. The discrete-time Kalman filter gain K_{f_d} is then obtained by solving (4.14) and (4.16). Once K_{f_d} is calculated, the state-space realization of the discrete-time LQG controller is given as:

$$K_{dLQG}(z) = \left[\begin{array}{c|c} \Phi_a - \Gamma_a K_{r\_k}(k) - K_{f\_k}(k) C_a & K_{f\_k}(k) \\ \hline -K_{r\_k}(k) & 0 \end{array}\right] \tag{4.24}$$

Figure 4.8 shows the singular values of the discrete-time LQG loop function $-K_{dLQG}G_{a\_d}$ (dash lines), compared with the singular values of discrete-time regulator loop function $K_{r\_d}(zI - \Phi_a)^{-1}\Gamma_a$ (solid lines), for $q = 10^{-2}$, 10^{-4}, 10^{-6}, 10^{-8} and 10^{-10}. As q is reduced, the discrete-time LQG loop gain approaches that of the optimal regulator loop gain. However, the recovery cannot be fully achieved for discrete-time design with $q = 10^{-6}$, with which a virtual full recovery is achieved for continuous-time LQG/LTR, as shown in Figure 3.6. Even if q is reduced to $q = 10^{-10}$, the complete loop transfer recover is not achieved as shown in Figure 4.9. Table 4.2 compares the system performance measures obtained for the closed-loop system when controlled by using K_{r_d} and K_{dLQG}. In the case of K_{dLQG}, the cross-over frequencies for $\bar{\sigma}(L)$ and $\underline{\sigma}(L)$ as well as the bandwidth ω_B are reduced when compared to K_{r_d}. Such reduction results in a more sluggish response to disturbances or set-point changes. The maximum peak of T, M_T, is increased from 1.2 *dB* to 1.5 *dB*, indicating some insignificant degradation of the closed-loop system's robustness and performance. Furthermore, the damping ratio of the electromechanical mode has reduced insignificantly from 66.9% to 66.4% when using discrete-time LQG/LTR as opposed to discrete-time LQR controller. Therefore,

some degradation in performance is observed but this degradation is not deemed to be consequential and it can be concluded that the satisfactory loop transfer recovery has been achieved for the discrete-time LQG/LTR controller.

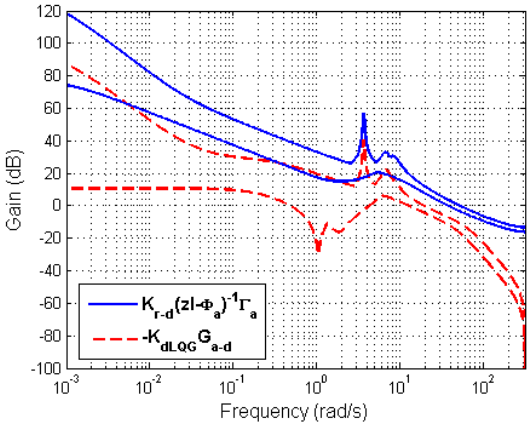

(a) $q=10^{-2}$

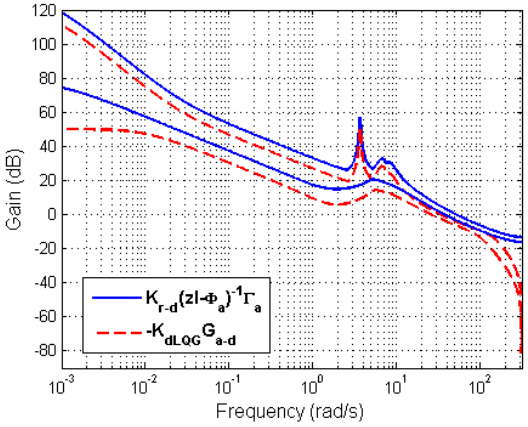

(b) $q=10^{-4}$

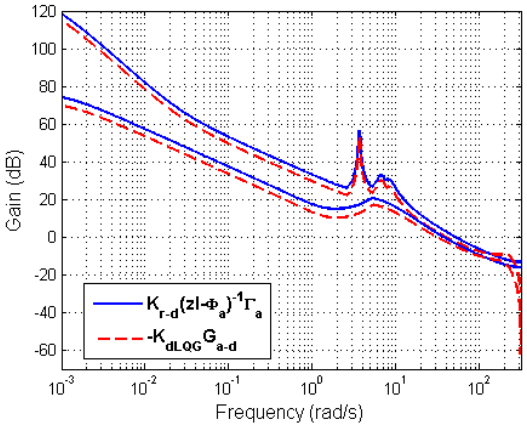

(c) $q=10^{-6}$

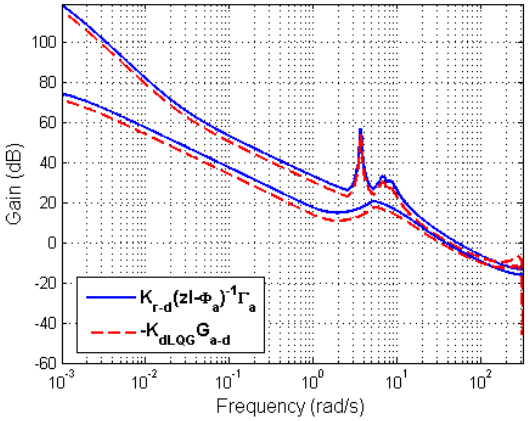

(d) $q=10^{-8}$

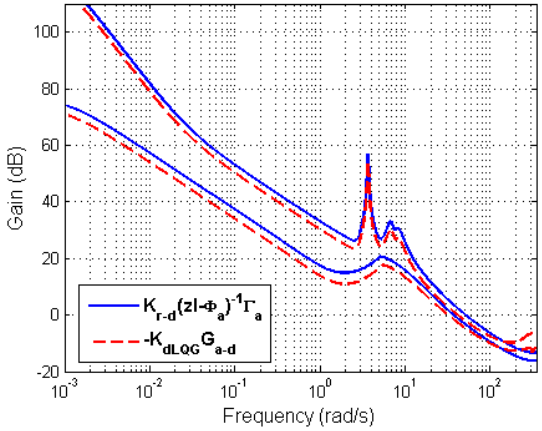

(e) $q=10^{-10}$

Figure 4.8 LTR for (a) $q=10^{-2}$, (b) $q=10^{-4}$, (c) $q=10^{-6}$, (d) $q=10^{-8}$, (e) $q=10^{-10}$

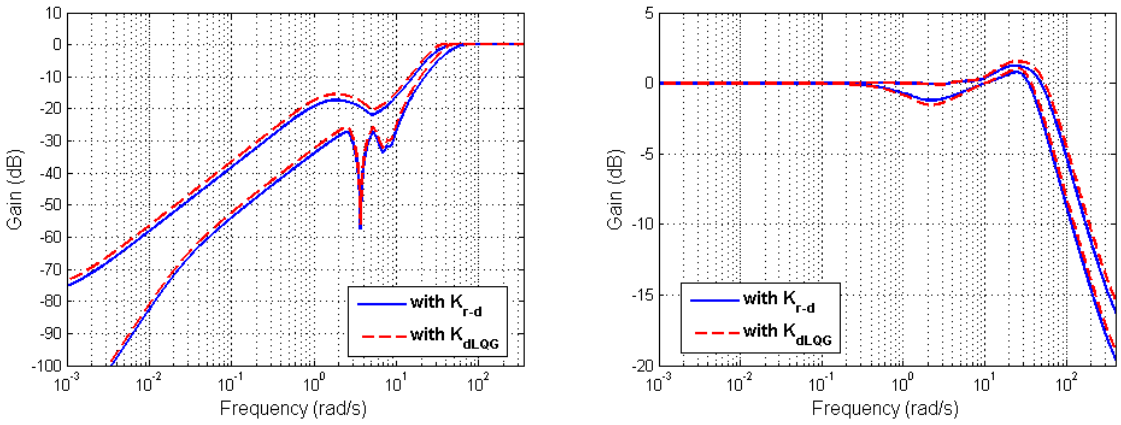

Figure 4.9 $\sigma(S)$ and $\sigma(T)$ of the closed-loop using K_{dLQG} and K_{r_d}

Table 4.2 System performance properties with K_{LQG}^{*}

Controller	Inter-area mode		M_S (*dB*)	M_T (*dB*)	ω_B (*rad/s*)	$\omega_{\underline{\sigma}(L)}$ (*rad/s*)	$\omega_{\bar{\sigma}(L)}$ (*rad/s*)	Roll-off Rate *dB/decade*
	$\zeta(\%)$	$f(Hz)$						
K_{r_d}	66.9	0.60	0	1.2	27.8	37.0	51.2	20
K_{dLQG}	66.4	0.60	0	1.5	24.6	35.8	49.3	20

4.5 Effects of Sampling Period

In Section 4.4, a supervisory discrete-time LQG/LTR controller was designed for the sampling period of $T_s = 0.01$ seconds. In this section, different values of sampling period are chosen and then their impact on system performance and robustness is assessed. These different sampling periods are selected to be: $T_s = 0.01$, 0.02, 0.05, 0.1 seconds. For each of these sampling period, the system open-loop model and the corresponding cost function of the LQG/LTR controller are discretised according to (4.1) and (4.9), respectively. Then the discrete-time controller is synthesised as detailed in Section 4.3. Singular value plots of *L*, *S* and *T* for the resulting closed-loop system are shown in Figure 4.10. One notable observation from Figure 4.10 is that loop gains reduce as the sampling period, T_s, increases indicating diminishing effect of feedback, which is somewhat expected. Table 4.3 also lists closed-loop system's performance measures for different sampling periods. In particular, it is

observed that as T_s increases, the cross-over frequencies for $\bar{\sigma}(L)$ and $\underline{\sigma}(L)$ as well as the bandwidth ω_B are reduced. The maximum peak of T, M_T, is increased from 1.1 *dB* up to 10.1 *dB* when T_s is increased from 0.01 to 0.1, indicating significant degradation in terms of the closed-loop system's performance and robustness. Also, the damping ratio of the critical mode is reduced from 67.1% to 62.8% as T_s is increased from 0.01 to 0.1. These results indicate that the sampling period is increased to an extent that the expected bandwidth, achieved using the continuous-time controller, violates the standard sampling theory [87]. More specifically, it is a standard rule in discrete-time control systems to specify closed-loop bandwidth to be at least ten times smaller than the sampling frequency, i.e. $f_s > 10\omega_B$ in *Hz*, where $f_s = 1/T_s$ [90]. Therefore, the reduction of the closed-loop system's bandwidth is necessary in order to retain some performance and robustness qualities while implementing discrete-time LQG/LTR controller with a relatively large sampling period.

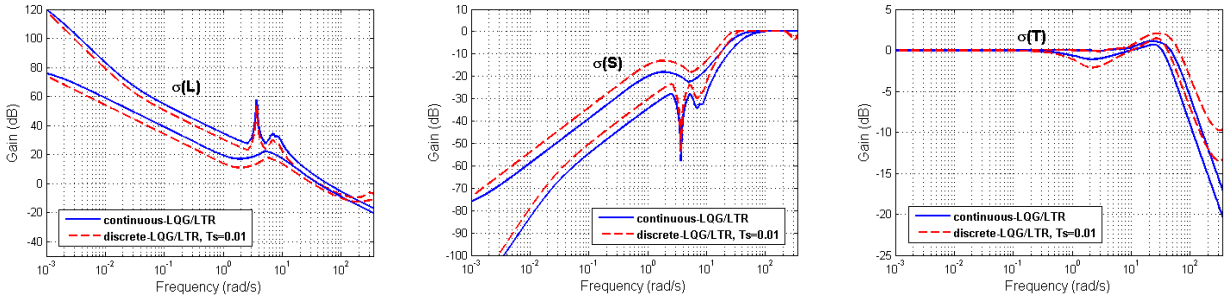

(a) $T_s = 0.01$

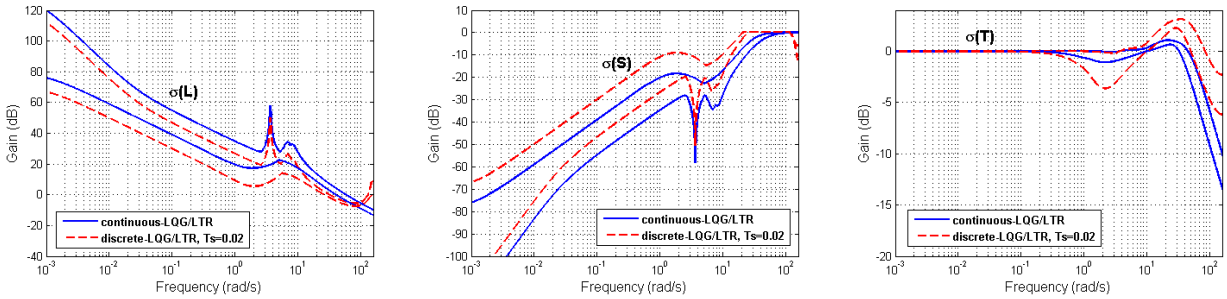

(b) $T_s = 0.02$

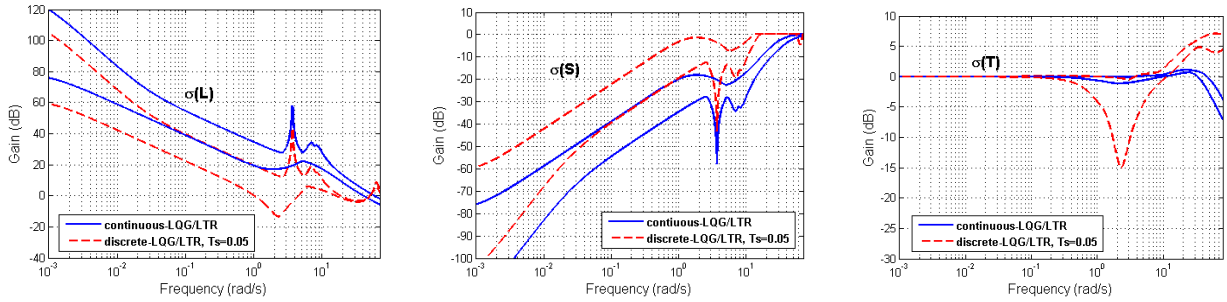

(c) $T_s = 0.05$

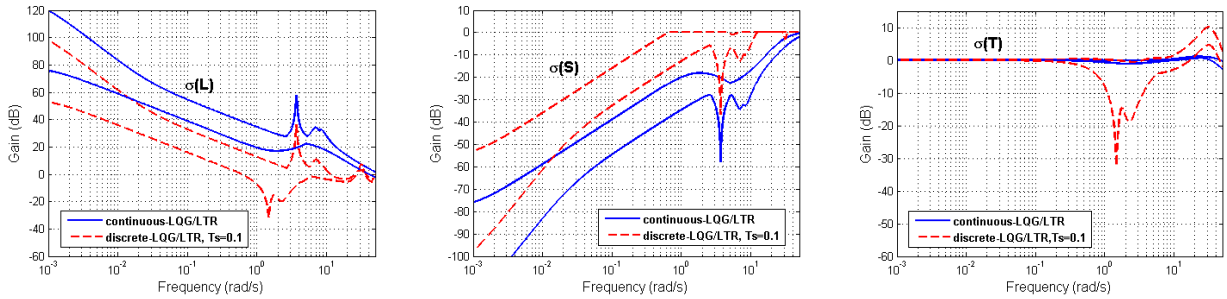

(d) $T_s = 0.1$

Figure 4.10 $\sigma(L)$, $\sigma(S)$ and $\sigma(T)$ for different sampling periods

Table 4.3 System performance properties for different sampling periods

T_s	critical mode		M_S	M_T	ω_B	$\omega_{\underline{\sigma}(L)}$	$\omega_{\bar{\sigma}(L)}$
	$\zeta(\%)$	$f(Hz)$	(dB)	(dB)	(rad/s)	(rad/s)	(rad/s)
Continuous-time	67.1	0.60	0	1.1	29.5	39.9	57.6
0.01	66.4	0.60	0	1.5	24.6	35.8	49.3
0.02	66.4	0.60	0	3.1	16.9	26.2	31.8
0.05	65.2	0.60	0	7.1	10.0	15.7	18.4
0.1	62.8	0.59	0	10.1	0.5	5.7	11.2

The closed-loop bandwidth ω_B obtained with $T_s = 0.01$ seconds, is found to be equal to 24.6 *rad/s*, as shown in Table 4.3. Therefore, the recommended sampling period should be no greater than 0.025 seconds in order not to violate the requirement that $f_s > 10\omega_B$. However, if the sampling period is to be increased above 0.025 seconds then the discrete-time LQG/LTR controller has to be redesigned with the reduced bandwidth in order to retain performance and robustness qualities.

The supervisory discrete-time LQG/LTR controller is firstly redesigned for $T_s = 0.01$ seconds, which would provide the benchmark controller against which other controllers with increased sampling period can be compared. According to (4.22), reduction in the bandwidth is achieved by reducing the scalar ratio between the cost function weights *Q* and *R*, ρ. The retuned value of ρ is equal to 1. The redesigned discrete-time controller is denoted as $K_{dLQG}^{'}$. Figure 4.11 shows the singular value plots of *L*, *S* and *T* using $K_{dLQG}^{'}$ for $T_s = 0.01$ seconds compared to that of its continuous-time counterpart. Corresponding system performance indicators are listed in Table 4.4. It is observed in Figure 4.11 that the performance of the redesigned discrete-time LQG/LTR controller is almost identical to that of the continuous-time controller up to the Nyquist frequency of 314 *rad/s*. By re-tuning the cost function weights, the closed-loop bandwidth ω_B is reduced from 24.6 *rad/s* down to 5.9 *rad/s*, which satisfies the sampling constraint $f_s > 10\omega_B$. Cross-over frequencies, closed-loop bandwidth and M_T are also significantly reduced. Finally, the damping of the inter-area mode is reduced from 66.4% down to 47.9%.

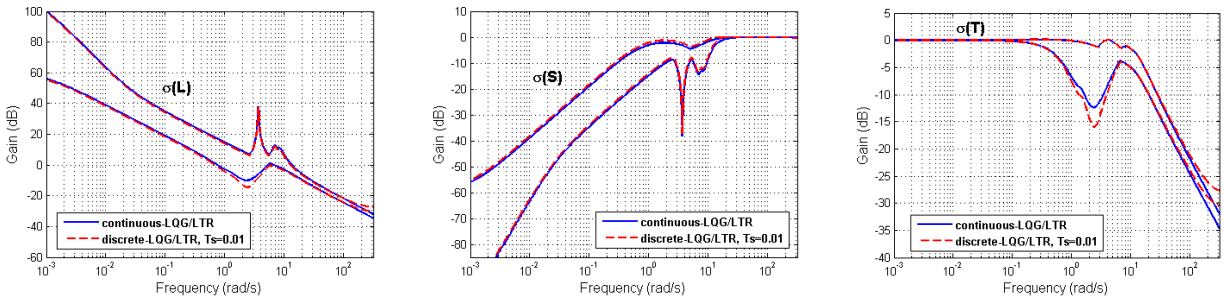

Figure 4.11 $\sigma(L)$, $\sigma(S)$ and $\sigma(T)$ using $K_{dLQG}^{'}$ for $T_s = 0.01$

Table 4.4 System performances for retuned controller

Controller	critical mode		M_S	M_T	ω_B	$\omega_{\underline{\sigma}(L)}$	$\omega_{\bar{\sigma}(L)}$
	$\zeta(\%)$	$f(Hz)$	(dB)	(dB)	(rad/s)	(rad/s)	(rad/s)
K_{dLQG}	66.4	0.60	0	1.5	24.6	35.8	49.3
Continuous-time	57.7	0.54	0	0.1	7.5	6.6	13.5
$K_{dLQG}^{'}$	47.9	0.60	0	0.1	5.9	5.7	12.5

It has been shown that the closed-loop system performance of the retuned discrete-time LQG/LTR controller $K_{dLQG}^{'}$ is very close to that of the equivalent continuous-time LQG/LTR controller. Now, the discrete-time LQG/LTR controller design procedure is repeated for other sampling periods and the resulting closed-loop system is assessed and compared to that obtained with controller $K_{dLQG}^{'}$. Figure 4.12 shows the singular value plots of *L*, *S* and *T* for sampling periods: $T_s = 0.02$, 0.05 and 0.1 seconds compared with $T_s = 0.01$ seconds. It is observed that loop gains are reduced as the sampling period, T_s, increases. Table 4.5 also lists closed-loop system's performance measures for different sampling periods. As T_s increases, the cross-over frequencies for $\bar{\sigma}(L)$ and $\underline{\sigma}(L)$ as well as the bandwidth ω_B are reduced. Highly satisfactory result, however, is that the maximum peak of *T*, M_T, remains almost unchanged when T_s is increased from 0.01 to 0.1. This fact indicates that the robustness of the closed-loop system is not greatly affected by the increase in the sampling period. Also, the damping ratio of the critical mode is reduced from 47.9% to 46.3% as T_s is increased from 0.01 to 0.1 seconds. This demonstrates that the closed-loop system performance and has deteriorated somewhat. Thus, the discrete-time LQG/LTR controller is retuned for sampling period $T_s = 0.1$ seconds in order to achieve the satisfactory performance and robustness.

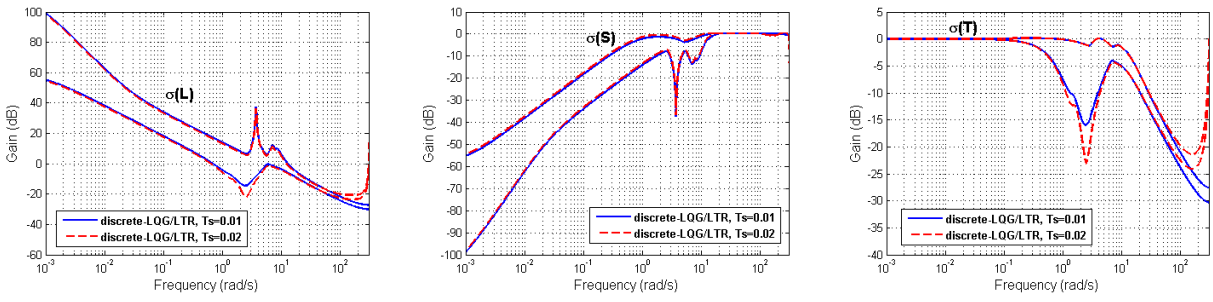

(a) $T_s = 0.01$ and 0.02

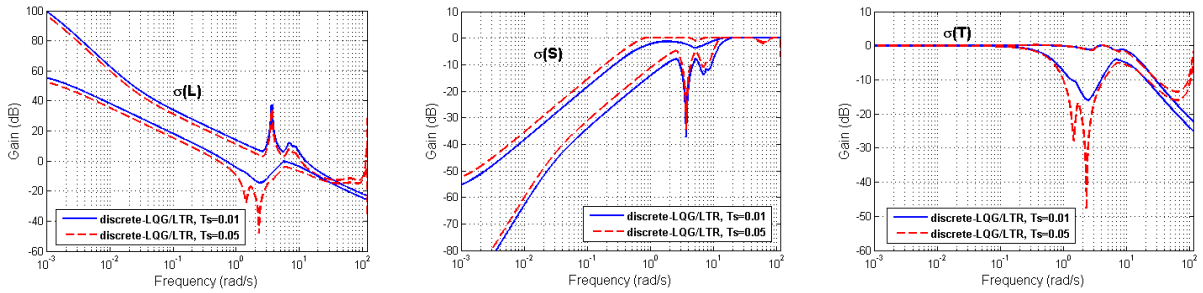

(b) $T_s = 0.01$ and 0.05

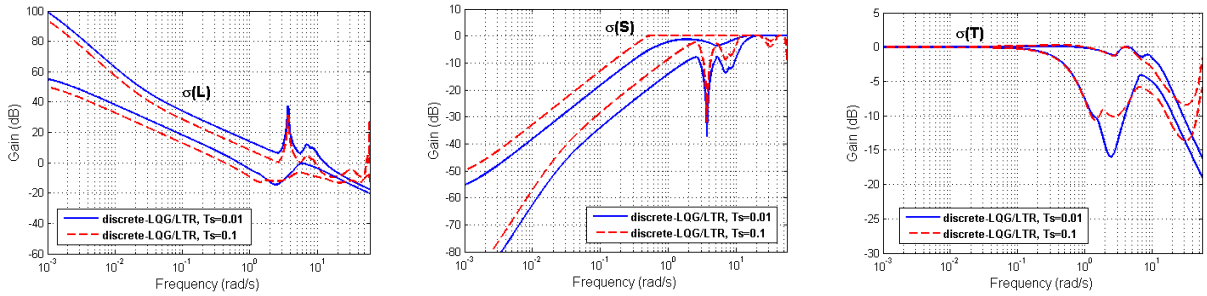

(c) $T_s = 0.01$ and Ts=0.1

Figure 4.12 $\sigma(L)$, $\sigma(S)$ and $\sigma(T)$ using K'_{dLQG} for different sampling periods

Table 4.5 System performances for different sampling periods

T_s	critical mode		M_S	M_T	ω_B	$\omega_{\underline{\sigma}(L)}$	$\omega_{\bar{\sigma}(L)}$
	$\zeta(\%)$	$f(Hz)$	(dB)	(dB)	(rad/s)	(rad/s)	(rad/s)
0.01	47.9	0.60	0	0.1	5.9	5.7	12.5
0.02	47.7	0.60	0	0.1	5.1	5.4	12.1
0.05	47.2	0.59	0	0.1	0.5	0.5	10.5
0.1	46.3	0.59	0	0.1	0.3	0.4	9.3

The discrete-time LQG/LTR controller with the sampling period of $T_s = 0.1$ seconds is retuned by increasing the cost function weights corresponding to Q_{P_e}, Q_{V_t} and $Q_{\Delta\omega}$ in Q_k by a factor of 5, and increasing the weight corresponding to integrator state by a factor of 2 in order to obtain the satisfied performance. The resulting discrete-time LQG/LTR controller is denoted as K^*_{dLQG}. Figure 4.13 shows the singular value plots of L, S and T of the system controlled by K^*_{dLQG}. Table 4.6 lists the closed-loop system's performance measures when the system is controlled by K^*_{dLQG} and by

K'_{dLQG}. It is clearly seen that the closed-loop system's performance is improved using the retuned discrete-time controller K^*_{dLQG}. Its performance in frequency domain is almost identical to the performance of the discrete-time controller K'_{dLQG} designed for the sampling period of $T_s = 0.01$ seconds. The cross-over frequencies for $\bar{\sigma}(L)$ and $\underline{\sigma}(L)$ are increased from 0.4 *rad/s* and 9.3 *rad/s* to 4.5 *rad/s* and 11.1 *rad/s*, respectively. System bandwidth ω_B is also increased from 0.3 *rad/s* to 4.8 *rad/s*, which indicates the faster response to set-point changes and persistent output disturbances. Finally, the damping ratio for the inter-area mode is increased from 46.3% to 47.3%. Therefore, the closed-loop system's performance for the retuned discrete-time controller with $T_s = 0.1$ seconds is satisfied. Its effectiveness and robustness will also be assessed by applying it onto the non-linear power system model in the next section.

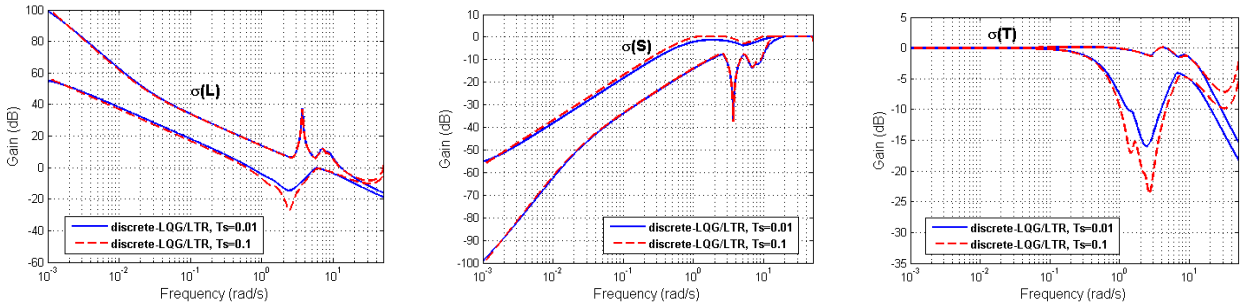

Figure 4.13 $\sigma(L)$, $\sigma(S)$ and $\sigma(T)$ using K^*_{dLQG}

Table 4.6 System performances using K'_{dLQG} and K^*_{dLQG}

Controller	critical mode		M_S	M_T	ω_B	$\omega_{\underline{\sigma}(L)}$	$\omega_{\bar{\sigma}(L)}$
	$\zeta(\%)$	$f(Hz)$	(dB)	(dB)	(rad/s)	(rad/s)	(rad/s)
K'_{dLQG}	47.9	0.60	0	0.1	5.9	5.7	12.5
K^*_{dLQG}	47.3	0.59	0	0.1	4.8	4.5	11.1

4.6 Non-linear Simulation

In order to properly assess the suitability of the supervisory discrete-time LQG/LTR controller designed for $T_s = 0.1$ seconds, K^*_{dLQG}, for the control of the considered power system, it is necessary to apply it onto the non-linear model of the power system and compare with controller $K^{'}_{dLQG}$, which is designed for $T_s = 0.01$ seconds.

4.6.1 Small Signal Stability

Firstly, an increase of 2.5% on the terminal voltage of Generator 2 is applied at time $t = 0.2$ seconds to simulate the small-signal disturbance. Dotted lines in Figure 4.14 represent the resulting response of the system controlled by $K^{'}_{dLQG}$, while the solid lines refer to the system response with controller K^*_{dLQG}. It is observed that the power system variables deviate further from their nominal values when controlled by K^*_{dLQG}. This demonstrates that the digitisation of the controller does introduce some deterioration of the closed-loop system performance. However, both controllers are shown to maintain the stability. This demonstrates that the retuned discrete-time LQG/LTR controller for sampling period 0.1 seconds is sufficiently effective when addressing the issue of wide-area damping control of the multi-machine power system.

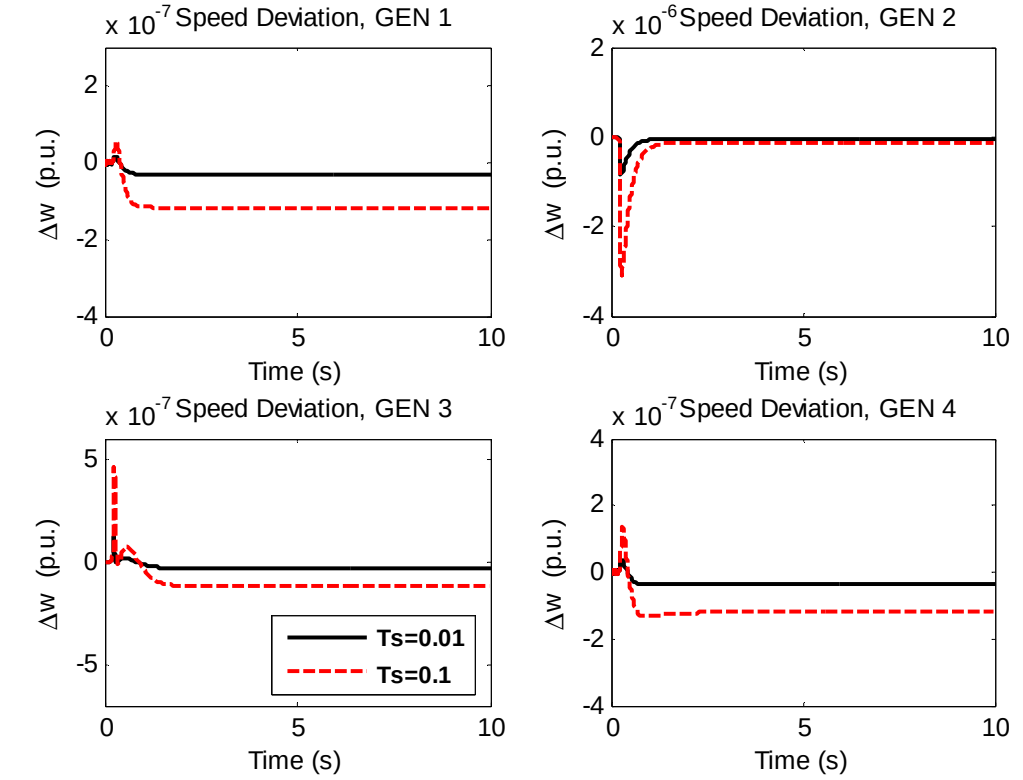
x 10^-7 Speed Deviation, GEN 1
Δw (p.u.)
Time (s)
x 10^-6 Speed Deviation, GEN 2
Δw (p.u.)
Time (s)
x 10^-7 Speed Deviation, GEN 3
Δw (p.u.)
Time (s)
Ts=0.01
Ts=0.1
x 10^-7 Speed Deviation, GEN 4
Δw (p.u.)
Time (s)

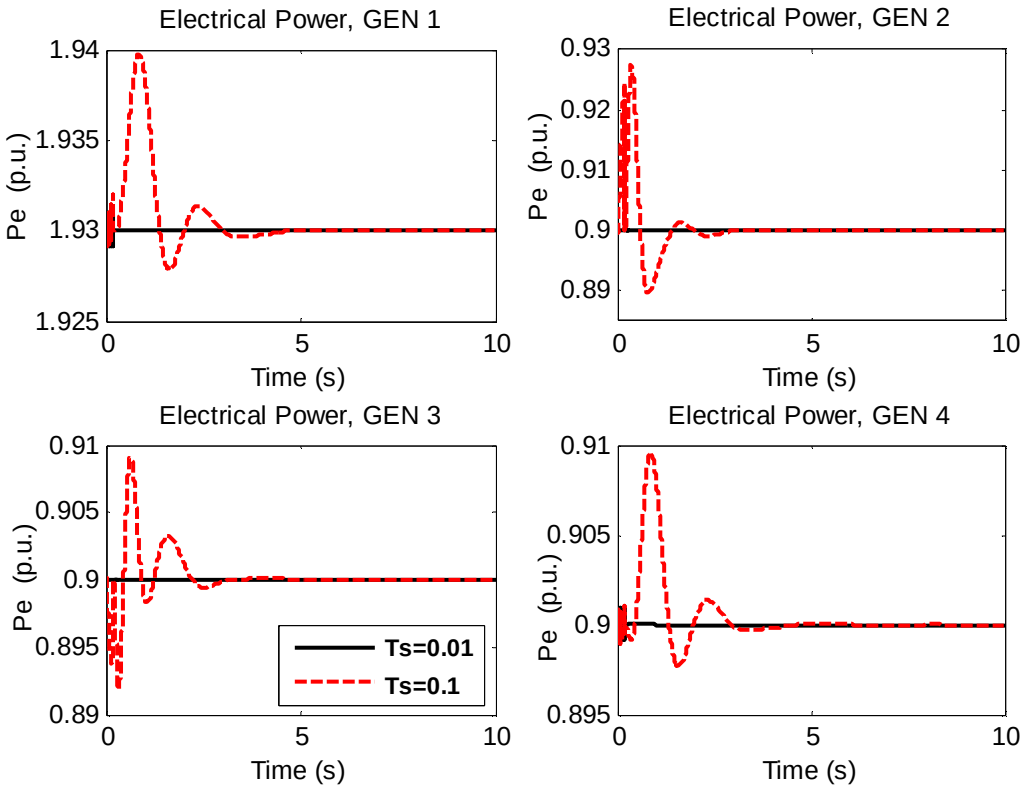
Electrical Power, GEN 1
Pe (p.u.)
Time (s)
Electrical Power, GEN 2
Pe (p.u.)
Time (s)
Electrical Power, GEN 3
Pe (p.u.)
Time (s)
Ts=0.01
Ts=0.1
Electrical Power, GEN 4
Pe (p.u.)
Time (s)

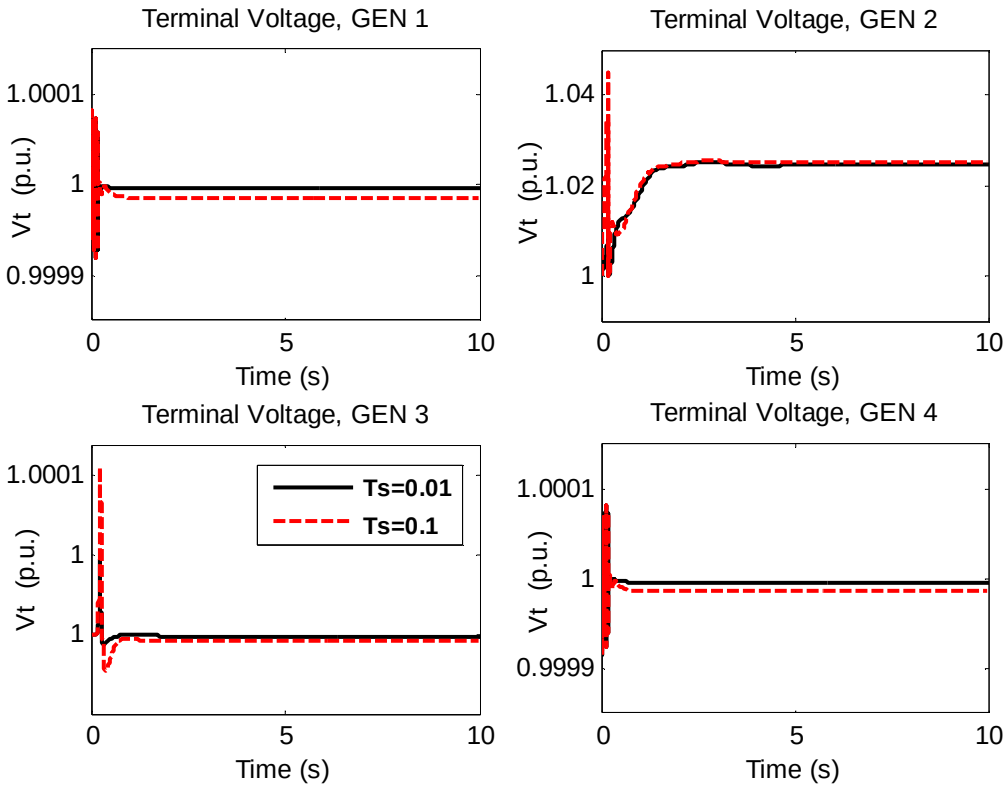

Figure 4.14 System responses to small disturbance

4.6.2 Large Disturbance Stability

In order to evaluate system performance in the presence of a large-signal disturbance, a three-phase short-circuit fault is applied on the bus 5 of the simulated power system at time $t = 1$ second. The fault is then cleared with auto-reclosing of the circuit breaker after 4 cycles (80 *ms*). The time response of the resulting speed deviation, electrical power and terminal voltage of generators are shown in Figure 4.15 for the power system controlled by K^{*}_{dLQG} (dashed lines) and for the one controlled by $K^{'}_{dLQG}$ (solid lines). Once again, it is clearly observed that the maximum deviation of the controlled variables is generally higher when employing K^{*}_{dLQG} compared to $K^{'}_{dLQG}$. Also, the settling time of the system controlled by K^{*}_{dLQG} is equal to 8 seconds, compared to the sampling time of 5 seconds for the system controlled by $K^{'}_{dLQG}$. The main discrepancy between the two responses in terms of the maximum deviation from the nominal value is observed for the variables related to generators 1

and 4 which are both located in Area 1. On the other hand, the regulation of the terminal voltages of generators 2 and 3 located in Area 2 is more satisfactory when using K^*_{dLQG}, which is somewhat surprising. Therefore, some deterioration in the performance is experienced as a result of discretisation. Nevertheless, it is clearly shown that the redesigned controller K^*_{dLQG} that utilises relatively large sampling period is effective in stabilising the power system and rejecting large-scale disturbance.

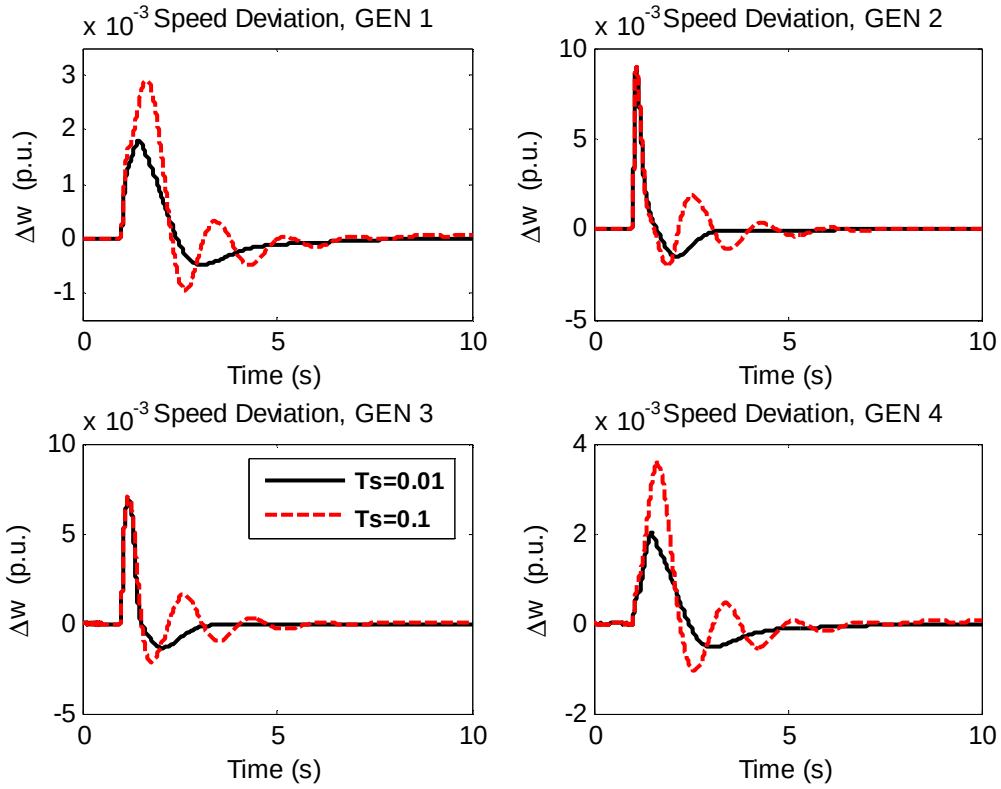

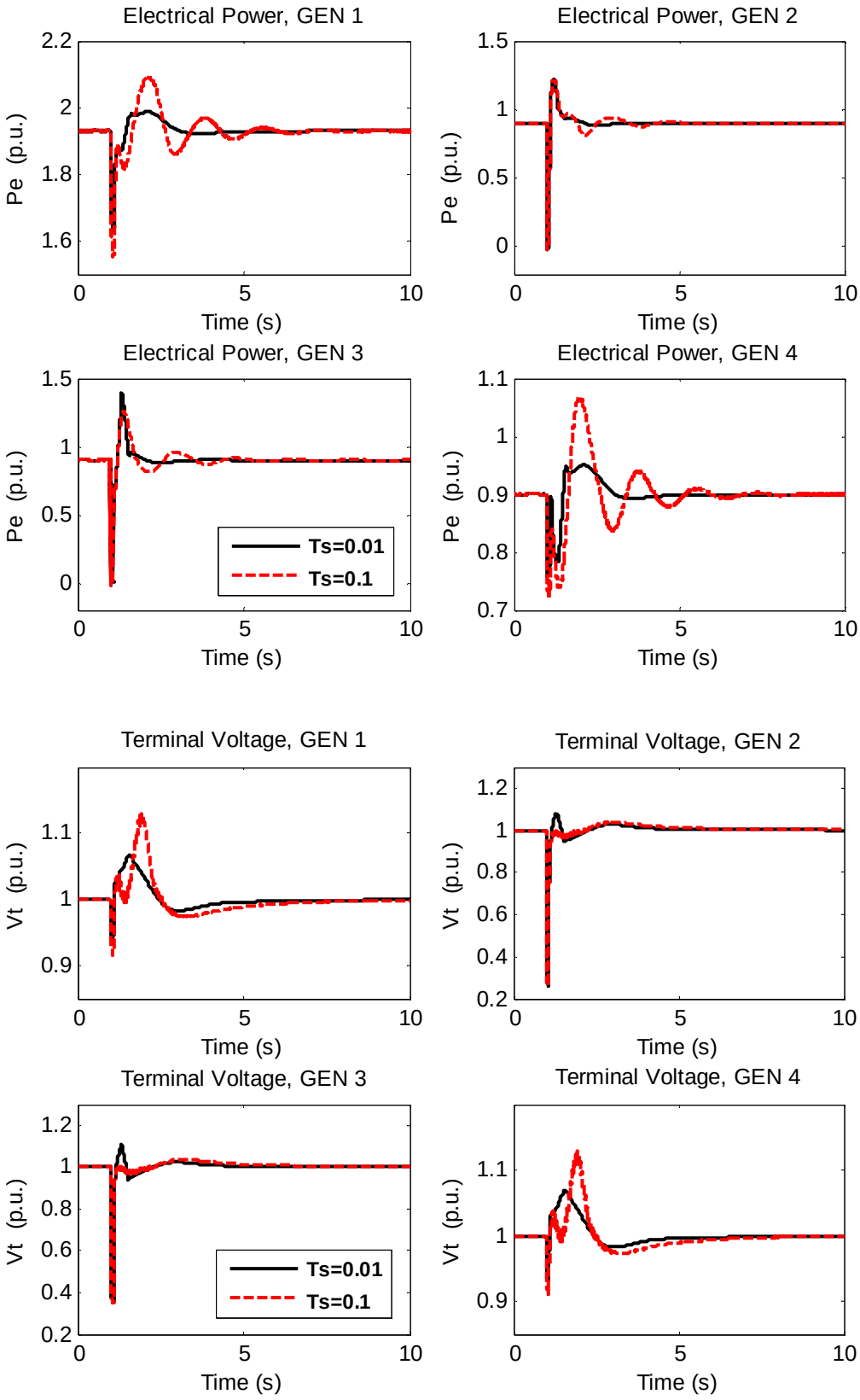

Figure 4.15 System responses to large disturbance

4.6.3 Robustness to Various Operating Conditions

Designed discrete-time supervisory controllers are assessed in terms of their robustness to the changing operating conditions. These various operating conditions are realized by changing the power transfer from Area 1 to Area 2 with the following different cases considered: (a) power transfer reduced by 10%; (b) power transfer reduced by 15%; (c) power transfer reduced by 20%; (d) power transfer reduced by 25%. Large-signal disturbance is a self-cleared three-phase fault applied at bus 5 at time $t = 1$ second with the self-clearing time of 80 *ms*. Solid lines and dotted lines in Figure 4.16 represent the resulting responses of electrical power output of the power system controlled by the supervisory discrete-time LQG/LTR controller K^*_{dLQG} and controller $K^{'}_{dLQG}$, respectively. It is observed that the peak of responses of the system controlled by K^*_{dLQG} is higher than when controlled by $K^{'}_{dLQG}$. Also the corresponding settling time of the system reponse is longer in the case of K^*_{dLQG} when compared to the system controlled by $K^{'}_{dLQG}$. In particular, for a large change of the power transfer from Area 1 to Area 2, i.e. power transfer reduced by 25%, the settling time of the response of the system controlled by K^*_{dLQG} and shown in Figure 4.16(d) is found to be 8.5 senconds, which is much longer than the settling time of 4.5 seconds recorded for the system controlled by $K^{'}_{dLQG}$. However, the stability is preserved by controller K^*_{dLQG} designed for $T_s = 0.1$ in the presence of a self-cleared three-phase fault and under different operating conditions, which is a welcoming result. Therefore, it is demonstrated that the designed supervisory discrete-time controller for $T_s = 0.1$, K^*_{dLQG}, is sufficiently robust when controlling power system under different operating conditions.

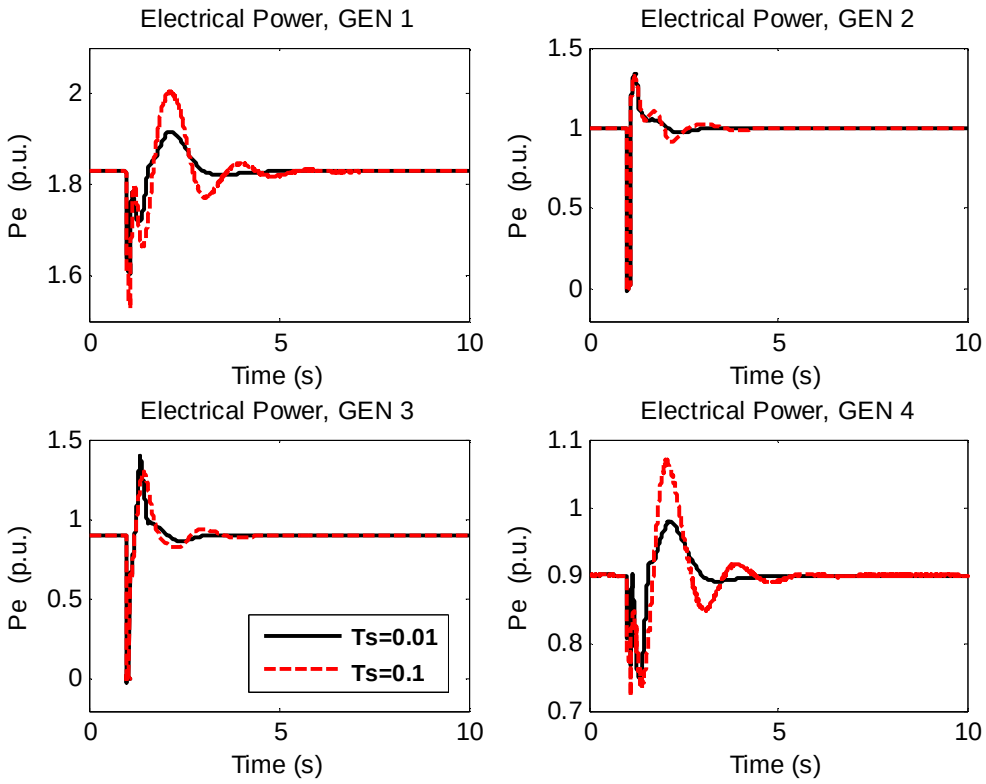

(a) Power transfer reduced by 10%

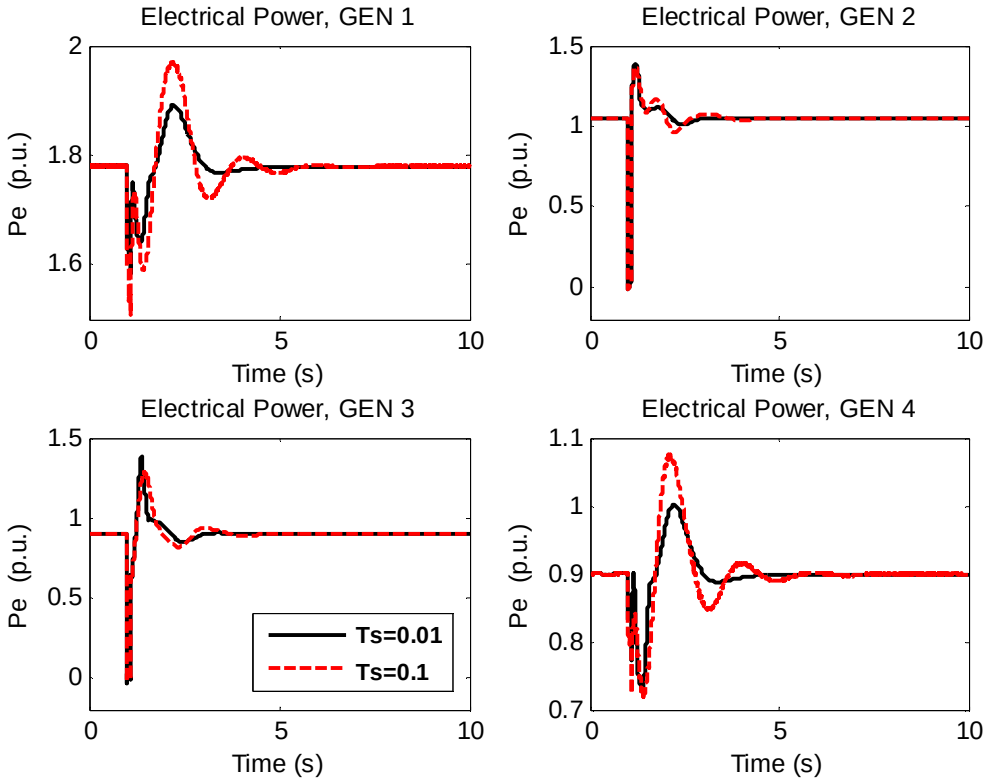

(b) Power transfer reduced by 15%

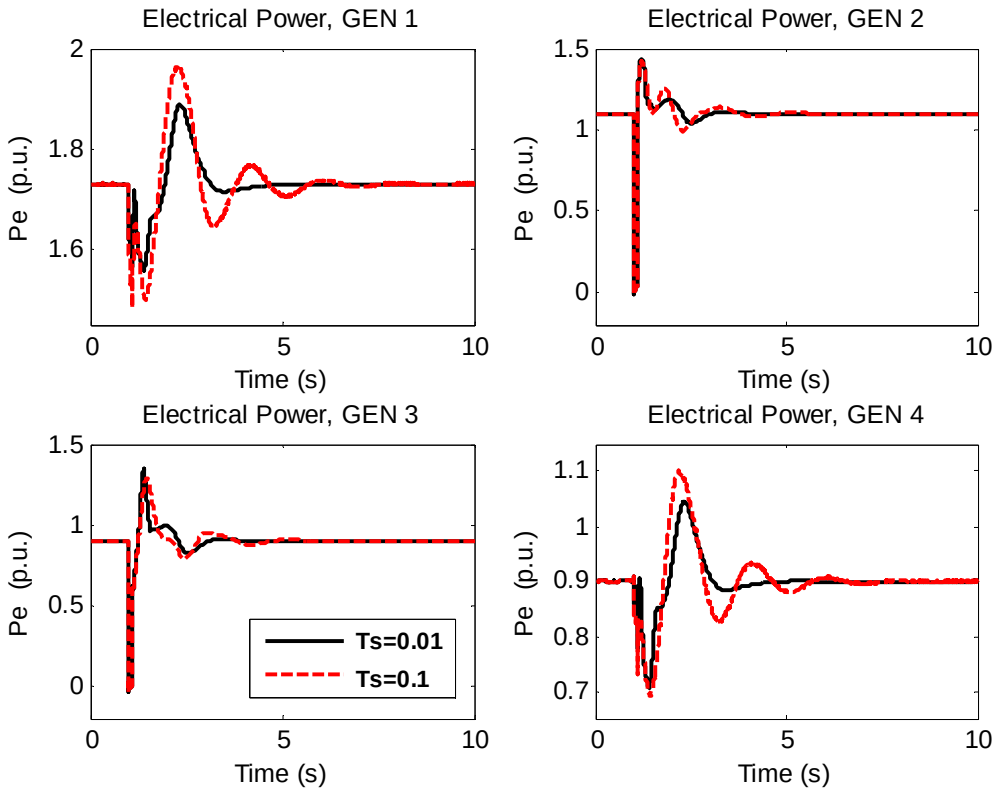

(c) Power transfer reduced by 20%

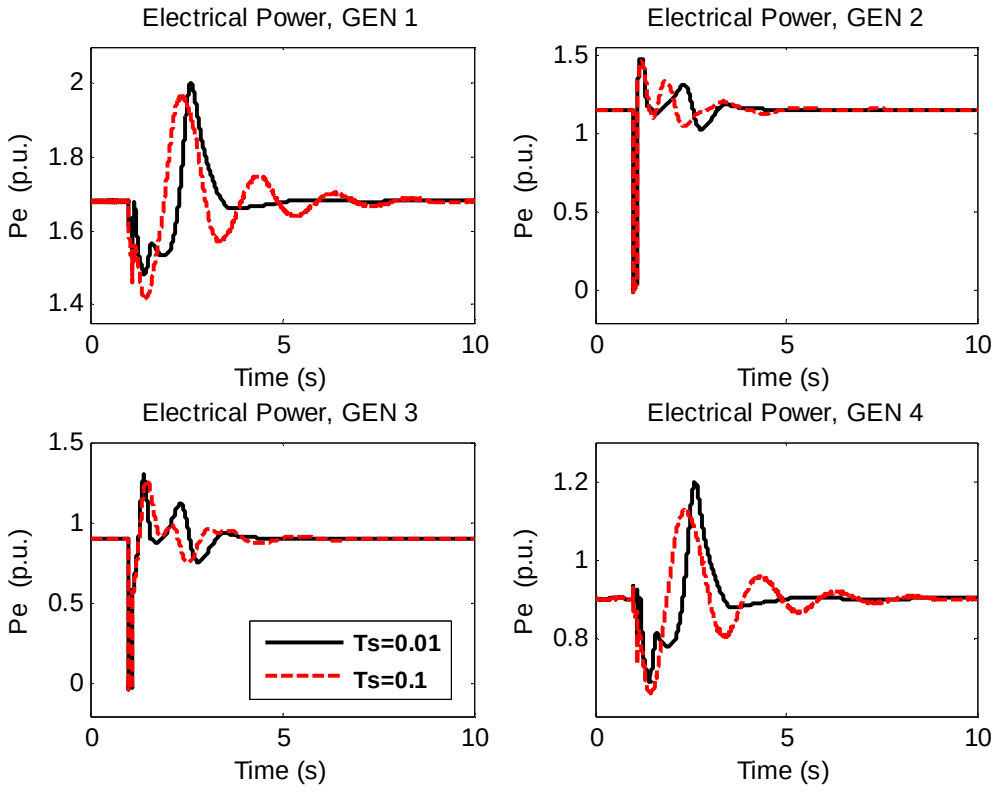

(d) Power transfer reduced by 25%

Figure 4.16 Electrical power output for various operating conditions

4.7 Discrete-Time LQG/LTR for Power System Installed with PSS

This section considers the application of the supervisory discrete-time LQG/LTR controller on the power system equipped with auxiliary PSS regulators, installed for each of the four generators. In many respects, this section is analogous to Section 3.7 that considered application of the continuous-time supervisory controller onto the power system equipped with the PSS regulators.

As already mentioned in Section 3.7, the linearised state-space model of the power system equipped with PSS regulators contains 51 states, 4 inputs and 12 outputs. This linearised continuous-time model is then discretised assuming the ZOH reconstruction. Resulting supervisory discrete-time LQG/LTR controller is synthesized by utilizing this model. In order to assess its effectiveness and robustness, the designed discrete-time LQG/LTR controller is applied to the non-linear power system model and assessed in terms of its ability to reject large-signal disturbance, which is a three-phase fault applied to one of the power system buses.

4.7.1 Discrete-Time LQG/LTR Controller

The discrete-time model is obtained by sampling the continuous-time augmented state-space model, G_{PSS_a}, given in (3.37) with the sampling period T_s. The resulting discrete-time state-space model is represented as follows:

$$\begin{aligned} x(k+1) &= \Phi_{PSS\_a} x(k) + \Gamma_{PSS\_a} u(k) + w_k \\ y(k) &= C_{PSS\_a} x(k) + v_k \end{aligned} \tag{4.25}$$

The same synthesis procedure as discussed in Section 4.4 is followed in this section to design the supervisory discrete-time LQG/LTR controller. The cost function weightings used for the discrete-time controller design are denoted as $Q_k^{'}$, $R_k^{'}$, $W_k^{'}$ and $V_k^{'}$, respectively. They are obtained by applying (4.7) and (4.3) to the weighting matrices Q_{P_e}, Q_{V_t} and $Q_{\Delta\omega}$ obtained in (3.34). Sampling period is chosen to be equal to $T_s = 0.1$ and the tuning is performed using two parameters analogous to ρ, which

was introduced in (4.22). These are ρ_1 and ρ_2 that correspond to the original system states and the integrator states, respectively. Appropriate values for these parameters are found be equal to $\rho_1 = 2$ and $\rho_2 = 8$. The resulting supervisory discrete-time LQG/LTR controller is denoted as K_{dLQG}^{p*} and is evaluated using both frequency-domain analysis tools, which assume linear system description, and time-domain simulations, which utilise non-linear system model. In addition, the performance and robustness of the system controlled by K_{dLQG}^{*}, which was designed in Section 4.5, is assessed. This additional assessment is performed in order to establish whether the controller designed for the system without Power System Stabilizers can be used without any modifications once these auxiliary local regulators are installed.

Figures 4.17 and 4.18 show the maximum and the minimum singular value plots of *L*, *S* and *T* of the system controlled by K_{dLQG}^{p*} and K_{dLQG}^{*}. Table 4.7 lists the corresponding performance measures obtained using the two controllers. In the case of K_{dLQG}^{p*}, the cross-over frequencies for $\bar{\sigma}(L)$ and $\underline{\sigma}(L)$ as well as the bandwidth ω_B are higher when compared to K_{dLQG}^{*}. In particular, system bandwidth is significantly increased from 0.9 rad/s to 5.8 rad/s, which indicates a faster closed-loop system response. Damping ratio of the inter-area mode is also increased from 51.6% to 57.8%, which further demonstrates the superiority of K_{dLQG}^{p*} over K_{dLQG}^{*} in terms of the improved damping of the inter-area electromechanical mode.

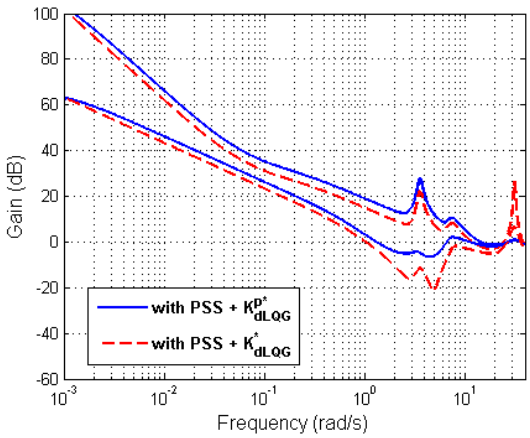

Figure 4.17 $\sigma(L)$ of the system with PSS using K_{dLQG}^{p*} and K_{dLQG}^{*}

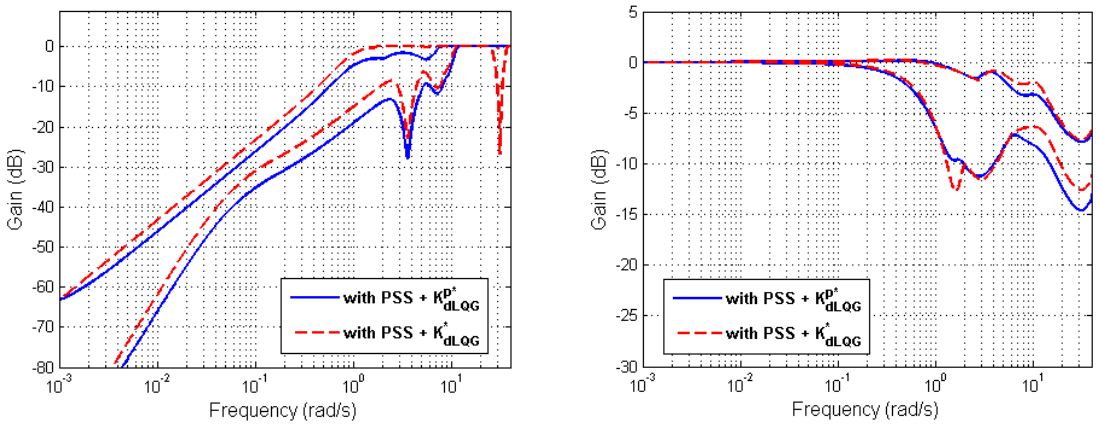

Figure 4.18 $\sigma(S)$ and $\sigma(T)$ of the system with PSS using K_{dLQG}^{p*} and K_{dLQG}^{*}

Table 4.7 System performance properties

Controller	Inter-area mode		M_S (*dB*)	M_T (*dB*)	ω_B (*rad/s*)	$\omega_{\underline{\sigma}(L)}$ (*rad/s*)	$\omega_{\bar{\sigma}(L)}$ (*rad/s*)
	ζ(%)	f(*Hz*)					
K_{dLQG}^{p*}	57.8	0.57	0	0.1	5.8	11.1	14.2
K_{dLQG}^{*}	51.6	0.57	0	0.2	0.9	1.1	11.8

4.7.2 Non-linear Simulation

The effectiveness and robustness of the designed discrete-time LQG/LTR controller is also assessed using the simulation of the non-linear power system model when subjected to a large-signal disturbance, which is a three-phase fault applied on the bus 5 at time t=1 second. The fault is then cleared with the auto-reclosing of the circuit breaker after 4 cycles (80 *ms*).

The time response of the system with PSS regulators installed but without supervisory controller is shown in Figure 4.19 with dotted lines. The solid lines and dash lines in Figure 4.19 represent the time responses obtained when the power system with the PSS regulators installed is controlled by the discrete-time controllers K_{dLQG}^{p*} and K_{dLQG}^{*}, respectively. Firstly, it is shown that PSS regulators alone provide sub-standard control of the power system with the settling time much greater than 10 seconds, thereby providing direct motivation for the development of the supervisory

multivariable controllers. Also, it is observed that the closed-loop system successfully recovers from the large disturbance using either of the two supervisory discrete-time controllers. In the case of K_{dLQG}^{p*}, the settling time of the response is reduced to 3.5 seconds, when compared to 5 seconds achieved using K_{dLQG}^{*}. Nevertheless, it is also shown that the controller K_{dLQG}^{*}, which was designed assuming the absence of PSS regulators, can cope sufficiently well in their presence without any need for re-tuning or re-design. This is a significant result as it demonstrates satisfactory level of robustness of the supervisory controller K_{dLQG}^{*}. More specifically, it is shown that once the supervisory controller is designed for the power system without PSS regulators, it requires no subsequent modifications after these auxiliary controllers are installed.

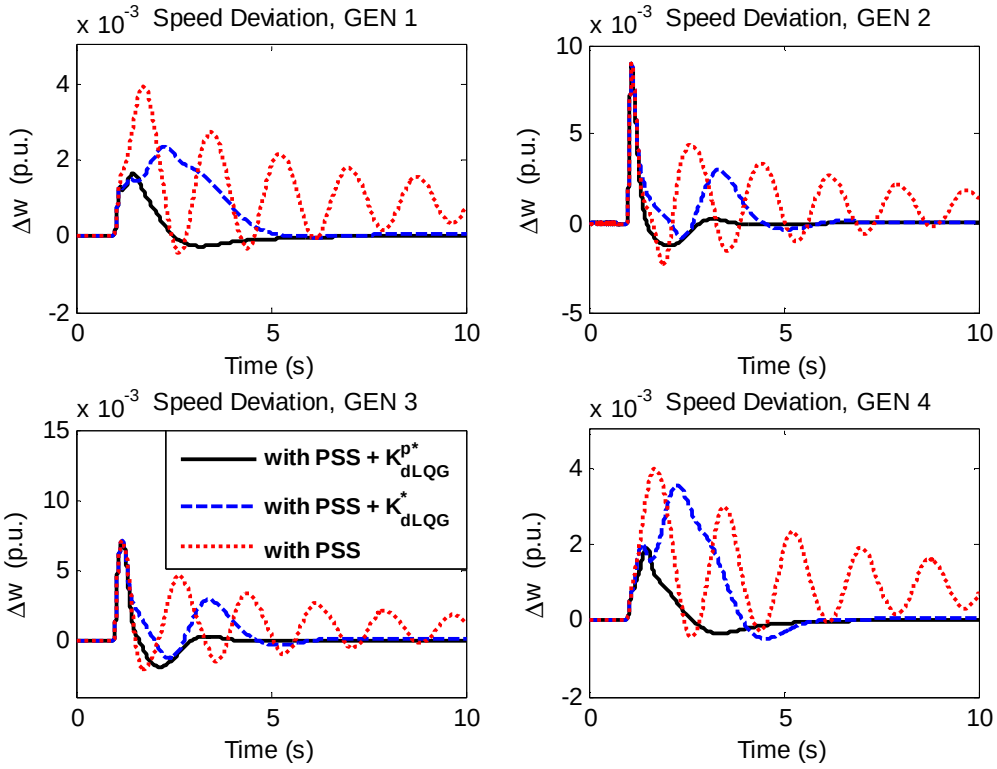

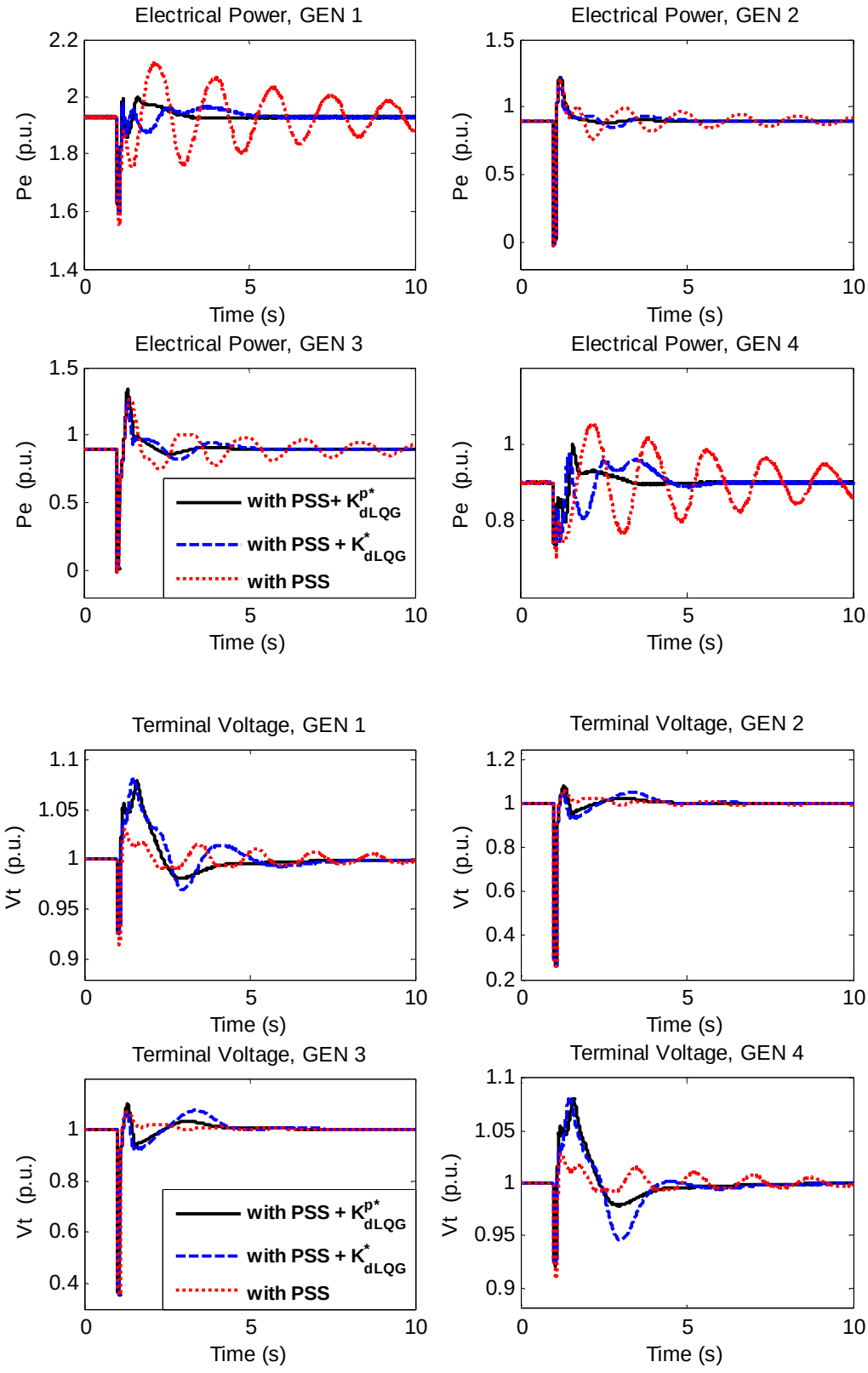

Figure 4.19 System responses of the power system with PSS to a self-cleared three-phase fault

4.9 Summary

In this chapter a supervisory discrete-time LQG/LTR controller was designed for the multi-machine power system using the frequency-domain analysis tools. This procedure comprises of converting continuous-time system model, given in (3.5), and the controller's cost function, given in (3.9), into their discrete-time equivalents, under the assumption that the zero-order-hold (ZOH) devices are used for the signal reconstruction. The optimal regulator loop transfer gain was recovered at the plant input in order to retain the robustness of the optimal regulator, which was verified using frequency analysis tools.

The effect of the sampling period on the performance of the resulting discrete-time LQG/LTR controller was investigated. It was shown using both the frequency-domain and the time-domain analysis that the closed-loop system performance and robustness deteriorated with an increase in a sampling period. However, it was also demonstrated that some of the performance and robustness can be recovered by reducing the bandwidth through the appropriate re-tuning of the cost function weights used to synthesise the supervisory discrete-time controller.

Designed controllers were assessed using small-signal and large-signal disturbances as well as the changes in the nominal operating conditions applied to the non-linear simulation model of the power system. Also, the comparison between the discrete-time and continuous-time LQG/LTR controllers was performed in both the frequency and time domain with the results demonstrating the effectiveness of the discrete-time LQG/LTR controller.

Finally, discrete-time LQG/LTR controller was implemented on the non-linear power system simulation with local PSS stabilizers installed on each of the four generators. The resulting closed-loop system was compared with its continuous-time counterpart using both the frequency-domain and the time-domain tools when subjected to the large disturbance in order to demonstrate its suitability in wide-area control applications.

Chapter 5

LQG/LTR for Multi-Machine Power System with Time-Delay

5.1 Introduction

Using the supervisory LQG/LTR control system architecture together with a large variety of measurement devices (e.g. PMU) and communication equipment, the wide-area control can be realized on a multi-machine power system. However, one of the main operational challenges for its implementation is the inevitable presence of time-delays, which occur due to the large geographical areas covered by these power systems. These time-delays may be caused by measurement processing, transmission and synchronization as well as the control signal calculation and transmission. It has been shown that time-delays can result in deteriorated performance of the supervisory control scheme [52–54]. Therefore, the impact of time-delays should be quantified so that their presence can be taken into consideration when designing wide-area control scheme for multi-machine power systems.

Communication time-delays caused by the transmission of measurement and control signals over large geographical distances depend primarily on the type of communication link used in the wide-area control systems. Typical time-delays for different communication link technologies are provided in Table 5.1 and are defined as the time from the measurement instant to the instant that the corresponding input signals arrive at control centre [60]. It is important to note that the time-delays

resulting from the processing and routing of signals are much smaller when compared to communication time-delays, thus can be neglected without loss of generality [30].

Table 5.1 Communication time-delays for different communication links

Communication link	Associated delay (*ms*)
Fiber-optic cables	100 ~ 150
Microwave links	100 ~ 150
Power line carier (PLC)	150 ~ 350
Telephone lines	200 ~ 300
Satellite link	500 ~ 700

The main aim of this chapter is to discuss the impact that the presence of the time-delays has on the performance of the closed-loop system. Firstly, in the case of the continuous-time control problem, the discussion focuses on the impact that the order with which rational approximation of the time-delay is made has on the damping of the electromechanical modes and the overall stability of a given power system. Also, two alternative approaches of approximating time-delays are considered and compared with each other. Secondly, in the case of the discrete-time control problem, it is shown that the time-delay does not need to be represented using rational approximation. Instead, the exact representation of the time-delay can be made as shown in Section 5.5.

5.2 Rational Approximation for Constant Time-Delay

For a fixed time-delay of τ, the Laplace domain transfer function is given as $e^{-s\tau}$ which is not rational and therefore not in a standard transfer function form. One typical approach for incorporating time-delays into the standard controller design is to apply Taylor Series expansion on $e^{-s\tau}$ in order to express it using finite-dimensional rational approximation [91]. The resulting transfer function is denoted by $R(s\tau)$, which can then be readily integrated into the standard design or the analysis of the closed-loop control system. Therefore, if the delay-free system that is to be controlled is represented by $G(s)$, then the aim of using rational approximation

is to approximate $e^{-s\tau}G(s)$ by $R(s\tau)G(s)$ as accurately as possible. In this chapter, the most commonly used rational approximations, namely Pade approximation and Bessel Thomason function, are used to approximate the time-delays and are compared to each other using frequency-domain and the time-domain analysis tools. It is important to point out that in the context of power system control, they tend to approximate communication delays using a simple 1st or 2nd order Pade Approximation [53, 55, 56]. These papers, however, do not compare different methods of approximating time-delays, and do not discuss the impact that the order of rational approximation has on the overall stability of a given power system. These deficiencies are addressed in this thesis.

5.2.1 Pade Approximation

A Pade approximant is the ratio of two polynomials constructed from the coefficients of the Taylor series expansion of a function. It was shown by Perron that for $e^{-s\tau}$, its $[m/n]$ $(m,n\in\mathbb{N}_0)$ Pade approximants can expressed by a ratio of two polynomials which are given in equation (5.1) [91]:

$$R_{mn}(s\tau)=\frac{P_{mn}(s\tau)}{Q_{mn}(s\tau)}=\frac{\sum_{j=0}^{m}\frac{(m+n-j)!m!}{j!(m-j)!}(-s\tau)^j}{\sum_{j=0}^{n}\frac{(m+n-j)!n!}{j!(n-j)!}(s\tau)^j} \tag{5.1}$$

It has been shown in [92] that for any denominator degree $n\geq 1$, the proper Pade approximant $[m/n]$ is stable if $n-2\leq m\leq n$. This provides the guideline when selecting the appropriate order of the numerator and denominator of Pade approximation and will be used in this chapter.

5.2.2 Bessel-Thomson Approximation

Bessel-Thomson is an alternative form of rational approximation that utilises the ratio of two polynomials. This method leads to family of low pass all-pole transfer functions, which give approximately constant time-delay over as large frequency

range as possible [93]. The transfer function of Bessel-Thomson approximation of order *n* is presented as follows:

$$R(s\tau) = \frac{\dfrac{2n!}{2^n \cdot n!}}{\displaystyle\sum_{i=0}^{n} \frac{(2n-i)!}{2^{n-i} \cdot i!(n-i)!}(s\tau)^i} \tag{5.2}$$

It is known that the higher order of the rational approximation, the more accurate approximation is. On the other hand, higher order of these rational approximations may result in increased computational burden due to the overall increase in the system model and therefore, the controller order [91]. In next section, a comparison of the frequency domain and time domain performance of Pade approximation and Bessel-Thomson approximation are performed.

5.2.3 Comparison of Pade and Bessel-Thomson Approximation

The rational approximation transfer function $R(s\tau)$, obtained using either (5.1) or (5.2), can be represented by the following state-space model:

$$\begin{aligned} \dot{x}_\tau &= a_\tau x_\tau + b_\tau u_\tau \\ y_\tau &= c_\tau x_\tau + d_\tau u_\tau \end{aligned} \tag{5.3}$$

where x_τ represents the state variables related to a modelled time-delay. Figure 5.1 shows the step responses of the 1st, 2nd, 3rd and 4th order Pade approximation and Bessel-Thomson approximation for 250 *ms* time-delay compared with the response of the actual time-delay. It is shown in Figure 5.1 that the lower order approximations sacrifice the accuracy. Also, Pade approximation results in an increased overshoot and more oscillatory behaviour when compared to its Bessel-Thomson approximation counterpart, while also resulting in a faster response. Figure 5.2 shows the phase response of the 1st, 2nd, 3rd and 4th order Pade and Bessel-Thomson approximations compared with the exact response of the time-delay for 150 *ms* (for fiber-optic cables) and 500 *ms* (for satellite links), respectively. The figure shows the phase responses at the typical frequency range of electromechanical modes, i.e. 0.1-2 *Hz* (0.6-12.5 *rad/s*). In the case of 150 *ms* time-delay, the second order Pade and Bessel-Thomson approximation are found to be sufficiently accurate.

However, for 500 *ms* time-delay, higher order of both Pade and Bessel-Thomson approximation are found to be necessary in order to represent time-delay more accurately.

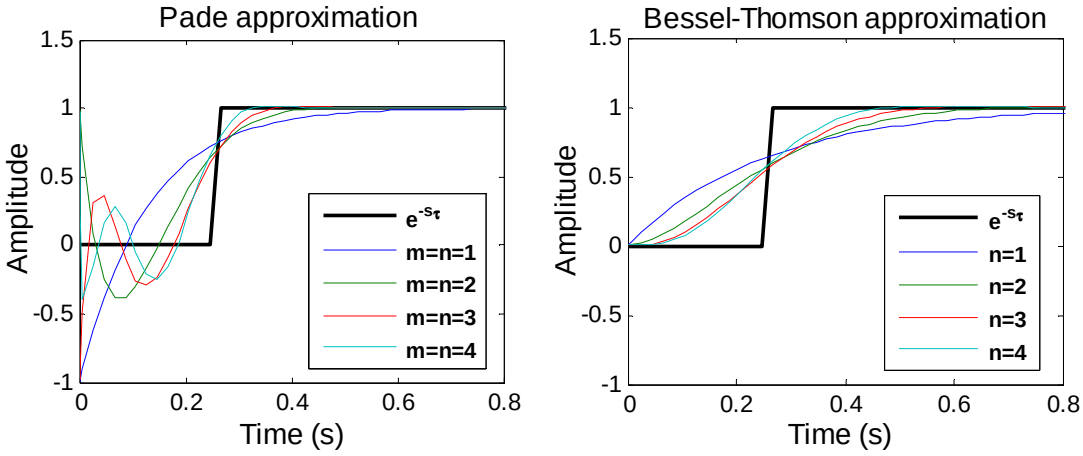

Figure 5.1 Step response of Pade and Bessel-Thomson approximation of $\tau = 250ms$

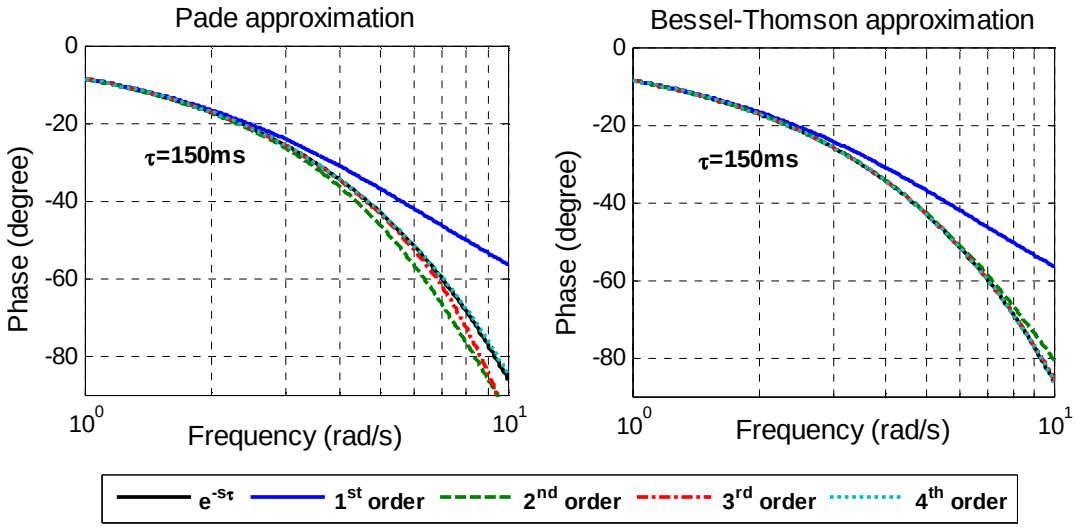

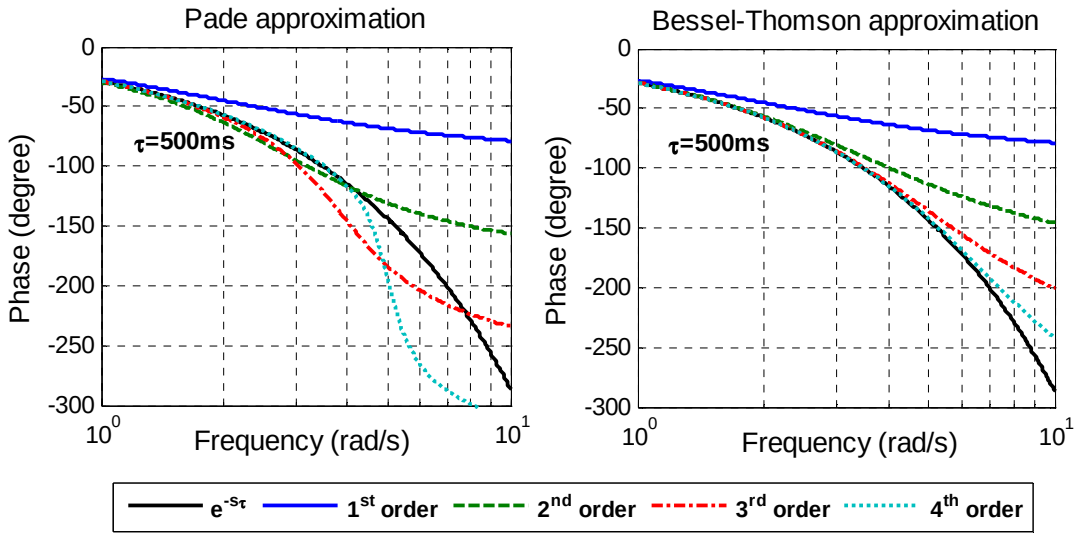

Figure 5.2 Phase responses of Pade & Bessel-Thomson approximation

5.3 Continuous-Time LQG/LTR for System with Time-Delay

5.3.1 Augmented System

The state-space representation of a deterministic continuous-time system has been provided in (3.5), which is rewritten here:

$$\begin{aligned} \dot{x} &= Ax + Bu \\ y &= Cx + Du \end{aligned} \tag{5.4}$$

Similarly, the communication time-delay can be expressed in the state-space form as follows:

$$\begin{aligned} \dot{x}_d &= A_d x_d + B_d u_d \\ y_d &= C_d x_d + D_d u_d \end{aligned} \tag{5.5a}$$

where x_d represents the state variables of the communication time-delay. If time-delay is the same for each input signal, then using Pade approximation or Bessel-Thomson approximation results in the following state-space representation:

$$A_d = \begin{bmatrix} a_{\tau 1} & 0 & \cdots & 0 \\ 0 & a_{\tau 2} & & \vdots \\ \vdots & & \ddots & 0 \\ 0 & \cdots & 0 & a_{\tau n} \end{bmatrix}, \quad B_d = \begin{bmatrix} b_{\tau 1} & 0 & \cdots & 0 \\ 0 & b_{\tau 2} & & \vdots \\ \vdots & & \ddots & 0 \\ 0 & \cdots & 0 & b_{\tau n} \end{bmatrix},$$
$$C_d = \begin{bmatrix} c_{\tau 1} & 0 & \cdots & 0 \\ 0 & c_{\tau 2} & & \vdots \\ \vdots & & \ddots & 0 \\ 0 & \cdots & 0 & c_{\tau n} \end{bmatrix}, \quad D_d = \begin{bmatrix} d_{\tau 1} & 0 & \cdots & 0 \\ 0 & d_{\tau 2} & & \vdots \\ \vdots & & \ddots & 0 \\ 0 & \cdots & 0 & d_{\tau n} \end{bmatrix}. \tag{5.5b}$$

Figure 5.3 shows the delay-free open-loop power system connected with the time-delay block.

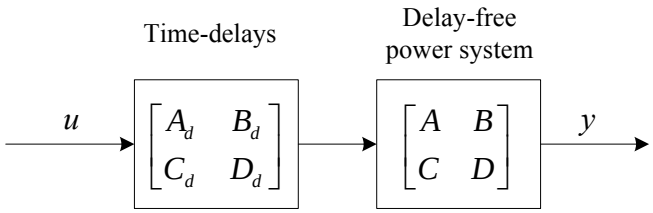

Figure 5.3 Delay-free power system connected with time-delay block

Time-delays can now be incorporated into the delay-free system's model by integrating (5.4) and (5.5) into the following augmented state-space model:

$$\begin{bmatrix} \dot{x} \\ \dot{x}_d \end{bmatrix} = \begin{bmatrix} A & BC_d \\ 0 & A_d \end{bmatrix} \begin{bmatrix} x \\ x_d \end{bmatrix} + \begin{bmatrix} BD_d \\ B_d \end{bmatrix} u$$
$$y = \begin{bmatrix} C & DC_d \end{bmatrix} \begin{bmatrix} x \\ x_d \end{bmatrix} + DD_d u \tag{5.6}$$

Thus the system with communication time-delay can be represented by the following form:

$$\dot{\tilde{x}} = \tilde{A}\tilde{x} + \tilde{B}u + w$$
$$y = \tilde{C}\tilde{x} + \tilde{D}u + v \tag{5.7a}$$

where

$$\tilde{A} = \begin{bmatrix} A & BC_d \\ 0 & A_d \end{bmatrix}, \ \tilde{B} = \begin{bmatrix} BD_d \\ B_d \end{bmatrix}, \ \tilde{C} = \begin{bmatrix} C & DC_d \end{bmatrix}, \ \tilde{D} = DD_d \,. \tag{5.7b}$$

and $\tilde{x} = [x^T \quad x_d^T]^T$ is the state vector of the augmented system model. w and v are the process noise and measurement noise, respectively, defined in (3.6). Also, u and

y are the input and output of the system model that incorporates communication delay along with the original open-loop dynamics.

It is important to note that for power system, the frequency response usually displays the characteristic with cross-over frequencies less than 10 *Hz*. Therefore, time-delay can be approximated with the order of the rational approximation greater than 2 and smaller than 4 in order to provide an accurate representation [94].

5.3.2 LQG/LTR Controller Design

In the previous section the system model incorporating communication time-delay was presented in the standard state space form, see (5.7). In addition, the integral action is also introduced into the deterministic model, which results in the following augmented state-space model:

$$\begin{aligned} \begin{bmatrix} \dot{\tilde{x}} \\ \dot{x}_i \end{bmatrix} &= \begin{bmatrix} \tilde{A} & 0 \\ \tilde{C} & A_i \end{bmatrix} \begin{bmatrix} \tilde{x} \\ x_i \end{bmatrix} + \begin{bmatrix} \tilde{B} \\ 0 \end{bmatrix} u \\ y &= \begin{bmatrix} \tilde{C} & 0 \end{bmatrix} \begin{bmatrix} \tilde{x} \\ x_i \end{bmatrix} + \tilde{D}u \end{aligned} \tag{5.8b}$$

with the denotation of

$$\tilde{A}_a = \begin{bmatrix} \tilde{A} & 0 \\ \tilde{C} & A_i \end{bmatrix},\ \tilde{B}_a = \begin{bmatrix} \tilde{B} \\ 0 \end{bmatrix},\ \tilde{C}_a = \begin{bmatrix} \tilde{C} & 0 \end{bmatrix},\ \tilde{D}_a = \tilde{D}\,. \tag{5.8b}$$

The transfer function of this augmented model is denoted as $\tilde{G}_a$. The separation theorem (3.8) ~ (3.16) and LTR procedure then can be applied to synthesize the continuous-time LQG/LTR controller for the system (5.8) as follows.

Step 5.1 Optimal State-Feedback. Design the optimal regulator for the augmented state-space model (5.8) with the symmetric weighting matrices $\tilde{Q} = \rho \tilde{M}^T \bar{Q} \tilde{M}$ and $\tilde{R} = I$. Choose $\tilde{M} = \tilde{C}_a$, $\bar{Q} = diag\{Q_{P_e}, Q_{V_t}, Q_{\Delta\omega}\}$, where ρ and Q_{P_e}, Q_{V_t}, $Q_{\Delta\omega}$ are selected by the control engineer such that the satisfactory system performance is achieved. The resulting optimal regulator gain is denoted as

$\tilde{K}_r$. Further details regarding optimal regulator design procedure are provided in Section 3.3.

Step 5.2 Loop Transfer Recovery (LTR) at plant input. The Kalman filter is designed for the augmented state-space model with $\tilde{W} = \tilde{\Gamma}\bar{W}\tilde{\Gamma}^T$ and $\tilde{V} = qI$. By setting $\tilde{\Gamma} = \tilde{B}_a$, the perfect recovery would be achieved as q tends to zero. The designed Kalman filter gain is denoted as $\tilde{K}_f$. Further details regarding LTR procedure are provided in Section 3.3.

The resulting LQG/LTR controller can then be expressed as follows:

$$\tilde{K}_{LQG}(s) = \left[\begin{array}{c|c} \tilde{A}_a - \tilde{B}_a\tilde{K}_r - \tilde{K}_f\tilde{C}_a & \tilde{K}_f \\ \hline -\tilde{K}_r & 0 \end{array}\right] \tag{5.9}$$

The 2nd, 3rd and 4th order Pade approximation and Bessel-Thomson approximation are utilized in approximating the time-delay, hence different LQG/LTR controllers are developed using the corresponding state-space models of the rational approximations. It is assumed that the delay for each signal in model (5.5) is the same. The properly tuned cost function weights Q_{P_e}, Q_{V_t}, $Q_{\Delta\omega}$ are set according to (3.34) and the weights ration is set to be equal to $\rho = 100$. Figure 5.4 shows the singular value plots of the LQG loop transfer function $-\tilde{K}_{LQG}\tilde{G}_a$, compared with that of the optimal regulator loop transfer function $\tilde{K}_r(sI - \tilde{A}_a)^{-1}\tilde{B}_a$ when $q = 10^{-8}$ by using the two rational approximations for time-delay $\tau = 250ms$. It is noted that the Pade approximation has unit gain at all frequencies.

It has been stated that higher order of the rational approximation results in more accurate approximation of time-delay. However, from the viewpoint of the performance of loop transfer recovery, higher order of the two approximations leads to increased discrepancy between the optimal regulator loop transfer function and the corresponding LQG loop transfer function shown in Figure 5.4. In the case of Pade approximation, cross over frequency of $\underline{\sigma}(L)$ is 15.0 *rad/s*, 12.3 *rad/s*, 11.5 *rad/s* for 2nd, 3rd and 4th order, respectively. Also, 100 *dB*/*decade* roll-off rate occurs at 220 *rad/s*, 100 *rad/s* and 60 *rad/s* for the increase in the order of Pade approximation. On the other hand, cross over frequency of $\underline{\sigma}(L)$ is 20.1 *rad/s*, 19.4 *rad/s*, 19.0 *rad/s*

when the order of Bessel-Thomson approximation is equal to 2, 3 and 4 respectively. Furthermore, 100 *dB*/*decade* roll-off rate occurs at 300 *rad/s*, 170 *rad/s* and 125 *rad/s* for the increase in the order of Bessel-Thomson approximation. Table 5.2 lists maximum peak of sensitivity function M_S and complementary sensitivity function M_T, as well as the system bandwidth ω_B of the closed-loop system by using different order delay approximations. In the case of Pade approximation, there is an insignificant increase in M_S and ω_B for the increase in the order, while M_T is decreased from 1.3 *dB* to 0.1 *dB* when the order is increased from 2 to 4, which demonstrates the superiority of the higher order Pade approximation. By using Bessel-Thomson approximation, M_S and M_T are significantly increased when the order is increased. In particular for 4th order, M_S and M_T are increased to 2.8 *dB* and 3.6 *dB*, respectively, which are higher in values when compared to the 4th order Pade approximation. This is undesirable due to the fact that the increase of M_S and M_T indicates deterioration in terms of the closed-loop system's performance and robustness. Therefore, it is clearly demonstrated that the Pade approximation is superior to Bessel-Thomson approximation of the time-delay.

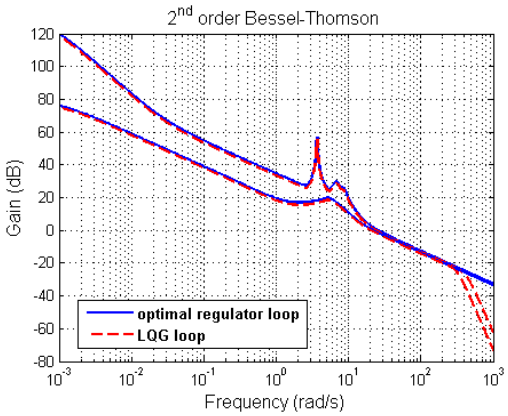

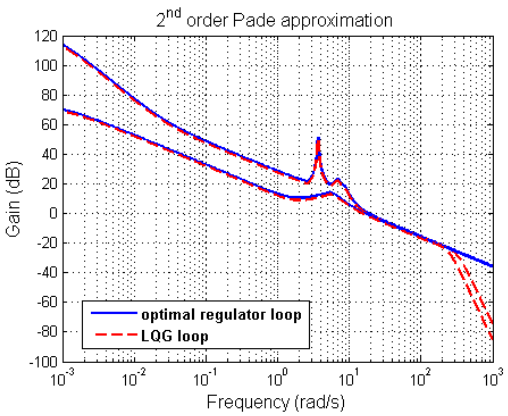

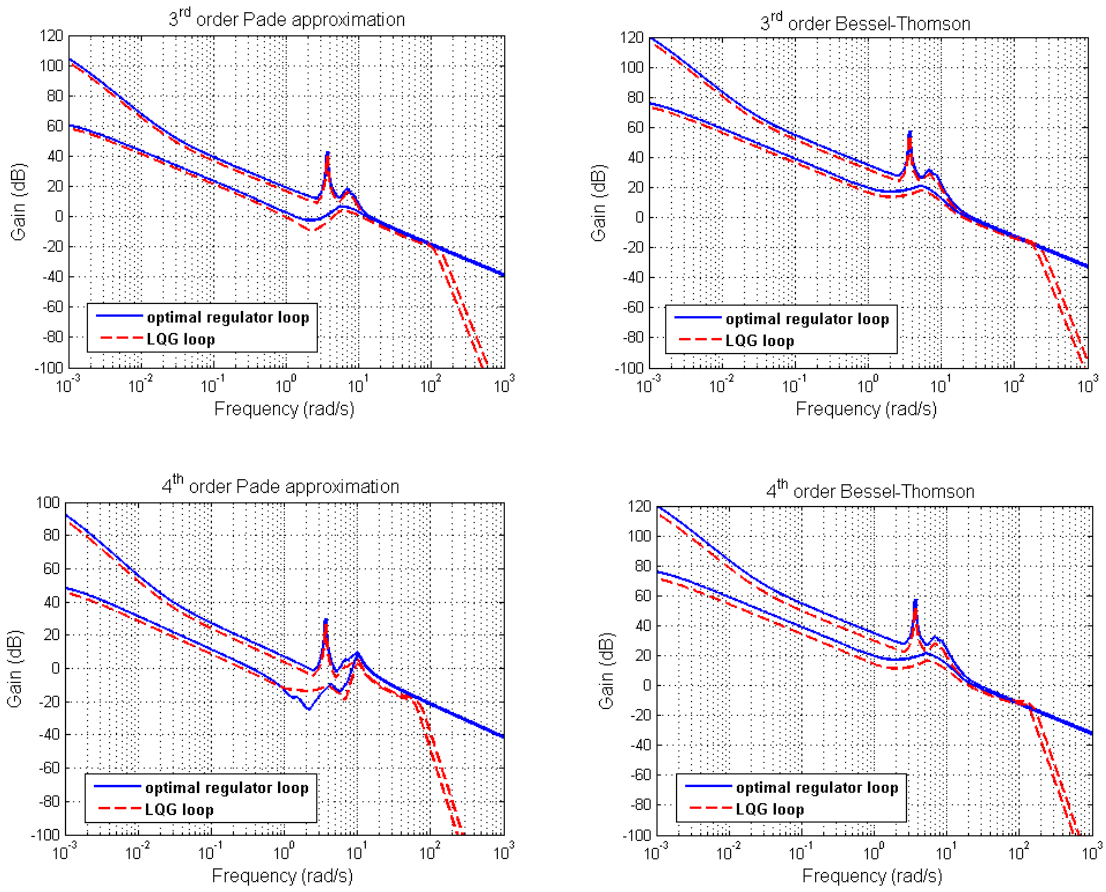

Figure 5.4 Singular values of L using Pade and Bessel-Thomson for $\tau = 250ms$

Table 5.2 System performance properties

Approximation Order	Pade approximation			Bessel-Thomson approximation		
	M_T (dB)	M_S (dB)	ω_B (rad/s)	M_T (dB)	M_S (dB)	ω_B (rad/s)
2	1.3	1.3	12.1	1.9	1.4	12.6
3	0.2	2.0	11.0	2.4	2.9	12.5
4	0.1	2.1	10.4	2.8	3.6	11.1

5.3.3 Evaluation using Linear System Analysis Tools

Communication time-delays are typically modelled using first or second order rational approximation [53, 55]. However, such low-order approximation may not be always appropriate, particularly in those cases for which time-delays are known to be relatively large. In order to investigate the impact that approximation order has on the performance of the closed-loop system, LQG controllers were designed with varying order of time-delay approximation. In the remaining sections of this chapter, LQG_P^n for $n = 2,3,4$ will be used to denote the supervisory continuous-time LQG/LTR controller designed for the time-delay approximated using Pade approximation in 2nd, 3rd and 4th order, respectively. LQG_B^n for $n = 2,3,4$ will denote the controller designed for the time-delay approximated using Bessel-Thomson approximation in 2nd, 3rd and 4th order, respectively. Finally, the LQG/LTR controller designed without consideration of the communication time-delays and designed in Chapter 3 will be denoted as LQG_0 and compared to LQG_P^n and LQG_B^n in this chapter.

5.3.3.1 Various Time-Delays

Table 5.3 and 5.4 list the system performance measures of the closed-loop system controlled by LQG/LTR controller using Pade approximation and Bessel-Thomson approximation of the 2nd, 3rd, and 4th order, respectively, for different communication time-delays and compared to LQG_0. The performance measures are maximum peak of the sensitivity function M_S and the complementary sensitivity function M_T, both of which are measured in *dB*, as well as the system bandwidth ω_B measured in *rad/s*. The observation of the increased M_S and M_T and the reduced ω_B demonstrate that the closed-loop system performance and robustness deteriorate for the increase in the communication time-delay for all considered LQG/LTR controllers. With LQG_0 controller, the value of M_T reaches 4.2 *dB* for a time-delay of 250 *ms*. This shows that the closed-loop system with LQG_0 exhibits high sensitivity to time-delays. With

controllers LQG_P^n and LQG_B^n for $n = 2,3,4$, the M_S and M_T are significantly reduced when compared to controller LQG_0 as shown in Table 5.3 and 5.4. This indicates improvement in the performance when using information regarding the time-delay to design the control system. It is also observed that M_S and M_T are smaller in the case of LQG controller that utilises Pade approximation compared to the one that uses the Bessel-Thomson approximation. Therefore, using frequency-domain tools it is shown that the most appropriate controller to use in the presence of time-delays is the one that utilises Pade Approximation.

Tables 5.5 and 5.6 list the damping of the inter-area mode using LQG_P^n and LQG_B^n for $n = 2,3,4$ and LQG_0 for different communication time-delays. Results show that LQG_0 only could maintain the closed-loop system stability for time-delay smaller than 250 *ms*, which is in accordance with the result stated above. For controllers LQG_P^n and LQG_B^n, higher order results in more damping provided to inter-area mode. In addition, the designed LQG/LTR controller using Pade approximation provides more damping to the inter-area mode than the controller that uses Bessel-Thomson approximation of the same order. Finally, it is observed that the system controlled by LQG_P^n could tolerate time-delay greater than 1 second, as shown in Table 5.5, while the time-delay tolerance of LQG_B^n is smaller than 800 *ms*.

It can be concluded that the designed LQG/LTR controllers accounting for communication time-delay, namely LQG_P^n and LQG_B^n, are more effective in stabilizing the power system than the conventional controller LQG_0. Higher order of the approximation results in more satisfactory system performance and robustness. Both system performance measures and damping of inter-area mode demonstrate the superiority of LQG/LTR controller designed using Pade approximation LQG_P^n compared to that of using Bessel-Thomson approximation LQG_B^n.

Table 5.3 System performance using Pade approximation for different time-delays

Time-delay τ	LQG_0			LQG_P^2			LQG_P^3			LQG_P^4		
	M_T	M_S	ω_B	M_T	M_S	ω_B	M_T	M_S	ω_B	M_T	M_S	ω_B
100 *ms*	1.9	1.1	11.8	1.3	1.2	15.5	0.1	1.5	13.1	0.1	0.7	12.4
250 *ms*	4.2	1.1	7.9	1.3	1.3	12.1	0.2	2.0	11.0	0.1	2.1	10.3
500 ms	4.3	2.0	4.9	1.4	1.3	8.1	0.4	2.5	7.2	0.2	2.5	7.0
800 ms	7.7	7.8	2.5	1.5	1.4	7.3	0.7	2.8	5.4	0.2	3.2	5.1
1 *s*	7.9	10.5	1.8	1.7	1.5	7.0	0.8	3.0	4.9	0.3	3.6	4.3
1.2 *s*	29.1	28.8	1.5	1.8	1.6	6.9	0.9	3.2	4.6	0.3	3.9	3.7
1.5 *s*	41.4	41.3	1.2	2.1	1.7	6.7	0.9	3.3	4.3	0.3	4.4	3.2

Table 5.4 System performance using Bessel-Thomson approximation for different time-delays

Time-delay τ	LQG_0			LQG_B^2			LQG_B^3			LQG_B^4		
	M_T	M_S	ω_B	M_T	M_S	ω_B	M_T	M_S	ω_B	M_T	M_S	ω_B
100 *ms*	1.9	1.1	11.8	1.7	1.3	19.0	1.9	2.5	17.5	2.3	2.9	15.9
250 *ms*	4.2	1.1	7.9	1.9	1.4	12.6	2.4	2.9	12.5	2.8	3.6	11.1
500 ms	4.3	2.0	4.9	2.0	1.4	9.6	2.8	2.9	8.3	3.4	3.7	7.2
800 ms	7.7	7.8	2.5	2.1	1.5	8.1	2.9	3.0	6.3	3.7	3.9	4.8
1 *s*	7.9	10.5	1.8	2.4	1.5	7.6	3.0	3.0	5.6	3.8	3.9	3.8
1.2 *s*	29.1	28.8	1.5	2.5	1.5	7.4	3.1	3.0	5.2	4.1	3.9	3.6
1.5 *s*	41.4	41.3	1.2	2.9	1.6	7.1	3.3	2.7	4.9	4.2	4.0	3.4

Table 5.5 Inter-area mode for different time-delays using LQG_P^4

Time-delay τ	LQG_0		LQG_P^2		LQG_P^3		LQG_P^4	
	$f(Hz)$	ζ (%)	$f(Hz)$	ζ (%)	$f(Hz)$	ζ (%)	$f(Hz)$	ζ (%)
100 *ms*	0.60	20.2	0.54	29.0	0.54	30.3	0.55	31.5
250 *ms*	0.60	3.4	0.54	28.1	0.55	29.2	0.55	31.1
500 ms	0.70	-9.6	0.54	27.5	0.55	28.7	0.55	30.5
800 ms	0.59	-11.3	0.55	20.2	0.55	26.3	0.56	30.0
1 *s*	0.55	-11.5	0.55	15.6	0.56	19.2	0.56	28.4
1.2 *s*	0.51	-15.1	0.55	10.7	0.56	14.6	0.56	26.5
1.5 *s*	0.50	-16.6	0.56	7.2	0.56	11.9	0.57	22.1

Table 5.6 Inter-area mode for different time-delays using LQG_B^4

Time-delay τ	LQG_0		LQG_B^2		LQG_B^3		LQG_B^4	
	$f(Hz)$	ζ (%)	$f(Hz)$	ζ (%)	$f(Hz)$	ζ (%)	$f(Hz)$	ζ (%)
100 *ms*	0.60	20.2	0.54	27.5	0.55	29.4	0.55	31.3
250 *ms*	0.60	3.4	0.55	26.1	0.55	28.8	0.56	30.2
500 ms	0.70	-9.6	0.55	11.0	0.56	15.6	0.57	27.4
800 ms	0.59	-11.3	0.56	7.8	0.58	10.2	0.60	17.3
1 *s*	0.55	-11.5	0.56	4.9	0.58	6.3	0.60	11.0
1.2 *s*	0.51	-15.1	0.56	2.1	0.59	3.0	0.59	7.0
1.5 *s*	0.50	-16.6	0.58	0.8	0.59	1.9	0.59	3.6

5.3.3.2 Delay Margin

In order to aid the comparison, *Delay Margin* term is introduced to quantify the ability of a given controller to retain stability when faced with the communication time-delays. More specifically, Delay Margin specifies maximum value of the time-delay that a given controller can tolerate before the overall closed-loop system exhibits instability. Therefore, the aim of a control engineer is to ensure that the Delay Margin is sufficiently large.

Delay margins for the stated controllers above are evaluated in this section. Table 5.7 lists the delay margins for the supervisory LQG/LTR controllers using Pade approximation and Bessel-Thomson approximation in different orders, as well as controller LQG_0. In case of the conventional controller, LQG_0 designed without consideration of time-delay, the delay margin is found to be equal to 160 *ms*. Clearly, this delay margin is not sufficient for the wide-area power system control for the use of different types of communication link [60]. For the controllers that account for the presence of time-delays, namely LQG_P^n and LQG_B^n for $n = 2,3,4$, it is clearly shown that the delay margin is significantly increased compared to LQG_0. Table 5.7 shows that the delay margin is increased for the increasing order of the approximation. In particular for Pade approximation, not only does the denominator order *n* increase the delay margin, but also the numerator degree *m* increases the delay margin. Also, the delay margin of the closed-loop system that uses Pade approximation to

synthesise controller is higher than using Bessel approximation with the same order. In particular, it can be observed that the closed-loop system using 4th order Bessel-Thomson approximation could only tolerate 520 *ms* time-delay, while the system using 4th order Pade approximation could tolerate 1.2 *s* time-delay, which is a sufficient communication time-delay tolerance for wide-area power system control application [60]. In conclusion, Table 5.7 clearly demonstrates the superiority of the controllers LQG_P^n and LQG_B^n compared to the conventional controller LQG_0 in terms of the robustness to the presence of time-delays.

Table 5.7 Delay margin for different controllers

Delay Margin	LQG_0	LQG_P^n					LQG_B^n
		$m=0$	$m=1$	$m=2$	$m=3$	$m=4$	
$n=1$	160 *ms*	220 *ms*	350 *ms*	—	—	—	220 *ms*
$n=2$	160 *ms*	300 *ms*	460 *ms*	600 *ms*	—	—	300 *ms*
$n=3$	160 *ms*	—	480 *ms*	650 *ms*	850 *ms*	—	400 *ms*
$n=4$	160 *ms*	—	—	680 *ms*	910 *ms*	1.2 *s*	520 *ms*

5.3.3.3 Various Operating Conditions

In this section the closed-loop system's performance and robustness are assessed in the presence of time-delays and under the changing operating conditions. The variation in power transfer from Area 1 to Area 2 provides these different operating conditions, which was realised by changing the generation power of Generators 2 and 3. Different controllers designed by considering the presence of time-delay, LQG_P^n and LQG_B^n for $n=2,3,4$, are applied onto the power system. Table 5.8 lists the delay margin for the six controllers and for each of the different operating conditions. Base case is denoted as the normal operating condition. It is observed that the increase of the power transfer from Area 1 to Area 2 significantly degrades the delay margin. For each operating condition, higher order of approximation results in larger delay margin and the delay margin resulting from the application of LQG_P^n is larger than that corresponding to LQG_B^n, which indicates the closed-loop system is

more robust to variation of time-delay and of operating conditions when using LQG_P^n than LQG_B^n.

Using 4th order of Pade and Bessel-Thomson approximations, the performance and robustness of the resulting closed-loop system are analysed. Tables 5.9 and 5.10 list the resulting frequencies and damping ratios of the inter-area mode for varying operating conditions and communication time-delays obtained when using LQG_P^4 and LQG_B^4, respectively. The damping of the inter-area mode is observed to be degraded by either the change in operating condition or the increase in the time-delay. As the power transfer increases, the damping of the inter-area mode is for both LQG_P^4 and LQG_B^4 and for different values of time-delays. Degradation of the damping is observed to be more prominent in the case of LQG_B^4 when compared to LQG_P^4. The inter-area mode becomes unstable in the case of LQG_B^4 for time-delays longer than 800 *ms*. On the other hand, controller LQG_P^4 sufficiently stabilises the system for all assessed time-delays, even under heavy power transfer.

It can be concluded that the communication time-delays and the changing operating condition result in the degradation of the performance observed through the reduction in the corresponding delay margin and the damping of the electromechanical mode. The closed-loop system is observed to be more robust when controlled using LQG_P^4 rather than LQG_B^4. These results will be verified in Section 5.5 using the non-linear simulation of the power system and observing time-domain results

Table 5.8 Delay margin for different power transfers

Power transfer increase: Area 1 to Area 2	Pade approximation			Bessel-Thomson approximation		
	LQG_P^2	LQG_P^3	LQG_P^4	LQG_B^2	LQG_B^3	LQG_B^4
Base case	**600 *ms***	**850 *ms***	**1.2 *s***	**300 *ms***	**400 *ms***	**520 *ms***
10%	580 *ms*	750 *ms*	1.1 *s*	260 *ms*	360 *ms*	450 *ms*
20%	500 *ms*	720 *ms*	1.1 *s*	240 *ms*	350 *ms*	450 *ms*
30%	420 *ms*	690 *ms*	1.0 *s*	200 *ms*	320 *ms*	420 *ms*
40%	380 *ms*	640 *ms*	950 *ms*	180 *ms*	290 *ms*	400 *ms*

Table 5.9 Inter-area mode for time-delays for different power transfers using LQG_P^4

Time-delay τ	Power transfer from area 1 to area 2									
	Base Case		Increase 10%		Increase 20%		Increase 30%		Increase 40%	
	$f(Hz)$	ζ (%)	$f(Hz)$	ζ (%)	$f(Hz)$	ζ (%)	$f(Hz)$	ζ (%)	$f(Hz)$	ζ (%)
100 *ms*	0.55	31.5	0.56	30.4	0.57	29.6	0.58	28.8	0.58	28.2
250 *ms*	0.55	31.1	0.56	29.5	0.57	28.8	0.58	27.6	0.58	27.1
500 ms	0.55	30.5	0.56	28.8	0.57	27.8	0.58	26.3	0.58	25.9
800 ms	0.56	30.0	0.56	28.0	0.57	26.0	0.58	25.1	0.58	24.8
1 *s*	0.56	28.4	0.56	26.8	0.57	25.2	0.58	24.7	0.58	23.9
1.2 *s*	0.56	26.5	0.57	25.4	0.58	23.0	0.58	21.6	0.58	20.3
1.5 *s*	0.57	22.1	0.59	21.9	0.60	20.1	0.61	19.2	0.61	18.6

Table 5.10 Inter-area mode for time-delays for different power transfers using LQG_B^4

Time-delay τ	Power transfer from area 1 to area 2									
	Base Case		Increase 10%		Increase 20%		Increase 30%		Increase 40%	
	$f(Hz)$	ζ (%)	$f(Hz)$	ζ (%)	$f(Hz)$	ζ (%)	$f(Hz)$	ζ (%)	$f(Hz)$	ζ (%)
100 *ms*	0.55	31.3	0.56	30.2	0.57	29.4	0.58	28.7	0.58	28.0
250 *ms*	0.56	30.2	0.57	29.0	0.58	28.2	0.59	27.5	0.59	26.8
500 ms	0.57	27.4	0.59	26.1	0.60	25.1	0.61	24.5	0.60	24.0
800 ms	0.60	17.3	0.61	16.0	0.62	15.2	0.63	14.7	0.62	14.6
1 *s*	0.60	11.0	0.61	10.1	0.62	9.5	0.62	9.3	0.62	9.2
1.2 *s*	0.59	7.0	0.61	6.4	0.62	6.1	0.62	6.1	0.62	5.8
1.5 *s*	0.59	3.6	0.60	3.5	0.61	3.3	0.62	3.1	0.62	2.5

5.3.4 Non-linear Simulation

The performance and robustness of the power system controlled by LQG_P^4, LQG_B^4 and LQG_0 in the presence of communication time-delays, are assessed in this section using the high-fidelity non-linear model of the power system in order to examine the suitability and effectiveness of the considered supervisory controllers. A large disturbance, which is a self-cleared three-phase fault, is applied onto the bus 5 at time t=1 second.

Figure 5.5 shows the speed deviation, electrical power output, and terminal voltage of each generator of the power system controlled by LQG_P^4 and LQG_0 respectively. The time-delay is equal to 160 *ms*, which is the delay margin of controller LQG_0 according to the results shown in Table 5.6. In the case of 160 *ms* time-delay, Figure 5.5 clearly shows that the power system controlled by LQG_0 is unstable when subjected to a large disturbance. This illustrates the importance of considering communication time-delays when designing supervisory wide-area controllers. On the other hand, controller that employs 4th order Pade Approximation in order to model the time-delays, denoted as LQG_P^4, is shown to maintain the stability with satisfactory response to the applied disturbance. This further demonstrates the benefit of including appropriate communication time-delay description into the model utilised by the wide-area controller.

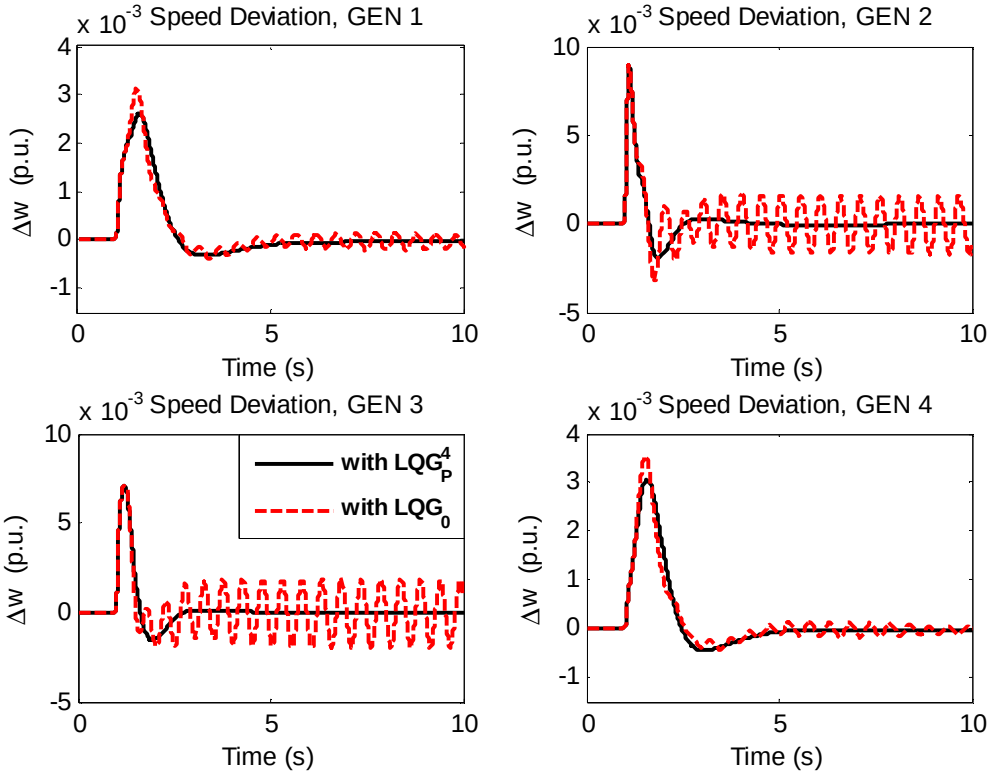

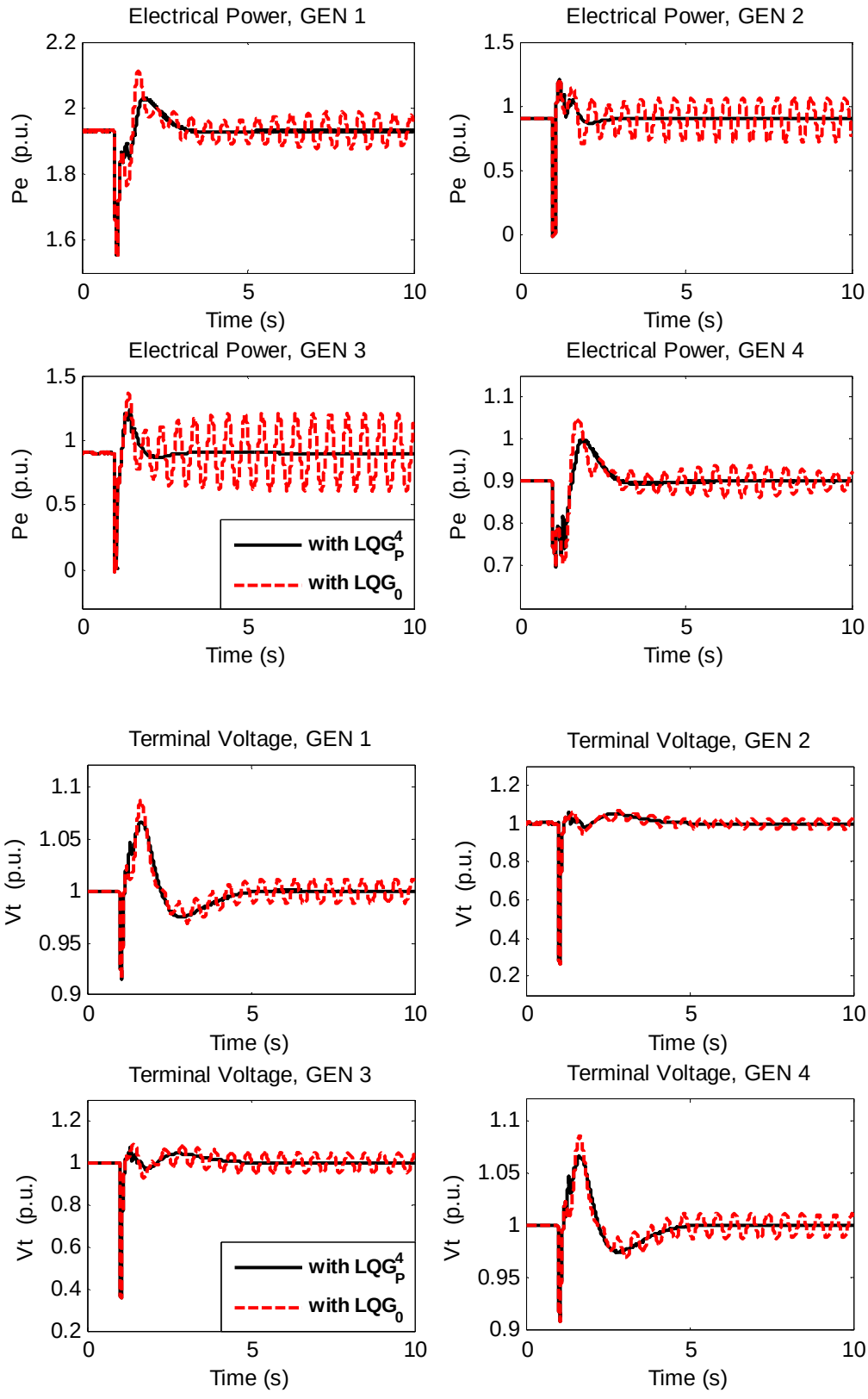

Figure 5.5 System response using LQG_P^4 and LQG_0 for $T_d = 160\,ms$

Figures 5.6 and 5.7 show the speed deviation for each generator of the power system controlled by controllers LQG_P^4 and LQG_B^4 in the presence of 250 *ms* and 520 *ms* time-delays, respectively, when subjected to a self-cleared three-phase fault. The corresponding responses of electrical power output and terminal voltage are shown in Appendix B. In case of 250 *ms* time-delay, both LQG_P^4 and LQG_B^4 can stabilize the power system when subjected to the large disturbance, as shown in Figure 5.6. This confirms the result shown in Table 5.6 that the delay margin for either of these two controllers is greater than 250 *ms*. It is also observed that the settling time of the closed-loop system controlled by LQG_P^4 is smaller than that of the system controlled by LQG_B^4, which indicates the benefit in using Pade approximation to model the time-delays when compared to Bessel-Thomson approximation. In the case of 520 *ms*, which is equal to value of the delay margin of LQG_B^4, controller LQG_B^4 cannot stabilize the power system when subjected to a large disturbance, as shown in Figure 5.7. On the other hand, it is clearly shown in Figure 5.7 that the power system can be recovered from the large disturbance controlled by controller LQG_P^4 for 520 *ms* time-delay. Responses in both Figure 5.6 and 5.7 demonstrate the superiority of the controller that employs Pade Approximation to represent time-delays when compared to the controller that utilises Bassel-Thomson Approximation to describe time-delays in terms of the closed-loop system response and its stability.

Figure 5.8 shows the speed deviation for each generator of the simulated power system controlled by LQG_P^4 when subjected to a large disturbance and with the communication time-delay of 1.3 *s*. The corresponding responses of electrical power output and terminal voltage of each generator are shown in Appendix B. In the case of 1.3 *s* time-delay, which exceeds the delay margin for controller LQG_P^4, Figure 5.8 shows that LQG_P^4 is not effective in stabilizing the power system when subjected to a large disturbance, which is in accordance with the result from frequency-domain analysis in Section 5.4.

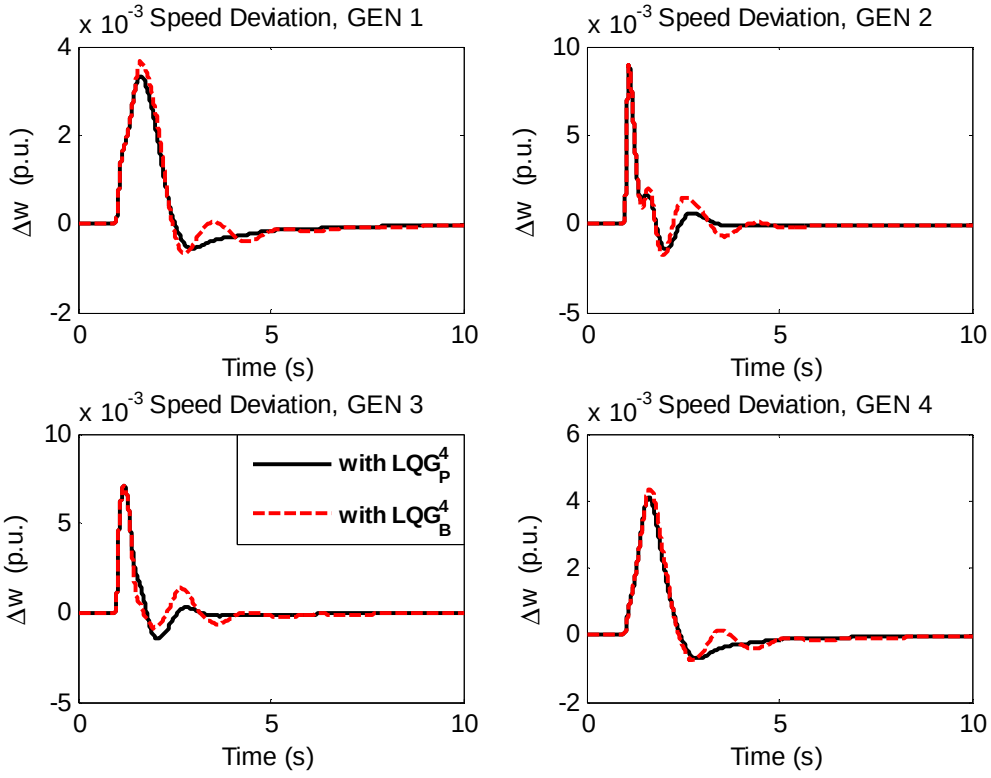

Figure 5.6 Speed deviation using LQG_P^4 and LQG_B^4 for $T_d = 250\,ms$

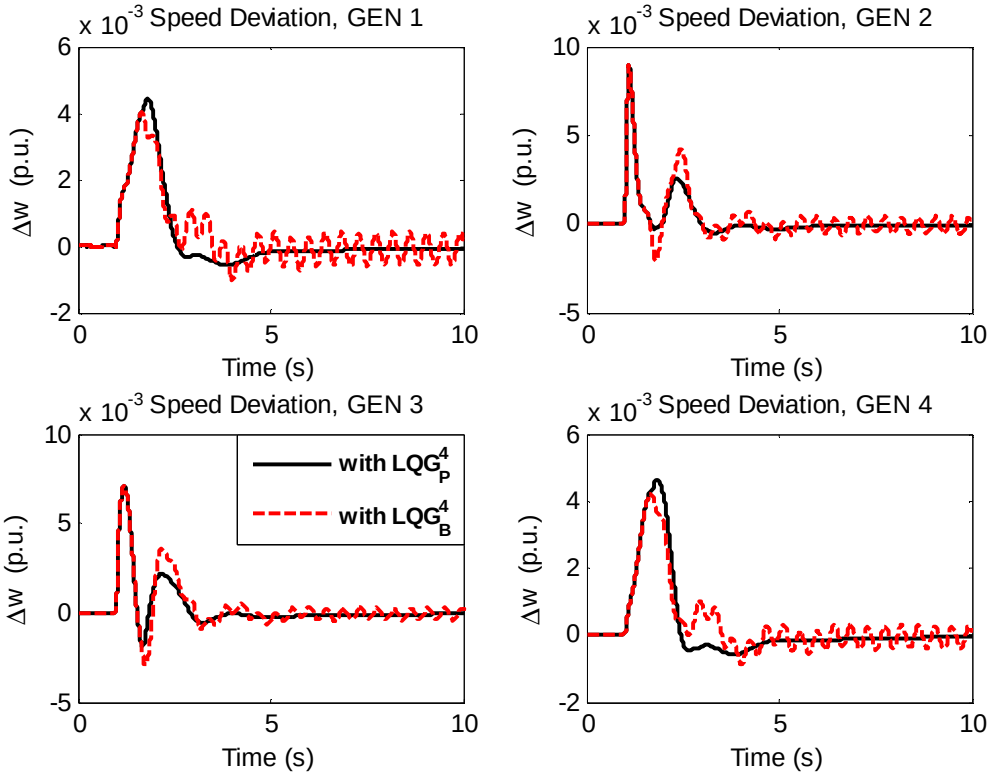

Figure 5.7 Speed deviation using LQG_P^4 and LQG_B^4 for $T_d = 520\,ms$

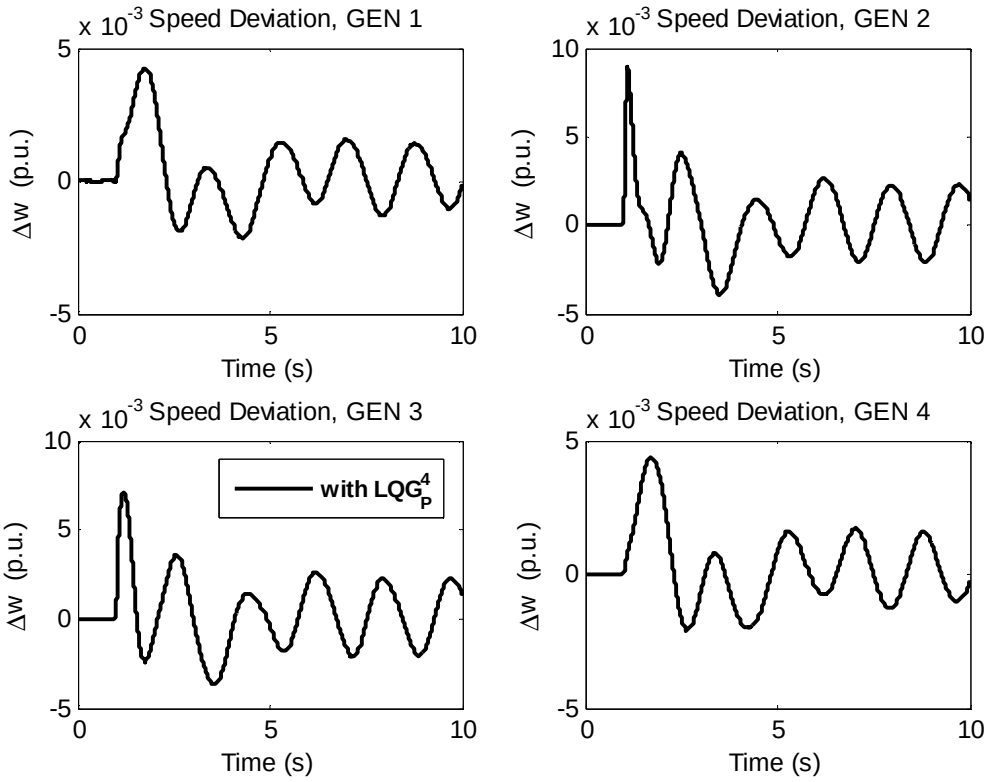

Figure 5.8 Speed deviation using LQG_P^4 for $T_d = 1.3\,s$

5.4 Discrete-Time LQG/LTR for System with Time-Delay

5.4.1 Disretising the System with Time-Delay

A continuous linear time-invariant system that includes a time-delay is described by:

$$\begin{aligned} \dot{x} &= Ax + Bu(t-\tau) + w \\ y &= Cx + v \end{aligned} \tag{5.10}$$

where $\tau > 0$ denotes a communication time-delay, w and v represent process and measurement noises respectively. In sampling (5.10), two cases are considered. The first case is when the time-delay τ less than one sampling period denoted as T_s. The second case is when the time-delay τ longer than one sampling period T_s. These two cases are considered below.

5.4.1.1 Delay Less than One Sampling Period

Firstly the deterministic case with $w = 0$, $v = 0$, is considered and the communication delay is assumed to be less than one sampling period T_s, i.e. $\tau < T_s$. Discretising the continuous-time plant (5.10) with sampling period T_s gives [95]

$$\begin{aligned} x(k+1) &= \Phi x(k) + \Gamma_0 u(k) + \Gamma_1 u(k-1) \\ y(k) &= Cx(k) \end{aligned} \tag{5.11}$$

where

$$\begin{aligned} \Phi &= e^{AT_s}, \\ \Gamma_0 &= \int_0^{T_s-\tau} e^{As} ds B, \\ \Gamma_1 &= e^{A(T_s-\tau)} \int_0^{\tau} e^{As} ds B. \end{aligned} \tag{5.12}$$

Defining $\tilde{x}(k) = \begin{bmatrix} x^T(k) & u^T(k-1) \end{bmatrix}^T$ as the augmented state vector, the resulting augmented state-space model of (5.11) is given by

$$\begin{aligned} \begin{bmatrix} x(k+1) \\ u(k) \end{bmatrix} &= \begin{bmatrix} \Phi & \Gamma_1 \\ 0 & 0 \end{bmatrix} \begin{bmatrix} x(k) \\ u(k-1) \end{bmatrix} + \begin{bmatrix} \Gamma_0 \\ I \end{bmatrix} u(k) \\ y(k) &= \begin{bmatrix} C & 0 \end{bmatrix} \begin{bmatrix} x(k) \\ u(k-1) \end{bmatrix} \end{aligned} \tag{5.13}$$

The extra state variable $u(k-1)$ which represents the past value of the control signal is introduced. The continuous-time system of (5.10) is infinite dimensional; however, the corresponding sampled system is a finite-dimensional system. Thus, the time-delay is represented exactly rather than described using rational approximation.

5.4.1.2 Delay Longer than One Sampling Period

If the communication delay is longer than one sampling period, then it can be represented as

$$\tau = (d-1)T_s + \tau',\ 0 \le \tau' < T_s \tag{5.14}$$

Where d is an integer, selected such that integration of $\dot{x}$ in (5.10) is over the sampling interval $\left[(k+d-1)T_s \quad (k+d)T_s\right]$. Therefore, the *ZOH* sampling of (5.10) is obtained as [95]:

$$\begin{aligned} x(k+1) &= \Phi x(k) + \Gamma_0 u(k-d+1) + \Gamma_1 u(k-d) \\ y(k) &= Cx(k) \end{aligned} \tag{5.15}$$

where Φ, Γ_0 and Γ_1 are given by (5.12) with τ replaced by τ'. The corresponding augmented state-space model is

$$\begin{aligned} \begin{bmatrix} x(k+1) \\ u(k-d+1) \\ \cdots \\ u(k-1) \\ u(k) \end{bmatrix} &= \begin{bmatrix} \Phi & \Gamma_1 & \Gamma_0 & \cdots & 0 \\ 0 & 0 & I & \cdots & 0 \\ \vdots & \vdots & \vdots & I & \vdots \\ 0 & 0 & 0 & \cdots & I \\ 0 & 0 & 0 & \cdots & 0 \end{bmatrix} \begin{bmatrix} x(k) \\ u(k-d) \\ \cdots \\ u(k-2) \\ u(k-1) \end{bmatrix} + \begin{bmatrix} 0 \\ 0 \\ \vdots \\ 0 \\ I \end{bmatrix} u(k) \\ y(k) &= \begin{bmatrix} C & 0 & \cdots & 0 & 0 \end{bmatrix} \begin{bmatrix} x(k) \\ u(k-d) \\ \cdots \\ u(k-2) \\ u(k-1) \end{bmatrix} \end{aligned} \tag{5.16}$$

and $\tilde{x}(k) = \left[x^T(k) \quad u^T(k-d) \quad \cdots \quad u^T(k-2) \quad u^T(k-1)\right]^T$ is the augmented state vector, with additional $d \cdot m$ extra states used to describe the delay [95].

The discrete-time augmented state-space model of the system with communication delays is given as:

$$\begin{aligned} \tilde{x}(k+1) &= \tilde{\Phi}\tilde{x}(k) + \tilde{\Gamma}u(k) + w_k \\ y(k) &= \tilde{C}\tilde{x}(k) + v_k \end{aligned} \tag{5.17}$$

where w_k and v_k denote process and measurement noise, respectively, and were originally introduced in (4.1).

Note that the augmented state vector means the dimension of the system can be considerably increased if the sampling period is relatively short compared with the time-delay, thus resulting in the increase of the LQG controller's dimensionality.

5.4.2 Controller Synthesis

To synthesize the discrete-time LQG controller for system (5.17), the discrete-time cost function given in (4.9) is utilized. Thus the discrete-time cost function for the discrete-time system with time-delay is represented as following. Note that it is assumed that $\tau < T_s$.

$$\begin{aligned} J_1^* &= \sum_{k=0}^{\infty} \tilde{x}(k)^T \tilde{Q}_k \tilde{x}(k) + u(k)^T \tilde{R}_k u(k) \\ &= \sum_{k=0}^{\infty} x(k)^T \tilde{Q}_k^1 x(k) + u(k-1)^T \tilde{R}_k^1 u(k-1) + u(k)^T \tilde{R}_k u(k) \end{aligned} \tag{5.18}$$

where $\tilde{x}(k) = \begin{bmatrix} x^T(k) & u^T(k-1) \end{bmatrix}^T$, and

$$\tilde{Q}_k = \begin{bmatrix} \tilde{Q}_k^1 & 0 \\ 0 & \tilde{R}_k^1 \end{bmatrix}, \quad \tilde{R}_k = \int_{\tau}^{T_s} \left[\Gamma(s-\tau)^T Q \Gamma(s-\tau) + R \right] ds. \tag{5.19a}$$

with

$$\tilde{Q}_k^1 = \int_0^{T_s} \Phi(s)^T Q \Phi(s) ds\,, \; \tilde{R}_k^1 = \int_0^{\tau} \left[\Gamma(s)^T Q \Gamma(s) + R \right] ds\,. \tag{5.19b}$$

$\Phi(s)$ and $\Gamma(s)$ are given by (4.7). It is assumed that $\tilde{Q}_k^1$ is positive semidefinite and that $\tilde{R}_k^1$ and $\tilde{R}_k$ are positive definite.

when $\tau > T_s$ and $\tau = (d-1)T_s + \tau'$, $0 \le \tau' < T_s$ the cost function is given by

$$J_2^* = \sum_{k=0}^{\infty} \tilde{x}(k)^T \tilde{Q}_k \tilde{x}(k) + u(k)^T \tilde{R}_k u(k) \tag{5.20}$$

where $\tilde{x}^T(k) = \begin{bmatrix} x^T(k) & u^T(k-d) & \cdots & u^T(k-2) & u^T(k-1) \end{bmatrix}^T$, and

$$\tilde{Q}_k = \begin{bmatrix} \tilde{Q}_k^1 & 0 & 0 & \cdots & 0 \\ 0 & \tilde{R}_k^d & 0 & \cdots & 0 \\ 0 & 0 & \tilde{R}_k^{d-1} & \cdots & 0 \\ \vdots & \vdots & \vdots & \ddots & \vdots \\ 0 & 0 & 0 & \cdots & \tilde{R}_k^1 \end{bmatrix}, \quad \tilde{R}_k = RT_s. \tag{5.21a}$$

with

$$\begin{aligned} \tilde{Q}_k^1 &= \int_0^{T_s} \Phi(s)^T Q \Phi(s) ds, \\ \tilde{R}_k^d &= \int_0^{\tau'} \left[\Gamma(s)^T Q \Gamma(s) + R \right] ds, \\ \tilde{R}_k^{d-1} &= \int_{\tau'}^{T_s} \left[\Gamma(s-\tau')^T Q \Gamma(s-\tau') + R \right] ds, \\ \tilde{R}_k^{d-2} &= \cdots = \tilde{R}_k^1 = RT_s. \end{aligned} \tag{5.21b}$$

$\Phi(s)$ and $\Gamma(s)$ are given by (4.7). It is assumed that $\tilde{Q}_k^1$ is positive semidifinite and that $\tilde{R}_k^d$, … , $\tilde{R}_k^1$ and $\tilde{R}_k$ are positive definite.

The discrete-time function J_1^* in its original form, given in (5.18) includes the crossover terms $x(k)^T \tilde{M}_0 u(k)$ and $x(k)^T \tilde{M}_1 u(k-1)$. However, it is assumed here that $\tilde{M}_0 = \tilde{M}_1 = 0$. The first term $\sum_{k=0}^{\infty} x(k)^T \tilde{Q}_k^1 x(k)$ is only affected by the sampling period T_s, and the second term $\sum_{k=0}^{\infty} u(k-1)^T \tilde{R}_k^1 u(k-1)$ is only affected by the delays τ. The third term $\sum_{k=0}^{\infty} u(k)^T \tilde{R}_k u(k)$ is affected by both T_s and τ.

Also, the discrete-time function J_2^* in its original form, given in (5.20) includes the crossover terms $x(k)^T \tilde{M}_0 u(k)$, $x(k)^T \tilde{M}_1 u(k-1)$, …, and $x(k)^T \tilde{M}_d u(k-d)$. It is assumed that $\tilde{M}_0 = \tilde{M}_1 = \cdots = \tilde{M}_d = 0$. The term of $u(k-d)$ is only affected by the value of τ' and is not affected by sampling period T_s. The term of $u(k-d+1)$ is affected by both T_s and τ'. The rest of the terms in function (5.20) are only affected T_s with no relation to τ'.

Given the discrete state-space model (5.17) for the continuous-time system with time-delay expressed in (5.10), the discrete-time LQG control problem is to find the optimal control law that minimizes the discrete-time cost function J_1^* or J_2^*. The block diagram of the power system controlled by the supervisory discrete-time LQG/LTR controller for the time-delay is depicted in Figure 5.9. Similarly to the controller synthesised in Section 4.4, the integral action is incorporated and the resulting augmented discrete-time state-space model is described in the form of (4.19). The corresponding state-space matrices are denoted as $\tilde{\Phi}_a$, $\tilde{\Gamma}_a$, $\tilde{C}_a$ and $\tilde{D}_a$. The augmented state-space transfer function is expressed as follows:

$$\tilde{G}_d = \tilde{C}_a \left(zI - \tilde{\Phi}_a \right)^{-1} \tilde{\Gamma}_a + \tilde{D}_a \tag{5.22}$$

The discrete-time LQG controller for the system with time-delay is then synthesized using the methodology described in Section 4.3. The discrete-time optimal regulator is synthesized by substituting $\tilde{\Phi}_a$ and $\tilde{\Gamma}_a$ into (4.11) as follows:

$$\tilde{K}_{r\_d} = \left(\tilde{R}_k^{'} + \tilde{\Gamma}_a{}^T \tilde{P}_r \tilde{\Gamma}_a \right)^{-1} \tilde{\Gamma}_a{}^T \tilde{P}_r \tilde{\Phi}_a \tag{5.23}$$

and $\tilde{P}_r$ is the positive semidefinite solution of DARE

$$\tilde{P}_r = \tilde{\Phi}_a{}^T \tilde{P}_r \tilde{\Phi}_a - \tilde{K}_{r\_d}{}^T \left(\tilde{R}_k^{'} + \tilde{\Gamma}_a{}^T \tilde{P}_r \tilde{\Gamma}_a \right) \tilde{K}_{r\_d} + \tilde{Q}_k^{'} \tag{5.24}$$

where $\tilde{Q}_k^{'}$ and $\tilde{R}_k^{'}$ are the corresponding weighting matrices. Thus, the discrete-time optimal state-feedback control law is constructed as:

$$u(k) = -\tilde{K}_{r\_d} \hat{\tilde{x}}(k) \tag{5.25}$$

The discrete-time Kalman filter is synthesized by applying $\tilde{\Phi}_a$ and $\tilde{\Gamma}_a$ into (4.13) – (4.17) with state vector $\tilde{x}$ and positive definite $\tilde{P}_f$. The discrete-time Kalman Filter gain is calculated as follows:

$$\tilde{K}_{f\_d} = \tilde{P}_f (k \mid k-1) \tilde{C}_a{}^T \left[\tilde{C}_a \tilde{P}_f (k \mid k-1) \tilde{C}_a{}^T + V_k \right]^{-1} \tag{5.26}$$

The discrete-time LQG controller for system described in (5.22) is represented in the following form:

$$\tilde{K}_{dLQG} = \left[\begin{array}{c|c} \tilde{\Phi}_a - \tilde{\Gamma}_a \tilde{K}_{r\_d}(k) - \tilde{K}_{f\_d}(k)\tilde{C}_a & \tilde{K}_{f\_d}(k) \\ \hline -\tilde{K}_{r\_d}(k) & 0 \end{array}\right] \tag{5.27}$$

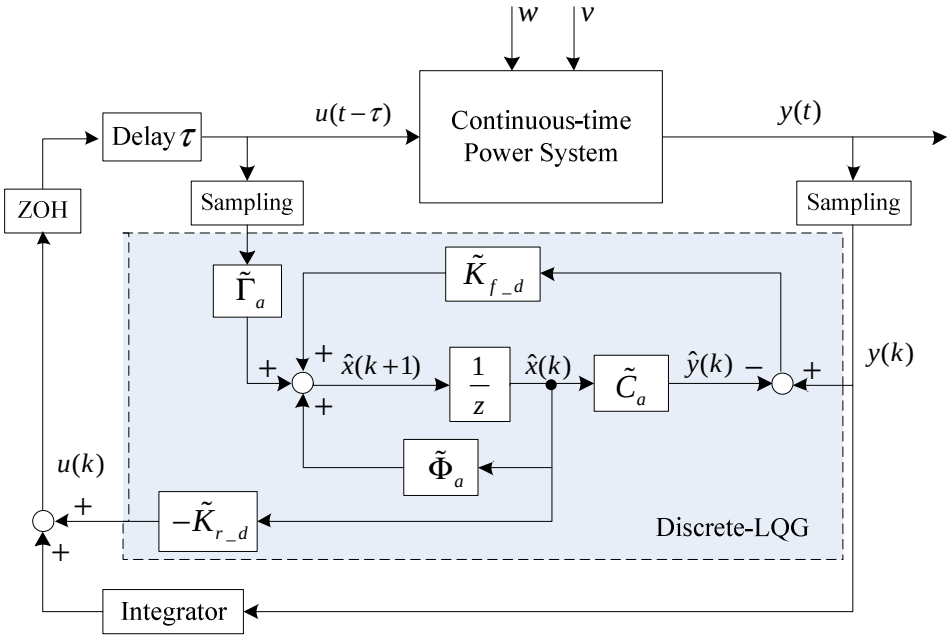

Figure 5.9 Schematic block diagram of the closed-loop system

5.4.3 Controller Design for Delayed-Power System

5.4.3.1 Delay Less than One Sampling Period

For the case of $\tau < T_s$, the augmented state-space model of the power system with delay is given by (5.14) with additional 12 states used to model the time-delay. The discrete-time optimal state-feedback is computed according to (5.25). By setting $T_s = 0.01$ seconds and $\tau = 0.005$ seconds which is shorter than one sampling period, the discrete-time optimal regulator gain $\tilde{K}_{r\_d}$, the discrete-time Kalman filter gain $\tilde{K}_{f\_d}$, and the discrete-time LQG controller $\tilde{K}_{dLQG}$ for system with time-delays is then synthesized via (5.22) – (5.26). The discrete-time cost function weights $\tilde{Q}_k'$ and $\tilde{R}_k'$ are obtained via (5.19) using the continuous-time cost function weights $\tilde{Q}$ and $\tilde{R}$ used in Section 5.3. W_k and V_k are the same as used in Section 4.4.2.

For the delayed-power system, the solid lines in Figure 5.10 show the singular value plots of the discrete-time optimal regulator loop function $\tilde{K}_{r\_d}(zI-\tilde{\Phi}_a)^{-1}\tilde{\Gamma}_a$, and the dashed lines represent the singular value plots of the discrete-time LQG loop function $-\tilde{K}_{dLQG}\tilde{G}_d$ for $q=10^{-2}$, 10^{-4}, 10^{-6} and 10^{-8}. As q decreases, the discrete-time LQG loop gain closely approaches the optimal regulator loop gain, which indicates the recovery is achieved at plant input. Figure 5.11 shows the singular value plots of sensitivity function S and complementary sensitivity function T of the recovered closed-loop system. Table 5.11 lists system performance measures obtained for the delayed-power system when controlled using $\tilde{K}_{r\_d}$ and $\tilde{K}_{dLQG}$. In case of $\tilde{K}_{dLQG}$, cross over frequencies of $\bar{\sigma}(L)$ and $\underline{\sigma}(L)$ as well as system bandwidth ω_B are reduced compared to $\tilde{K}_{r\_d}$. The maximum peak of T, M_T , is increased from 1.2 *dB* to 1.5 *dB*, indicating the degraded robustness and performance. However, system performances and robustness using $\tilde{K}_{dLQG}$ are still satisfied in the presence of the time-delays. The damping ratio of the electromechanical mode is reduced from 60.9% to 54.1% when using $\tilde{K}_{dLQG}$ as opposed to $\tilde{K}_{r\_d}$. Therefore, some degradation in performance is observed but this degradation is acceptable.

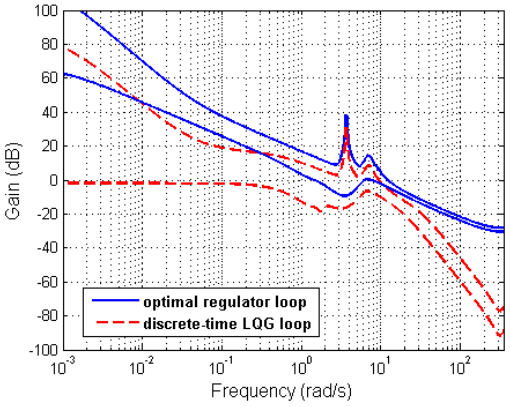

(a) $q=10^{-2}$

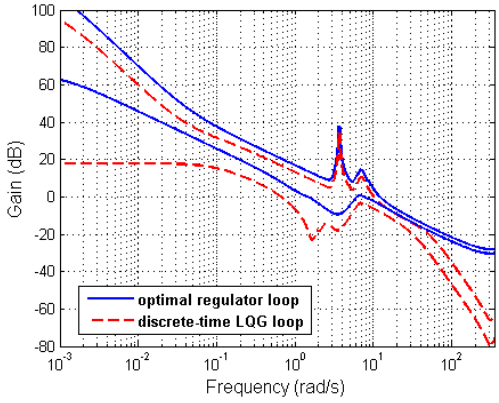

(b) $q=10^{-4}$

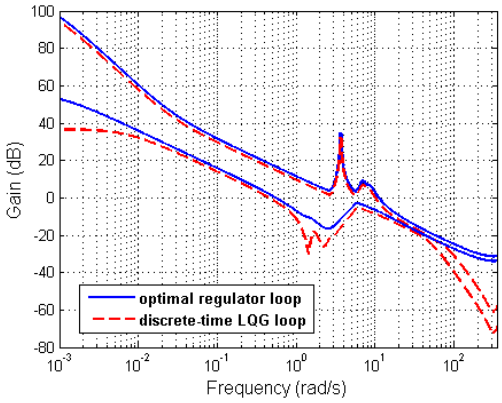

(c) $q = 10^{-6}$

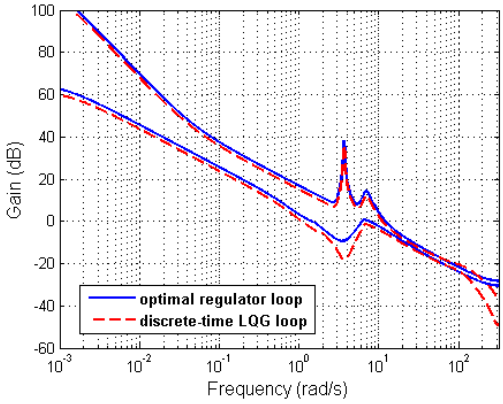

(d) $q = 10^{-8}$

Figure 5.10 LTR for (a) $q = 10^{-2}$, (b) $q = 10^{-4}$, (c) $q = 10^{-6}$, (d) $q = 10^{-8}$

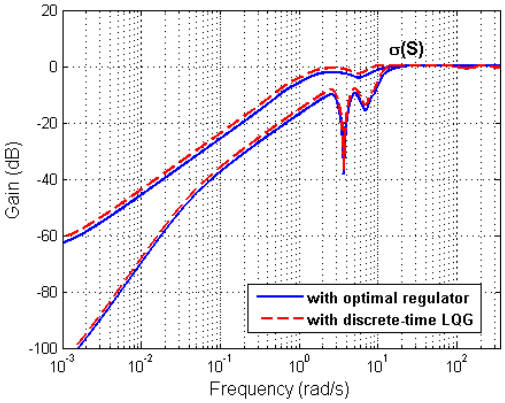

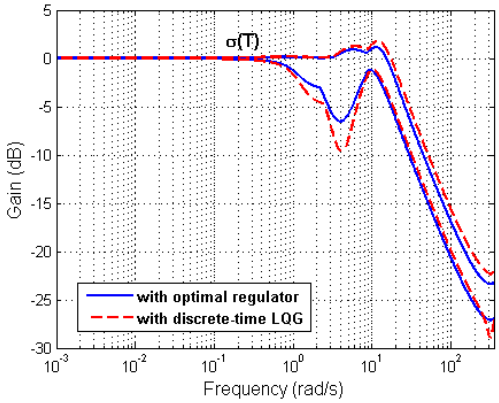

Figure 5.11 $\sigma(S)$ and $\sigma(T)$ for $\tilde{K}_{r\_d}$ and $\tilde{K}_{dLQG}$

Table 5.11 System performance measures for $\tilde{K}_{r\_d}$ and $\tilde{K}_{dLQG}$

Controller	Inter-area mode		M_S (dB)	M_T (dB)	ω_B (rad/s)	$\omega_{\underline{\sigma}(L)}$ (rad/s)	$\omega_{\bar{\sigma}(L)}$ (rad/s)
	ζ (%)	f (Hz)					
$\tilde{K}_{r\_d}$	60.9	0.56	0	1.2	7.2	7.5	12.2
$\tilde{K}_{dLQG}$	54.1	0.55	0	1.5	5.5	6.4	11.0

5.4.3.2 Delay Longer than One Sampling Period

In the case of $\tau > T_s$, the delay can be expressed using (5.15). The augmented state-space model of the power system with delay is then given by (5.18). The discrete-

time optimal state-feedback gain is obtained using (5.23). The weighting matrices in the corresponding cost function given in (5.20), namely $\tilde{Q}_k$ and $\tilde{R}_k$, are obtained using (5.21) while W_k and V_k are the same as those specified in Section 4.4.2. For the design of discrete-time LQG/LTR controller, sampling period is set to $T_s = 0.01$ seconds, the assessed delays are $\tau = 0.1$ and 0.5 seconds. The recovery at the plant input is achieved by designing the discrete-time Kalman filter, so that the discrete-time LQG loop function $-\tilde{K}_{dLQG}\tilde{G}_d$ closely approaches to the discrete-time optimal regulator loop function $\tilde{K}_{r\_d}(zI - \tilde{\Phi}_a)^{-1}\tilde{\Gamma}_a$ as q tends to zero, as described in Section 4.3.4.

Figure 5.12 shows the singular value plots of the recovered discrete-time LQG loop function $-\tilde{K}_{dLQG}\tilde{G}_d$ (solid line) for $\tau = 0.1$, and 0.5 seconds compared to that of the controller designed for $\tau = 0.005$ seconds. It is observed that the loop gain is reduced for the same value of q due to the increase in time-delay, which indicates that system performance and robustness deteriorate when the time-delay is increased. Table 5.12 lists closed-loop system performance measures obtained for the delayed-power system when controlled using $\tilde{K}_{dLQG}$ for 0.005, 0.1 and 0.5 seconds time-delay, respectively. For the increase of time-delay, cross over frequencies of $\bar{\sigma}(L)$ and $\underline{\sigma}(L)$ as well as system bandwidth ω_B are significantly reduced compared to time-delay of 0.005 seconds. The maximum peak of T, M_T, is increased from 1.5 *dB* to 1.8 *dB* when the time-delay is increased from 0.005 seconds to 0.5 seconds, indicating the degraded robustness and performance. Furthermore, the damping ratio of the inter-area mode is reduced from 54.1% to 35.7% for the increase of time-delay. Therefore, the degradation in performance is observed for the increase of time-delay, but this degradation is acceptable as long as the time-delay is no greater than 0.5 seconds. This demonstrates the effectiveness of the designed discrete-time LQG/LTR controller for the power system with communication time-delays.

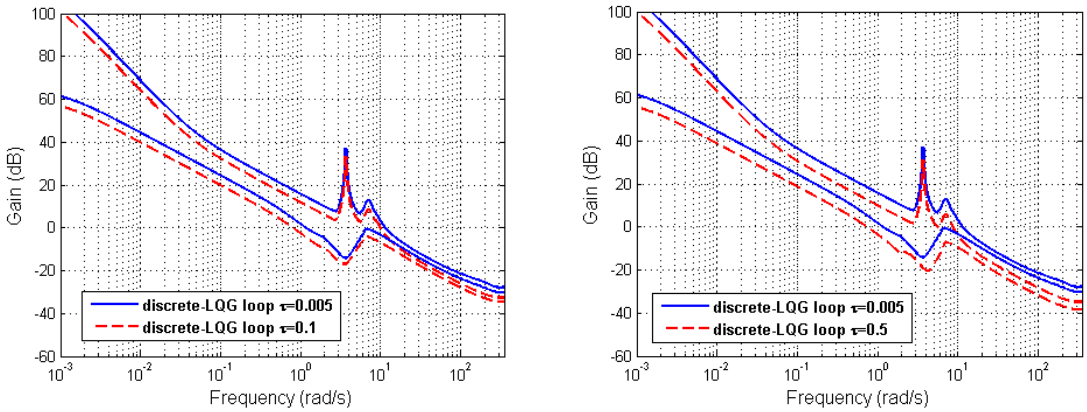

(a) $\tau = 0.1\ s$ (b) $\tau = 0.5\ s$

Figure 5.12 LTR for $\tau = 0.1$, and $0.5\ s$

Table 5.12 System performance measures using $\tilde{K}_{dLQG}$

Time-delay τ	Inter-area mode		M_S (dB)	M_T (dB)	ω_B (rad/s)	$\omega_{\underline{\sigma}(L)}$ (rad/s)	$\omega_{\bar{\sigma}(L)}$ (rad/s)
	$\zeta(\%)$	$f(Hz)$					
5 *ms*	54.1	0.55	0	1.5	5.5	6.4	11.0
100 *ms*	38.1	0.57	0	1.6	4.9	5.4	9.9
500 *ms*	35.7	0.58	0	1.8	3.5	4.6	8.2

For delay $\tau = 0.1,\ 0.5$ seconds, $10 \cdot 12$ and $50 \cdot 12$ additional states are included in the augmented state-space model of the system in (5.17), respectively. Thus, the dimension of the augmented state-space model will be large if the delay is much longer than the sampling period, hence the dimension of the controller. This may results in the increased computational burden.

5.4.4 Evaluation using Linear System Analysis Tools

This section reports on the results obtained when assessing the performance and robustness of the closed-loop system incorporating discrete-time LQG/LTR controller designed in Section 5.5 using the linearised model of a power system. The controller that incorporates the communication time-delays, denoted as LQG_m, is compared to the conventional discrete-time controller that ignores the presence of the time-delays LQG_{d0}, which was designed and detailed in Section 4.4.

5.4.4.1 Delay Margin

Delay margins for discrete-time controllers LQG_{d0} and LQG_m are identified for different sampling periods and are listed in Table 5.13. It is observed that the delay margin for controller LQG_{d0} is quite small and is further reduced from 120 *ms* to 100 *ms* when the sampling period is increased from 0.01 seconds to 0.1 seconds. This delay margin is shorter than the delay margin for continuous-time controller LQG_0, found to be equal to 160 *ms* in Section 5.4.2, due to the discretisation of the controller. In case of controller LQG_m, the delay margin is significantly increased to be as long as 1.4 seconds compared to 120 *ms* achieved by LQG_{d0} with the sampling period of $T_s = 0.01$ seconds. This demonstrates suitability of LQG_m in the power system applications with communication time-delays. Also, the increase in sampling period has an insignificant deterioration on the delay margin for controller LQG_m. One other very important observation is that the delay margin for the designed discrete-time LQG/LTR controller LQG_m using sampling period of $T_s = 0.01$ seconds is larger than that achieved by the continuous-time controller that uses 4th order Pade approximation LQG_P^4. This indicates the benefit of using discrete-time controllers rather than their continuous-time counterparts when dealing with the communication time-delays. The reason is primarily due to the fact that the design of LQG_m incorporates the exact time-delay description into the state-space model of the system, while controller LQG_P^4 is designed by representing the time-delay with rational Pade approximation.

Table 5.13 Delay margin for different sampling periods

Sampling period (second)	Delay Margin	
	LQG_{d0}	LQG_m
0.01	120 *ms*	1.4 *s*
0.02	115 *ms*	1.3 *s*
0.05	110 *ms*	1.1 *s*
0.1	100 *ms*	1.1 *s*

5.4.4.2 Frequency Domain Analysis

The performance and the robustness of the closed-loop system comprising of the power system controlled by the designed discrete-time LQG/LTR controller LQG_m are evaluated in the presence of communication time-delays and different sampling periods using linearised power system model and frequency-domain tools. The assessed time-delays range from 50 *ms* to 1.2 seconds. Sampling periods of 0.01, 0.05, and 0.1 seconds are utilized when designing the discrete-time LQG/LTR controllers.

Table 5.14 lists system performance measures of the closed-loop system controlled by LQG_m for different time-delays and sampling periods in terms of maximum peak of *T*, denoted as M_T, and system bandwidth, denoted as ω_B. For every sampling period, M_T is found to increase for the increasing value of time-delay, while ω_B is decreased when time-delay is increased from 50 *ms* up to 1.5 *s*. This indicates that system performance and robustness are degraded for the increasing communication time-delay. In particular, M_T exceeds 2 *dB* for the time-delay longer than 1 second for all sampling periods. In addition, M_T is increased and ω_B is decreased for the increase of sampling period for any constant time-delay. This finding demonstrates that system performance and robustness are degraded by the increase in the sampling period used when implementing controller, which is in accordance with the results in Chapter 4.

Tables 5.15 and 5.16 list the damping ratio and the frequency of the inter-area electromechanical mode for various time-delays using discrete-time controllers LQG_{d0} and LQG_m, respectively. For each sampling period utilized in designing LQG_{d0}, the damping of inter-area mode is dramatically reduced down to negative value, indicating onset of the closed-loop system's instability, as the time-delay is increased from 50 *ms* to 1.5 *s*, as shown in Table 5.15. On the other hand, the inter-area mode for all time-delays within the delay margin, as well as for different sampling periods, is well-damped using controller LQG_m as shown in Table 5.16. It is also observed that inter-area damping is degraded for the increase in either the time-delay or sampling period. However, such degradation is insignificant and the resulting system performance and robustness are still satisfied when using controller LQG_m.

Table 5.14 System performance measures using LQG_m

Time-delay τ	Sampling Period (second)					
	0.01		0.05		0.1	
	M_T (*dB*)	ω_B (*rad/s*)	M_T (*dB*)	ω_B (*rad/s*)	M_T (*dB*)	ω_B (*rad/s*)
50 *ms*	1.5	5.3	1.5	4.8	1.7	4.3
100 *ms*	1.6	4.9	1.6	4.0	1.7	3.8
250 ms	1.7	4.1	1.8	3.6	1.9	3.1
500 *ms*	1.8	3.5	1.9	2.9	1.9	2.5
800 ms	1.8	3.0	1.9	2.7	2.0	2.0
1 *s*	2.0	2.5	2.2	2.1	2.2	1.6
1.2 *s*	2.6	0.8	2.8	0.6	3.1	0.2
1.5 *s*	2.8	0.4	3.0	0.1	3.2	0.1

Table 5.15 Damping of inter-area mode for time-delays using LQG_{d0}

Time-delay τ	Sampling Period (second)					
	0.01		0.05		0.1	
	$f(Hz)$	$\zeta(\%)$	$f(Hz)$	$\zeta(\%)$	$f(Hz)$	$\zeta(\%)$
50 *ms*	0.53	20.4	0.53	20.1	0.54	19.7
100 *ms*	0.54	19.5	0.55	18.9	0.55	17.3
250 *ms*	0.57	2.5	0.57	1.4	0.58	1.0
500 *ms*	0.54	-12.6	0.56	-14.1	0.57	-16.8
800 *ms*	0.55	-15.7	0.56	-16.8	0.56	-17.2
1 *s*	0.55	-16.6	0.55	-17.7	0.56	-18.8
1.2 *s*	0.54	-18.7	0.54	-19.1	0.54	-20.3
1.5 *s*	0.54	-20.2	0.54	-21.9	0.53	-22.1

Table 5.16 Damping of inter-area mode for time-delays using LQG_m

Time-delay τ	Sampling Period (second)					
	0.01		0.05		0.1	
	$f(Hz)$	$\zeta(\%)$	$f(Hz)$	$\zeta(\%)$	$f(Hz)$	$\zeta(\%)$
50 *ms*	0.55	38.5	0.56	37.2	0.57	35.7
100 *ms*	0.56	38.1	0.56	35.7	0.57	33.2
250 *ms*	0.57	37.5	0.58	33.2	0.59	29.4
500 *ms*	0.59	35.7	0.59	27.9	0.60	22.9
800 *ms*	0.58	34.1	0.59	24.5	0.60	19.4
1 *s*	0.57	33.2	0.58	22.9	0.59	17.8
1.2 *s*	0.56	32.5	0.57	21.5	0.58	16.5
1.5 *s*	0.56	29.8	0.56	19.3	0.58	14.2

5.4.4.3 Various Operating Conditions

Changes in the operating conditions, identical to those used in Section 5.4.2, are utilised to assess the robustness of the discrete-time controller in the presence of the communication time-delays. The sampling period is set equal to 0.01 seconds. Table 5.17 lists the delay margin for various different operating conditions for controller LQG_m compared to controller LQG_{d0} and controller LQG_P^4. For the increase in the

power transfer from Area 1 to Area 2, the delay margin for LQG_{d0} is significantly reduced from 120 *ms* to only 55 *ms*, and the delay margin for LQG_P^4 is reduced from 1.2 seconds to 950 *ms* detailed in Section 5.4. However, in the case of controller LQG_m, the delay margin is insignificantly reduced for the increase of power transfer from 1.4 seconds to 1.0 second, which demonstrates the robustness of the discrete-time controller designed for the nominal operating conditions and incorporating the model for communication time-delays. It is also observed that the delay margin for LQG_m is greater than that for LQG_P^4 for each considered operating condition due to the fact that the time-delay is represented exactly in discrete-time formulation rather than using Pade approximation. This is a very important result that demonstrates the superiority of the controller LQG_m when compared to LQG_P^4 in terms of the closed-loop system robustness to the changing operating conditions and in the presence of communication time-delays. Such superiority is due to the fact that the discrete-time controller design incorporates exact model of the time-delay rather than its rational approximation.

Table 5.18 lists the damping ratio and the frequency of the inter-area mode for different operating conditions and various time-delays when using controller LQG_m. The damping of the inter-area mode is degraded for either the change in operating condition or the increase in the time-delay. However, the inter-area mode is well-damped for various operating conditions and different time-delays when the power system is controlled by LQG_m, which demonstrates its effectiveness and robustness.

Table 5.17 Delay margin for different power transfers for LQG_{d0}, LQG_m, LQG_P^4

Power transfer increase: Area 1 to Area 2	LQG_{d0}	LQG_m	LQG_P^4
Base case	**120 ms**	**1.4 *s***	**1.2 *s***
10%	110 *ms*	1.4 *s*	1.1 *s*
20%	85 *ms*	1.2 *s*	1.1 *s*
30%	70 *ms*	1.1 *s*	1.0 *s*
40%	55 *ms*	1.0 *s*	950 *ms*

Table 5.18 Inter-area mode for time-delays for different power transfers using LQG_m

Time-delay τ	Power transfer from area 1 to area 2									
	Base Case		Increase 10%		Increase 20%		Increase 30%		Increase 40%	
	$f(Hz)$	ζ (%)	$f(Hz)$	ζ (%)	$f(Hz)$	ζ (%)	$f(Hz)$	ζ (%)	$f(Hz)$	ζ (%)
100 *ms*	0.55	38.5	0.55	34.9	0.55	34.4	0.54	33.6	0.54	32.8
200 *ms*	0.56	38.1	0.55	32.4	0.55	31.9	0.55	31.2	0.54	30.5
500 *ms*	0.57	37.5	0.56	27.2	0.56	26.7	0.55	26.2	0.55	25.7
800 *ms*	0.59	35.7	0.57	23.9	0.56	23.5	0.56	23.0	0.55	22.7
1 *s*	0.58	34.1	0.57	22.3	0.56	21.8	0.55	21.5	0.54	21.1
1.2 *s*	0.57	33.2	0.56	20.9	0.55	20.5	0.55	20.2	0.53	19.9

Note that the results in this section were all obtained assuming power system is represented by its linear model. In order to expand on this analysis, non-linear model of the power system is utilised in the next section.

5.4.5 Non-linear Simulation

In this section, the designed discrete-time LQG/LTR controller LQG_m is applied onto the non-linear model of the power system and the resulting performance is compared to that obtained using controller LQG_{d0}, as well as that of using continuous-time controller LQG_P^4 detailed in Section 5.4. A large disturbance, in a form of a self-cleared three-phase fault occurring on bus 5 at simulation time equal to 1 second, is applied onto the power system.

5.4.5.1 *Case 1*: Comparison between LQG_{d0} and LQG_m

Figure 5.13 shows the speed deviation, electrical power output and terminal voltage of each generator using supervisory discrete-time controller LQG_m compared to LQG_{d0} for time-delay $\tau = 120$ *ms*. Note that this is the delay margin for LQG_{d0}, which is clearly shown in Figure 5.13. On the other hand, the discrete-time controller that uses information regarding time-delays, namely LQG_m, maintains the stability with satisfactory response to the applied disturbance. This demonstrates the

effectiveness and the superiority of the designed discrete-time controller LQG_m. Note that the delay margin related to LQG_{d0} is somewhat smaller than that obtained for its continuous-time counterpart in Section 5.4. This is mainly due to the discretisation of the system dynamics.

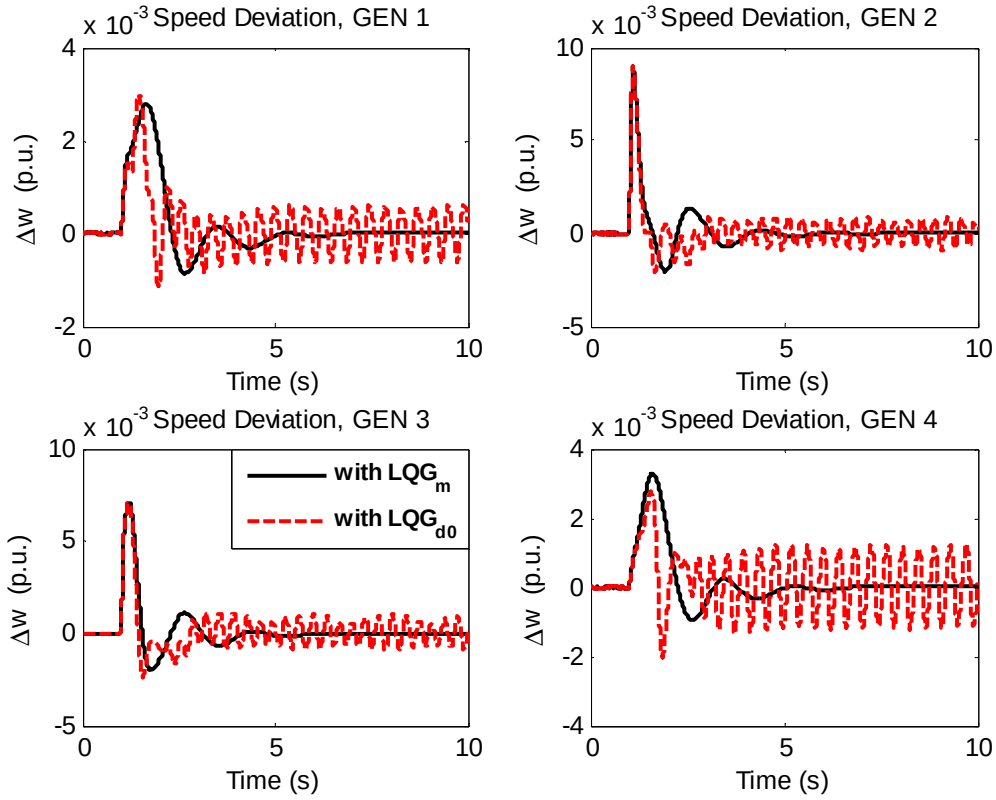

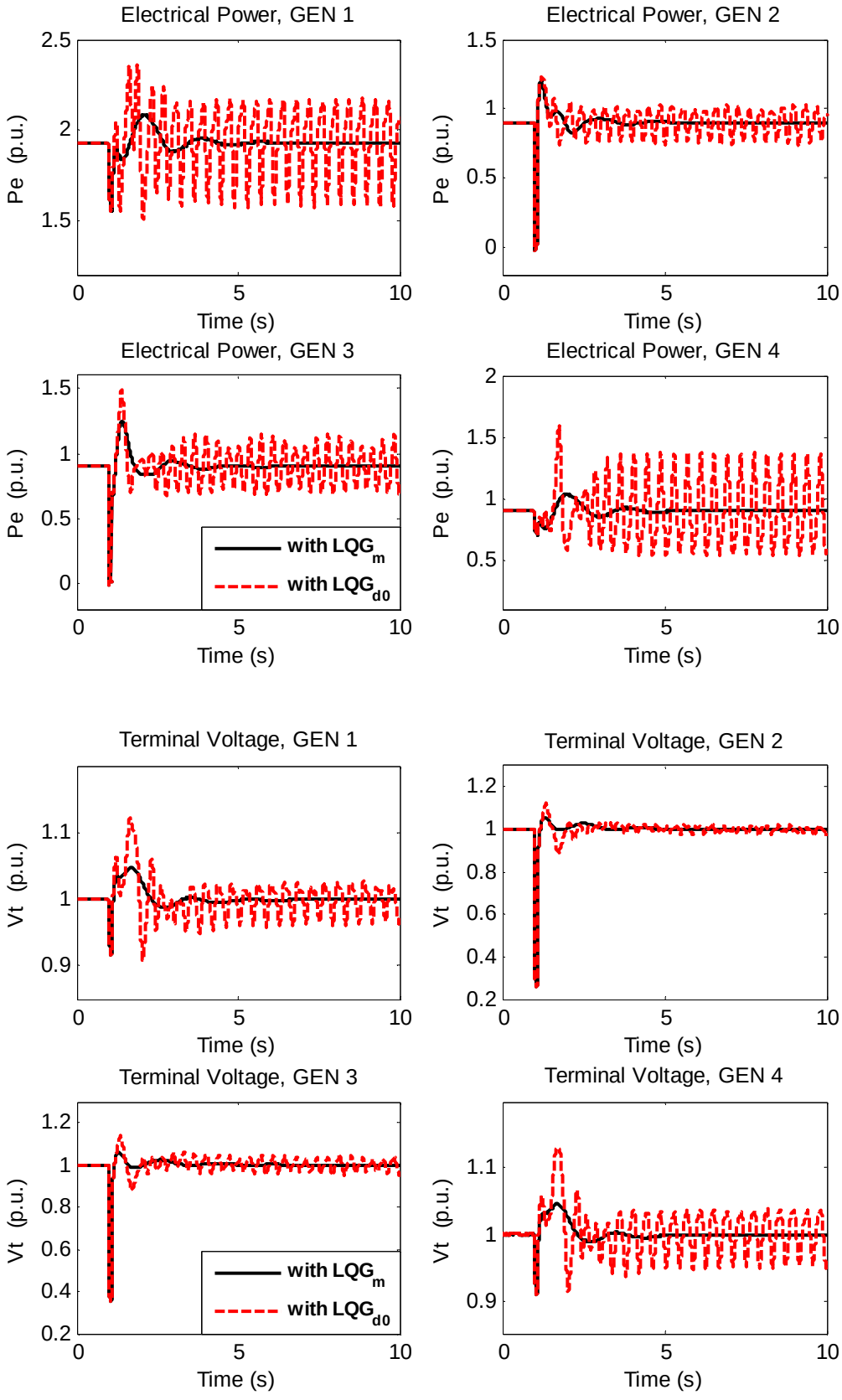

Figure 5.13 System responses using LQG_m and LQG_{d0} for $\tau = 120\,\text{ms}$

5.4.5.2 *Case 2*: Comparison between LQG_m with $T_s = 0.01$ and LQG_m with $T_s = 0.1$

Next, the impact of the sampling period on the performance of the discrete-time controller in the presence of communication time-delays is investigated and the main results are shown in Figure 5.14 and 5.15. These figures show the speed deviation for each generator of the power system controlled by controller LQG_m designed using sampling period $T_s = 0.01$ and $T_s = 0.1$ second in the presence of 500 *ms* and 1 *s* time-delays, respectively, and when subjected to a self-cleared three-phase fault. In the case of 500 *ms* time-delay, the results are shown in Figure 5.14 and indicate that LQG_m with either $T_s = 0.01$ seconds or $T_s = 0.1$ seconds can stabilize the power system when subjected to a large disturbance. It is also observed that the settling time of the response of the power system controlled by LQG_m using $T_s = 0.01$ is shorter than that of using $T_s = 0.1$, which indicates that the use of shorter sampling period results in larger bandwidth and, therefore, faster response, which is somewhat expected. In the case of 1 second time-delay controller LQG_m using for $T_s = 0.1$ seconds sampling period cannot stabilize the power system when subjected to a large disturbance, as shown in Figure 5.15. This result confirms the finding that the delay margin for this controller is equal to 1.0 second. On the other hand, it is clearly shown that the power system can be recovered from the large disturbance when controlled by controller LQG_m using $T_s = 0.01$ second sampling period. Hence, the controller with the faster sampling rate has higher delay margin compared to the controller that utilises longer sampling period.

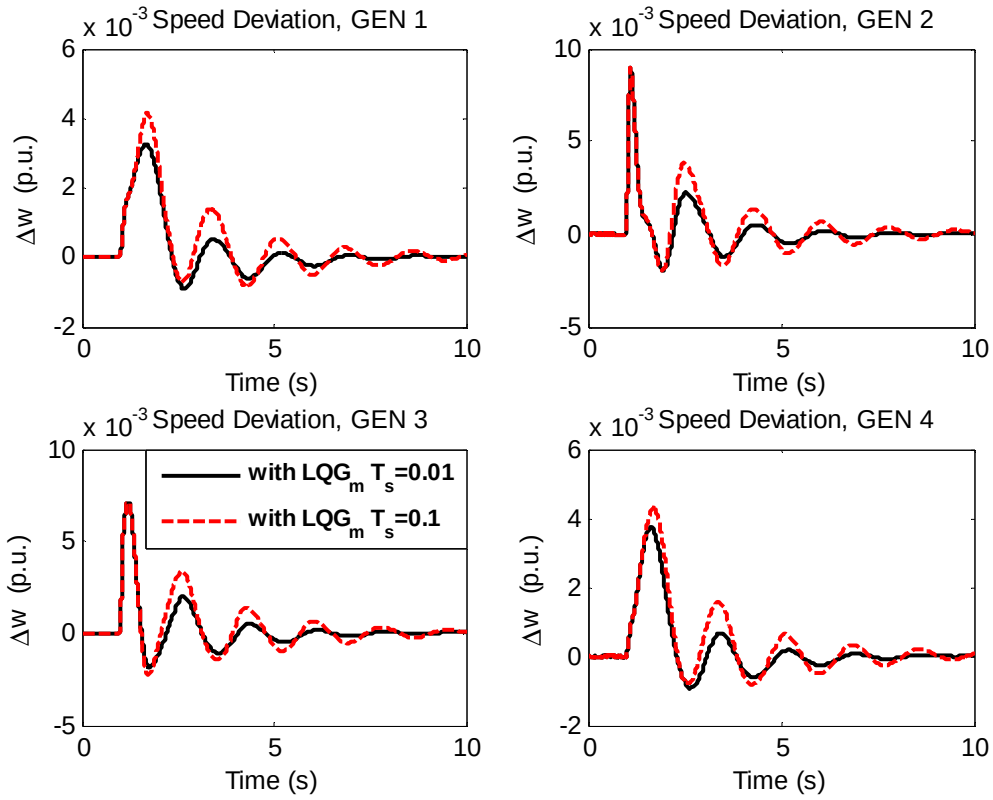

Figure 5.14 System responses using LQG_m for $\tau = 500\,ms$: $T_s = 0.01$ vs. $T_s = 0.1$

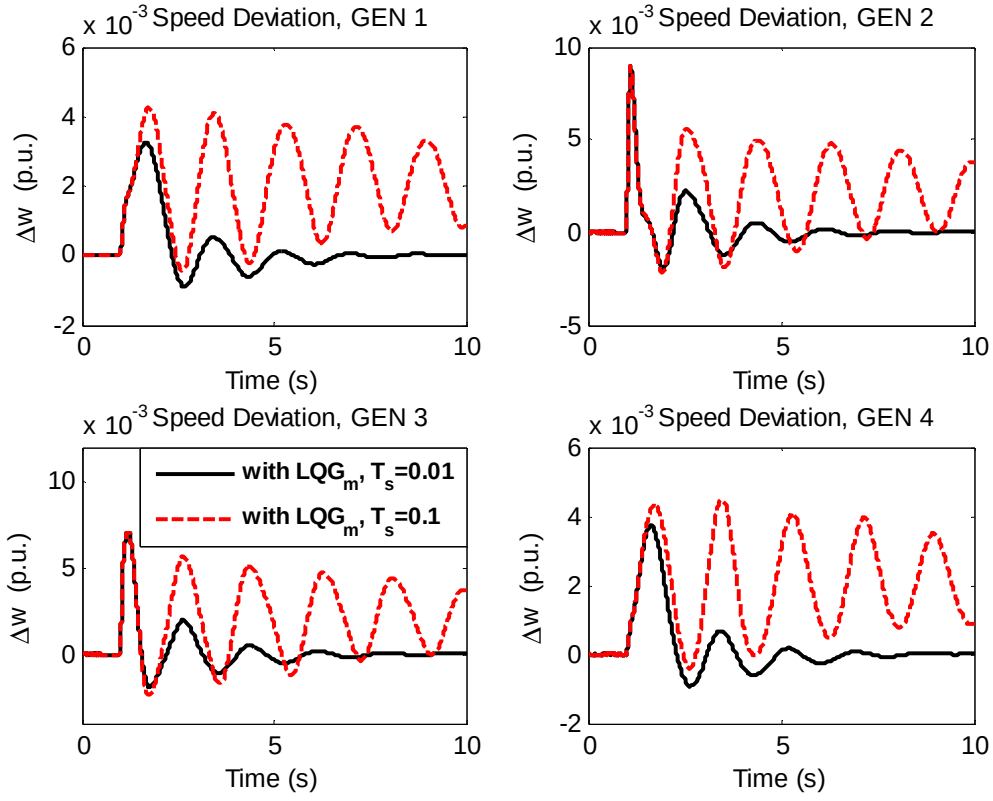

Figure 5.15 System responses using LQG_m for $\tau = 1.1s$: $T_s = 0.01$ vs. $T_s = 0.1$

5.4.5.3 *Case 3*: Comparison between LQG_m with $T_s = 0.01$ and LQG_P^4

Figure 5.16 shows the speed deviation, electrical power output and terminal voltage of each generator obtained when using supervisory discrete-time controller LQG_m using $T_s = 0.01$ seconds and the LQG_P^4 controller for time-delay $\tau = 1.2$ seconds. Note that this is the delay margin for LQG_P^4. The power system controlled by LQG_P^4 could not be recovered from a large disturbance for 1.2 seconds time-delay, which is clearly shown in Figure 5.13. On the other hand, the discrete-time controller LQG_m maintains the stability with satisfactory response to the applied disturbance. This demonstrates the effectiveness and the superiority of the designed discrete-time controller LQG_m due to the fact that the time-delays are represented exactly using discrete-time formulation rather than using rational approximation.

Figure 5.17 shows the speed deviation of each generator of the power system controlled by LQG_m using $T_s = 0.01$ when subjected to a large disturbance for 1.4 seconds time-delay. It is shown that the power system controlled by LQG_P^4 could not be recovered from the large disturbance when the time-delay exceeds the delay margin.

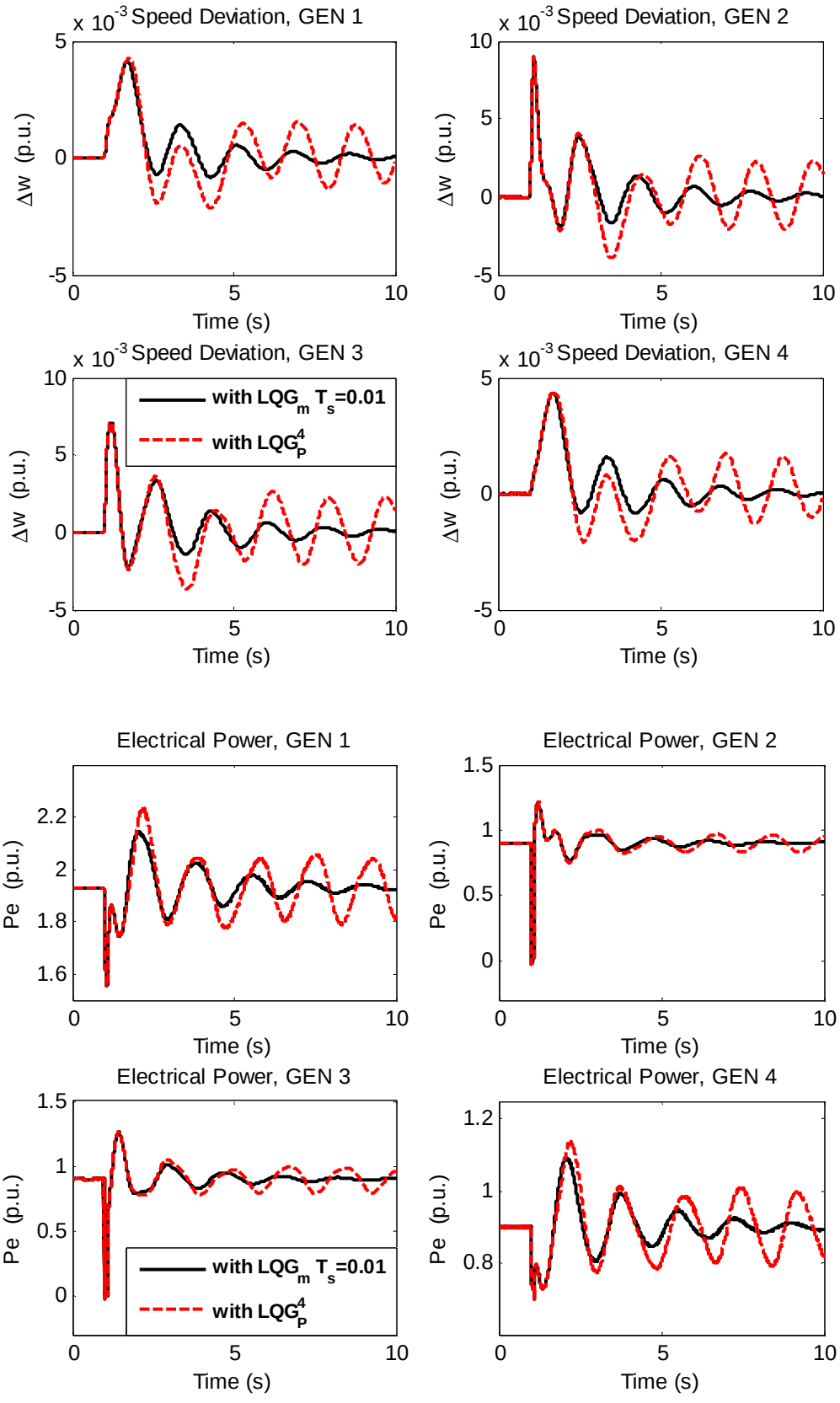
x 10^-3 Speed Deviation, GEN 1
x 10^-3 Speed Deviation, GEN 2
x 10^-3 Speed Deviation, GEN 3
x 10^-3 Speed Deviation, GEN 4
Δw (p.u.)
Time (s)
with LQG_m T_s=0.01
with LQG_P^4
Electrical Power, GEN 1
Electrical Power, GEN 2
Electrical Power, GEN 3
Electrical Power, GEN 4
Pe (p.u.)

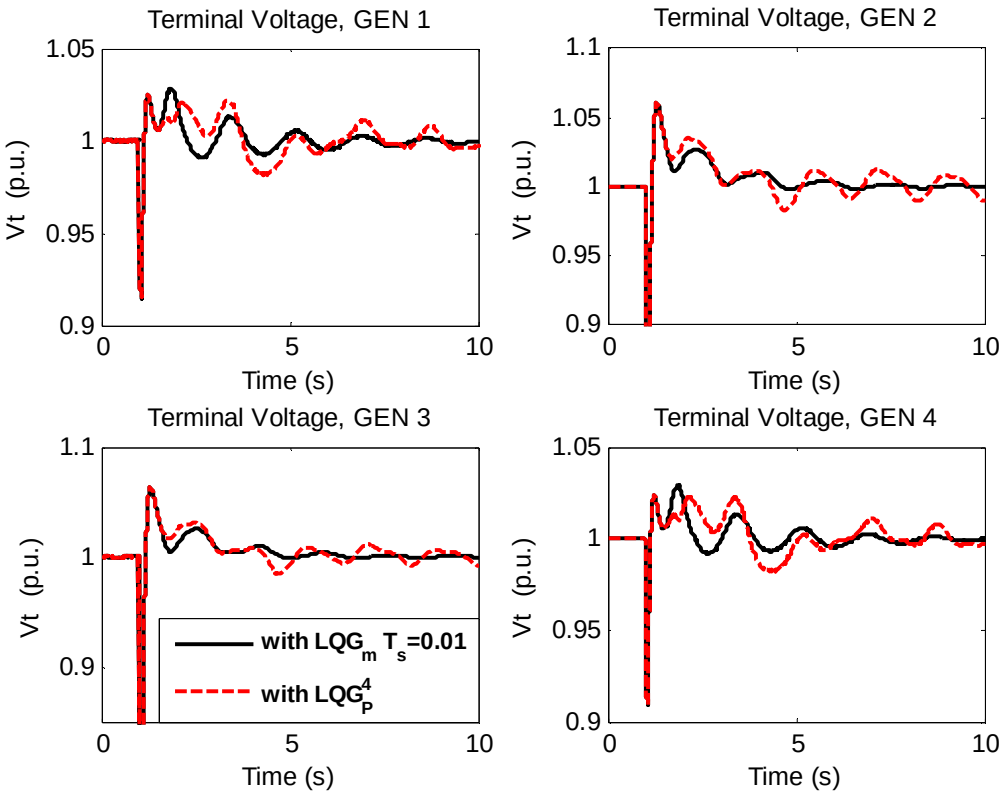

Figure 5.16 System responses using LQG_m in $T_s = 0.01$ and LQG_P^4 for $\tau = 1.2\,s$

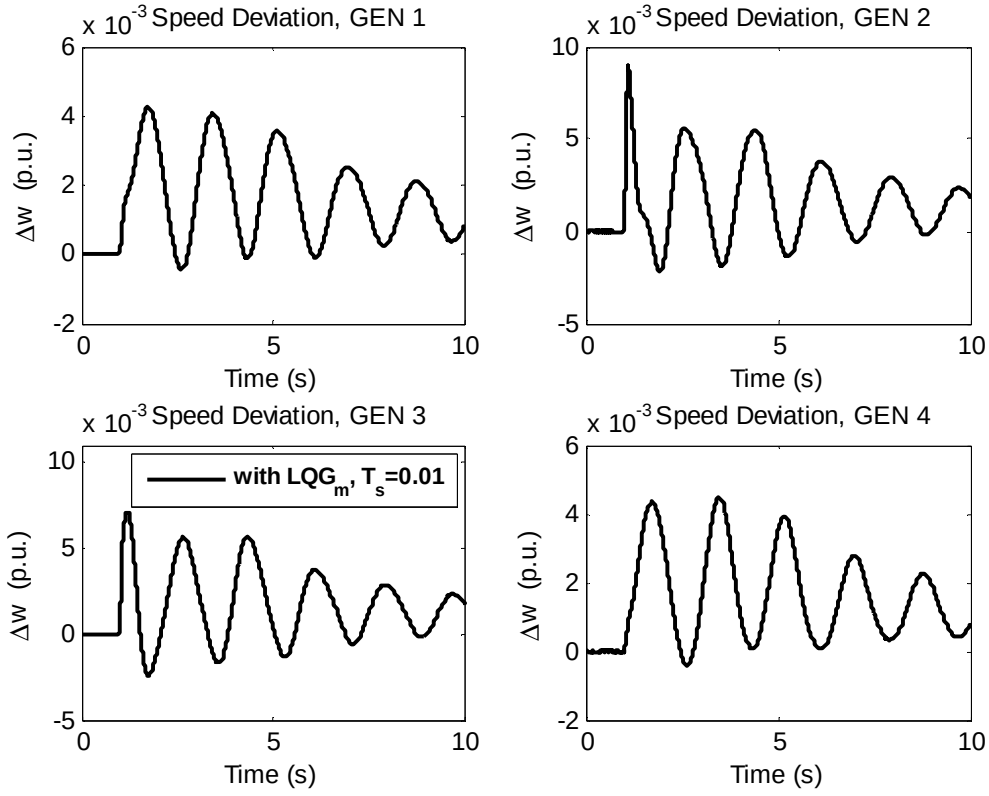

Figure 5.17 System responses using LQG_m in $T_s = 0.01$ for $\tau = 1.4\,s$

5.5 Summary

This chapter focused on the design of the supervisory continuous-time and discrete-time controllers for the power system in the presence of communication time-delays. Continuous-time controllers were designed by firstly representing time-delay in the rational form using Pade Approximation and Bassel-Thomson Approximation. These were then assessed using linear representation of the power system and utilising frequency-domain analysis tools. Also, the continuous-time controllers were compared in the time-domain using non-linear simulation model of the power system. It was clearly demonstrated that the controller utilising Pade approximation achieves much better performance and robustness when compared to that designed using Bassel-Thomson approximation. Order of the time-delay approximation was also varied in order to assess its impact on the performance. The result of this assessment was that the 4^{th} order approximation is the most appropriate for this particular power system application.

Also, discrete-time controller was designed using exact representation of the time-delay rather than resorting to rational approximation. As a result of using exact time-delay model, discrete-time controller was shown to achieve larger time-delay margin when compared to its continuous-time counterpart.

In conclusion, it has been clearly shown that the proposed continuous-time and discrete-time LQG/LTR controllers can tolerate longer time-delays compared with the conventional LQG/LTR controllers designed without any consideration of the communication time-delays. Also, discrete-time control formulation is found to be more appropriate when dealing with communication time-delays because it uses their exact representation rather than rational approximation during controller design. The effectiveness and the robustness of the proposed controllers for various time-delays and different operating conditions were verified using both small signal and large signal disturbances.

Chapter 6

Supervisory Controller Development using Extended Kalman Filter for System with Unknown Time-Delay

6.1 Introduction

In the previous chapter, the continuous-time and discrete-time LQG/LTR controllers were designed assuming a presence of a known and constant communication time-delay existing between them and the power system. However, this assumption may be highly inappropriate in circumstances in which they are unknown and/or time-varying. Therefore, in this chapter the Extended Kalman Filter (EKF) is designed and used to continuously estimate the time-delay so that it can be used to update the prediction model, which is utilised by the supervisory LQG/LTR controller. Both the simple single-input single-output system and the nonlinear power system model are used to demonstrate the benefits of the proposed scheme. Also, the proposed control scheme is compared with the conventional discrete-time LQG controller that assumes time-delay to be non-existent in order to demonstrate its effectiveness and applicability to multi-machine power systems. Effectiveness and performance of the closed-loop system controlled by supervisory LQG/LTR coupled with EKF filter is verified using both the small-signal and large-signal stability studies involving the non-linear power system model.

6.2 Estimation of Unknown Time-Delay

It was shown in Chapter 5 that an effective way to incorporate time-delay into a standard transfer function is to represent it in the rational form using the Pade approximation of the appropriate order. In this form the actual value of the time-delay appears as a linear model parameter. As a result, the Extended Kalman Filter can be used to estimate this parameter value so that it can be incorporated into the prediction model used by the supervisory wide-area controller.

6.2.1 Augmented Model

Using Pade approximation (5.1), it has been shown that the augmented model of the system with the constant time-delay can be represented by (5.6). Therefore, the time-delay can be represented as a parameter that is assumed to linearly affect the dynamics of the process. In order to be able to estimate this parameter by using Extended Kalman Filter, auxiliary state of the state-space model is created by making the substation $x_e = 1/\tau$ where τ represents unknown time-delay for the open-loop system model specified in (5.6). Then the new augmented system model containing auxiliary state variable can be defined as follows:

$$\begin{aligned} \dot{\bar{x}} &= \bar{A}\bar{x} + \bar{B}u \\ y &= \bar{C}\bar{x} + \bar{D}u \end{aligned} \tag{6.1a}$$

where $\bar{x}(t) = \begin{bmatrix} x^T(t) & x_d^T(t) & x_e^T(t) \end{bmatrix}^T$. The structure of the state-space model matrices in (6.1a) is given as:

$$\begin{aligned} \begin{bmatrix} \dot{x}(t) \\ \dot{x}_d(t) \\ \dot{x}_e(t) \end{bmatrix} &= \begin{bmatrix} A & BC_d & 0 \\ 0 & A_d & 0 \\ 0 & 0 & 0 \end{bmatrix} \begin{bmatrix} x(t) \\ x_d(t) \\ x_e(t) \end{bmatrix} + \begin{bmatrix} BD_d \\ B_d \\ 0 \end{bmatrix} u(t) \\ y(t) &= \begin{bmatrix} C & DC_d & 0 \end{bmatrix} \begin{bmatrix} x(t) \\ x_d(t) \\ x_e(t) \end{bmatrix} + DD_d u(t) \end{aligned} \tag{6.1b}$$

By incorporating the state space model for the time-delay, given in (5.5), into (6.1b), the state-space model given in (6.1b) is a function of the time-delay τ. Note that the state-space model matrices $\bar{A}$ and $\bar{B}$ are the functions of $\bar{x}$ because A_d and B_d depend on the value of $x_e(t)$. Therefore the model expressed in (6.1) is non-linear.

It is important to note that the number of state variables for the system given in (6.1) will be higher than that for the original system defined in (5.6). In particular, if for a given system the number of the plant state, input and output variables is equal to *n*, *m* and *r* respectively, then, assuming the *k*-th order Pade approximation is used, the dimension of x_d is $(k \cdot m) \cdot 1$. Subsequently, the dimension of $\bar{x}$ is $(n + k \cdot m + 1) \cdot 1$. If, however, time-delay is assumed to be the same for each channel, then only one auxiliary state variable is required. In this chapter it is assumed that the time-delays are all equal to each other so dimensionality of $\bar{x}$ is $(n + k \cdot m + 1) \cdot 1$. Such assumption is used to demonstrate the benefit of the proposed approach. It is, however, expected that its generalisation to the case with different time-delays present in different channels can be easily accomplished at the expense of increased computational burden.

Discretisation

The sampling procedure described in Chapter 4 and taken from [95] is applied in order to discretise the continuous-time augmented model given in (6.1). The resulting discrete-time model is provided in (6.2):

$$\begin{aligned} \bar{x}(k+1) &= \bar{\Phi}(\bar{x})\bar{x}(k) + \bar{\Gamma}(\bar{x})u(k) \\ y(k) &= \bar{C}\bar{x}(k) + \bar{D}u(k) \end{aligned} \tag{6.2a}$$

$$\begin{aligned} \bar{\Phi} &= e^{\bar{A}T_s} = I + \bar{A}\Psi \\ \bar{\Gamma} &= \int_0^{T_s} e^{\bar{A}s} ds \bar{B} = \Psi \bar{B} \end{aligned} \tag{6.2b}$$

Where the structure of the state vector is the same as that of the continuous-time model and is given as $\bar{x}(k) = \begin{bmatrix} x^T(k) & x_d^T(k) & x_e^T(k) \end{bmatrix}^T$, T_s is the sampling interval and the state transition matrix is given as:

$$\bar{\Psi} = \int_0^{T_s} e^{\bar{A}s} ds = IT_s + \frac{\bar{A}T_s^2}{2!} + \frac{\bar{A}^2 T_s^3}{3!} + \cdots + \frac{\bar{A}^i T_s^{i+1}}{(i+1)!} + \cdots$$

Note that both $\bar{\Phi}$ and $\bar{\Gamma}$ depend on $\bar{x}$, hence model given in (6.2) is non-linear. This is due to the fact that $\bar{A}$ and $\bar{B}$ are non-linear functions of $x_e(t)$, which represents the value of the time-delay.

6.2.2 Estimation of Time-Delay using Extended Kalman Filter

In order to estimate the state vector of the non-linear model (6.2), the Extended Kalman Filter (EKF) is utilised. EKF is the well-known recursive algorithm used to estimate states for the nonlinear systems. For the nonlinear system model, a linearisation procedure is usually performed in order to get an approximate linear representation. The EKF can then be used to estimate the system states by applying the standard Kalman Filter algorithm on this approximated linear model [96].

The non-linear model (6.2) with the standard exogenous inputs *w* and *v*, which denote process disturbances and measurement noise respectively, is represented as

$$\begin{aligned} \bar{x}(k+1) &= f(\bar{x}(k), u(k)) + w \\ y(k) &= h(\bar{x}(k), u(k)) + v \end{aligned} \tag{6.3}$$

where $\bar{x}(k) = \begin{bmatrix} x^T(k) & x_d^T(k) & x_e^T(k) \end{bmatrix}^T$, *w* and *v* represent the process disturbances and the measurement noise, respectively, as defined in (3.5). Functions $f(\cdot)$ and $h(\cdot)$ depict non-linear dynamics of the system. Let $F(k), H(k)$ be the Jacobian matrices corresponding to $f(\cdot)$ and $h(\cdot)$, respectively. They are formally defined as:

$$\begin{aligned} F_{\bar{x}}(k) &= \left.\frac{\partial f(\bar{x}(k), u)}{\partial \bar{x}(k)}\right|_{\hat{\bar{x}}(k), u}, \qquad F_u(k) = \left.\frac{\partial f(\bar{x}(k), u)}{\partial u}\right|_{\hat{\bar{x}}(k), u}, \\ H_{\bar{x}}(k) &= \left.\frac{\partial H(\bar{x}(k))}{\partial \bar{x}}\right|_{\hat{\bar{x}}(k), u}, \qquad H_u(k) = \left.\frac{\partial H(\bar{x}(k))}{\partial u}\right|_{\hat{\bar{x}}(k), u}. \end{aligned} \tag{6.4}$$

The discrete extended Kalman Filter algorithm is performed by recursively executing the following four steps.

Step 1 – Initialization

Initialize $P(0|0)$ and $\hat{\bar{x}}(0|0) = \left[\hat{x}(0|0) \quad \hat{x}_d(0|0) \quad \hat{x}_e(0|0)\right]^T$. P is defined as the error covariance of states $\bar{x}$.

Step 2 – Prediction

$$\hat{\bar{x}}(k+1|k) = f(\hat{\bar{x}}(k|k), u) \tag{6.5}$$

$$\hat{y}(k) = h(\hat{\bar{x}}(k|k)) \tag{6.6}$$

$$P(k+1|k) = F_{\bar{x}}(k)P(k|k)F_{\bar{x}}(k)^T + F_u(k)W_2F_u(k)^T + W_1 \tag{6.7}$$

Step 3 – Measurement Update

$$L(k+1) = P(k+1|k)H_{\bar{x}}{}^T(H_{\bar{x}}P(k+1|k)H_{\bar{x}}{}^T + V)^{-1} \tag{6.8}$$

$$P(k+1|k+1) = (I - L(k+1)H_{\bar{x}})P(k+1|k) \tag{6.9}$$

$$\hat{\bar{x}}(k+1|k+1) = f(\hat{\bar{x}}(k+1|k), u) + L(k+1)(y(k) - \hat{y}(k)) \tag{6.10}$$

Step 4 – Repeat

Increment the time and go back to Step 2.

Here, W_1 is the covariance matrix of the system noise, W_2 is the covariance matrix of the input noise and V is the covariance matrix of the output noise. W_1 and W_2 are nonnegative definite symmetric matrices while V is a positive definite symmetric matrix. $L(k)$ is the Kalman Filter gain at time step k and $\hat{\bar{x}}(k|k)$ is the estimate of $\bar{x}(k|k)$ at time step k.

The algorithm provided above consists of two main steps: prediction and measurement update. During the prediction step, the predicted state vector $\hat{\bar{x}}(k+1|k)$ and the state error covariance matrix $P(k+1|k)$ are computed. During the measurement update step, estimated state vector $\hat{\bar{x}}(k+1|k+1)$ is obtained as the sum of the predicted state vector $\hat{\bar{x}}(k+1|k)$ and the correction term. Also, at the measurement update step the estimated state error covariance matrix $P(k+1|k+1)$ is calculated based on Kalman filter gain L. The schematic representation of the extended Kalman filter algorithm applied on the system with input time-delay is showed in Figure 6.1.

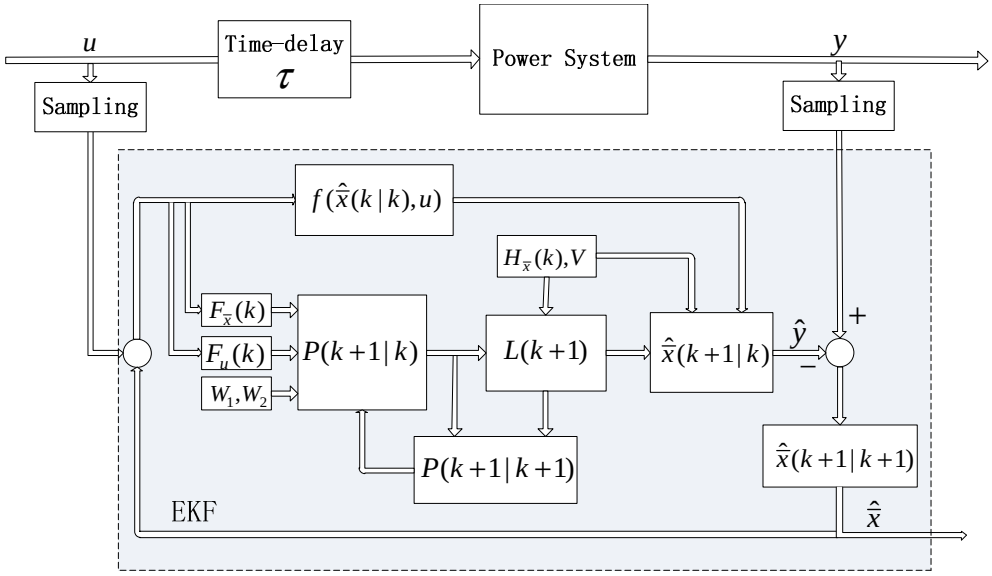

Figure 6.1 Schematic Representation of Extended Kalman Filter

6.2.3 EKF for First Order Pade Approximation

In order to clearly illustrate the proposed method the time-delay is firstly represented by the 1st order Pade approximation:

$$e^{-s\tau} \approx \frac{1-0.5\tau s}{1+0.5\tau s} \tag{6.11}$$

The state-space model representing time-delay model (5.5) is given as: $A_d = diag\{a_\tau, a_\tau, ..., a_\tau\}$, $B_d = diag\{b_\tau, b_\tau, ..., b_\tau\}$, $C_d = diag\{c_\tau, c_\tau, ..., c_\tau\}$, and $D_d = diag\{d_\tau, d_\tau, ..., d_\tau\}$ with

$$\begin{aligned} a_\tau &= -\frac{2}{\tau},\ b_\tau = \frac{2}{\tau}, \\ c_\tau &= 2, \quad d_\tau = -1. \end{aligned} \tag{6.12}$$

Substituting (6.6) into (6.1) results in the following augmented state-space model:

$$\begin{aligned} \begin{bmatrix} \dot{x}(t) \\ \dot{x}_d(t) \\ \dot{x}_e(t) \end{bmatrix} &= \begin{bmatrix} A & 2B & 0 \\ 0 & -2x_e & 0 \\ 0 & 0 & 0 \end{bmatrix} \begin{bmatrix} x(t) \\ x_d(t) \\ x_e(t) \end{bmatrix} + \begin{bmatrix} -B \\ 2x_e \\ 0 \end{bmatrix} u(t) \\ y(t) &= \begin{bmatrix} C & 0 & 0 \end{bmatrix} \begin{bmatrix} x(t) \\ x_d(t) \\ x_e(t) \end{bmatrix} - Du(t) \end{aligned} \tag{6.13}$$

The equivalent discrete-time model, introduced in (6.2), for 1st order Pade approximation is then given as follows:

$$\begin{bmatrix} x(k+1) \\ x_d(k+1) \\ x_e(k+1) \end{bmatrix} = \begin{bmatrix} I + T_s A & 2T_s B & 0 \\ 0 & I - 2T_s x_e(k) & 0 \\ 0 & 0 & I \end{bmatrix} \begin{bmatrix} x(k) \\ x_d(k) \\ x_e(k) \end{bmatrix} + \begin{bmatrix} -B(T_s + \frac{T_s^2 A}{2}) + 2T_s^2 x_e(k) B \\ 2x_e(k)(T_s - T_s^2 x_e(k)) \\ 0 \end{bmatrix} u(k) \tag{6.14}$$

$$y(k) = \begin{bmatrix} C & 0 & 0 \end{bmatrix} \begin{bmatrix} x(k) \\ x_d(k) \\ x_e(k) \end{bmatrix} - Du(k)$$

where $\bar{x}(k) = \begin{bmatrix} x^T(k) & x_d^T(k) & x_e^T(k) \end{bmatrix}^T$.

Then $f(\cdot)$ and $h(\cdot)$, defined in (6.3), and $F(k)$ and $H(k)$, defined in (6.4), can be represented using (6.15) and (6.16), respectively.

$$f(k) = \begin{bmatrix} (I + T_s A)x(k) + T_s B x_d(k) + \frac{T_s^2}{2} B x_e(k) u(k) \\ (1 - T_s x_e(k)) x_d(k) + (T_s - \frac{T_s^2}{2} x_e(k)) x_e(k) u(k) \\ x_e(k) \end{bmatrix}, \quad h(k) = Cx(k). \tag{6.15}$$

$$F_{\bar{x}}(k) = \left. \frac{\partial f(\bar{x}(k), u)}{\partial \bar{x}(k)} \right|_{\hat{\bar{x}}(k), u}$$

$$F_{\bar{x}}(k) = \begin{bmatrix} I + T_s A & T_s B & \frac{T_s^2}{2} B u(k) \\ 0 & 1 - T_s x_e(k) & -T_s x_d(k) + (T_s - T_s^2 x_e(k)) u(k) \\ 0 & 0 & I \end{bmatrix} \tag{6.16a}$$

$$F_u(k) = \left. \frac{\partial f(\bar{x}(k), u)}{\partial u} \right|_{\hat{\bar{x}}(k), u} = \begin{bmatrix} \frac{T_s^2}{2} B x_e(k) \\ (T_s - \frac{T_s^2}{2} x_e(k)) x_e(k) \\ 0 \end{bmatrix} \tag{6.16b}$$

$$H_{\bar{x}}(k) = \left.\frac{\partial H(\bar{x}(k))}{\partial \bar{x}}\right|_{\hat{\bar{x}}(k)} = \begin{bmatrix} C & 0 & 0 \end{bmatrix} \tag{6.16c}$$

6.2.4 EKF for Second Order Pade Approximation

Time-delay can also be represented by the 2nd order Pade approximation as follows:

$$e^{-s\tau} \approx \frac{\frac{1}{12}\tau^2 s^2 - \frac{1}{2}\tau s + 1}{\frac{1}{12}\tau^2 s^2 + \frac{1}{2}\tau s + 1} \tag{6.17}$$

The state space matrices of the approximated time-delay are derived as follows:

$$\begin{aligned} a_\tau &= \begin{bmatrix} 0 & 1 \\ -\frac{12}{\tau^2} & -\frac{6}{\tau} \end{bmatrix}, \quad b_\tau = \begin{bmatrix} 0 \\ \frac{12}{\tau^2} \end{bmatrix}, \\ c_\tau &= \begin{bmatrix} 0 & -\tau \end{bmatrix}, \qquad d_\tau = 1. \end{aligned} \tag{6.18}$$

The augmented state variables are then $x_d = \begin{bmatrix} x_{d1}^T & x_{d2}^T \end{bmatrix}^T$. By substituting (6.18) into (6.1) and introducing the auxiliary state x_e, the overall augmented model can be represented as:

$$\begin{aligned} \begin{bmatrix} \dot{x}(t) \\ \dot{x}_{d1}(t) \\ \dot{x}_{d2}(t) \\ \dot{x}_e(t) \end{bmatrix} &= \begin{bmatrix} A & 0 & -Bx_e^{-1} & 0 \\ 0 & 0 & 1 & 0 \\ 0 & -12x_e^2 & -6x_e & 0 \\ 0 & 0 & 0 & 0 \end{bmatrix} \begin{bmatrix} x(t) \\ x_{d1}(t) \\ x_{d2}(t) \\ x_e(t) \end{bmatrix} + \begin{bmatrix} B \\ 0 \\ 12x_e^2 \\ 0 \end{bmatrix} u(t) \\ y(t) &= \begin{bmatrix} C & 0 & -Dx_e^{-1} & 0 \end{bmatrix} \begin{bmatrix} x(t) \\ x_{d1}(t) \\ x_{d2}(t) \\ x_e(t) \end{bmatrix} + Du(t) \end{aligned} \tag{6.19}$$

where $\bar{x}(k) = \begin{bmatrix} x^T(k) & x_{d1}^T(k) & x_{d2}^T(k) & x_e^T(k) \end{bmatrix}^T$.

Following discretisation, the system model in (6.2) incorporating 2nd order Pade approximation is given as follows:

$$\begin{bmatrix} x(k+1) \\ x_{d1}(k+1) \\ x_{d2}(k+1) \\ x_e(k+1) \end{bmatrix} = \begin{bmatrix} I+T_sA & 0 & -T_sx_e^{-1}B & 0 \\ 0 & I & T_s & 0 \\ 0 & -12T_sx_e^2 & I-6T_sx_e & 0 \\ 0 & 0 & 0 & I \end{bmatrix} \begin{bmatrix} x(k) \\ x_{d1}(k) \\ x_{d2}(k) \\ x_e(k) \end{bmatrix}$$

$$+T_s \begin{bmatrix} (I+\frac{T_sA}{2})B-6T_sx_eB \\ 6T_sx_e^2 \\ 12x_e^2(I-3T_sx_e) \\ 0 \end{bmatrix} u(k) \tag{6.20}$$

$$y(k) = \begin{bmatrix} C & 0 & -Dx_e^{-1} & 0 \end{bmatrix} \begin{bmatrix} x(k) \\ x_{d1}(k) \\ x_{d2}(k) \\ x_e(k) \end{bmatrix} + Du(k)$$

Now, $f(\cdot)$ and $h(\cdot)$ in (6.3) and $F(k)$ and $H(k)$ in (6.4) can be represented using (6.21) and (6.22) respectively:

$$f = \begin{bmatrix} (I+T_sA)x(k) - T_sBx_{d2}(k)x_e^{-1}(k) + T_s[I+\frac{T_s}{2}A-6T_sx_e(k)]Bu(k) \\ x_{d1}(k) + T_sx_{d2}(k) + 6T_s^2x_e^2(k)u(k) \\ -12T_sx_e^2(k)x_{d1}(k) + (I-6T_sx_e(k))x_{d2}(k) + 12T_sx_e^2(k)(I-3T_sx_e(k)u(k) \\ x_e(k) \end{bmatrix} \tag{6.21}$$

$$h = Cx(k)$$

$$F_{\bar{x}}(k) = \begin{bmatrix} I+T_sA & 0 & -T_sx_e^{-1}B & T_sx_{d2}x_e^{-2}B - 6T_s^2Bu \\ 0 & I & T_s & 12T_s^2x_eu \\ 0 & -12T_sx_e^2 & I-6T_sx_e & -24T_sx_{d1}x_e - 6T_sx_{d2} + (24T_sx_e - 108T_s^2x_e^2)u \\ 0 & 0 & 0 & I \end{bmatrix} \tag{6.22a}$$

$$F_u(k) = \begin{bmatrix} T_s[I+\frac{T_s}{2}A-6T_sx_e]B \\ 6T_s^2x_e^2 \\ 12T_sx_e^2(I-3T_sx_e) \\ 0 \end{bmatrix} \tag{6.22b}$$

$$H_{\bar{x}}(k) = \begin{bmatrix} C & 0 & 0 & 0 \end{bmatrix} \tag{6.22c}$$

6.3 Numerical Example I

6.3.1 First Order Pade Approximation

The estimation by EKF discussed in the previous section will now be illustrated using a numerical examples. First of all, a second order SISO system is considered with the transfer function expressed as:

$$g_1(s) = \frac{1}{s(10s+1)} \tag{6.23}$$

The state space matrices of this system are given as:

$$\begin{aligned} A &= \begin{bmatrix} -0.1 & 0 \\ 1 & 0 \end{bmatrix}, \quad B = \begin{bmatrix} 1 \\ 0 \end{bmatrix}, \\ C &= \begin{bmatrix} 0 & 0.1 \end{bmatrix}, \qquad D = 0. \end{aligned} \tag{6.24}$$

Time-delay, τ, is approximated by 1st order Pade approximation given in (6.5). The actual time-delay applied is $\tau = 1$ second. The sampling interval of the simulation is set to be $T_s = 0.01$ seconds. The input applied is the random number signal. The weightings $W = diag\{W_1, W_2\}$ and V are chosen to be the following:

$$W_1 = diag\{w_{11}, w_{22}, w_{33}\} = diag\left\{10^{-5} I_{2\times 2}, 10^{-2}, 1\right\}, \; W_2 = 1, \; V = 10^{-4}. \tag{6.25}$$

where W_1 is the model error covariance matrix, W_2 is the input noise covariance matrix, and V is the output noise covariance matrix. The estimated $\hat{x}_e$ is then obtained by applying EKF procedure in order to estimate the time-delay τ, which is given by $\hat{\tau} = 1/\hat{x}_e$.

A. Investigating Impact of Different Initial Conditions

The initial realization of $P(0|0)$, which is the error covariance of states $\bar{x}$, is chosen to be the identity matrix. The initial values of the estimated state vector $\hat{\bar{x}}(0|0) = \left[\hat{x}^T(0|0) \quad \hat{x}_d^T(0|0) \quad \hat{x}_e^T(0|0)\right]^T$ can be chosen arbitrarily. In this experiment $\hat{x}(0|0)$ and $\hat{x}_d(0|0)$ are set to be equal to zero while the initial estimate of the time-delay, i.e. $\hat{x}_e(0|0)$, was varied in order to assess its impact on the

performance of the proposed scheme. Figure 6.2 shows the estimated time-delay $\hat{\tau}$ for four different choices of $\hat{x}_e(0|0)$. It is observed in the figure that for each of the four initial values of $\hat{\tau}$, the estimated time-delay converges to the true value of $\tau = 1$. Interestingly, convergence is observed to be much faster for those cases for which the initial estimate of the time-delay is higher than the true value. This phenomenon will be considered in the future research work expected to continue following PhD thesis submission.

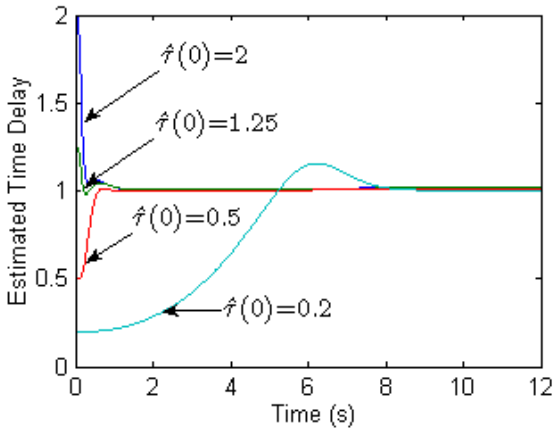

Figure 6.2 Estimated time-delay using EKF for different initial conditions

B. Investigating Impact of Different Weighting Functions

In order to investigate the impact of different weighting functions, $\hat{x}_e(0|0)$ is set to be equal to 0.5, w_{11}, w_{22}, W_2 and V are set according to (6.19). Time-delay estimation error is defined as the difference between the estimated time-delay and the actual time-delay, that is $\hat{\tau} - \tau$. Figure 6.3(a) shows the estimation error for different weightings on $\hat{x}_e$, namely $w_{33} = 10^{-2}, 10^{-1}, 1, 10, 10^2$. It is observed in Figure 6.3(a) that larger values of w_{33} result in more oscillatory response of the estimation error. On the other hand, the estimation error for small value of w_{33} is less oscillatory but with a steady state error.

The results have also shown that the estimation is not largely affected by the changes in the weighting W_2. On the other hand, the changes in the weightings w_{11}, w_{22} and V do have significant effect on the estimation. This is demonstrated in Figure 6.3(b),

which plots the estimation error for different values of w_{11}, w_{22} and V while setting $w_{33}=1$. In particular, it can be observed that the increase in w_{11}, w_{22} and V results in the positive estimation bias, i.e. estimate is higher than the true value of the time-delay.

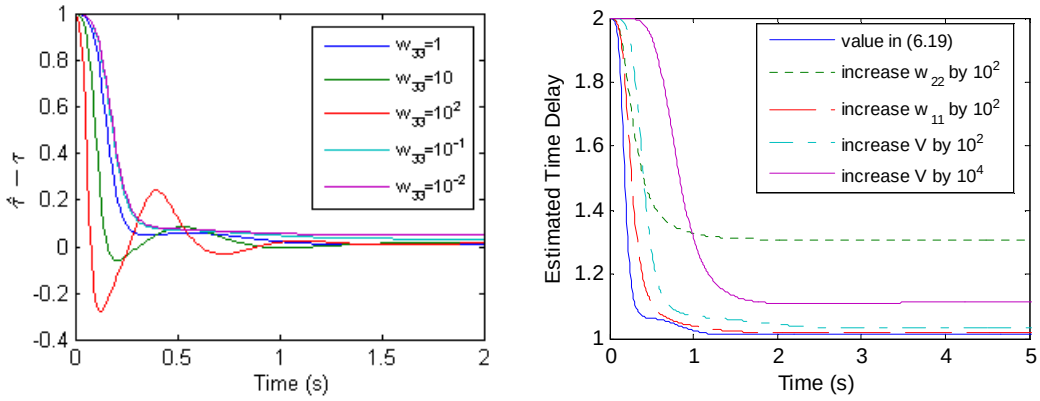

(a) (b)

Figure 6.3 Estimation errors for different EKF cost function weightings

6.3.2 Second Order Pade Approximation

Using the numerical example system specified in (6.17) and (6.18), the second order Pade approximation (6.11) is applied in this section. The actual time-delay applied is kept at $\tau=1$ second. The sampling interval is kept at Ts=0.01 seconds while the input signal is the same as that used in Section 6.3.2. The weightings specified in (6.25) are applied with $W_2=\begin{bmatrix}1 & 0\\ 0 & 1\end{bmatrix}$ due to the fact that the second order Pade approximation is used for the time-delay.

The initial realization of $P(0|0)$ is set to be identity matrix. The estimated state vector is represented by $\hat{\bar{x}}(k)=\begin{bmatrix}\hat{x}^T(k) & \hat{x}_{d1}^T(k) & \hat{x}_{d2}^T(k) & \hat{x}_e^T(k)\end{bmatrix}^T$ with the initial conditions of the estimated state vector set as: $\hat{x}(0|0)=0$, $\hat{x}_{d1}(0|0)=0$, and $\hat{x}_{d2}(0|0)=0$, $\hat{x}_e(0|0)$ = 0.5. Figure 6.4 shows the time-delay estimation error by using first order Pade approximation and the second order Pade approximation. It is observed in Figure 6.4 that the convergence of the estimation using 2nd order Pade approximation is much faster and free of steady state error. Therefore, when utilising

EKF to estimate time-delay, 2nd order Pade approximation is to be preferred when compared to the 1st order Pade approximation.

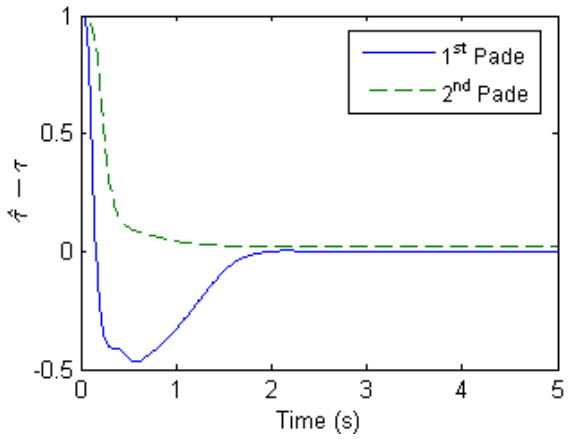

Figure 6.4 Time-delay estimation error for 1st and 2nd order Pade Approximation

6.4 Modified Discrete-Time LQG

The supervisory discrete-time LQG controller is designed in conjunction with the EKF estimator, discussed in previous sections of this chapter, in order to improve the robustness of the wide-area control scheme when dealing with the inevitable presence of communication delays. The main difference of the proposed LQG controller, when compared to the conventional LQG, is that the estimated states are obtained by using the EKF filter instead of the standard linear Kalman Filter. The proposed approach is named as modified discrete-time LQG (MDLQG) approach. The discrete-time LQG is designed initially assuming that there is no time-delay, until the estimated value of time-delay is provided by EKF. The estimated time-delay is then applied to update the proposed discrete-time LQG procedure detailed in Section 5.5 [97]. Figure 6.5 shows the configuration of the modified discrete-time LQG control algorithm.

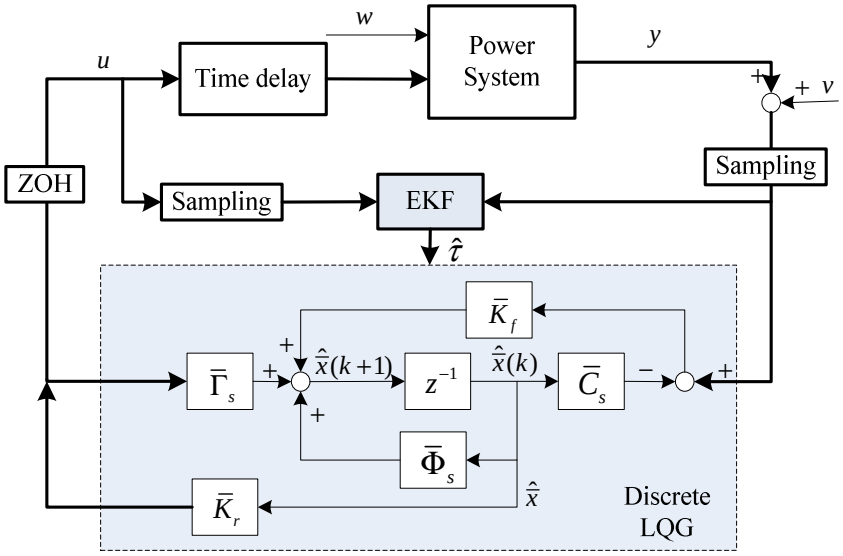

Figure 6.5 Configuration of MDLQG

As described in the previous sections, the estimation of the unknown time-delay is achieved using the Extended Kalman Filter based on the discrete-time augmented model specified in (6.2). Also, the proposed discrete-time LQG controller is designed using the augmented model of (6.2) with the process and measurement noise. The state-space representation of the model considered during the synthesis is given as follows:

$$\begin{aligned} \bar{x}_s(k+1) &= \bar{\Phi}_s \bar{x}_s(k) + \bar{\Gamma}_s u(k) + w \\ y(k) &= \bar{C}_s \bar{x}_s(k) + \bar{D}_s u(k) + v \end{aligned} \tag{6.26}$$

where $\bar{x}_s(k) = \begin{bmatrix} x^T(k) & x_d^T(k) \end{bmatrix}^T$, and $\bar{\Phi}_s$, $\bar{\Gamma}_s$, $\bar{C}_s$, $\bar{D}_s$ are the sub-matrix blocks of $\bar{\Phi}$, $\bar{\Gamma}$, $\bar{C}$, $\bar{D}$ corresponding to the first two states respectively.

The discrete-time LQG control problem is to find the optimal control law which minimizes the cost function (5.18) or (5.20), depending on the length of the estimated time-delay. The discrete-time LQG procedure (5.23) – (5.27) is then applied to obtain the optimal LQG controller, which has the following structure:

$$\bar{K}_{LQG}(s) = \left[\begin{array}{c|c} \bar{\Phi}_s - \bar{\Gamma}_s \bar{K}_r - \bar{K}_f \bar{C}_s & \bar{K}_f \\ \hline -\bar{K}_r & 0 \end{array}\right] \tag{6.27}$$

In the following sections of this chapter LQG_{d0} denotes the conventional discrete-time LQG controller, which does not consider the time-delay. On the other hand, $ELQG_p$ denotes the modified discrete-time LQG controller that incorporates EKF-based estimate of the time-delay.

6.5 Numerical Example II

6.5.1 Unknown Constant Time-Delay

The proposed MDLQG approach described in the previous section is applied to another numerical example system in this section. In particular, LQG is applied on the 4th order SISO system with the following transfer function:

$$g_2(s) = \frac{2.5}{s^2(s^2+1)} \tag{6.28}$$

Note that that this system has two poles at the origin and two poles on the imaginary axis at $0+j$ and $0-j$. Hence this system is open-loop unstable.

The first order Pade approximation (6.5) is applied to synthesize $ELQG_p$ in this example. The sampling period is set to $T_s = 0.01$ seconds. The weightings are set as:

$$W_1 = diag\{w_{11}, w_{22}, w_{33}\} = diag\left\{10^{-5} I_{4\times 4}, 1, 1\right\},\ \ W_2 = 1,\ \ V = 10^{-2}. \tag{6.29}$$

where w_{11}, w_{22}, w_{33} are the weightings associated with the plant states, time-delay approximation state and x_e, respectively. The initial realization of $P(0|0)$ is chosen to be identity matrix, and the initial estimate $\hat{\bar{x}}(0|0)$ to be $\begin{bmatrix} 0 & 0 & 2 \end{bmatrix}^T$, i.e. $\hat{\tau}(0) = 0.5$. The actual time-delay applied is 1 second. Figure 6.6 shows that the estimated time-delay approaches a true value fairly quickly.

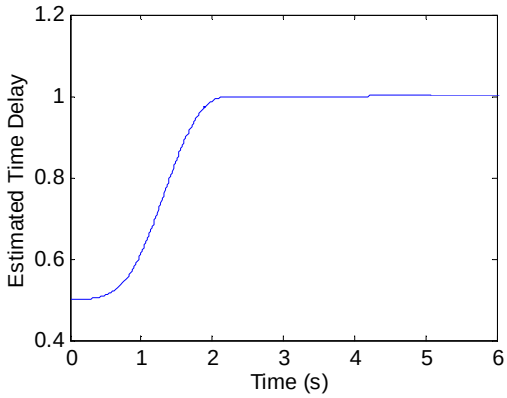

Figure 6.6 Estimated time-delay using EKF

The estimate of time-delay is then fed into the supervisory discrete-time LQG controller, $ELQG_p$, in order to adequately control the system in the presence of the unknown time-delay. The state weighting Q and the control weighting R are chosen as follows:

$$Q = 0.1 \times \bar{C}^T \bar{C} \qquad R = 1 \tag{6.30}$$

The conventional discrete-time LQG controller, LQG_{d0}, is also synthesized with the same weightings as those specified in (6.30). Based on the estimated states of the augmented model, the Kalman filter gain is obtained for $ELQG_p$, denoted as $\bar{K}_f$ and for LQG_{d0}, denoted as K_{f0}, shown as follows:.

$$\bar{K}_f = \begin{bmatrix} -0.0161 \\ 0.0549 \\ 0.0725 \\ 0.0381 \\ -0.0002 \end{bmatrix}, \quad K_{f0} = \begin{bmatrix} -0.003 \\ 0.001 \\ 0.0061 \\ 0.007 \end{bmatrix} \tag{6.31}$$

Then the optimal state-feedback control gain is obtained for $ELQG_p$, denoted as $\bar{K}_r$ and for LQG_{d0}, denoted as K_{r0}, shown as follows:

$$\bar{K}_r = \begin{bmatrix} 7.0964 \\ 4.9214 \\ 7.3205 \\ 2.4658 \\ 9.8312 \end{bmatrix}^T, \quad K_{r0} = \begin{bmatrix} 2.7348 \\ 3.7499 \\ 4.8399 \\ 2.4658 \end{bmatrix}^T \tag{6.32}$$

Figure 6.7 shows the step responses of the system controlled by $ELQG_p$ and LQG_{d0} when subjected to the unknown communication time-delay. It is clearly observed in Figure 6.7 that the conventional discrete-time LQG controller cannot stabilize the system. On the other hand, the $ELQG_p$ controller retains stability, thereby demonstrating the effectiveness of the proposed MDLQG approach. Note that during the early stages of the simulation controllers behave similarly, which is due to the fact that the time-delay is not properly estimated by the associated EKF filter during the first 5 seconds..

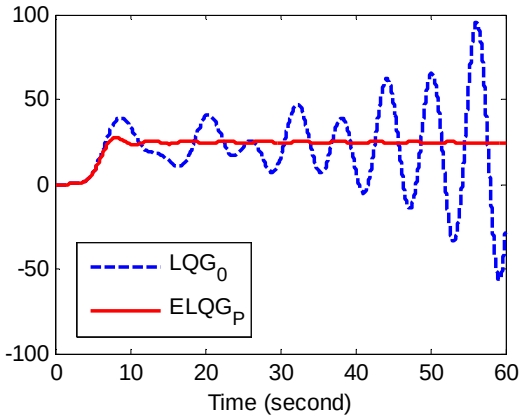

Figure 6.7 Step response for unknown constant time-delay

6.5.2 Unknown Varying Time-Delay

In the previous examples, the unknown time-delay considered was assumed to be constant. The example in this subsection demonstrates the estimation of the unknown and time-varying delay using EKF. In particular, the time-delay variation is described as a ramp function, varying at a steady rate of 0.5 per second during 10-second time interval:

$$\tau = 0.5t, \quad 0 \le t \le 10 \tag{6.33}$$

where t is the simulation time.

The first order Pade approximation is applied to model the varying time-delay given in (6.33) and the resulting augmented state-space model is given in the form described in (6.7). The corresponding state-transition matrix, $\bar{\Phi}$, is given as:

$$\bar{\Phi} = \begin{bmatrix} A & 2B & 0 \\ 0 & -2x_e & 0 \\ 0 & 0 & -0.5x_e \end{bmatrix}$$

The functions $f(\cdot)$ and $h(\cdot)$ are then obtained with the corresponding Jacobian matrices $F(k)$ and $H(k)$. Details of the derivations of $f(\cdot)$, $h(\cdot)$, $F(k)$ and $H(k)$ are provided in the Appendix C.

System described in (6.22) is also used in this sub-section. The sampling period is set to $T_s = 0.01$ seconds. The weightings are selected to be $W_1 = diag\{10I_{4\times4}, 10^2, 1\}$, $W_2 = 10$, $V = 10$. The initial realization of $P(0|0)$ is chosen to be th identity matrix while the initial augmented state estimates $\hat{x}(0|0)$ and $\hat{x}_d(0|0)$ are equal to zero. In order to examine the full range of the time-delay values, the initial value of $\hat{\tau}(0|0)$ is set to be as small as possible, i.e. $\hat{\tau}(0|0) = 0.01$ which leads to $\hat{x}_e(0|0) = 100$. Figure 6.8 shows the estimated time-delay compared with the actual time-delay, which appear to be almost identical to each other. This figure further illustrates that the proposed method can also be used in the cases where the unknown time-delay is time-varying.

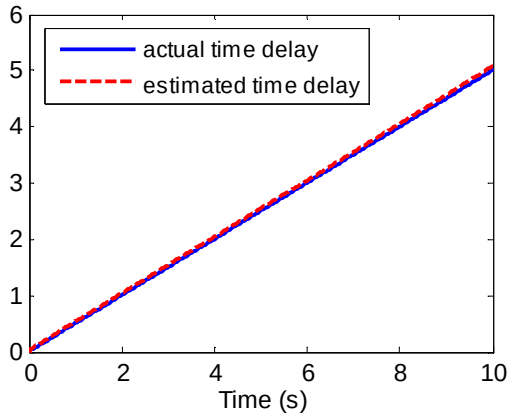

Figure 6.8 Estimation of the unknown varying time-delay

Using the estimated time-delay, controller $ELQG_p$ is then synthesized according to the procedure proposed in this chapter and applied to the system described in (6.22). Also, the controller LQG_{d0} that ignores the presence of the time-delay is implemented and compared to $ELQG_p$. The state weighting Q and control weighting

R are chosen to be the same as in (6.23). Figure 6.9 shows the responses of the two considered controllers. It is clearly observed that, for this particular scenario, conventional controller LQG_{d0} is unable to stabilise the system while the proposed control scheme is capable to maintain stability in the presence of time-varying time-delay. Initial similarity of the two responses during the first 10 seconds of the simulation is due to the fact that the EKF filter takes some time to properly estimate the true value of the time-delay.

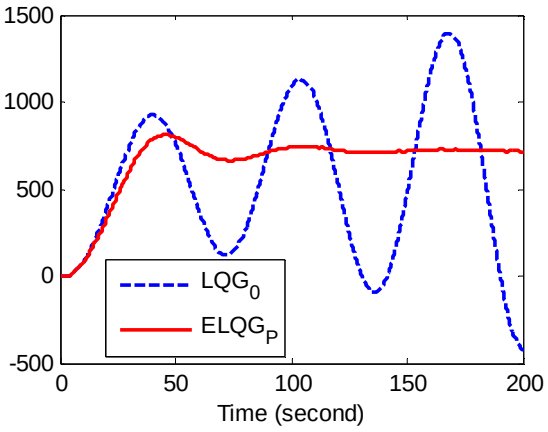

Figure 6.9 Step response for unknown varying time-delay

6.6 MDLQG for Wide-Area Damping Control

In this section, the proposed MDLQG control system is applied onto the 2-area 4-machine power system simulation in order to demonstrate its benefits. The linearised power system model used throughout the thesis is a 4-input 12-output state-space model. The order of the linearised model, with PSS regulators installed, is equal to 51. If the time-delay is modelled by 1st order Pade approximation, the order of the augmented model utilised by the MDLQG control system is 56. Evaluation of the performance is made based on the time-domain results using both small-signal and large-signal disturbances.

6.6.1 Estimation of Unknown Time-Delays

The actual time-delay is assumed to be equal to 0.8 seconds. The sampling period T_s is set as 0.01 seconds. The initial conditions are taken to be as following:

$$\hat{\hat{x}}(0) = \begin{bmatrix} 0_{n\times n} & 0_{m\times m} & x_e(0) \end{bmatrix}^T, \quad P(0\,|\,0) = 0.1 I_{(n+m+1)\times(n+m+1)},$$

$$W = \begin{bmatrix} 10^{-4} I_{(n+m)\times(n+m)} & 0 \\ 0 & 10^{-2} \end{bmatrix}, \quad V = I_{r\times r}.$$

where *n*, *m* and *r* are the state, input and output dimensions respectively and defined in (3.5). $x_e(0)$ is the initial value of x_e defined in (6.1), which represents the inverse of the initial time-delay estimate, i.e. $x_e = 1/\tau$. By changing the value of $x_e(0)$, its impact on the estimation performance of the EKF filter is investigated next. Figure 6.10 depicts the estimation of the unknown time-delays with different initial conditions. It is shown in Figure 6.10 that EKF provides fast and accurate estimation of the time-delays. Also, it is apparent from Figure 6.10 that large initial values result in faster convergence of the estimates.

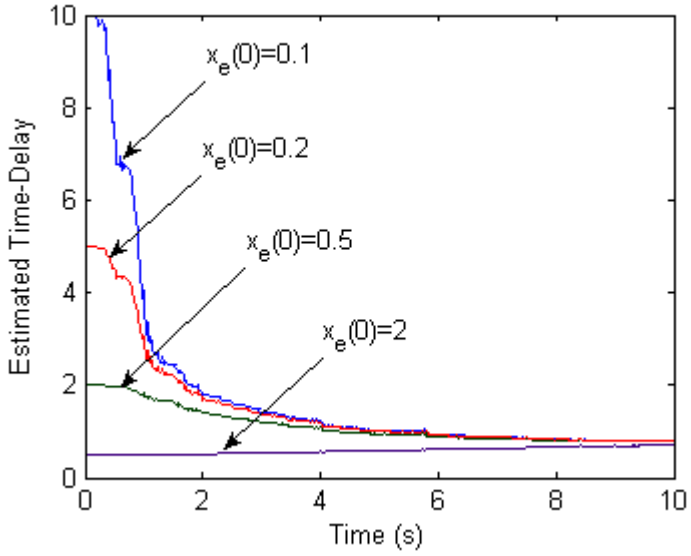

Figure 6.10 Estimated time-delay for different initial values

6.6.2 Results

The estimated time-delay is then incorporated into the supervisory discrete-time LQG controller by updating the state-space model matrices (6.26). This modified controller is denoted as $ELQG_P$. The state weighting *Q* and control weighting *R* are chosen as:

$$Q = 10^{-2} \times I_{n'\times n'}, \quad R = 10^{-1} \times I_{m\times m}.$$

Here, $n'=56$ is the state dimension of the model used in designing the controller. The conventional discrete-time LQG controller without consideration of the time-delay, LQG_{d0}, is also designed with the same cost function weights. The simulation results are obtained by applying different disturbances and time-delays onto the power system in order to compare $ELQG_P$ and LQG_{d0}.

Case 1 Small Signal Stability

A 2.5% reference voltage increase for Generator 2 is applied at 1 second. Therefore, the steady-state terminal voltage V_t of Generator 2 after the disturbance is applied is equal to 1.025 p.u.. Figure 6.11 shows the electric power and terminal voltage of Generator 2 for the cases where the overall power system is controlled by the supervisory controllers $ELQG_P$ and LQG_{d0}. Two different values of input time-delays are implemented, namely 0.8*s* and 1.2*s*, and the corresponding results are shown in Figure 6.11(a) and Figure 6.11(b) respectively. It can be clearly seen that the conventional discrete-time controller LQG_{d0}, cannot stabilize the power system following a small-signal disturbance. On the other hand, based on the estimation of the unknown time-delay, the final electric power and the terminal voltage of the power system with unknown input time-delays reach the steady-state values controlled by the proposed LQG controller $ELQG_P$ for both 0.8 seconds and 1.2 seconds input time-delays.

Case 2 Large Disturbance Stability

A three-phase fault is implemented on the bus 7 at time t=1 second, with a self-clearing time of 80 *ms*. This scenario simulates likely large-signal disturbance and is used to further assess the proposed controller. Figure 6.12 shows the performance of Generator 2 of the power system controlled by the two controllers $ELQG_P$ and LQG_{d0} respectively. The same input time-delays as in *case 1* are implemented. As the large disturbance occurs and a 0.8*s* input time-delay exists in the power system, Figure 6.12(a) shows that the oscillations of the power system cannot be damped when the system is controlled by the conventional discrete-time LQG controller LQG_{d0}. The damping is even worse when a longer input time-delay 1.2*s* is applied

as shown in Figure 6.12(b). On the other hand, based on the estimated time-delay, the post-fault rotor angle speed and the electric power of the power system controlled by controller $ELQG_p$ can reach the nominal steady-state values. This demonstrates the fact that the transient stability of the power system is greatly improved in the case of the supervisory discrete-time controller $ELQG_p$ that uses continuously updated time-delay estimates.

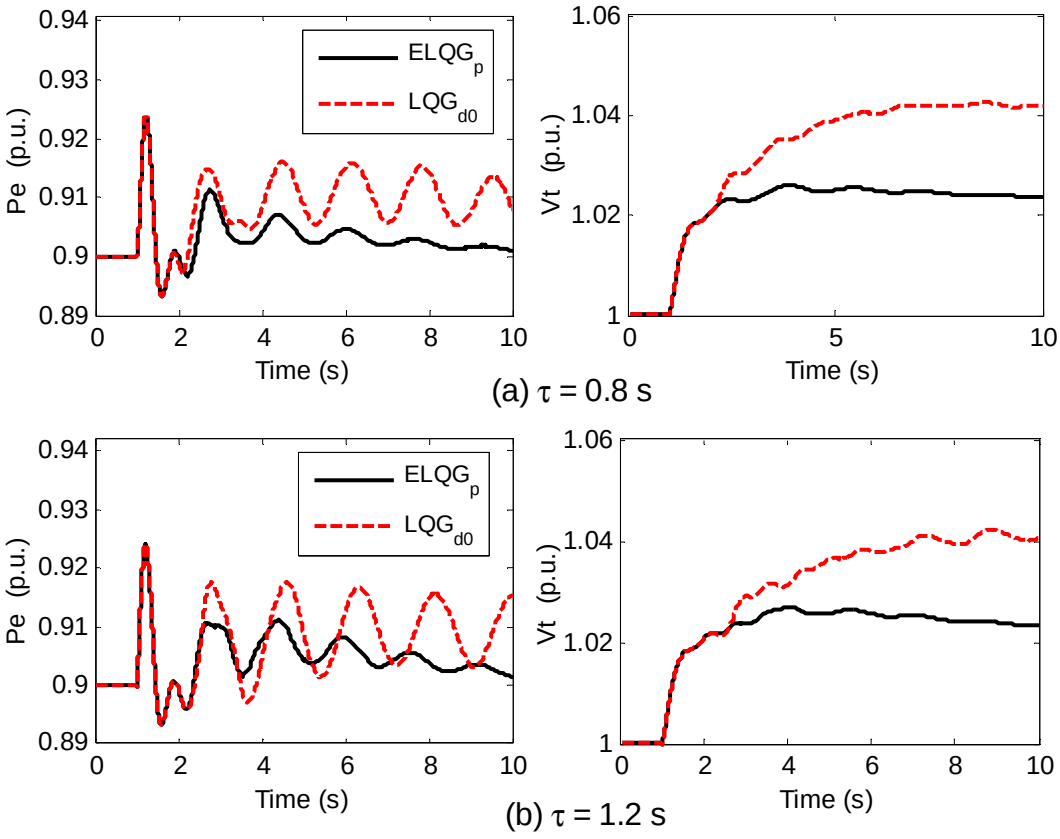

Figure 6.11 Electric Power & Terminal Voltage of Gen 2

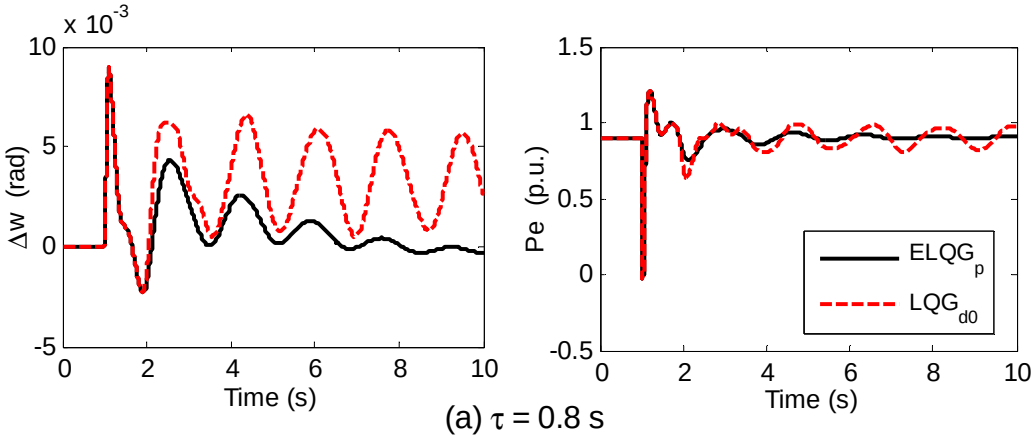

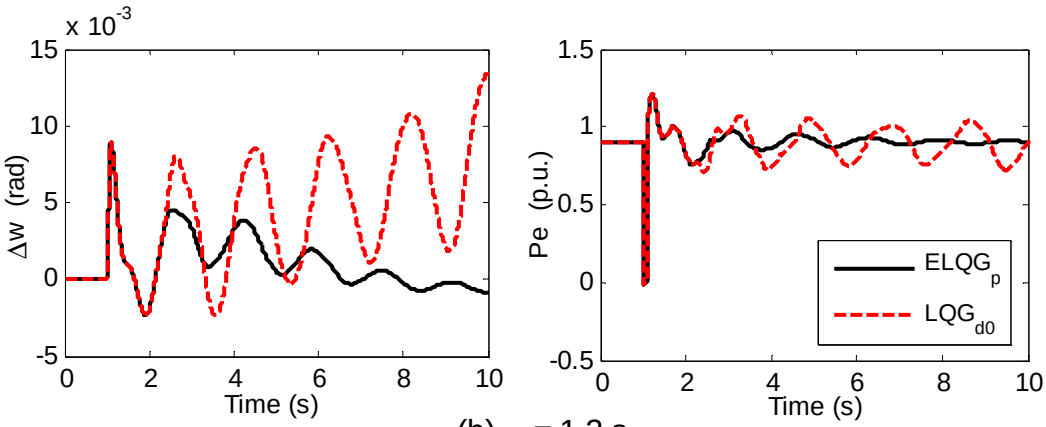

(b) τ = 1.2 s

Figure 6.12 Speed Deviation & Electric power of Gen 2

6.7 Summary

The Extended Kalman Filter (EKF) procedure for the estimation of the unknown time-delay is presented in this chapter. It is done by augmenting the state-space model of the system with additional state variables that are related to values of the actual time-delays, i.e. $x_e = 1/\tau$. The resulting augmented model is a non-linear function of the state and input, which is linearised by utilising Taylor Series expansion and deriving the corresponding Jacobian matrices. The first order and the second order Pade approximation are both used to demonstrate the proposed EKF procedure. Firstly, the estimation performance of the proposed EKF filter is assessed by using a numerical example of a second order system. The effect of the initial condition and the weightings on the estimation as well as the comparison of 1st order and 2nd order Pade approximation are also discussed in this section. Then, in Section 6.5 the numerical example of a 4th order open-loop unstable SISO system is used to demonstrate the effectiveness of the proposed control system that combines the LQG controller with the EKF filter. The MDLQG controller is also applied on the simulated 2-area, 4-machine power system in section 6.6. Both the small signal stability and large disturbance stability are examined to show the effectiveness of the proposed controller $ELQG_P$ for the unknown communication time-delay.

Chapter 7

Conclusions and Future Work

7.1 Conclusions

This thesis focused on the design of supervisory wide-area controllers, using optimal control theory, and the assessment of the impact that the communication time-delays have on the performance and the robustness of the resulting closed-loop system. Also, the impact that the discretisation of the controller has on the performance of the closed-loop system was investigated. This is particularly important when considering practical implementation of any control scheme that has to be realized using digital computers, which, while constantly improving in terms of their computational power, require finite time to execute any algorithm. This may be particularly acute in the cases where the scale of the system is very large and the dominant dynamics are relatively fast, as is the case with the power system studied in this thesis.

Supervisory wide-area controller was firstly designed in Chapter 3 using continuous-time LQG/LTR approach that relies on the optimal control theory and provides relatively simple method of developing multivariable control systems that guarantee nominal stability and are tuned using relatively small number of parameters. Its performance and robustness were assessed using both frequency-domain tools, assuming linear representation of the power system dynamics, and time-domain simulation results that utilised non-linear power system model. Results clearly illustrats the benefit in employing supervisory controller, which maintains closed-loop stability in the presence of both small-signal and large-signal disturbances.

After the successful design of the continuous-time controller, the next step was to design its discrete-time equivalent in Chapter 4 and to assess the impact that the assumed sampling period has on the performance and the robustness of the resulting closed-loop system. Once again, the assessment was performed using both frequency-domain and time-domain tools. Results indicated some deterioration in the performance as a result of increasing sampling period. However, the approach of reducing the bandwidth by changing a single parameter in the cost function was shown to successfully recover some of the performance and the robustness.

Developments described above were conducted assuming that there are no communication time-delays present, even though this may be highly inappropriate assumption given the large-scale of the modern interconnected power systems. Therefore, the consideration of time-delays was introduced in Chapter 5 when designing both continuous-time and discrete-time supervisory controller. The benefit of accounting for the time-delay was clearly demonstrated in both frequency-domain and time-domain. Additionally, the superiority of discrete-time controller compared to its continuous-time counterpart when dealing with time-delays was demonstrated. This superiority is primarily due to the fact that the design of discrete-time controller incorporates the exact time-delay description into the state-space model of the power system, while the continuous-time controller is designed by representing time-delay with rational Pade approximation.

However, development of the supervisory controllers that incorporate time-delays was conducted under an assumption that these time-delays are known, which may be highly inappropriate in some circumstances. In order to address this issue, modified supervisory controller was proposed that utilises Extended Kalman Filter to estimate the actual time-delay. That information was then fed into supervisory controller by updating its prediction model. Simulation results obtained using numerical examples and non-linear power system model demonstrated benefits of the proposed scheme for both time-invariant and time-varying delays, both of which were assumed to be unknown and had to be estimated.

Finally, it should be pointed out that the main focus of the thesis was on the specific wide-area control problem involving a particular network topology. However, the

presented methodology can be easily applied to other wide-area control problems involving different network topologies.

7.2 Directions for Future Research

Model Predictive Control (MPC) will be an obvious next control methodology to be considered, due to its close connection to discrete-time LQG control technique and its ability to provide real-time constraint management. In order to facilitate this future development, the methods used in this thesis to tune LQG/LTR controller and to assess its performance and robustness can be directly re-utilized when considering Model Predictive Control. This is primarily due to the similarity between discrete-time LQG/LTR and MPC in terms of the problem formulation and the structure of the solution, particularly when the constraints are inactive [98].

There has been a number of recent publications proposing various methods of designing Model Predictive Control such that the robustness to a particular type of uncertainty can be ensured. These methods will be investigated in terms of their applicability to deal with the communication time-delays. Also, the methodology of implementing MPC controllers using distributed architecture will be explored. This may be particularly relevant in wide-area power system applications where the large size and the criticality of a system may prohibit the use of the centralised control architecture.

However, due to the fact that the MPC control methodology employs on-line numerical optimisation routine, which is executed at each sampling instant, the impact of the sampling period on the performance is likely to be very important. This impact needs to be fully understood in order to be able to mitigate its negative impact on the performance of the closed-loop system. The tools used in this thesis to assess impact of the sampling period on the performance of the discrete-time LQG/LTR controller will be re-used to assess that impact in the case of the Model Predictive Control.

Impact of discretisation should also be conducted in the future work for the case of robust H_∞ control technique using those very same tools that were utilised in this thesis. This would facilitate practical application of H_∞ control methodology to power systems.

Issues regarding the application of Extended Kalman Filter will also need to be considered. In particular, further case studies will need to be conducted in order to comprehensively assess its suitability in other wide-area control problems. Also, further understanding of how to tune EKF estimator in various power system applications will be necessary in order to facilitate its acceptance as a viable tool in tackling the impact of communication time-delays.

Considering the complexity of existing and future networks, a number of control loops will be so designed to support each other in order to make sure the stability of power systems. This will be particularly challenging in future networks with a complex and very diverse generation mix (e.g. parallel operation of inflexible nuclear power plants based on Pressurized Water Reactors, Combined Cycle Gas Turbines, Wind Turbines of different types, *etc*.), existence of High Voltage Direct Current connectors, energy storage units and strong requirements to minimize the economical costs of the system operation. However, this thesis is the contribution which will help future large scale power systems to operate in a more secure and reliable manner.

Appendices

Appendix A

A.1 Test Power System Parameters and Data

Original data are taken from [6.3]. All values are in p.u. based on machine rating.

Table A.1 Load flow data

Contingency 1 (original)					
Voltage, p.u.	Angle, °	P_G, p.u.	Q_G, p.u.	P_L, p.u.	Q_L, p.u.
1	0	1.93	0.488276	0.5	0.3
1	16.8226	0.9	0.345003	0.1	0.05
1	16.133	0.9	0.448285	0.1	0.08
1	-1.76168	0.9	0.278265	0.1	0.07
0.975949	12.7335	0	0	0.75	0.36
0.995251	-3.69526	0	0	1.08	0.03
0.977207	-12.0312	0	0	1.15	0.45
0.995935	-2.05713	0	0	0.85	0.21

Table A.2 Line data

Line	Start Bus	End Bus	R, p.u.	X, p.u.	G, p.u.	B, p.u.
1	2	3	0	0.45	0	-2.22222
2	2	5	0	0.09	0	-11.1111
3	3	5	0	0.07	0	-14.2857
4	5	7	0	0.47	0	-2.12766
5	7	6	0	0.47	0	-2.12766
6	1	8	0	0.025	0	-40
7	4	6	0	0.05	0	-20
8	6	8	0	0.04	0	-25
9	4	8	0	0.04	0	-25

Table A.3 Generator Data

Gen	R_a	X_d	$X_d^{'}$	$X_d^{''}$	$T_{d0}^{'}$	$T_{d0}^{''}$	X_q	$X_q^{'}$	$X_q^{''}$	$T_{q0}^{'}$	$T_{q0}^{''}$	H
1	0	0.86	0.121	0.089	5.9	0.33	0.828	0.198	0.089	0.535	0.078	13.3
2	0	1.445	0.316	0.179	5.26	0.028	0.959	0	0.162	0	0.159	4.27
3	0	0.86	0.121	0.089	5.9	0.33	0.828	0.198	0.089	0.535	0.078	6.34
4	0	0.86	0.121	0.089	5.9	0.33	0.828	0.198	0.089	0.535	0.078	10.34

Table A.4 AVR Data & PSS Data

Parameter	K_{AVR}	T_{AVR}	T_W	T_A	T_B
Values	198	0.055	5	0.0563	0.1126

A.2 Modelling of Generators

Generator 1 is the reference generator of this 2-area 4-machine power system. Generator 2 is the salient pole machine, while both Generate 3 and 4 are round rotor machines. The state space model of each machine is given as follows, where *x*, *u* and *y* is the state, input and output matrices of each machine, respectively.

Generator 1 – Reference machine (5^{th} order state-space model)

$$x = \left[E_q^{''} \quad E_q^{'} \quad E_d^{''} \quad E_d^{'} \quad \Delta\omega \right]^T$$

$$u = \left[I_d \quad I_q \quad E_{fd} \quad \left(P_m - P_e \right) \right]^T$$

$$y = \left[E_q^{''} \quad E_d^{''} \quad \Delta\omega \quad E_q^{'} \quad E_d^{'} \right]$$

$$\dot{x}=\begin{bmatrix} -\frac{1}{T_{d0}^{''}} & \frac{1}{T_{d0}^{''}} & -\frac{1}{T_{d0}^{'}} & 0 & 0 & 0 \\ 0 & -\frac{1}{T_{d0}^{'}} & 0 & 0 & 0 & 0 \\ 0 & 0 & -\frac{1}{T_{q0}^{''}} & \frac{1}{T_{q0}^{''}} & 0 & 0 \\ 0 & 0 & 0 & \frac{1}{T_{q0}^{'}} & 0 & 0 \\ 0 & 0 & 0 & 0 & 0 & 0 \end{bmatrix} x + \begin{bmatrix} -\frac{X_d^{'}-X_d^{''}}{T_{d0}^{''}} - \frac{X_d-X_d^{'}}{T_{d0}^{'}} & 0 & \frac{1}{T_{d0}^{'}} & 0 \\ -\frac{X_d-X_d^{'}}{T_{d0}^{'}} & 0 & \frac{1}{T_{d0}^{'}} & 0 \\ 0 & \frac{X_q^{'}-X_q^{''}}{T_{q0}^{''}} & 0 & 0 \\ 0 & \frac{X_q-X_q^{'}}{T_{q0}^{'}} & 0 & 0 \\ 0 & 0 & 0 & \frac{1}{2H} \end{bmatrix} u$$

$$y=\begin{bmatrix} 1 & 0 & 0 & 0 & 0 \\ 0 & 0 & 1 & 0 & 0 \\ 0 & 0 & 0 & 0 & 1 \\ 0 & 1 & 0 & 0 & 0 \\ 0 & 0 & 0 & 1 & 0 \end{bmatrix} x$$

Generator 2 – Salient pole machine (5th order state-space model)

$$x=\begin{bmatrix} E_q^{''} & E_q^{'} & E_d^{''} & \Delta\delta & \Delta\omega \end{bmatrix}^T$$

$$u=\begin{bmatrix} I_d & I_q & E_{fd} & \left(P_m-P_e\right) & \Delta\omega_{ref} \end{bmatrix}^T$$

$$y=\begin{bmatrix} E_q^{''} & E_d^{''} & \Delta\delta & \Delta\omega & E_q^{'} \end{bmatrix}$$

$$\dot{x} = \begin{bmatrix} -\frac{1}{T_{d0}^{''}} & \frac{1}{T_{d0}^{''}} - \frac{1}{T_{d0}^{'}} & 0 & 0 & 0 \\ 0 & -\frac{1}{T_{d0}^{'}} & 0 & 0 & 0 \\ 0 & 0 & -\frac{1}{T_{q0}^{''}} & 0 & 0 \\ 0 & 0 & 0 & 0 & 2\pi f_0 \\ 0 & 0 & 0 & 0 & 0 \end{bmatrix} x$$

$$+ \begin{bmatrix} -\frac{X_d^{'} - X_d^{''}}{T_{d0}^{''}} - \frac{X_d - X_d^{'}}{T_{d0}^{'}} & 0 & \frac{1}{T_{d0}^{'}} & 0 & 0 \\ -\frac{X_d - X_d^{'}}{T_{d0}^{'}} & 0 & \frac{1}{T_{d0}^{'}} & 0 & 0 \\ 0 & \frac{X_q - X_q^{'}}{T_{q0}^{'}} & 0 & 0 & 0 \\ 0 & 0 & 0 & 0 & -2\pi f_0 \\ 0 & 0 & 0 & \frac{1}{2H} & 0 \end{bmatrix} u$$

$$y = \begin{bmatrix} 1 & 0 & 0 & 0 & 0 \\ 0 & 0 & 1 & 0 & 0 \\ 0 & 0 & 0 & 1 & 0 \\ 0 & 0 & 0 & 0 & 1 \\ 0 & 1 & 0 & 0 & 0 \end{bmatrix} x$$

Generator 3&4 – Round rotor machine (6th order state-space model)

$$x = \begin{bmatrix} E_q^{''} & E_q^{'} & E_d^{''} & E_d^{'} & \triangle\delta & \triangle\omega \end{bmatrix}^T$$

$$u = \begin{bmatrix} I_d & I_q & E_{fd} & \left(P_m - P_e\right) & \triangle\omega_{ref} \end{bmatrix}^T$$

$$y = \begin{bmatrix} E_q^{''} & E_d^{''} & \triangle\delta & \triangle\omega & E_q^{'} & E_d^{'} \end{bmatrix}$$

$$\dot{x}=\begin{bmatrix} -\frac{1}{T_{d0}^{''}} & \frac{1}{T_{d0}^{''}} & -\frac{1}{T_{d0}^{'}} & 0 & 0 & 0 \\ 0 & -\frac{1}{T_{d0}^{'}} & 0 & 0 & 0 & 0 \\ 0 & 0 & -\frac{1}{T_{q0}^{''}} & \frac{1}{T_{q0}^{''}} & 0 & 0 \\ 0 & 0 & 0 & -\frac{1}{T_{q0}^{'}} & 0 & 0 \\ 0 & 0 & 0 & 0 & 0 & 2\pi f_0 \\ 0 & 0 & 0 & 0 & 0 & 0 \end{bmatrix} x$$

$$+\begin{bmatrix} -\frac{X_d^{'}-X_d^{''}}{T_{d0}^{''}} & -\frac{X_d-X_d^{'}}{T_{d0}^{'}} & 0 & \frac{1}{T_{d0}^{'}} & 0 & 0 \\ & -\frac{X_d-X_d^{'}}{T_{d0}^{'}} & 0 & \frac{1}{T_{d0}^{'}} & 0 & 0 \\ & 0 & \frac{X_q^{'}-X_q^{''}}{T_{q0}^{'}} & 0 & 0 & 0 \\ & 0 & \frac{X_q-X_q^{'}}{T_{q0}^{'}} & 0 & 0 & 0 \\ & 0 & 0 & 0 & 0 & -2\pi f_0 \\ & 0 & 0 & 0 & \frac{1}{2H} & 0 \end{bmatrix} u$$

$$y=\begin{bmatrix} 1 & 0 & 0 & 0 & 0 & 0 \\ 0 & 0 & 1 & 0 & 0 & 0 \\ 0 & 0 & 0 & 0 & 1 & 0 \\ 0 & 0 & 0 & 0 & 0 & 1 \\ 0 & 1 & 0 & 0 & 0 & 0 \\ 0 & 0 & 0 & 1 & 0 & 0 \end{bmatrix} x$$

A.3 Modelling of Exciter & AVR

The application of the generator excitation system to this 4-machin 8-bus power system is shown in Figure A.1, which is a 2nd order exciter & AVR. The transfer function of the regulator and the voltage limits are given as follows.

$$V_o = K_{AVR}\frac{1+2s}{1+10s}\frac{1}{1+sT_{AVR}}V_i = E_{fd}$$

$$V_{R\max}=5.5,\ V_{R\min}=-5.5$$

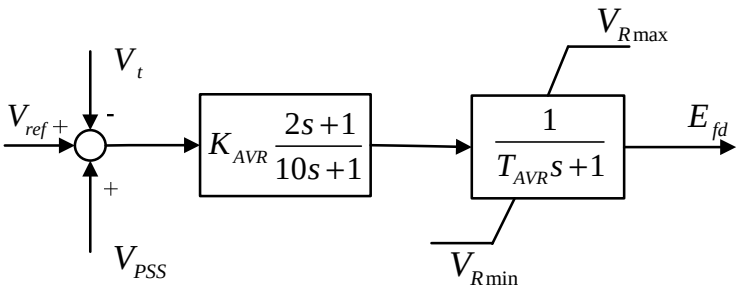

Figure A.1 Block diagram of 2nd order Exciter&AVR

A.4 Full eigenvalues of the Test Power System without PSS

Table A-5 Eigenvalues of the 35st order open-loop power system

$-8760.3 \pm 65.3i$	$-50.8192 \pm 0.5810i$	-17.0586	$-0.0353 \pm 3.6734i$
-6546.3	-39.1665	-14.7143	-1.3026
-6238.0	-31.9022	$-7.6715 \pm 7.2435i$	0.0000
$-2244.4 \pm 139.9i$	-28.7463	$-8.5474 \pm 4.4955i$	$-0.5689 \pm 0.2066i$
$-2080.7 \pm 235.5i$	-26.9679	$-1.1962 \pm 8.2158i$	-0.5312
-93.5768	-17.4607	$-0.8186 \pm 6.9826i$	-0.5078
-0.5139			

Appendix B

B.1 System Responses to 250 *ms* Time Delay

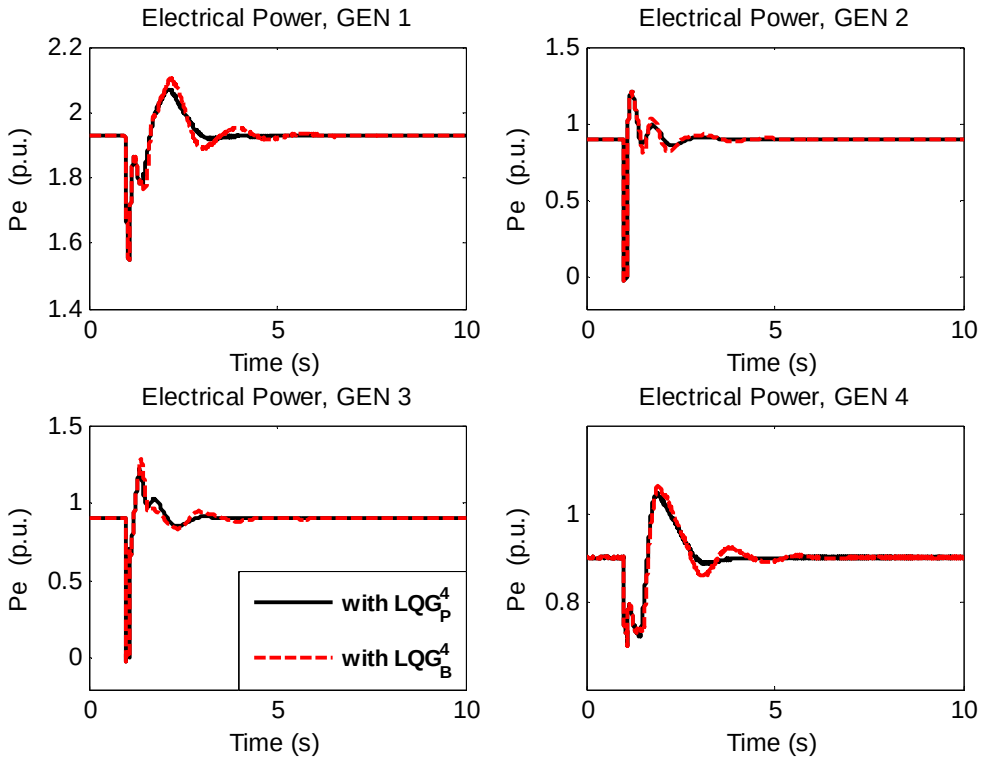

Figure B.1 Electrical Power using LQG_P^4 and LQG_B^4 for $T_d = 250\ ms$

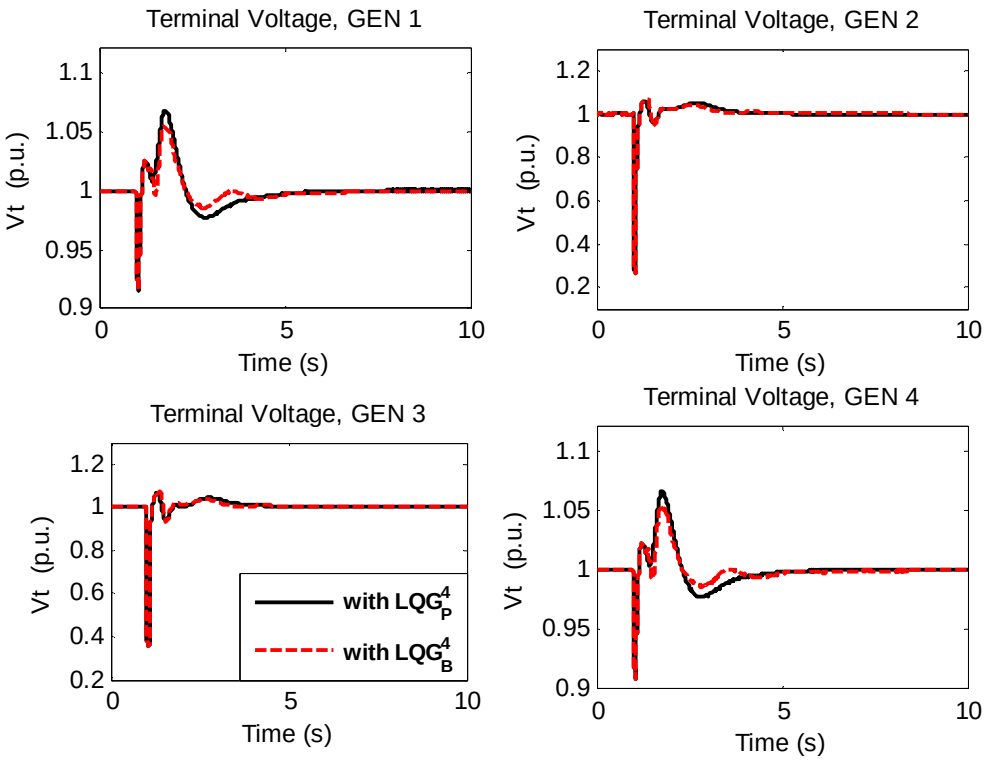

Figure B.2 Terminal voltage using LQG_P^4 and LQG_B^4 for $T_d = 250\ ms$

B.2 System Responses to 520 *ms* Time Delay

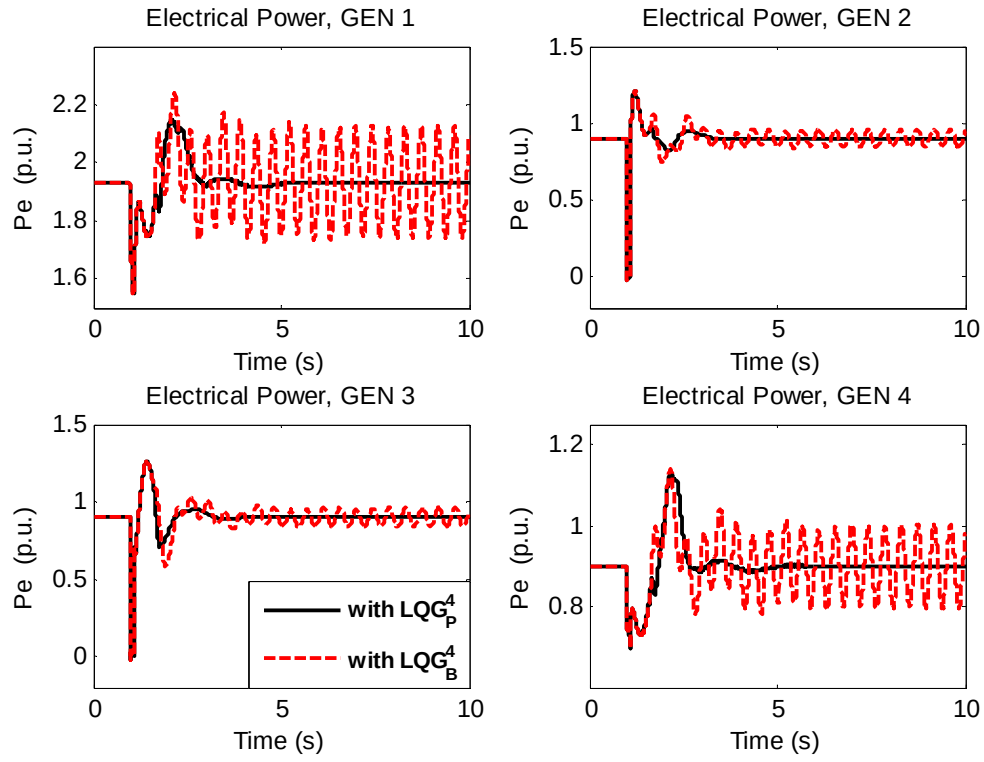

Figure B.3 Electrical Power using LQG_P^4 and LQG_B^4 for $T_d = 520\ ms$

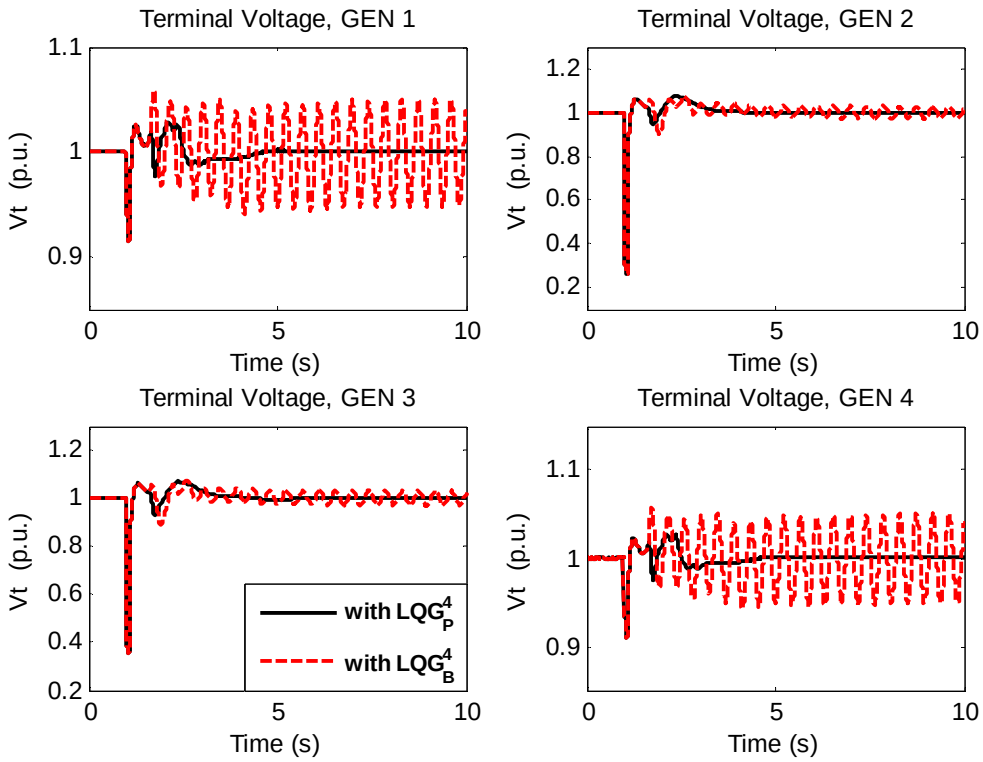

Figure B.4 Terminal voltage using LQG_P^4 and LQG_B^4 for $T_d = 520\ ms$

B.3 System Responses to 1.3 seconds Time Delay

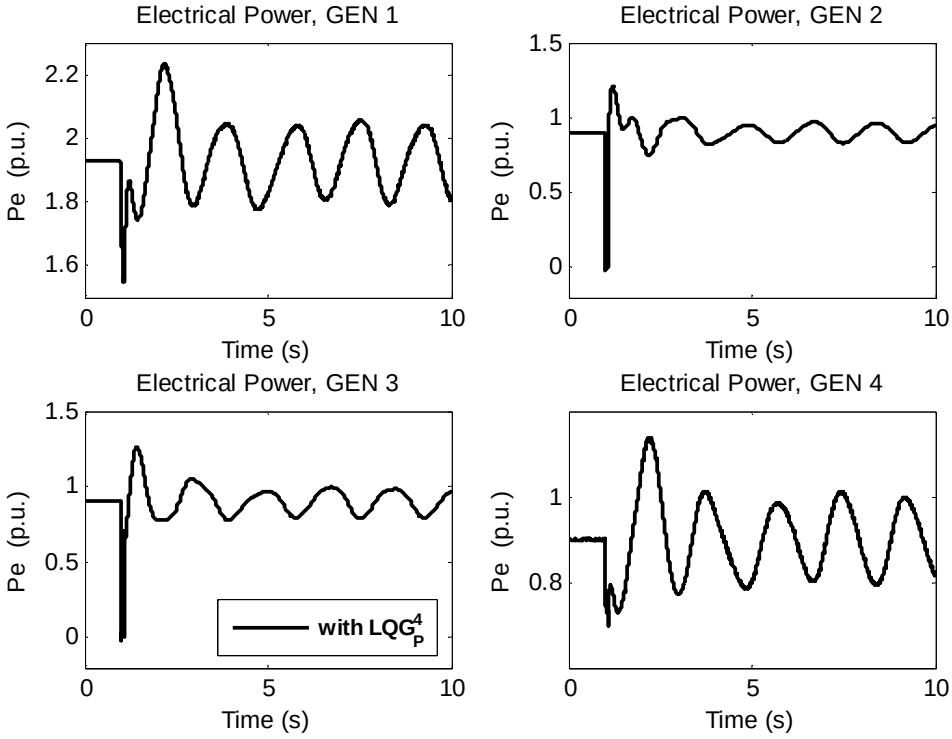

Figure B.5 Electrical Power using LQG_P^4 for $T_d = 1.3\ s$

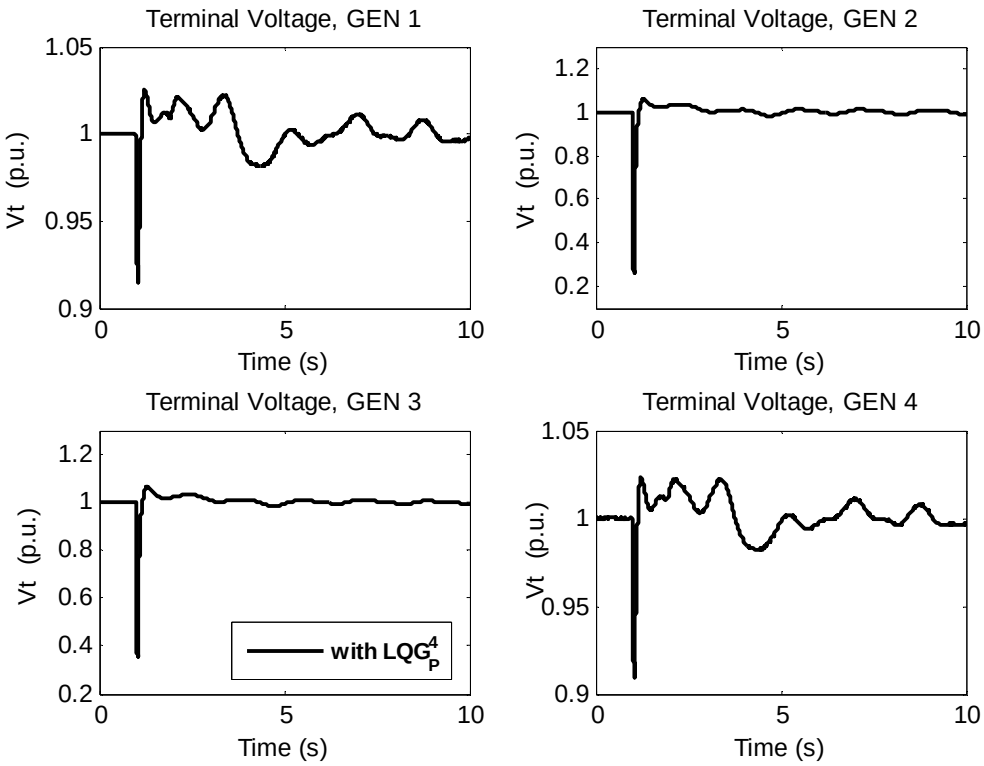

Figure B.6 Terminal voltage using LQG_P^4 for $T_d = 1.3\ s$

Appendix C

The discrete-time augmented model for unknown time delay given in (6.33) is expressed as follows.

$$\begin{bmatrix} x_p(k+1) \\ x_d(k+1) \\ x_e(k+1) \end{bmatrix} = \begin{bmatrix} I+T_sA & 2T_sB & 0 \\ 0 & I-2T_sx_e(k) & 0 \\ 0 & 0 & I-0.5T_sx_e(k) \end{bmatrix} \begin{bmatrix} x_p(k) \\ x_d(k) \\ x_e(k) \end{bmatrix} + \begin{bmatrix} -B(T_s+\frac{T_s^2A}{2})+2T_s^2x_e(k)B \\ 2x_e(k)(T_s-T_s^2x_e(k)) \\ 0 \end{bmatrix} u(k) \tag{C.1}$$

$$y(k) = \begin{bmatrix} C & 0 & 0 \end{bmatrix} \begin{bmatrix} x_p(k) \\ x_d(k) \\ x_e(k) \end{bmatrix} - Du(k)$$

The nonlinear model $f(\cdot)$, $h(\cdot)$ are presented as follows:

$$f(\bar{x}(k),u(k)) = \begin{bmatrix} (I+T_sA)x(k)+T_sBx_d(k)+\frac{T_s^2}{2}Bx_e(k)u(k) \\ (1-T_sx_e(k))x_d(k)+(T_s-\frac{T_s^2}{2}x_e(k))x_e(k)u(k) \\ I-0.5T_sx_e(k) \end{bmatrix} \tag{C.2}$$

$$h(\bar{x}(k)) = Cx(k)$$

The Jacobian matrices of $f(\cdot)$, $h(\cdot)$, $F(k)$ and $H(k)$ are the linearization of the nonlinear model (C.2) by using the current estimation of states $\hat{\bar{x}}(k)$ and input *u* are expressed as

$$F_{\bar{x}}(k) = \left.\frac{\partial f(\bar{x}(k),u)}{\partial \bar{x}(k)}\right|_{\hat{\bar{x}}(k),u}$$

$$F_{\bar{x}}(k) = \left.\begin{bmatrix} I+T_sA & T_sB & \frac{T_s^2}{2}Bu(k) \\ 0 & 1-T_sx_e(k) & -T_sx_d(k)+(T_s-T_s^2x_e(k))u(k) \\ 0 & 0 & I-T_sx_e(k) \end{bmatrix}\right|_{\hat{\bar{x}}(k),u} \tag{C.3}$$

$$F_u(k) = \left.\frac{\partial f(\bar{x}(k), u)}{\partial u}\right|_{\hat{\bar{x}}(k),u} = \left.\begin{bmatrix} \frac{T_s^2}{2} B x_e(k) \\ (T_s - \frac{T_s^2}{2} x_e(k)) x_e(k) \\ 0 \end{bmatrix}\right|_{\hat{\bar{x}}(k),u} \tag{C.4}$$

$$H_{\bar{x}}(k) = \left.\frac{\partial H(\bar{x}(k))}{\partial \bar{x}}\right|_{\hat{\bar{x}}(k)} = \begin{bmatrix} C & 0 & 0 \end{bmatrix} \tag{C.5}$$

References

[1] P. Kundur, *Power System stability and control*. California: McGraw-Hill, Inc, 1994.

[2] J. Paserba, "Analysis and Control of Power System Oscillations," *CIGRE Special Publication 38.01.07*, Technical Brochure 111, 1996.

[3] B. C. Pal, "Robust Damping Control of Inter-area Oscillations in Power System with Super-conducing Magnetic Energy Storage Devices," PhD thesis, Imperial College of Science Technology and Medicine, Department of Electrical and Electronic Engineering, 1999.

[4] L. Pereira, "Cascade to Black," *IEEE Power & Energy*, vol. 2, no. 3, pp. 54-57, 2004.

[5] UCTE, "Final Report on the Disturbances of 4 November 2006," 2006. [online] available: *www.geocities.jp/ps_dictionary/blackout/Final-Report-20070130.pdf*

[6] M. Klein, G. J. Rogers, S. Moorty, P. Kundur, "Analytical Investigation of Factors Influencing Power System Stabilizers Performance," *IEEE Trans. on Energy Conversion*, vol. EC-7, no. 3, pp. 382-388, 1992.

[7] E. V. Larsen, and D. A. Swann, "Applying Power System Stabilizers, Part II: Performance Objectives and Tuning Concepts," *IEEE Trans. on Power Apparatus and Systems*, vol. PAS-100, no. 6, pp. 3025-3033, 1981.

[8] A. Murdoch, S. Venkataraman, R. A. Lawson, and W. R. Pearson, "Integral of Accelerating Power Type PSS Part 1 - Theory, Design and Tuning Methodology," *IEEE Trans. on Energy Conversion*, vol. 14, pp. 1658-1663, 1999.

[9] W. Gu, and K. E. Bollinger, "A Self-tuning Power System Stabilizer for Wide-Range Synchronous Generator Operation," *IEEE Trans. on Power Systems*, vol. 4, no. 3, pp. 1191-1199, 1989.

[10] M. E. Aboul-Ela, A. A. Sallam, J. D. McCalley, and A. A. Fouad, "Damping Controller Design for Power System Oscillations using Global Signals," *IEEE Trans. on Power Systems*, vol. 11, no. 2, pp. 767-773, 1996.

[11] P. Zhang and A. H. Coonick, “Coordinated Synthesis of PSS Parameters in Multi-Machine Power Systems using the Method of Inequalities Applied to Genetic Algorithms,” *IEEE Trans. on Power Systems*, vol. 15, no. 2, pp. 811-816, 2000.

[12] E.V. Larsen, J. J. Sanchez-Gasca, and J. H. Chow, “Concepts for Design of FACTS Controllers to Damp Power Swings,” *IEEE Trans. on Power Systems*, vol. 10, no. 2, pp. 948-956, 1995.

[13] Y. H. Song and A. T. Johns, *Flexible ac transmission systems(FACTS)*. London, U.K.: IEE Press, 1999.

[14] Systems Oscillations Working Group, “Inter-area Oscillations in Power Systems,” *IEEE Power Engineering Society*, Oct, 1994.

[15] J. J. Sanchez-Gasca, “Coordinated Control of two facts devices for damping interarea oscillations,” *IEEE Trans. on Power system*, vol. 13, pp. 428-434, 1998.

[16] C. Gama, L. Angquist, G. Ingestrom, and M. Noroozian, “Commissioning and Operative Experience of TCSC for Damping Power Oscillation in the Brazilian North-South Interconnection,” CIGRE 2000 session, Paris, paper 14-104, 2000.

[17] L. Cai and I. Erlich, “Fuzzy Coordination of FACTS controllers for damping power system oscillations,” presented at *International Symposium on Modern Electric Power Systems*, Wroclaw, 2000.

[18] B. Chaudhuri, B. C. Pal, A. C. Zolotas, I. M. Jaimoukha, and T. C. Green, “Mixed-sensitivity approach to H_∞ control of power system oscillations employing multiple FACTS devices,” *IEEE Trans. on Power System*, vol. 18, no. 3, pp. 1149-1156, Aug, 2003.

[19] L. J. Cai and I. Erlich, “Simultaneous Coordinated Tuning of PSS and FACTS Damping Controllers in Large Power Systems,” *IEEE Trans. on Power Systems*, vol. 20, pp. 294-300, 2005.

[20] K. M. Son and J. K. Park, “On the Robust LQG Control of TCSC for Damping Power System Oscillations,” *IEEE Trans. Power Syst.*, vol. 15, no. 4, pp. 1306-1312, 2000.

[21] I. Kamwa, R. Grondin, D. Asber, J. P. Gingras, and G. Trudel, “Large-scale Active-load Modulation for Angle Stability Improvement,” *IEEE Trans. on Power Systems*, vol. 14, no. 2, pp. 582-590, 1999.

[22] J. H. Chow, J. J. Sanchez-Gasca, H. Ren, and S. Wang, “Power System Damping Controller Design using Multiple Input Signals,” *IEEE Control Systems Magazine*, vol. 20, no. 4, pp. 82-90, 2000.

[23] I. Kamwa, R. Grondin, and Y. Hebert, “Wide-area Measurement based Stabilizing Control of Large Power Systems-A Decentralized/Hierarchical

Approach," *IEEE Trans. on Power Systems.*, vol. 16, no. 1, pp. 136-153, Feb. 2001.

[24] V. Terzija, G. Valverde, D. Cai, P. Regulski, V. Madani, J. Fitch, S. Skok, M. Begovic, and A. Phadke, "Wide Area Monitoring, Protection and Control of Future Electric Power Networks", *Proceedings of IEEE*, vol. 99, no. 1, pp. 80-93, 2011.

[25] B. Chaudhuri and B. Pal, "Robust Damping of Multiple Swing Modes Employing Global Stabilizing Signals with A TCSC," *IEEE Trans. on Power Systems*, vol. 19, no. 1, pp. 499-506, Feb. 2004.

[26] M. Klein, L. Le, G. Rogers, S. Farrokpay, and N. Balu, " H_∞ Damping Controller Design in Large Power System," *IEEE Trans. on Power Systems*, vol. 10, no. 1, pp. 158-166, Feb. 1995.

[27] Z. Hu and J. V. Milanovic, "Damping of Inter-area Oscillations by WAM based Supplementary Controller," in *Proc. IEEE Power Engineering Society General Meeting*, Tampa, FL, 2007.

[28] H. Ni, G. T. Heydt, and L. Mili, " Power System Stability Agents using Robust Wide Area Control," *IEEE Trans. on Power Systems*, vol. 17, no. 4, pp. 1123-1131, Nov. 2002.

[29] S. Skogestad, and I. Postlethwaite, *Multivariable Feedback Control: Analysis and Design*. John Wiley and Sons, UK, 1996.

[30] A. Almutairi, "Enhancement of Power System Stability using Wide Area Measurement System Based Damping Controller," PhD thesis, School of Electrical and Electronic Engineering, The University of Manchester, 2010.

[31] A. C. Zolotas, B. Chaudhuri, I. M. Jaimoukha, and P. Korba, "A Study on LQG/LTR Control for Damping Inter-Area Oscillations in Power Systems," *IEEE Trans. on Control Systems Technology*, vol. 15, no. 1, pp. 151-160, 2007.

[32] J. M. Maciejowski, *Multivariable Feedback Design*. Addison-Wesley, New York, USA, 1989.

[33] B. D. O. Anderson, and J. B. Moore, *Optimal Control – Linear Quadratic Methods*: Prentice-Hall, 1989.

[34] F. L. Lewis, and V. L. Syrmos, *Optimal Control*. Wiley, 1995.

[35] M. J. Grimble, "Minimization of a Combined H_∞ and LQG Cost-function for a Two-degrees-of-freedom Control Design," *Automatica*, vol. 25, no. 4, pp. 635-638, 1989.

[36] M. J. Grimble, "Horizontal Axis Wind Turbine Control: Comparison of Classical, LQG and H_∞ Design," *Dynamics and Control*, vol. 6, no. 2, pp. 143-161, 1996.

[37] H. Kwakernaak, "Optimal Low-Sensitivity Linear Feedback Systems," *Automatica*, vol. 5, no. 3, pp. 279-285, 1969.

[38] J. C. Doyle, and G. Stein, "Robustness with Observers," *IEEE Trans. on Automatic Control*, vol. AC-24, no. 4, pp. 607-611, 1979.

[39] J. C. Doyle, and G. Stein, "Multivariable feedback design: concepts for a classical/modern synthesis," *IEEE Trans. on Automatic Control*, vol. AC-26, no. 1, pp. 4-16, 1981.

[40] G. Stein, and M. Athans, "The LQG/LTR Procedure for Multivariable Feedback Control Design," *IEEE Trans. on Automatic Control*, vol. AC-32, no. 2, pp. 105-144, 1987.

[41] G. Radman, "Design of Power System Stabilizer based on LQG/LTR Formulations," *Proc. Ind. Appl. Soc. Ann. Meeting/Conf. Record*, pp.1787-1792, 1992.

[42] B. Dalela, and G. Radman, "A Study of Multivariable Supplementary Power System Stabilizers," Proceedings of the 37th Annual North American, Power Symposium, pp. 134-140, 23-25, Oct. 2005.

[43] H. E. Shaalan, "The Application of Linear Multivariable Control to An AGC System," *Twenty-Fifth Southeastern Symposium on System Theory*, pp. 130-134, 7-9 March, 1993.

[44] F. Fatehi, J. R. Smith, and D. A. Pierre, "Robust Power System Controller Design based on Measured Models," *IEEE Trans. on Power Sysems.*, vol. 11, no. 2, pp. 774-780, 1996.

[45] F. P. deMello, L. N. Hannett, D. W. Parkinson, and J. S. Czuba, "A Power System Stabilizer Design using Digital Control," *IEEE Trans. on Power Apparatus and Systems*, vol. PAS-101, no. 8, pp. 2860-2867, 1982.

[46] K. J. Runtz, A. S. A. Farag, D. W. Huber, G. S. Hope, and O. P. Malik, "Digital Control Scheme for a Generating Unit," *IEEE Trans. on Power Apparatus and Systems*, vol. PAS-92, no. 2, pp. 478-483, 1973.

[47] K. Hirayama, Y. Tone, K. Takagi, H. Murakami, M. Shibata, H. Nagamura, and Y. Takagi, "Digital AVR Application to Power Plants," *IEEE Trans. on Energy Conversion*, vol. 8, pp. 602-609, Dec. 1993.

[48] K. E. Bollinger, L. Nettleton, T. Greenwood-Madsen, and M. Salyzyn, "Experience with Digital Power System Stabilizers at Steam and Hydro Generating Stations," *IEEE Trans. on Energy Conversion*, vol. 8, no. 2, pp. 172-177, June 1993.

[49] L. N. Chen, H. Tanaka, K. Katou, Y. Nakamura, "Stability Analysis of Digital Control of Power Systems," *Electric Power System Research*, vol. 55, no. 2, pp. 79-86, 2000.

[50] K. J. Astrom and B. Wittenmark, *Computer Controlled Systems: Theory and Design*. Prentice-Hall, 1984.

[51] B. Chaudhuri, Rajat Majumder and B. C. Pal, "Wide-Area Measurement-Based Stabilizing Control of Power System Considering Signal Transmission Delay," *IEEE Trans. on Power Syst.*, vol. 19, no. 4, pp 1971-1979, 2004.

[52] J. W. Stahlhut, T. J. Browne, G. T. Heydt, and V. Vittal, "Latency Viewed as A Stochastic Process and Its Impact on Wide Area Power System Control Signals," *IEEE Trans. on Power Systems*, vol. 23, no. 1, pp.84-91, 2008.

[53] H. X. Wu, H. Ni, and G. T. Heydt, "The Impact of Time Delay on Robust Control Design in Power Systems," *IEEE Power Engineering Society Winter Meeting*, vol. 2, no. 2, pp.1511-1516, 2002.

[54] J. Y. Zhang, and Y. Z. Sun, "Effect of Delayed Input on Oscillation Damping using Wide Area Power System Stabilizer," in *Proc. IEEE Transmission and Distribution Conference & Exhibition: Asia and Pacific*, pp. 1-4, 2005.

[55] J. H. Chow, J. J. Sanchez-Gazca, R. Haoxing, and S. Wang, "Power System Damping Controller Design using Multiple Input Signals," *IEEE Control Systems Magazine*, vol. 20, no. 4, pp.82-90, 2000.

[56] D. Dotta, A. S. e Silva, and I. C. Decker, "Wide-Area Measurements-Based Two-Level Control Design Considering Signal Transmission Delay," *IEEE Trans. on Power Systems*, vol. 24, no. 1, pp.208-216, 2009.

[57] T. Zabaiou, F. A. Okou, L. –A. Dessaint, and O. Akhrif, "Time-delay Compensation of a Wide-area Measurements-based Hierarchical Voltage and Speed Regulator," *Canadian Jour. Elect. & Computer Eng.*, vol. 33, no. 2, pp. 77-85, 2008.

[58] Rajat Majumder, B. Chaudhuri, B. C. Pal, and Qing-Chang Zhong, "A Unified Smith Predictor Approach for Power System Damping Control Design Using Remote Signals," *IEEE Trans. on Power Syst.*, vol. 13, no. 6, pp. 1063-1068, 2005.

[59] H. X. Wu, S. Tsakalis Konstantinos, and G. T. Heydt, "Evaluation of Time Delay Effects to Wide-Area Power System Stabilizer Design," *IEEE Trans. on Power Syst.*, vol. 19, no. 4, pp 1935-1941, 2004.

[60] Biju Naduvathuparambil, M. C. Valenti, and A. Feliachi, "Communication Delays in Wide-area Measurement Systems," in *Proc. of the 40th Southeastern Symposium on System Theory*, pp. 118-122, 2002.

[61] Z. J. Hu, "H∞ control of inter-area oscillations based on WAMs considering signals transmission delay," *Proceedings of IEEE ICIEA*, May 23-25, 2007, Harbin, China, pp. 1453-1458.

[62] F. P. DeMello and C. Concordia, "Concepts of Synchronous Machine Stability as Affected by Excitation Control," *IEEE Trans. on Power Apparatus and Systems*, vol. 88, no. 4, pp. 316-324, 1969.

[63] E. V. Larsen and D. A. Swann, "Applying Power System Stabilizers Part I: General Concepts," *IEEE Trans. on Power Apparatus and Systems*, vol. 100, pp. 3017-3024, 1981.

[64] M. J. Gibbard, "Coordinated Design of Multimachine Power System Stabilizers based on Damping Torque Concepts," *IEE Proceedings Generation, Transmission and Distribution*, vol. 135, no. 4, pp. 276-284, 1988.

[65] P. Kundur, "Investigation of Low Frequency Inter-area Oscillation Problem in Large Interconnected Power Systems," *Canadian Electrical. Association*, Ontario Hydro, Toronto, 1993.

[66] Systems Oscillations Working Group, "Inter-area Oscillations in Power Systems," *IEEE Power Engineering Society*, Oct 1994.

[67] J. Paserba, "Analysis and Control of Power System Oscillation," *CIGRE Special Publication 37.01.07*, Technical Brochure 111, 1996.

[68] I. Kamwa and L. Gerin-Lajoie, "State-Space System Identification-Toward MIMO Models for Modal Analysis and Optimization of Bulk Power Systems," *IEEE Trans. on Power Systems*, vol. 15, no. 1, 2000.

[69] D. N. Kosterev, C. W. Talyor, and W. Mittelstadt, "Model Validation for the August 10, 1996 WSCC System Outage," *IEEE Trans. on Power Systems*, vol. 14, no. 3 pp, 967-979, 1999.

[70] U.S.-Canada Power System Outage Tack Force: Final Report on the August 14, 2003 Blackout in the United States and Canada (on line).

[71] J. Machowski, J. Bialek, and J. R. Bumby, *Power system dynamics and stability*. Warsaw, Durham: John Wiley and Sons, 1997.

[72] P. M. Anderson and A. A. Fouad, *Power System Control and Staiblity*, 2nd ed. New Jersey: IEEE Press, 2003.

[73] M. Saidy and F. M. Hughes, "An extended block diagram transfer function model of a synchronous machine," *Electrical power & energy systems (Elsevier)*, vol. 18, pp. 139-142, 1996.

[74] C. A. Canizares, "Power Flow and Transient Stability Models of FACTS Controllers for Voltage and Angle Stability Studies," *IEEE/PES World*

Meeting Panel on modelling, Simulations and Application of FACTS Controllers in Angle and Voltage Stability Studies, Singapore, 2000.

[75] J. V. Milanovic, "The Influence of Loads on Power System Electromechanical Oscillations," in *Electrical and Computer Engineering*. Newcastle, New South Wales: University of Newcastle, pp. 191, 1996.

[76] K. Ogata, *Modern Control Engineering*, 4th ed. Minnesota: Prentice Hall, 2002.

[77] G. C. Verghese, I. J. Perez-Arriaga, and F. C. Schweppe, "Selective Modal Analysis with Application to Electric Power Systems, Part I: Heuristic Introduction, Part II: The Dynamic Stability Problem," *IEEE Trans.*, vol. PAS-101, no. 9, pp. 3117-3134, 1982.

[78] G. Rogers, *Power system oscillations*. Kluwer, 2000.

[79] M. Klein, G. J. Rogers, P. Kundur, "A fundamental study of inter-area oscillations," *IEEE Trans. Power systems*, vol. 6, pp. 914-921, Aug. 1991.

[80] M. C. Menelaou and D. C. Macdonald, "Supplementary Signals to Improve Transient Stability On-line Application to a Micro-generators," *IEEE Trans. on Power Apparatus and Systems*, vol. PAS-101, no. 9, pp. 3543-3550, 1982.

[81] A. Ferreira, J. Barreiros, W. Barra, and J. Brito-de-Souza, "A Robust Adaptive LQG/LTR TCSC Controller Applied to Damp Power System Oscillations," *Electric Power Systems Research*, vol. 77, no. 8, pp. 956-964, 2007.

[82] R. E. Kalman, "When is a linear control system optimal?," *Journal of Basic Engineering – Transaction on ASME – Series D*, vol. 86, pp. 51-60, 1964.

[83] M. G. Safonov, and M. Athans, "Gain and phase margin for multiloop LQG regulators," *IEEE Trans. on Automatic Control*, vol. AC-22, no. 2, pp. 173-279, 1977.

[84] A. E. Bryson, and Y. C. Ho, *Applied Optimal Control*. Halsted Press, Washington, D.C., 1975.

[85] B. D. O. Anderson, and J. B. Moore, *Linear Optimal Control*. Englewood Cliffs, NJ: Prentice-Hall, 1971.

[86] H. Hanselmann, "Implementation of Digital Controllers – A Survey," *Automatica*, vol. 23, no. 1, pp. 7-32, 1987.

[87] G. F. Franklin, J. D. Powell, and M. Workman, *Digital Control of Dynamic Systems*. 3rd ed. Reading, MA: Addison Wesley Longman, 1997.

[88] L. G. Van Willigengurg, “Computation of the Digital LQG Regulator and Tracker for Time-Varying Systems,” *Optimal Control Applications & Methods*, vol. 13, pp. 289-299, 1992.

[89] Y. Zang, “Design of Wide-area Damping Control Systems for Power System Low-frequency Inter-area Oscillations,” PhD thesis, Washington State University, School of Electrical Engineering and Computer Science, 2007.

[90] R. H. Middleton, and G. C. Goodwin, *Digital Control and Estimation. A Unified Approach*. Prentice-Hall, Inc., 1990.

[91] E. B. Saff, and R. S. Varga, *Pade and rational approximation: theory and applications*. Academic Press, New York, 1977.

[92] James Lam, “Model Reduction of Delay Systems using Pade Approximants,” *International Journal of Control*, vol. 57, no. 2, pp. 377-391, 1993.

[93] S. M. Kashmiri, S. A. P. Haddad, and W. A. Serdijin, “High-Performance Analog Delays: Surpassing Bessel-Thomoson by Pade-Approximation Gaussians,” *IEEE International Symposium on Circuits and Systems*, pp. 2349-2352, 21-24 May, 2006 .

[94] J. B. He, C. Lu, X. M. Jin, and P. Li, “Analysis of Time Delay Effects on Wide Area Damping Control,” in *Proc. IEEE Asia Pacific Conference on Circuits and Systems*, Macao, pp. 758-761, 2008.

[95] K. J. Astrom, and B. Wittenmark, *Computer Controlled Systems: Theory and Design*. Prentice-Hall, 1984.

[96] K. Chui Charles, and Guanrong Chen, *Kalman Filtering with Real-Time Applications*. Springer, Berlin, Heidelberg, 2009.

[97] Yang, X. J. and O. Marjanovic, “LQG Control with Extended Kalman Filter for Power System with Unknown Time-Delays,” IFAC, Italy, 2011.

[98] J. M. Maciejowski, *Predictive Control with Constraints*. Prentice-Hall. Harlow UK, 2002.

[99] H. H. Rosenbrock and P. D. McMorran, “Good, Bad, or Optimal?,” *IEEE Trans. Automatic Control*, vol. AC-16, no. 6, pp. 552-554, 1971.

[100] I. M. Horowitz and U. Shaked, “Superiority of Transfer Function Over State-Variable Methods in Linear Time-invariant Feedback System Design,” *IEEE Trans. Automatic Control*, vol. AC-20, no. 1, pp. 84-97, 1975.

[101] A. Probst, M. E. Magana, and O. Sawodny, “Using a Kalman Filter and a Pade Approximation to Estimate Random Time Delays in a Networked Feedback Control System,” *Control Theory and Applications*, vol. 4, no. 11, pp. 2263-2272, 2009.